The University Of Sheffield.

Biomass derived Activated Carbon as Electrode Materials for Electrochemical Double layer Capacitors (EDLC)

A thesis submitted to

The University of Sheffield

By

Yan Yan Farm

For the degree of
Doctor of Philosophy

Project Supervisors:
Dr. Denis Cumming
Dr. James McGregor

Chemical and Biological Engineering Department,
The University of Sheffield,
The United Kingdom.
July 2019

Acknowledgments

I would like to convey my deepest appreciation to Prof. Peter J. Hall for providing his constant encouragement and invaluable support. I would like to express my sincere gratitude to Dr. Denis Cumming and Dr. James McGregor for their understanding, patient and constant feedbacks throughout my Ph.D. writing stage and for taking over as my supervisors towards the final stages of my Ph.D. despite their busy schedule.

I also like to acknowledge Dr. Anthony Rennie and Dr. Vitor Martins for their valuable guidance in the laboratory, endless feedbacks, and helpful discussions. Without their help, this thesis would not have been completed. A further appreciation goes to Mark Jones, James Grinham and Andrew Fairburn for their technical support and advice. Thank you to Dr. Laurynas Pukenas for the endless support and guidance with the XPS analysis software. Thank you also to Stephen Atkin in the Chemistry department who performed the elemental analysis. Appreciations also go to Sorby center for providing the SEM facility and the NEXUS group at Newcastle University for the XPS analysis.

My special gratitude extended to the Ministry of Higher Education, Malaysia (MoHE) and the Universiti Malaysia Sabah (UMS) for financial support.

To my husband, Aroland Kiring, who was pursuing his Ph.D. at the Department of Automatic Control and Systems Engineering, thank you for your endless support despite the stress that you are coping in your research and challenges as new parents for our baby in Sheffield. I'm lucky to have you by my side and I cherish every single moment of my time being a mother to our first daughter, Hannah Grace. We have the privilege of watching Hannah grow up every day and that I would not want to miss out. Your positive support gives me the strength to have our newborn baby, Sarah Anne while amending this thesis. All the up and down experiences with both of you were unregretfully in my life. To my family, thank you for your encouragement and support. Thank you also to those I have failed to mention, but who have contributed directly or indirectly toward the production of my thesis.

Abstract

The development of biomass-derived activated carbon as electrode materials for electrical double-layer capacitors (EDLCs) are receiving much attention because of the environmental impacts and economic value. Most of the published work are using chemically activated carbon, there is not much research on the development of biomass-derived activated carbon (AC) using physically activated carbon for supercapacitors applications. In the present work, AC derived from five selected waste biomass were prepared using a two-step CO_2-activation method. Symmetrical two-electrode coin cell using AC derived wastes biomass as electrode material was assembled to study the electrochemical performance in the organic electrolyte, 1 M $TEABF_4$ in PC. The chemical composition and the porous structure of Marabú derived AC are greatly influenced by the carbonization heating rate and the activation holding time. M10V8 exhibits the highest surface area of $1977 m^2g^{-1}$ and delivers ~20F/g at $1Ag^{-1}$ with good cyclability. The performance of Marabú derived AC was investigated in ionic liquid [EMIM][BF_4]. Specific capacitance up to $32Fg^{-1}$ at $1Ag^{-1}$ was achieved using M10V8 in the ionic liquid system. However, great energy degradation was observed. Next, the effect of CO_2 activation temperatures (950^0C and 1000^0C) was studied using spent coffee ground (CG) as the carbon precursor. CG as carbon material which treated with activation temperature of 1000^oC and up to 100mins (C10W10) exhibited the highest specific capacitance ($22Fg^{-1}$) and energy density of ~$15Whkg^{-1}$ when operating at $400Wkg^{-1}$ in 1 M $TEABF_4$ in PC. AC with the activation temperature of 950^0C only provides specific capacitance of less than $3Fg^{-1}$. This elucidated that the AC properties are strongly dependent on CO_2 activation temperature applied. High burn-off and high thermal sensitivity have limited the possibility of rubberwood (RW) in EDLC applications. Although same activation condition was applied to produce ACs from Malaysia wood pellets (MS) and oil palm empty fruit bunch pellets (EFB), porosities and surface area of ACs highly depends on the selection of biomass as the activated carbon precursors. An ideal EDLC CV curve without any Faradaic reaction was observed although high ash content is observed in both biomass-derived ACs. The impurities, however, accelerated the cell aging problem with great energy loss. Overall, this research has proven the great potential of CO_2 activation to prepare high surface area AC from biomass for EDLC applications.

Table of Contents

List of Figure

List of Table

1 Introduction

1.1 Background and motivation

Energy is the key driver for the sustainable development of economic and social growth in the world. Based on BP 2017 data [1], fossil fuel is the world's leading primary sources for industrial, transportation, electricity, commercial and residential sectors, which accounts for 87% of the world's total energy consumption in 2015. The World Energy Council 2013 [2] estimated that in the year 2050 the energy consumption will reach nearly double as compared to the current consumption due to the rising of the world population. A steep increase of global energy consumption and depletion of fossil fuel are motivating the world towards cleaner energy resources to meet with the global energy demand. Based on recent BP's Energy outlook 2017, global energy demand will increase by 30% in the year 2035 and the renewable energy is projected to be the fastest-growing source of energy (7.6% of average rate per year), which generated from solar geothermal, biomass, biofuels and wind sources (Figure 1-1).

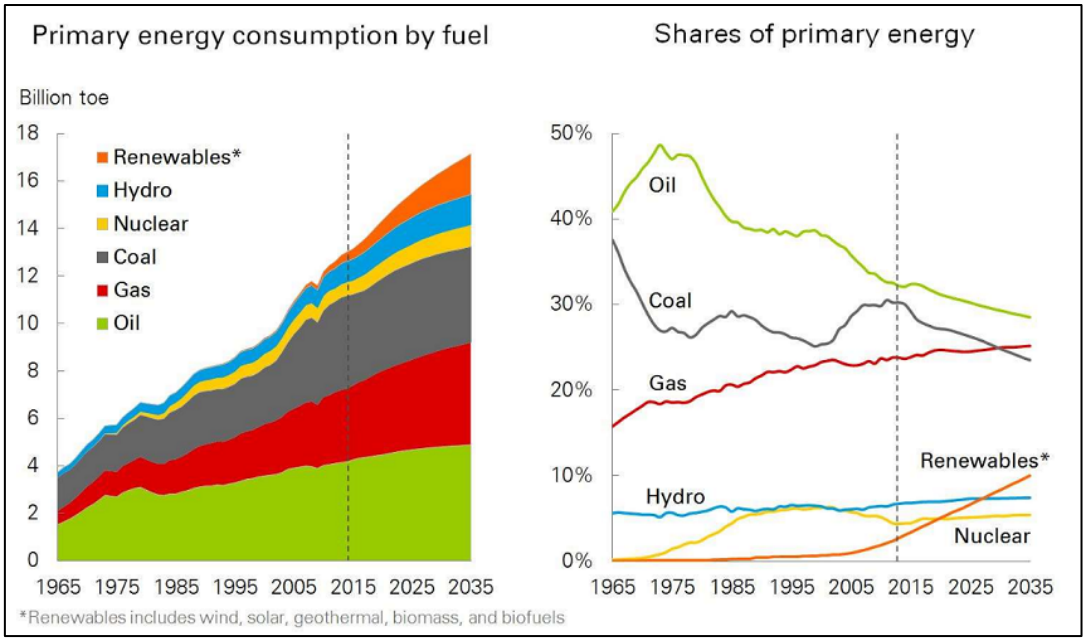

Figure 1-1: World primary energy consumption and shares of primary energy in 1965 - 2015 and projection until 2035.[1]

In the UK, the energy contributed from the renewable energy sources such as wind, hydropower, and wastes biomass has increased from 1% in the year 1998 to 9% of the total UK energy consumption in the year 2015[3]. From Figure 1-2, the primary production of energy from renewable sources in the European Union (EU) countries has risen by three times in the year 2016 as compared to its value in the year 1990. By the year 2020, the EU is projecting to raise nearly four times of its renewable energy production from wind, biomass and hydro as compared to the year 1995. In this case, energy storage systems such as supercapacitors can contribute to balance the power grids and maintain stable and safe electricity supply. Electricity from an intermittent power plant such as wind power, tidal power, and solar power can be stored in an energy storage system during the energy harvesting period to maintain the supply of energy to demand when the production falls below the consumption.

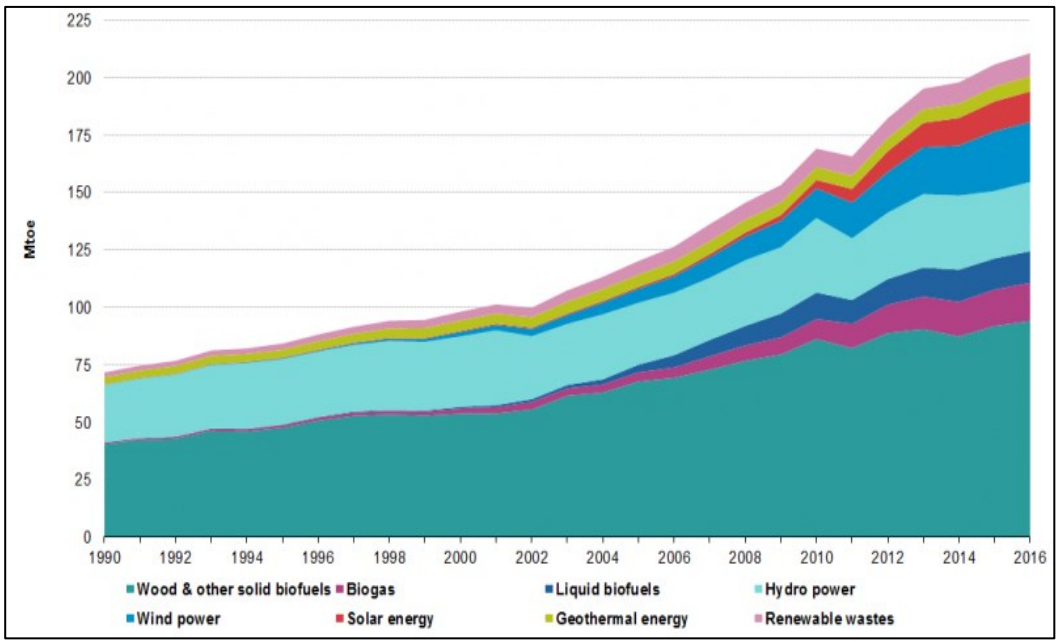

Figure 1-2: Primary production of energy from renewable sources EU 1990-2016[4]

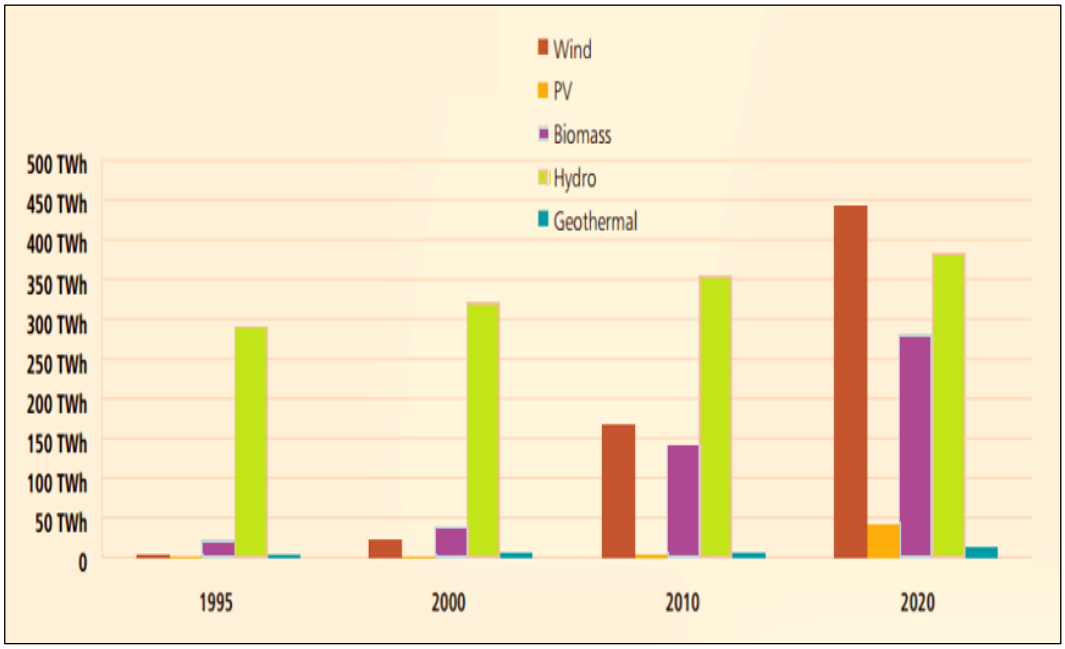

Figure 1-3: EU target for renewable energy production (1995 to 2020)[5]

Moreover, a smaller, lighter and thinner size of energy storage systems is more practical to be embedded with the current electronic devices such as laptops, smartphones, notepads, global positioning systems, and etc. This allows the users to carry and use the portable electronic devices in any place even in a case of power disruption. The supercapacitor is the energy storage system with higher cycling efficiency (~98%), an enhanced power density and a better cycle lifetime (~10^6) when compared with batteries [6] has the potential in above applications.

According to one of the Europe based market research company, IDTechEx, the supercapacitor market is expected to grow up to a value of $ 6 billion USD in the year 2024 [7], and about 30% compound annual growth rate over the next decade where the market is expected to further expand in transportation and grid leveling sectors (Figure 1-4). There is a proven example in-vehicle application that an additional supercapacitor system allows the hybrid Toyota TS040 car racing to be used as a temporary four-wheel car drive by boosting the engine power from engine 530HP up to 830HP.

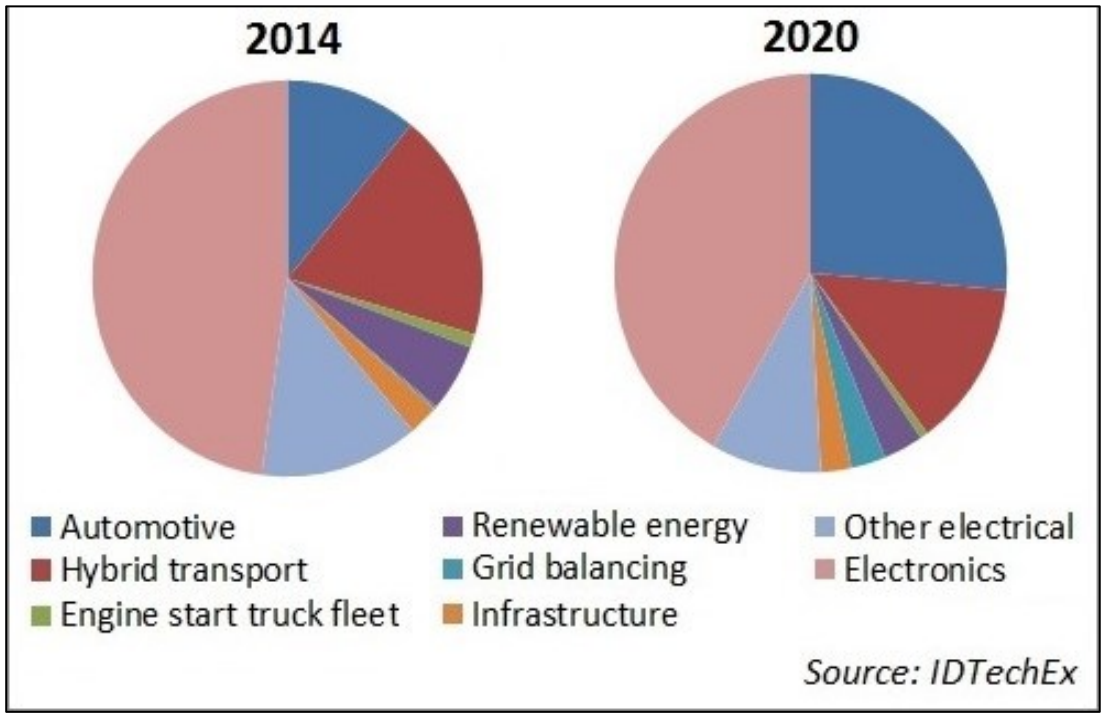

Figure 1-4: Supercapacitor global market applications in the year 2014 and 2020[7]

Figure 1-5 illustrates the Ragone plot for various energy storage devices. The main limitation of EDLC is its low specific energy as compared with batteries. The current specific energy achievement for supercapacitors is limited around 5-10Whkg^{-1} [8, 9], which is 3 to 15 times lower than that of batteries. In order to realize the potential of supercapacitor in a wide range of applications, various attempts are made to increase their energy density. The energy density of a supercapacitor is proportional to the electrochemical stability window (ESW) of its electrolyte. The current development of supercapacitors involved in replacing their electrolyte with a higher ESW such as an organic electrolyte (~2.5V) or an ionic liquid (~3.5V) [10, 11]. In additions, another form of carbons such as carbon nanotubes, carbide-derived carbon, carbon aerogel, and graphene are also explored to investigate their potential as an electrode material for the energy storage systems. However, most of the systems are restricted by the high production costs and difficulties in mass production to meet with the demand of commercial markets [12].

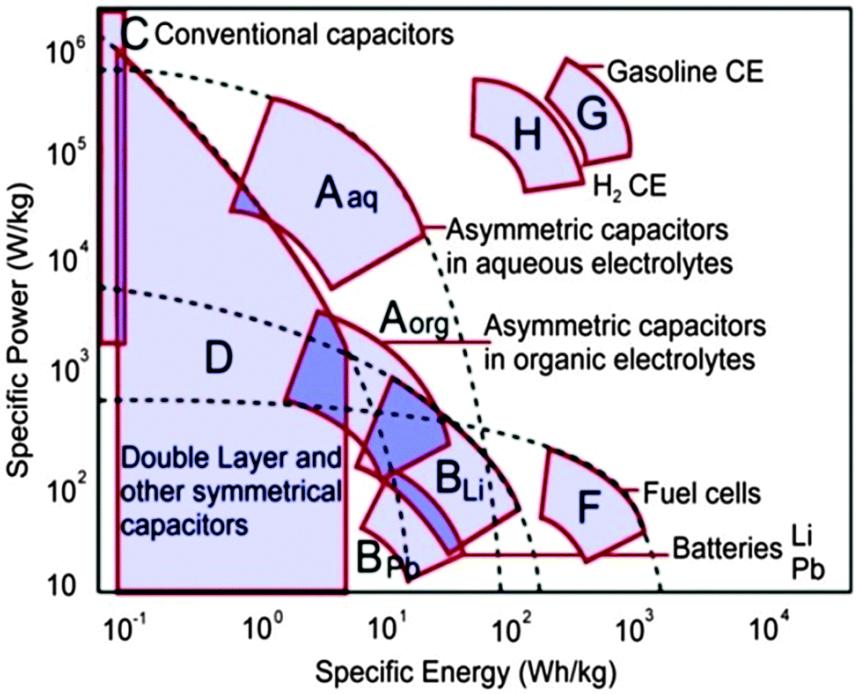

Figure 1-5: Ragone plot (specific power against specific energy) for various energy storage devices [13]

Based on the energy storage mechanism of supercapacitors, their capacitance depends greatly on the specific surface area of activated carbon (AC). Thus, there are various carbon activation methods to create a higher surface area of AC. To date, most of the recent reported activated carbons derived from biomass are prepared by chemical activation to achieve higher surface area [14]. However, irregular morphology and structure of AC were observed with chemical activation [15]. Chemical activation also leads to AC surface doping and thus this hinders from a clear understanding of the actual charging-discharging process of supercapacitors. The additional cost is also involved for post-process to remove the excess chemical from the AC. Some of the chemicals such as zinc salt or phosphoric acid might possibly produce secondary environment pollutant as disposal [16].

As compared with chemical activation, there is no much study using CO_2 activated carbon derived from biomass as electrode material for supercapacitors applications. CO_2 activation involves no extra post-process to purify the AC and it does not involve any harsh chemical. Thus, the original structure of AC is preserved. It is beneficial to investigate the correlation between the operating principle of an EDLC system and the original structure of AC. Recently, an outstanding performance was reported with AC derived spore as a symmetrical two-electrode cell in the organic electrolyte with high current density up to $20Ag^{-1}$, good cycling and thus leads to a high energy density of 57 W h kg^{-1} and power density of 17 kW kg^{-1} [15]. Thus, this has proven the potential to produce biomass-derived activated carbon using CO_2 activation.

Generally, ACs are produced at relatively low cost nowadays. The production cost of a high-performance AC is about half of the production cost of supercapacitor [17]. Thus, lowering the production cost of high-performance AC for supercapacitor applications is one of the targets to meet the massive market demand in the future. Recently, research interests have been devoted to the preparation of AC from wastes biomass as electrode materials for supercapacitor applications and proven comparable performance as compared with the performance of commercial supercapacitors.

1.2 Aim and Objectives

Most of the reported work on activated carbon derived from biomass are using chemical activation. Despite there is a proven outstanding performance of supercapacitor using of AC derived from spore using physical activation[15], there is not much research on activated carbon derived from biomass using physical activation as electrode materials for EDLC applications. Therefore, the core objective and focus of this thesis are to convert the selected biomass waste as high surface area activated carbon using CO_2 physical activation and characterized to investigate the potential of the biomass as electrode material for electrochemical double-layer capacitor (EDLC) applications.

The objectives of this research project are as follow:

1. To convert the selected biomass (Marabú wood, spent coffee ground (CG), oil palm empty fruit bunch pellets (EFB), rubberwood stem (RW) and Malaysia wood pellets (MW)) to high surface area activated carbon (AC) using CO_2 physical activation.
2. To characterize and investigate the potential of the prepared ACs as electrode materials for EDLC applications.
3. To evaluate the electrochemical behavior of ACs derived biomass as electrode materials for EDLC application in organic electrolyte.
4. To evaluate and compare the electrochemical behavior of ACs derived Marabú as electrode material for EDLC in organic electrolytes and ionic liquid.
5. To investigate the correlations between the operating principle of EDLC and the properties of AC derived from biomass by comparing their performance with commercial ACs as the electrode materials in EDLC

1.3 Outline of the thesis

This thesis contains 9 chapters, there are:

i. Chapter 1 presents the background and motivation of this thesis project, hypothesis, the aim and objectives of the study.
ii. Chapter 2 presents a literature review on the working principle, the current development activation methods, electrolytes, and biomass-derived AC as electrode materials for supercapacitors.
iii. Chapter 3 contains the characterization of precursors, the preparation and characterization of AC. The procedure to prepare the symmetrical two-electrode coin cells and electrochemical characterization of EDLC is also presented in this Chapter.
iv. Chapter 4 discusses the research results of thermal analysis and characterization of precursors and ACs.
v. Chapter 5 presents the overall electrochemical performance of EDLC using AC derived from Marabú in the organic electrolyte and ionic liquid.
vi. Chapter 6 presents the effect of CO_2 activation temperature on the preparation of AC derived from spent coffee grounds (CG) used as carbon electrode material in an organic electrolyte based EDLC.
vii. Chapter 7 involves the study of the potential of three wastes biomass from Malaysia agriculture industries used as electrode material for EDLC application based on the experimental data of capacitive behavior and also the resistance of the systems.
viii. Chapter 8 provides an overall discussion on the effect of the properties of the prepared ACs derived from selected biomass on the electrochemical performances of the symmetrical two-electrode EDLC.
ix. Chapter 9 elucidates an overall conclusion, the key contribution of this project and the suggestions for the future work of this project.

2 Literature Review

In this chapter, the background overview of the activated carbon (AC) derived from biomass as carbon electrode materials for EDLC application is presented. The first part of this chapter focuses on the working principle, the configuration of an EDLC and the common performance evaluations for an EDLC, reviewed in section 2.1-2.3. Electrolytes and electrode materials as key factors influencing the electrochemical performance of an EDLC are reviewed in section 2.4-2.5. Activated carbon is used as the common active material in the electrode of an EDLC. Two common activation methods for the preparation of ACs from biomass used as the carbon precursors, physical and chemical activation methods are reviewed in section 2.6. The latest review of the biomass-derived AC for EDLC application and the details of the biomass selection for the project are presented in Section 2.7. Finally, a summary of the chapter is presented in Section 2.8.

2.1 The Working Principle and properties of Supercapacitors

Supercapacitors also knew as electrochemical double-layer capacitors (EDLCs) or ultracapacitors are high-power electrochemical energy storage devices. As compared to an ordinary capacitor, supercapacitors can store much higher capacity and energy density due to the high surface area of the active material in electrodes. Although the structure of a supercapacitor is quite similar as compared to a battery, the mechanism of energy storage in supercapacitors is different as they store energy electrostatically on the surface of the active material without involving any redox reaction. Moreover, EDLCs provide higher charge-discharge rate (60-120s) since EDLC achieves charging and discharging through simple adsorption and release of ions without involving any redox reaction. Besides, EDLCs has high cycling efficiency (~98%), enhanced power density (more than 1000-1500Wkg^{-1}) and excellent cyclability (~10^6 cycles) [6, 18].

An EDLC consists of two high surface area porous electrodes immersed in an electrolyte and isolated by a porous separator. Supercapacitor electrodes are usually a mixture of AC with a polymer binder and high conductivity materials. Carbon black (CB) is commonly used as an additive to improve the conductivity of electrode with not more than 5% mass in electrode [19]. Polytetrafluoroethylene (PTFE) or polyvinylidene fluoride (PVDF) are commonly applied as polymer binder in the supercapacitor electrode. The selection of separator is important to avoid self-discharge or any chemical reaction with electrolyte and at the same time have good ionic conductivity and ion movement during the charge and discharge process[20]. Current collectors are essential in an EDLC to conduct the electrical current from each electrode. Metal foil or polymer-coated on carbon can be used [21] as current collectors for the

energy storage system. Aluminum is commonly used metal as the current collector for EDLC due to its low cost, durability and the stability in organic and IL electrolyte. They are several other metals current collectors available such as Nickel foils [22], Copper, platinum and stainless steel. The selection of current collector for EDLC is based on its high chemical resistivity and anti-corrosive with the electrolytes.

The charging process of an EDLC starts when voltage is applied across its porous electrodes, the positive electrode attracts the opposite sign of electrolyte ions and charges accumulate on the surface of the electrode, while the negative electrode attracts positive electrolyte ions. The EDLC delivers energy when the discharging process occurs. Generally, a pure EDLC store energy based on electric double-layer capacitance from charge accumulation on the surface if both electrode surface without any charge transfer involves across the interface between electrolyte and electrode.

Besides of the electric double layer behavior, a supercapacitor also can store energy by involves rapidly reversible redox reactions on the electrode surface, which is called as Pseudocapacitor. Pseudo-capacitance occurs when carbon electrode contains functional groups, which create chemical and electrochemical interactions with electrolyte in the cell [23]. This effect can be further enhancing the specific capacitance of a supercapacitor by coupled with the EDL capacitance. When the enthalpy of ion-electrode interactions deviates weakly from its average value, the pseudo-capacitance will exhibit a sharp peak at certain voltage values. The presence of the sharp peaks (redox peaks) in CV curve signatures of the redox charging process. The difference between the faradaic reaction in batteries and in supercapacitors is the reactions in supercapacitors are a rapid reversible process without any phase change of electrode molecules or chemical bonds. The pseudo effect is attributed by the attachment of the de-solvated ions (redox ions) on the same charges electrode surface as shown in Figure 2-1. Besides, there are ion pairs with solvent (solvated ions) appear in the solvent could hinder the ion diffusion on the electrode surface in the capacitor devices[24].

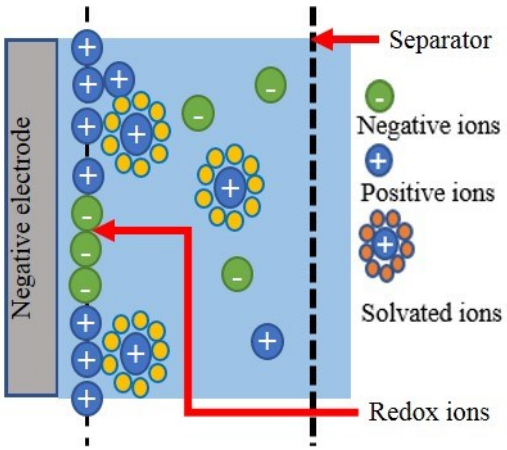

Figure 2-1: Simplified diagram of a double layer with redox ions which contributed to the faradaic charge-transfer of the pseudocapacitance.

2.1.1 The Double Layer Mechanism

Based on the electric double layer mechanism, the energy storage of EDLCs is dependent on the interfacial area between the electrolyte ions and the electrode. The electrolyte ions distribute themselves across the separator and attach to the surface of the pores in the active materials. Thus, high surface area and the proper pore size of electrode materials that fit the size of the ion of electrolyte are important to enhance the energy storage[25, 26].

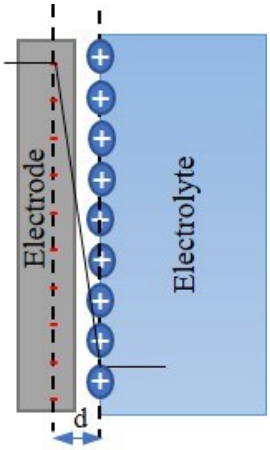

Figure 2-2: The Helmholtz layer

There are three models of the electrical double layer introduced to describe the behavior in EDLC: (a) the Helmholtz model, (b) the Gouy-Chapman model and (c) the Stern model. The Helmholtz model describes the double layer effect by two surfaces of opposite charge and is separated by a small distance (Figure 2-2) which depends on the concentration of the electrolyte and the size of the ion [27]. The Gouy-Chapman model further improved the Helmholtz model by considering the charge distribution of

ions due to thermal motion, as referred to a diffuse layer (Figure 2-3). However, The Gouy-Chapman model overestimated the performance of highly charged EDLCs. Stern's model, which is a combination of the Helmholtz model with the Gouy-Chapman model was introduced with two clear regions of ion distributions: The capacitive contribution of the Helmholtz layer (C_H) and the diffusion layer (C_D). The capacitance of double layer (C_{DL}) can be expressed as Equation 2-1[28]:

$$\frac{1}{C_{DL}} = \frac{1}{C_H} + \frac{1}{C_D} \qquad \textbf{Equation 2-1}$$

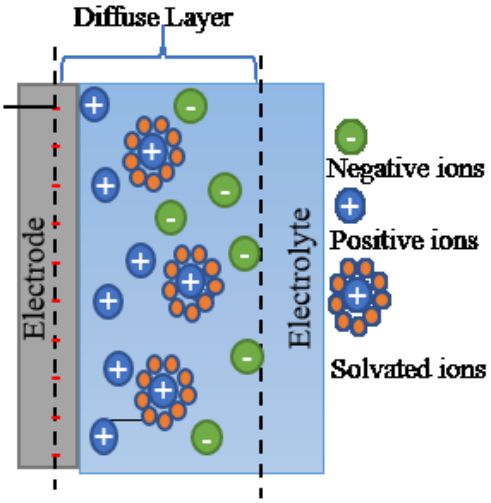

Figure 2-3: The Stern model

Grahame model (Figure 2-4) further detailed the Stren's model by divided the Stern layer as the inner Helmholtz plane (IHP) and outer Helmholtz plane. The IHP passes through the center of the specifically adsorbed ions (ions in direct contact with an electrode) while the OHP passes through the centers of non-specifically ions (those solvated ions).

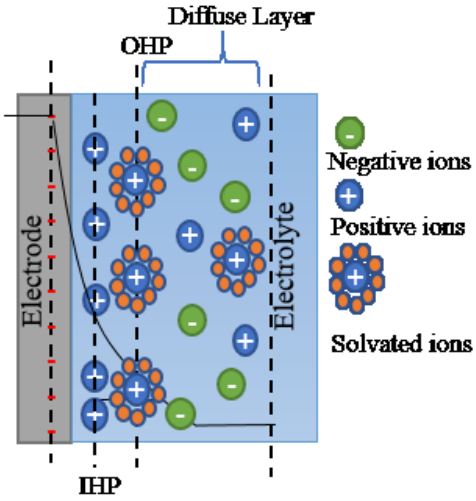

Figure 2-4: The Grahame Model

2.2 Two-electrode vs Three-electrode EDLC

Symmetrical two-electrode or three-electrode cells are commonly assembled for EDLC performance evaluation. Three-electrode cells are usually assembled for research purposes [21] which consists of a working electrode (WE), a counter electrode (CE) and a reference electrode (RE) as shown in Figure 2-5(a). The WE is generally coated with active materials such as activated carbon or another form of carbon that is under study. A CE is an electrode to measure the potential of the WE without participating in the electrochemical reaction of the cell. It usually made of inert material such as platinum, gold or glassy carbon. The total surface of a CE is higher than a WE to avoid it being the limiting factor in the kinetics of the electrochemical process as the current is flowing between the WE and the CE. While the RE is used to provide a stable potential for controlled regulation of the working electrode [29] and allows the measurement of the potential of the WE without passing the current through.

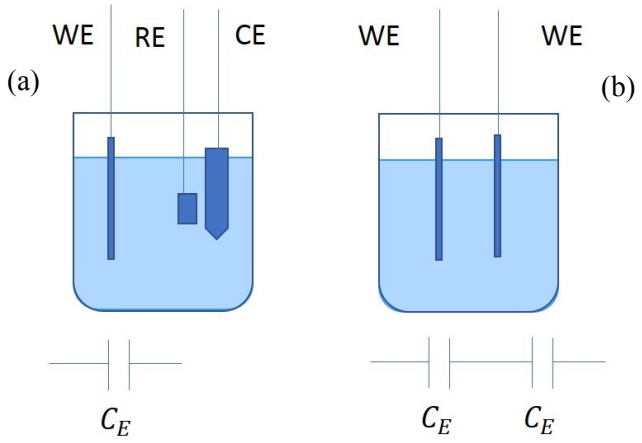

Figure 2-5: Schematic view of (a) Three-electrode and (b) two-electrode cell setup. The working electrode (WE), Reference Electrode (RE) and Counter electrode (CE)

The set-up of three-electrode and two-electrode cells can lead to differences in capacitive value. The measurement of the capacitance for three-electrode cells is usually higher than the real two-electrode devices[21, 30]. Despite the lower capacitance value, the measurement of two-electrode cells better represents the actual performance of the EDLCs real practice [28]. There are two symmetrical working electrodes in a two-electrode cell as shown in Figure 2-5(b).

Assuming the mass of active electrode material as *m*, the capacitance of a single electrode (C_E) is equal to the specific capacitance (C_{3e}) of the three-electrode cell, which can be calculated by dividing by the mass of active electrode material as shown in Equation 2-2.

$$\boldsymbol{C_{3e} = \frac{C_E}{m}} \qquad \textbf{Equation 2-2}$$

For a symmetrical two-electrode cell, which is equivalent to a practical EDLC, the total capacitance (C_{t2e}) can be obtained using Equation 2-3.

$$\boldsymbol{\frac{1}{C_{t2e}} = \frac{1}{C_E} + \frac{1}{C_E}} \qquad \textbf{Equation 2-3}$$

Since the mass from each electrode in the symmetrical two-electrode cell is equal, the relationship of the capacitance from the two-electrode cell and a single electrode in the measured three-electrode as in Equation 2-4,

$$\frac{1}{C_{t2e}} = \frac{2}{C_E}$$ **Equation 2-4**

By considering the specific capacitance of each electrode is identical, thus the specific capacitance (C_{2e}) of two-electrode cells as Equation 2-5,

$$C_{2e} = \frac{C_{t2e}}{2m} = \frac{C_E}{4m}$$ **Equation 2-5**

By comparing the Equation 2-2 and Equation 2-5, the specific capacitance of a three-electrode system is 4 times of a two-electrode cell [21, 28, 30] as in Equation 2-6.

$$C_{3e} = 4C_{2e}$$ **Equation 2-6**

In this work, two-electrode EDLC was assembled to reflect the actual specific capacitance as a real commercial device.

2.3 The performance evaluation of EDLCs

Generally, the performance of an EDLC can be determined based on (a) the capacitance, (b) the power density, (c) the energy density (d) the cyclic stability and the (e) equivalent series resistance (ESR) of the cell. Capacitance is the ability of an EDLC to hold energy by accumulating electric charges on the surface and its electrodes. The capacitance can be measured by Equation 2-7, where C represents capacitance (Farads), Q symbolizes charge (Coulombs) and V represents the potential (Volts).

$$C = \frac{Q}{V}$$ **Equation 2-7**

The energy stored in an ideal EDLC is proportional to the capacitance (C) and the square of potential (V) or ESW of electrolyte as represented by Equation 2-8.

$$E = \frac{1}{2}CV^2$$ **Equation 2-8**

Thus, the specific energy or energy density is calculated by the amount of energy stored per unit mass of the active material of the cell.

The specific energy ($Whkg^{-1}$) can be derived from galvanostatic experiments over the duration of the discharge, t_d (s) [31, 32] as shown by Equation 2-9, where *m* represents the total active mass in both electrodes.

$$E_{specific} = i \int \frac{V}{3.6\ X\ m} . dt \qquad \textbf{Equation 2-9}$$

The specific power (Wkg^{-1}) of an EDLC can be derived by considering the specific energy over the discharge time using Equation 2-10.

$$P_{specific} = \frac{E_{specific\ X\ .3600}}{t_d} \qquad \textbf{Equation 2-10}$$

ESR is one of the non-ideal behaviors of an EDLC. A high value of ESR represents the high internal resistance appears in the cell which degrades the performance by showing a high IR drop, noise or high potential drop. The IR drop from the discharge curve of the GC test is the common method to evaluate the ESR[21]. By applying Ohm's law, the ESR can be determined using Equation 2-11.

$$R_{ESR} = \frac{\Delta V}{\Delta I} \qquad \textbf{Equation 2-11}$$

There are various methods employed in research and industries to evaluate the performance parameters of an EDLCs. Among all the evaluation methods, Cyclic voltammetry (CV), Galvanostatic charge and discharge (GC) and electrochemical impedance spectroscopy (EIS) is commonly applied to evaluate the performance of EDLC. The capacitance, power and energy densities and equivalent series resistance (ESR) of an EDLC can be calculated from three basic parameters (potential, current and time).

2.4 Electrolytes

The type of electrolyte applied in the cell has a great effect on the capacitance of the EDLC. Each type of electrolytes has different electrochemical stability window (ESW). The ESW of an electrolyte is the potential range, which an EDLC operates without any decomposition or oxidation of its electrolyte. Based on the Equation 2-8, the energy of an EDLC is proportional to the square of potential (V) or the ESW of the electrolyte.

Thus, an electrolyte with wider ESW delivers higher energy density. In addition, other properties of EDLC such as internal resistance, the rate of energy released, operating temperature range and cyclic stability are greatly affected by the selection of the electrolyte [33]. The solubility and viscosity of electrolyte can greatly affect the thermal stability and the operating temperature range of EDLCs. In general, the liquid electrolytes for EDLCs application are categorized into three major types: aqueous electrolytes, organic electrolytes, and ionic liquids.

Besides of the ESW of the electrolytes can bring impact on the performance of an EDLC, ion size and matching between pore size and ion size are also the factors that affect the capacitance of the supercapacitors [33]. However, there are limited findings discuss the correlations between the performance of EDLC and the pore size of the electrode materials in a different type of electrolytes system. Zeller et. al. [34] found that the contribution of the effective surface area to the capacitance of an EDLC is varies depending on the electrolytes used. The capacitance of the EDLC depends on the specific surface area of the electrode materials in the acid-based electrolyte system. While the capacitance depends only to the external surface area in an organic-based system. The finding is contrary to as reported by Zhou et. al. [35] that the specific capacitance is influenced by the specific surface area and the high mesoporosity of activated carbon in organic electrolyte based supercapacitors.

2.4.1 Aqueous Electrolytes

Aqueous electrolytes can be categorized into acidic, alkaline, and neutral electrolytes. Among all the electrolytes used, KOH[36-41] and H_2SO_4 [42-45] are the most used electrolytes for EDLC research purposes in published literature. Aqueous electrolytes are attractive due to their high conductivity, low cost, thermally stability and easy to assemble in the atmosphere.

Aqueous electrolytes have high conductivity as compared to organic and IL electrolytes. The ionic conductivity of 30% H_2SO_4 electrolyte achieves a high value up to ~1Scm^{-1} [46], while organic electrolyte, $TEABF_4$/PC only exhibits ionic conductivity of ~0.02Scm^{-1} [47]. The higher ionic conductivity of electrolyte in an EDLC leads to a lower equivalent series resistance (ESR) and provides a better power density in an EDLC[23] with faster charge and discharge stages. However, the operating voltage of an aqueous-based EDLCs is relatively low (~1V) due to the narrow ESW (1.299V)[28]. Moreover, the aqueous electrolyte is easily electrolyzed to generate gases which cause problems such as swelling. The use of acid electrolytes could lead to corrosion problems in the cell, hence cell component which made of gold or platinum is necessary to overcome this problem. The operating temperature ranges are also restricted to the water freezing point and boiling point.

Various attempts have been reported to further extend the ESW of aqueous electrolytes. The ESW was extended to 2.3V for 5M $LiNO_3$ aqueous electrolyte by the constant current method [48]. Attention to different electrode materials to improve the ESW of an aqueous solution such as the use of carbon nanotubes with MnO_2 has resulted in an ESW of 2V for KNO_3 aqueous solution[49]. However, the maximum ESW is still restricted at about 2V [50] which is yet below the ESW of commercially available organic electrolytes (~2.5-2.7V) [18] Currently, the maximum ESW of 3.2V was reported using a saturated aqueous electrolyte of sodium perchlorate without producing any gases[50].

2.4.2 Organic Electrolytes

The organic electrolyte also called as the non-aqueous electrolyte. As compared to aqueous electrolytes, organic electrolytes are compatible with Al components in a cell which reduces the cost of a device. Although organic electrolytes are lower in conductivity, higher cost and requires more complicated assembly procedure as compared to aqueous solutions, most of the commercially available supercapacitors are using an organic-based electrolyte with wider ESW [18, 51]. As refer to the Equation 2-2, the wider ESW provide a significantly higher in both energy and power densities of an EDLC. Most of the commercial EDLCs use organic electrolyte in ESW range of 2.5-2.7V with either acetonitrile (ACN) or propylene carbonate (PC) as solvents[33]. PC as the preferable employed organic electrolyte although ACN showing much lower internal resistance than PC[28]. As referred to Table 2-1, the viscosity of ACN (0.3mPa s) is comparatively lower than PC (2.5mPa s) at a temperature of 25°C[51]. However, ACN suffers from high toxicity and flammability properties. Thus, PC have considered as a safer alternative for ACN. In order to operate in maximum ESW of electrolyte, the water content is needed to be ensured lower than 5ppm [52].

Table 2-1: Physical properties of PC and ACN with 0.65M of TEABF4 at 25°C [33]

Type of solvent	Relative permittivity	viscosity (cp)	Boiling point (°C)	Melting point (°C)	Molecular weight	Ionic conductivity ($mScm^{-1}$)
PC	65	2.5	242	-49	102	10.6
ACN	36	0.3	82	-49	41	49.6

In general, the specific capacitance in aqueous-based EDLCs is higher than the organic-based electrolyte [34, 44, 53]. As compared to the aqueous electrolytes, the sizes of cation and anions are larger for organic electrolytes[33]. This might limits the diffusion of electrolyte ions through the pores

of the carbon materials that smaller than the electrolyte ions. Therefore, it is important to have a matching pore size with the electrolyte ions to enhance the specific capacitance of an EDLC.

2.4.3 Ionic Liquids

Ionic liquids (IL) are room temperature molten salts with a low melting point below 100°C[54]. An IL usually consists of the high asymmetric size of cations and anions. This unique combination allows ILs to have the flexibility to tune its physical and chemical properties by modifying the substituent groups or the cation/anion pair [55-57]. Owing to their unique properties, ILs have received high attention as alternative electrolytes for EDLC[31, 32, 58-60]. In addition, ILs have the advantages of high thermal and chemical stability, non-flammable nature and the negligible volatility[31, 32]. Higher power and energy densities of IL-based EDLCs have been reported as compared to organic and aqueous based EDLCs, which is attributed to their wider ESW (3.5-4V) among all the types of electrolytes available for EDLCs[10, 61].

However, the relatively low ionic conductivity (~0.01scm^{-1})[62] and high viscosities of ILs hinder their practical use in commercial EDLC markets. As refer to Table 2-2, $EMIMBF_4$ has a relatively high ionic conductivity of 14mS cm^{-1}. However, this is still much lower as compared to the conductivity of organic electrolytes as given in Table 2-1. Furthermore, the viscosity of $EMIMBF_4$ [51] is comparatively much higher than the viscosity of ACN based or PC based organic electrolytes with a viscosity of 0.3 cp and 2.5 cp, respectively (Table 2-1). The ILs could be problematic to operate at low temperature as ILs have a low melting point of just above 273K[28]. At different temperature condition, ILs contains varies the length of hydrocarbon chains and so as the size of the cations with varies sizes of solvated and un-solvated ions, hence it is important to study the matching between the size of carbon electrode with the size of electrolytes ions[63]. Besides, the cost of ILs is much higher than organic electrolytes with complicated handling procedure, to ensure there is no water content in the IL.

Table 2-2: Physical properties of EMIMBF4, IL at 25°C

Type of solvent	Relative permittivity [64]	viscosity (cp) [51]	Boiling point (°C)	Melting point (°C)	Molecular weight	Ionic conductivity (mScm^{-1})[65]
$EMIMBF_4$	13.9±0.4	41	>350	15	197.97	14.1

2.5 Electrode Materials

The capacitance and energy storage of an EDLC is highly dependent on the characteristics of the electrode material used. Based on the double layer mechanism of EDLCs, the specific surface area of the electrode greatly influences the capacitance of a cell. However, the measured capacitance is not linearly proportional to the specific surface area of the electrode materials[51, 66, 67]. The surface area of the electrode materials does not fully contribute to the capacitance in EDLC. If the pore size of the carbon material could be smaller than the electrolyte ions and hinders the accessibility of electrolyte ions[60]. The matching pore size of the electrode materials with the electrolyte ions greatly enhances the double layer capacitance[33, 58]. In addition, the functional groups on the carbon surface are found to be beneficial for the performance of EDLC by improving the wettability of materials and creating the Faradaic effect[67, 68]. Therefore, there have been various attempts to creates new electrodes materials to enhance the capacitance of EDLCs.

Generally, there are three major categories of electrode materials for EDLC and pseudo- capacitor applications: (a) carbon-based (b) conductive polymer and (c) metal oxides[66]. Conductive polymer and metal oxides materials are considered as Faradaic materials[66], which are contributing to the charge storage and involving reversible surface redox reaction. An overview of electrode materials for EDLC and pseudocapacitor is given in Table 2-3.

Table 2-3: Common electrode materials for EDLC and pseudocapacitors

EDLC	Pseudocapacitor
• Activated carbon (AC)[12, 69-71]	• Conductive polymers [77]
• Graphene[72, 73]	• Metal oxides [78]
• Carbon nanotubes (CNT)[74]	• Metal hydroxides[79]
• Carbide-derived carbon[75]	• Functionalized carbon[80]
• Carbon aerogels[76]	
• Templated carbons[61]	

2.6 Activated Carbon

AC with the high surface area is widely used for industries applications, such as air and water purification, food and beverage, pharmaceutical, catalytic function[81]. Virtually all AC for supercapacitors productions is using coconut shells as precursors[17]. Conversion of biomass wastes to

high-value-added products such as AC with high surface area is one of the effective ways to reduce the environmental impact of biomass wastes disposal issue.

Generally, physical activation and chemical activation are the common active methods to convert biomass to activated carbon based on different experimental conditions. Single or two-step process can be applied in the preparation of AC using chemical activation. For conventional activation method, physical activation in which a two-step process involving pyrolysis or carbonization process, followed by activation to prepare AC.

2.6.1 Carbonization

Carbonization is a thermal degradation process for converting organic materials to carbon-rich residues through pyrolysis in the absence of oxygen. The carbon-rich residues also called as char, bio-oil and combustible gases are derived from the process. Carbonization is an essential step to remove the excess moisture and volatile in the biomass prior to physical activation. The carbonization temperature is associated with the energy to break the chemical bonds of the biomass to form the fundamental carbon structure and the porosity on the char[82].

Various studies focus on the carbonization temperature and the heating rate to control the yield and the composition of the carbonized samples [82-90]. There is a study reported that the lower surface area of char derived from rice straw at the high heating rate at a heating temperature of 900^{o}C[91]. Similar observation on the pyrolysis of oil palm frond fiber by reducing the heating rate from 30 to 10^{o}Cmin^{-1}, the specific surface area of the char increases from 398 to 555m^{2}g^{-1} [82]. In contrast, surface area and pore volume increase with the heating rate were observed on char derived from eucalyptus [84]. Cetin et. al. [92] explained that at high heating rate led to the char reactivity and thus larger porosity formed. Although there are several studies on the effect of heating rate, there is still no consistency conclusions on the structure and porosity of the char production.

2.6.2 Activation

Activation process creates and enhances the porosity of char by removing disordered regions and blockage by decomposed volatile. However, the increase in porosity and surface area of activated carbon dependents on the properties of the precursors, the carbonization conditions and also the selection of activation method[28]. Different methods such as physical, chemical, physiochemical (a

combination of chemical and physical activation) and microwave-induced activation are being employed for the preparation of activated carbon.

2.6.3 Chemical activation

Chemical activation involves chemical active agent such as phosphoric acid (H_3PO_4), Zinc chloride ($ZnCl_2$), Sodium hydroxide (NaOH), potassium carbonate (K_2CO_3), Ferric chloride ($FeCl_3$), and potassium hydroxide (KOH) [14, 81] to enhance the surface area and pore volume of ACs. Chemical activation process usually involves only a single-step process, which allows volatile removal and activation integrated into a single step at a relatively lower temperature simultaneously. In the activation process, the chemical acts as a dehydrating or oxidizing agent to intensify the pyrolytic decomposition and reduce the production of volatile products, resulting in charring and development of the porous structure. Activated carbons (ACs) prepared by chemical activation show higher specific surface areas, a better porous structure and higher yields than those prepared by physical activation [81, 93, 94]. Thus, it can be seen from Table 2-5 that most of the biomass-derived ACs are prepared by chemical activation as electrode materials for EDLC. Among all the chemical activating agents, KOH is the most popular chemical activating agent. KOH activation produces AC with the high specific surface area up to $4000 m^2 g^{-1}$ and well-defined pore size distribution[95]. However, the actual activation mechanism of KOH activation is snot clearly understood by researchers yet.

There are also some disadvantages of chemical activation process such as corrosiveness of the process. Chemical activation leads to surface doping [71] and additional functional groups [96] and also harsh chemicals can affect the structure and morphology[15]. An additional washing stage is needed after the chemical activation process to remove excess activating agent which results in additional costs for the production of electrode materials production. Some of the chemicals such as zinc salts or phosphoric acids might possibly produce secondary environment pollutant as disposal [16, 97].

2.6.4 Physical activation

Generally, physical activation requires a two-step process. It involves carbonization of raw materials to remove volatile in biomass (refer to section 2.6.1) followed by activation in the presence of an oxidizing agent such as carbon dioxide (CO_2), steam or air at elevated temperature to enhance porosity and surface area to produce activated carbon.

Carbon activation using CO_2 is a highly endothermic reaction to allow CO_2 to reacts with carbon and produce carbon monoxide (Equation 2.12). Carbon monoxide produced during the CO_2 activation process creates a gasification reaction to develop porosity in carbon. An oxidizing agent penetrates into the internal structure of char with the assist of high temperature and further remove carbon atoms during the gasification process, which results in opening and widening of the inaccessible pores[98]. This reaction is called a Boudouard reaction, named after Octave Leopold Boudouard who investigated this equilibrium in 1899 [99].

$$\boldsymbol{C + CO_2 \rightleftharpoons 2CO} \qquad \Delta H = 172 \text{ kJ/mol} \qquad \textbf{Equation 2-12}$$

The reaction takes place during the gasification of coal and other carbon-rich materials to produce activated carbon. The gasification shows significant role in temperature higher than 900°C [100].

Steam activation is another popular manufacturing process to produce activated carbon, particularly from coconut shell and coal. The reactions involve Equation 2-13 - 2-14. The carbon and steam reaction results in producing hydrogen gas and carbon monoxide.

$$\boldsymbol{C + H_2O = H_2 + CO} \qquad \Delta H = +131 \text{ kJ/mol} \qquad \textbf{Equation 2-13}$$

$$\boldsymbol{CO + H_2O = H_2 + CO_2} \qquad \Delta H = -41 \text{ kJ/mol} \qquad \textbf{Equation 2-14}$$

Boudouard reaction occurs at the same time due to large quantities of CO_2 generated as described in Equation 2-14 during a high-temperature condition[101].

Table 2-4: Physical activation of biomass precursors

Biomass	Pre-activation Treatment	Activation agent	Activation duration (hr)	Activation temperature (^{0}C)	Highest S_{BET}[a] (m^2g^{-1})	S_{micro} (m^2g^{-1})	Vt (cm^3g^{-1})	V_{micro} (cm^3g^{-1})	V_{meso} (cm^3g^{-1})	V_{micro}/V_t	D (nm)	Reference
Spores[b]	pyrolysis	CO_2	6hr	900	3053	-	1.43	0.83	0.59	0.58	-	[15]
Oak	pyrolysis	CO_2	1	900	1126	-	0.5204	0.4929	0.0275	0.947	<1	[102]
Eucalyptus	Pyrolysis	CO_2	1	900	1490	-	0.8	0.66	-	0.825	2.15	
Wattle wood	Pyrolysis	CO_2	5	800	1032	-	0.56	0.46	-	0.82	2.17	[103]
coconut leaves[a]	Pyrolysis	CO_2	0.5	900	492.9	-	0.369	0.245	-	0.664	16.83	[104]
Sugarcane bagasse	Pyrolysis	CO_2	2	800	410	8.2	-	-	-	-	1.8	[105]
Sucrose [a]	pyrolysis	CO_2	6	900	1941	-	0.9192	0.8745	0.04469	0.951	-	[106]
Coffee endocarp [a]	Pyrolysis	CO_2	3	800	1083	-	0.46	0.44	-	0.956		[107]
Cattails[a]	Pyrolysis	CO_2	4	800	441	-	0.33	-	-	-	<2.09	[108]
Coffee endocarp	pyrolysis	CO_2	6	700	1287		0.64	0.53		0.828		[109]
		steam	2	700	630	-	0.35	0.33	-	0.94		

Biomass	Pre-activation Treatment	Physical Activation agent	Activation duration (hr)	Activation Heating temperature (^{0}C)	Highest S_{BET}[a] (m^2g^{-1})	S_{micro} (m^2g^{-1})	Vt (cm^3g^{-1})	V_{micro} (cm^3g^{-1})	V_{meso} (cm^3g^{-1})	V_{micro}/V_t	D (nm)	Reference
Corn cob	pyrolysis	CO_2	1.33	900	1705	1000	0.884	0.452	0.404	0.511	1.54	[110]
		steam	0.83	900	1315	1035	0.657	0.485	0.148	0.738	1.48	
Olive bagasse	pyrolysis	Steam	0.75	900	1106	659	0.6067	0.4012	0.2055	0.6612		[111]
Cherry blossom petals [a]	pyrolysis	Air	1	300	509	-	-	-	-	-	3.6	[112]

[an] as electrode materials for aqueous-based EDLCs application; [b] as electrode materials for non-aqueous based EDLCs application

Table 2.4 summarized the physical activation using different physical activating agents on biomass precursors. Most of the biomass were carbonized before being further treated at a high activation temperature in the range of 700-900°C under CO_2 activation. The surface area of the biomass-derived ACs varies from 410 – 3035m^2g^{-1} with mainly microporous and small amount of mesoporous. Among all the CO_2 activated carbon, Jin et. al.[15] achieved the highest surface area of 3053m^2g^{-1} for Lotus spores with 0.58 ratio of V_{micro}/V_t. An AC was prepared from coconut leaves activated under CO_2 activation at temperatures from 700-1000°C. A higher V_{micro}/V_t ratio of 0.664 was observed for the AC prepared from coconut leaves [104]. However, the AC showed a lower surface area of 492.9m^2g^{-1} with an increase in total pore volume and micropore volume was observed when activation temperature increased from 700 to 900°C and a complete burnt-off at 1000°C.

AC derived from sugarcane bagasse [105] were prepared under a different heating temperature from 400-800°C and further activated with CO_2 at high-temperature of 800°C. It is observed that the BET surface area of ACs increased from 300 to 410m^2g^{-1} with increasing the carbonization temperature from 400 to 700°C. In contrast, the microporous surface area of the carbons decreased from 153 to 85m^2g^{-1}. For AC prepared at a carbonization temperature of 800°C, the surface area dropped to 355m^2g^{-1} with a higher microporous surface area of 118m^2g^{-1}.

Few studies on the comparison of biomass-derived ACs prepared by CO_2 and steam activation are reported. Nabais et. al. [109] claimed that CO_2-ACs from coffee endocarp achieve higher BET surface area in the range of 426 - 1287 m^2g^{-1} when compared with ACs prepared by steam activation with BET surface area of 355 - 630 m^2g^{-1}. In contrast, the V_{micro}/V_t ratio for CO_2 ACs is slightly lower than the ratio for steam ACs. It is also found that steam activation achieved a higher activation rate due to a mild reaction between the carbons' structure and CO_2. The same observation was reported by Chang et. al. [110] with an AC derived from corn cobs using CO_2 and steam activation. Higher surface area for CO_2 -AC than steam-AC was obtained with the effect of activation holding time from 20-120mins under two different temperatures: 800°C and 900°C. The CO_2-AC with the highest surface area of 1705m^2g^{-1} shows lower V_{micro}/V_t ratio (0.511), while a lower BET surface area of 1315m^2g^{-1} was achieved by steam activation at 900°C with a higher ratio of microporous volume (0.738).

Román el. at., [113] studied the pore development of olive stone using CO_2, steam, and a mixture of CO_2/steam activation. In contrast with the finding of Nabais *et al.* [109] and Chang *et. al.*[110], they found that the surface area of CO_2 activated carbon (446 - 603 m^2g^{-1}) is lower than steam activated carbons (808 - 1074 m^2g^{-1}) and CO_2/steam activated carbon (674 - 1187 m^2g^{-1}). The pore size development various with different activation agents applied to produce AC. CO_2 activation creates narrow micropores (less than 2nm) and further widens them as longer activation time applied while steam activation produces various sizes on the carbon from an early stage of the process. González et. al [101] also observed that CO_2 and steam activation mainly develop micropores in walnut shell derived AC. As the longer activation is applied, pores in carbon were widened and higher burn-off was reported. In this case, a higher BET surface area of 542-1339 $m^2g^{-1}$was reported for steam activation.

Based on the above literature, a biomass selection and a physical activation agent determine the development of the surface area, pore structure and pore size distribution of an AC. Among the three available physical agents, CO_2 activation method successfully produces AC with the higher surface area, although longer activation time and higher heating temperature are required for the process.

2.6.4.1 The Benefits

Physical activation is clean and easy to handle without involving any harsh chemical that could possibly damage the original carbon structure. Thus, physical activation might retain the unique morphologies and carbon structure of biomass-derived AC. This could provide a clear understanding of how the actual morphology and structure of biomass-derived AC as electrodes influence the electrochemical performances of EDLCs. Besides, no further post-process is needed to purify AC from the excess chemicals, thus this could save the AC production cost.

2.6.4.2 The Challenges

Despite the benefits and advantages that physical activation offers, there are also some challenges and obstacles to using physical activation on biomass. A physical activation requires longer activation time due to the 2-step activation and a higher temperature is needed to ensure all the volatile and tars are completely removed from the carbon structure. For example, Ruiz-Fernández *et. al.*[114] prepared ACs from vine shoots using CO_2 and KOH activation. The CO_2 activation required a longer activation time (3 hr in total for carbonization and activation) and a higher activation temperature (750°C) to produce AC with a surface area of 293-572m^2g^{-1}. In contrast, KOH activation only needed a shorter treatment time (2hrs) and a lower temperature (500°C) to produce AC with a higher surface area of (791-1726m^2g^{-1}). As compared to chemical activation, a CO_2-AC derived from biomass achieves lower surface area [93, 114]. This has promoted most of the recent studies on chemical AC as supercapacitors electrode materials and thus, research on activated carbon derived from biomass using physical activation for EDLCs application is relatively low and insufficient [36, 39, 40, 42-45, 94, 115, 116].

2.7 A review of wastes Biomass-derived AC for EDLCs Applications

Carbon contributes to about half of the materials' cost of a supercapacitor [17]. In order to meet the massive market volume in the future, various attempts are in progress to reduce the cost of these energy storage systems. Waste biomass from industries and agricultural has the potential to be used as a precursor to producing carbon due to their low-cost and abundant supplies.

Many research studies have investigated the performance of biomass-based EDLCs in aqueous electrolyte [33]. However, aqueous electrolytes have a narrower ESW (~1.23V) resulting in lower

energy density and power density in an EDLC. Besides, the development of a cost-efficient current collector with high interfacial resistance is a substantial challenge for EDLC in an aqueous electrolyte to overcome the harsh aging condition [117]. EDLCs with a wider ESW of the electrolytes such as organic electrolytes or ionic liquid can store higher energy, thus deliver much higher energy density and power density[44]. In addition, most of the available commercial EDLCs use organic electrolytes [23, 33, 117] with $TEABF_4$/AN used as the most common electrolyte for EDLCs[118]. Table 2-5 presents some of the recently published works for the AC derived from biomass wastes used as electrode material for ELDCs' application with the organic or ionic liquid used as an electrolyte and provides a comparison of EDLCs performance when an aqueous electrolyte and a non-aqueous electrolyte is used.

A comparison of EDLC performance in 1 M H_2SO_4 aqueous and $EMIMBF_4$ ionic liquid was conducted using KOH-AC from rice straw [44]. The AC was prepared by carbonization at 600°C for 4 hr. The carbonized sample was then mixed with KOH with a mass ratio of 1:3 and heated up at 600°C for 1 hr in Argon condition. AC with the maximum surface area of $1007 m^2 g^{-1}$ and a mixture of micro/mesopores was obtained. The EDLC in the aqueous electrolyte achieved a much higher specific capacitance of ($156 Fg^{-1}$) than in $EMIMBF_4$ ($80 Fg^{-1}$). The lower capacitance achieved in the IL could be due to the large ion size of $EMIM^+$ in IL causes larger ion transportation resistance of IL[10]. Despite that, the wider ESW (2.5V) of $EMIMBF_4$ promotes a higher energy density of $17.4 Whkg^{-1}$, compared with an energy density of $7.8 Whkg^{-1}$ achieved with the narrower ESW (1.2V) for the H_2SO_4 electrolyte.

Besides, it can be seen in Table 2-5 that most of the biomass-derived AC were treated using KOH-chemical activation. This is because of the higher surface area and wider pore size for ACs derived from biomass using KOH-chemical activation process as, compared to physical activation. Although many research works have reported that the specific capacitance has a high correlation with BET surface area. However, this is not the case for all the biomass-derived ACs as listed in Table 2-5.

Wang et. al. [10] studied the AC production from pine tree sawdust powder using KOH and H_3PO_4 activation, respectively. KOH activation was conducted with KOH/biomass weight ratio of 1:4. The mixture was heated up to 850°C with a heating rate of $10°C min^{-1}$ for 1hr. The KOH-activated carbon with a BET surface area of $1018 m^2 g^{-1}$ delivers a capacitance value of $131 Fg^{-1}$ in $EMIMBF_4$ and 65 Fg^{-1} at $1 Ag^{-1}$. KOH-AC from rice straw [44] with a similar surface area ($1007 m^2 g^{-1}$) achieved about 80 Fg^{-1} in $EMIMBF_4$ at $0.5 Ag^{-1}$. For H_3PO_4 activation, the biomass was impregnated with H_3PO_4 under NH_3 flow for 2 hr at 1000°C and further washed using HCl. The H_3PO_4 activated sample shows BET surface area up to $2207 m^2 g^{-1}$ with high mesopores volume of $0.99 cmg^{-}1$, which is 3 times higher than the KOH-activated sample. The capacitance of H_3PO_4 activated sample with IL electrolyte displayed about $224 Fg^{-1}$ and $146 Fg^{-1}$ in the organic electrolyte, 1M TEABF4/AN. The study also has related the ratio of microporous in the total pore volume of AC to the ratio of capacitance performance in the IL and the

organic electrolyte. The trend reveals that microspore size between 0.9 to 2nm has a more significant effect on capacitance in IL.

AC samples were prepared using pistachio shell as precursors [116] through KOH activation at 750°C for 3 hrs under argon flow. The effect of KOH/biomass weight ratio (1:1, 3:1 and 5:1) was studied and large surface areas of 1069 m^2g^{-1} with a high micropore volume ratio of 83% was obtained for AC prepared with a KOH/biomass weight ratio of 3. A capacitance of 313 Fg^{-1} was achieved with a symmetric-electrode EDLC system in 6 M KOH aqueous electrolyte, while a lower capacitance was achieved in 1M TEABF4 in EC-DEC electrolyte at the scan rate of $2mVs^{-1}$. The higher energy density of $39Whkg^{-1}$ and a larger power density of $286kWkg^{-1}$ were reported for the EDLC in the selected organic electrolyte.

Eucalyptus wood sawdust was used to prepare AC under the effect of KOH activation pyrolysis temperature of 700-800°C[119]. The maximum BET surface area of up to $2967m^2g^{-1}$ was obtained using KOH/biomass weight ratio of 4, at 800°C. A higher carbon activation temperature of 800°C on Eucalyptus wood sawdust leads to a higher specific capacitance up to ~$236Fg^{-1}$ in a two-electrode EDLC in 1M $TEABF_4$ in AN at a sweep rate of $1mVs^{-1}$ and the ideal rectangular shape of CV observation suggested that activation of 800°C significantly less resistance to the ion adsorption with at fastest sweep rate of 100 mVs^{-1}. This work also claimed that the presence of mesopores in carbon electrode is not an essential condition for rapid ion transport. A higher specific capacitance of up to ~$175Fg^{-1}$ at a current density of $20Ag^{-1}$ was achieved by AC with high micropores as compared to hierarchical porous graphitic carbon (HPGC) with a high volume of mesopores as reported by Wang *et.al.* [120].

Besides of KOH activation, ACs derived from biomass using $ZnCl_2$ and H_3PO_4 were reported [121, 122]. He *at. al.* [121] prepared AC from peanut shell using $ZnCl_2$ activation with assisted microwave heating and conventional heating. Peanut shells were soaked with $ZnCl_2$ with a mass ratio of 4:1 and dried before further activated using a conventional heating technique at 850°C for 1 hr in the N_2 flow. For microwave heating, the dried mixture was heated for 20mins under microwave power of 600W. A high surface area of $1634m^2g^{-1}$ was obtained for AC prepared using conventional heating and $ZnCl_2$ with a high percentage of mesopores, which is 82% of the total pore volume. However, the AC electrode showed a large deviation from an ideal EDLC rectangular shape of the CV curve in 1 M Et_4NBF_4/PC organic electrolyte. This might be due to some resistance to ion in the selected organic electrolyte to reach the internal surface of the electrode due to the narrow micropores. Sugarcane bagasse was used to prepared AC under different concentrations (20-60wt%) of $ZnCl_2$ [122] with assisted microwave irradiation under N_2 atmosphere. The pore size of prepared AC increases from 2.5 to 7nm with the

increase in the concentration of $ZnCl_2$ from 20% to 60%. The prepared AC with a concentration of 30% $ZnCl_2$ solution exhibited the highest BET surface area ($1489 m^2g^{-1}$) with mainly mesopores and a small portion of micropores. A symmetric EDLC with prepared AC in EMIMBF4 in electrolyte were studied. AC prepared with 40% $ZnCl_2$ concentration (AC-40) with slightly lower surface area $1416 m^2g^{-}1$ presents the highest specific capacitance of $138 Fg^{-1}$. This indicates that the pore size of AC-40 (4.6nm) allowed the largest accessible interface area between electrode and electrolyte at a low current density of $200 mAg^{-1}$. At higher current densities, AC-60 delivered the highest specific capacitance and revealed that the larger pore size of the AC promotes the ion transport behavior in IL.

Among all listed AC precursors in Table 2-5, Zhang et al [123] obtained the highest surface area AC from lotus- pollens, up to $3037 m^2g^{-1}$ and a large mesoporous volume of $1.86 cm^3g^{-1}$. The AC was prepared through hydrothermal treatment at 180^0C for 12 hrs followed by KOH activation process. A mixture of KOH/ biomass with a mass ratio of 4:1 was heated up to 900^0C at a heating rate of $5^0 Cmin^{-1}$ for 1 hr under Argon flow. A symmetric cell with the prepared AC showed a specific capacitance of ~ $207 Fg^{-1}$ at a current density of $1 Ag^{-1}$ in $EMIMBF_4$ electrolyte with a gravimetric energy density of ~$88 Whkg^{-1}$, while the symmetric EDLC exhibits $185 Fg^{-1}$ and a gravimetric energy density of ~$46 Whkg^{-1}$ in the organic electrolyte, 1M $TEABF_4$/AN.

Although KOH- activated carbon generally exhibits higher surface area, a high surface area of up to $3035 m^2g^{-1}$ from spores derived AC using CO_2 activation was reported [15] for EDLC application in an organic electrolyte, 1M $TEABF_4$/AN. The AC was prepared by carbonization at 700°C for 2 hrs and further activated at 900°C for 6 hr. Although KOH-activated carbon derived from spores achieved similar surface area, CO_2 –AC from spores delivered a much higher V_{micro}/V_t ratio of 0.58. A higher specific capacitance of up to $308 Fg^{-1}$ was delivered using CO_2 –AC as an electrode in symmetric EDLC system, which is even higher than KOH-AC from lotus pollens in the same organic electrolyte, 1M $TEABF_4$/AN. A maximum energy Density with $57 Whkg^{-1}$ and a power density of 17 $KWkg^{-1}$ was delivered by the EDLC. This indicates that physical activation is also possible to achieve a high surface area as high as the surface areas obtained by KOH activation.

Table 2-5: Summary of biomass-derived AC for EDLCs application using organic electrolyte and IL

Carbon Precursors	Pre-activation Treatment	Activation method	Activation duration	Highest S_{BET}[a] (m^2g^{-1})	V_{micro}/V_t	Highest capacitance Symmetric ELDC (Fg^{-1})	Measurement at	Energy Density ($Whkg^{-1}$)	Power density ($KWkg^{-1}$)	Electrolyte	Reference
Spores	pyrolysis	CO_2	6hr	3053	0.58	308	$1mVs^{-1}$	57	17	1M $TEABF_4$/AN	[15]
Pistachio nutshell	pyrolysis	KOH	3hr	1069	0.83	215	$2mVs^{-1}$	39	286	1 M $TEABF_4$ in EC-DEC	[116]
Lotus Pollens	hydrothermal	KOH	12hr	3037	0.18	185/207	$1Ag^{-1}$	46/88	-	1 M $TEABF_4$/AN neat EMIMBF4	[123]
Pine tree sawdust	-	KOH	1hr	1018	0.533	65/130	$1Ag^{-1}$	18/46	-	1 M $TEABF_4$/AN neat $EMIMBF_4$	[10]
		H_3PO_4 + NH_3	2hr	2207	0.31	133/185	$1Ag^{-1}$	26/92	-		
Neem dead leaves	pyrolysis	-		1230		88	$2A\ g^{-1}$	56	-	1 M $LiPF_6$ in EC–DEC	[124]
Peanut shell	-	$ZnCl_2$	1hr	1552	0.18	99	$50mAg^{-1}$	19.3	1007	1M Et4NBF4/PC	[121]

Carbon Precursors	Pre-activation Treatment	Activation method	Activation duration	Highest S_{BET}[a] (m^2g^{-1})	V_{micro}/V_t	Highest capacitance Symmetric ELDC (Fg^{-1})	Measurement at	Energy Density ($Whkg^{-1}$)	Power density ($KWkg^{-1}$)	Electrolyte	Reference
Sugarcane bagasse	-	$ZnCl_2$ /microwave irradiation	15mins	1465	0.326	40	$2Ag^{-1}$	9.2	2.5	$EMIMBF_4$	[122]
Eucalyptus wood sawdust	hydrothermal	KOH	1hr	2967	0.89	~175	$20Ag^{-1}$	-	-	$TEABF_4$/AN	[119]
Sucrose	pyrolysis	CO_2	2, 4, 6 hr	1941	0.95	172/148	$1mVs^{-1}$	-	-	EdMPNTf_2N neat $EMIMBF_4$	[106]
Lotus root shell	Pyrolysis	KOH	2hr	2961	-	345	$0.5Ag^{-1}$	13.9	6.4	KOH	[40]
Rice straw	Pyrolysis	KOH	1hr	1007	-	156/80	0.5 A g^{-1}	7.8/17.4	150/126	1 M H_2SO_4 neat $EMIMBF_4$	[44]

2.7.1 The selected Biomass wastes

In this project, five different types of waste biomass were selected to prepare activated carbons. There are Marabú weed (MW), palm oil empty fruit bunch wood pallets (EFB), Malaysia wood pellets (MSW), Rubberwood (RW) and used coffee grounds (CG).

2.7.1.1 Marabú Weed from Cuba

Marabú weed with scientific name as *Dichrostachys cinerea* is a thorny and rapidly growing wood scrub. The woody shrub is originally from Africa and was brought to the Caribbean in the 19th century as a decorative flower [125]. Thousands of hectares arable land was abandoned due to the decline of the Cuban sugar industry when the Soviet bloc collapsed. Thus, this has given Marabú an advantage to invade the agriculture land. Today, there are abundant lands covered by this severe invasive species in Cuba. It covered 1.2Mha in Cuba, which represents about 11% of Cuban territory and 20% of arable land [126]. Marabú is categorized as hardwood as its density could reach up to 1kgm^{-3}. This makes possible the energy use of this biomass to high value-added products such as activated carbon in various applications.

2.7.1.2 Spent Ground Coffee from Columbia

Used/ Spent coffee grounds were selected as one of the precursors in this project. There are approximately 8 billion metric tons of coffees produced in the year 2015[127] and most of them are disposed of as waste coffee grounds by the coffee beverage manufacturers. The used coffee grounds, in this case, were supplied by Colcafe S.A.S, Columbia.

2.7.1.3 Malaysia agriculture by-products

Three Malaysia agriculture by-products are selected as activated carbon precursors, EFB pellets, Malaysia wood pellets, and RW. Malaysia is currently one of the top producers of palm oil, wooden furniture, and rubber gloves in global[128]. Large quantities of waste biomass are generated from the manufacturing process and agricultural industries. There are at least 168 million tons of biomass wastes generated annually in Malaysia. EFB pellets are made from shredded EFB fiber, which is one of the by-products from oil palm agriculture industry. These EFB pellets were purchased from biofuel resource, Malaysia [129]. The dimensions of EFB pellet is in length of less than 30mm with a diameter

of 6, 8 and 10mm. Malaysia wood pellets used in this work were purchased from Dinxings (M) Sdn. Bhd., Malaysia. These wood pellets are made from sawdust, which produced from wood processing and furniture factories and sawmills. These biomass pellets are used as fuel for a boiler grating system. RW was supplied by a local farmer in Malaysia. Rubber brunches from old rubber trees that no longer able to produce latex were collected as samples in the present work.

2.8 Summary

Supercapacitors are electrochemical energy storage devices with high power density and able to rapid store and release energy. However, the low specific energy density of supercapacitors limits its potential in electric-vehicles application and grid leveling sectors. Besides, lowering the production cost of the supercapacitors is another target to expand and meet the high market demand in the future. Thus, research interests on preparing ACs with the high surface area from waste biomass as electrode materials for supercapacitors applications. Based on the literature review, ACs can be derived from waste biomass with a high surface area. Thus, this helps in reducing the production cost of the supercapacitors and also helps in reducing the risk of pollution to the environment by reuse the by-products from waste biomass. The porosities, surface area, and surface structure greatly depend on the properties of the selected of biomass as the AC precursors. There is a growing interest in the development of AC derived from biomass using chemical activation techniques, but less attention was paid on the CO_2 activation technique for supercapacitor applications. The review has shown the development of the surface area, pore structure and pore size distribution of an AC are highly depending on the AC precursors and the selected physical activation agent. Among the three available physical agents, CO_2 activation method successfully produces AC with the higher surface area, although longer activation time and higher heating temperature are required for the process. Prior to CO_2 activation, carbonization is an important pre-activation step to remove the moisture and volatile matter from the carbon precursors and further create the fundamental carbon structure and porosity. The right carbonization temperature and heating rates are the keys to removing most of the impurities and low in ash content for AC production. Besides, the contact time of the carbonized sample with the activation agent is essential to produce the optimum yield and create AC with the high surface area. The focus of this research is therefore to investigate the effect of the carbonization and CO_2 activation to yield, porosities and surface area and structure of AC derived from waste biomass. Despite the variety of biomass has been used on CO_2 activation, the use of Marabú and biomass materials from Malaysia to produce AC using CO_2 activation has not found to have been reported. This chapter also highlights the correlations between the electrochemical performance of an EDLC and the properties of AC derived from biomass using standard electrolytes with a wider ESW. The selection of electrolyte with wider

ESW delivers higher energy density in supercapacitors. Therefore, this research world able to provide a valuable addition to the knowledge of carbon activation and energy storage applications. Throughout the investigation on electrochemical behaviors of EDLCs including CV, GC, cycling stability and EIS will be applied in this study. This, together with comparing with the performance with the commercial activated carbon to provide a better understanding of how the porosities, surface area and the purities of the carbon affects the electrochemical performance in EDLC.

3 Experimental Section

There are five sections in this chapter to describes the detail of analytical analysis methods and experimental set up for this project. Section 3.1 describes the preparation of carbon precursors. Section 3.2 introduces the details of the analytical methods used for the characterization of carbon precursors, carbonized samples, ACs derived from the selected biomass and electrolytes. Section 3.3 describes the experimental setup and the methodologies for the carbonization and CO_2 activation process. Section 3.4 presents the procedure on the electrode fabrication and an EDLC symmetric two-electrode coin cells construction. Section 3.5 discusses the electrochemical measurement techniques and experiments to test the performance of the cells.

3.1 Carbon Precursors Preparation

Commercially activated carbon (YP80F, Kuraray Co. Ltd) which prepared by coconut shell and five biomass wastes were selected to study their potential as alternative AC precursors for carbon electrode in EDLC applications, which are Marabú wood, EFB pellets, MW pellets, rubberwood and spent coffee grounds (CG). Prior to carbonization process, Marabú, EFB pellets, MS pellets, and RW were cut into small chunks (1-1.5cm) expect the spent coffee ground (CG).

3.2 Analytical methods

3.2.1 Ultimate Analysis

The elemental composition analysis of biomass samples was conducted using a CHNS analyzer (Vario MICRO cube CHN/S analyzer) to determine the percentage of carbon, hydrogen, and nitrogen. The analysis was carried out at the Department of Chemistry, The University of Sheffield. About 1.5-2mg of the sample was weighed and sealed within a tin capsule for analysis. Each sample was individually flushed with inert gas to remove atmospheric nitrogen. The sample was sent to rapid combustion at approximately 1200°C. The sample was combusted and reduced to produce N_2, CO_2, H_2O, and SO_2. These gases were captured by an adsorption tube and the components were separated on a column before sending to the thermal conductivity detector. The signal from the thermal conductivity was integrated and calculated as a percentage of each element in the sample with a tolerance of ± 0.3 %[130]. A blank was used to ensure the consistency between the different runs. Each sample was tested in duplicates.

3.2.2 Thermogravimetric Analysis (TGA)

Thermogravimetric analysis (TGA) is a common thermal analysis technique used to determine the composition of a sample by measuring the mass changes of the sample as a function of temperature and time in a controlled atmosphere. When the exothermic reaction occurs with a fixed heating rate, the weight loss profile of a sample is measured. The derivative of the mass loss profile, which also called as Derivative Thermogravimetric analysis (DTG) is used to determine the actual temperature where the highest rate of the mass reduction occurs.

Mettler Toledo TGA/DSC1 STARe instrument was used to conduct the TGA analysis using proximate analysis (2015) method. Proximate analysis (2015) is one of the common methods to identify the composition of carbon, coals, and cokes such as moisture, volatile, fixed carbon and ash content. A sample of 10-15mg was placed in an alumina oxide crucible alongside an empty crucible used as a reference. The sample mass changes were recorded when the furnace started to heat up from 25°C to 950°C with a heating rate of $10°Cmin^{-1}$ under gas nitrogen flowing. Initially, samples were heated from 25°C to 127°C at a rate of 10^0Cmin^{-1} under gas nitrogen flow and were maintained for 10 mins. This step is to ensure moisture in the sample has been completely removed and the mass recorded. The temperature was then further increased to 927°C at 10^0Cmin^{-1}. The sample was held at this temperature for 5mins to allow the complete removal of the volatile components. The furnace was then cooled to 827^0C and the gas was switched to oxygen for 30mins. Combustion occurs and thus results in the mass loss in this step, which represents the fixed carbon in the sample. The furnace was then set to cool down to room temperature and the remaining mass in the crucible as referred to the ash content of the sample.

3.2.3 N_2 adsorption isotherm for porous characterization

All the samples were vacuum dried at 120°C for overnight and further degassed under vacuum using a VacPrep 061 Degas system (Figure 3-1) at 250°C overnight before the N_2 adsorption isotherm analysis. The specific surface area and porosity of AC samples were measured by N_2 adsorption-desorption using a Micromeritics 3Flex instrument (Figure 3-2) at a temperature of 77K. This step is to ensure all the adsorbed gasses on are removed from the porous structure of the samples. The degassed sample was weighted before a place at the Micromeritics 3Flex unit. The degassed sample was dosed with a specific amount of gas N_2 which then evacuated to obtain the quantity of gas absorbed by the sample over a relative pressure range P/P_0 in the range of 0.1-0.998, where P_0 is the saturation pressure

of nitrogen at 77K. The total specific surface area was obtained by the Brunauer–Emmett–Teller (BET) theory, mesoporous and the pore volume was obtained by the Barrett-Joyner-Halenda (BJH) method. The microporous surface was obtained using the t-plot method while the micropore volume was calculated based on Dubinin-Radushkevitch DR equation (DR)[131]. The data were further evaluated using the 3Flex software.

Figure 3-1: VacPrep 061 Sample degas system

Figure 3-2: Micromeritics 3Flex equipment

BET measures the surface area of a sample based on gas adsorption to determine the overall specific surface area. In this work, the BET surface area of a sample was determined based on the adsorption of gas N_2. The volume of gas N_2 adsorbed on the surface of the AC is measured at the boiling point of gas N_2 by assuming the gas condenses onto the surface in monolayer. The amount of adsorbed gas is correlated to the total surface of the samples.

BJH [132] is a pore size distribution determination method commonly applied to nitrogen desorption data to measure the mesoporous in a sample. BJH technique assumes a pore is in cylindrical pore shape, the gas condenses onto pore wall in multilayer and inner capillary volume occurs in the remaining pore volume [28]. It uses the modified Kelvin equation (Equation 3-1)[133] to relate the amount of adsorbate removed from the pores of the sample. Where parameter γ is the surface tension of liquid adsorbate, V represents the molar volume of the adsorbate, R the gas constant, T the absolute temperature, and θ the contact angle between the liquid adsorbate and solid surface.

$$\ln\left(\frac{P}{P_0}\right) = \frac{-2\gamma V}{r_k RT} cos\theta \qquad \textbf{Equation 3-1}$$

The t-plot method [134] is a typical technique to determine the microporous volume and the specific surface area of a sample by considering the adsorbed film thickness based on Halsey equation (Equation 3-2[135]). The surface area of a sample is strictly determined by considering the micropore filling is completed. In, the parameter of A, B and D in Equation 3-2 are adsorbate dependent constants which can be determined experimentally.

$$t = A[\frac{B}{ln(\frac{P}{P_0})}]^c \qquad \textbf{Equation 3-2}$$

In the DR model, the adsorbate is assumed in the liquid state and the volume of micropores is measured based on the volume filled with the adsorbate. The DR equation is given as in Equation 3-3[131].

$$ln\, w = \ln(V_0\rho) - \kappa\left(\frac{RT}{\beta}\right)^2 \quad [ln\left(\frac{P_o}{P}\right)]^2 \qquad \textbf{Equation 3-3}$$

Where V_0 is the maximum volume of adsorbent per adsorbed mass, κ is a constant that reflects the pore size distribution of the adsorbent with respect to pore volume. and β is the affinity coefficient of the characteristic curves. The micropore volume can be determined by referring to the intercept, $\ln(V_0\rho)$ of the linear plot of ln w vs [ln $(\frac{P_o}{P})$][28].

3.2.4 Scanning Electron Microscope (SEM)

The surface morphology of AC samples was recorded using the SEM Inspect-F50 (FEI, Oregon, USA) which was coupled with Energy Dispersive X-ray spectrometer (EDX) to carry out the elemental analysis (Figure 3-3). SEM is an instrument comprised of a field emission gun (FEG) to emit electron with accelerating voltage from 200V to 30kV under high vacuum conditions (10^{-10} to 10^{-11} Torr). The vacuum condition is to avoid any small particles in the air that could deflect the electron onto the samples, and thus obscuring the results. SEM images were recorded on SEM at accelerating voltage of 10-15keV with a working distance of approximately 10mm. Series of magnetic condenser lenses help in focusing the beam on the specimen (objective lens) and adjust the spot diameter (condenser lens). The spot size of 3nm was used to scan across the surface of all the activated carbon samples. A beam of electrons generated from FEG hits on the activated carbon and therefore emitting secondary electrons from the surface of the sample. An Everhart-Thornley detector in SEM Inspect F50 collects the secondary electrons and demonstrates the topographic information of the samples. Energy Characteristic X-ray was emitted from the surface and shows the special characteristics for an element. Thus, the characteristic X-ray of AC samples was collected by EDX to determine their elemental analysis.

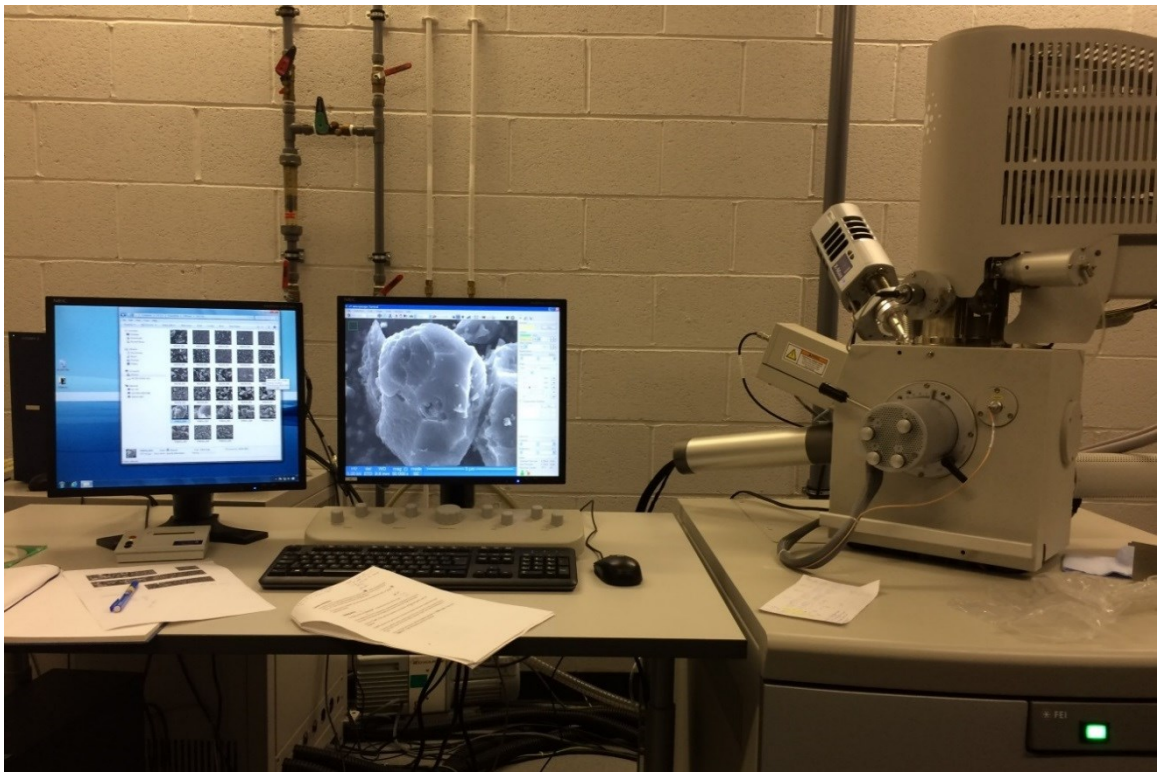

Figure 3-3: SEM Inspect-F50 (FEI, Oregon, USA)

3.2.5 Raman Spectroscopy

Raman spectroscopy is widely used to provide information on the composition and crystal structures based on the Raman shift. Raman spectroscopy is a scattering technique used to observe the vibrational, rotational or lower frequency modes in a sample based on Raman effect/ scattering which is the shift in wavelength of the inelastically scattered radiation. First, a sample is illuminated with a monochromatic light source, laser. During the scattering process, each molecule has different scattering by interacting with molecular vibrations. The gained or lost energy happens when the photos exchange part of their energy with molecular vibration in the samples, called a Raman shift as shown in Figure 3-4 (a). There is a light that scatters off without any energy changes is called Rayleigh scattered as shown in Figure 3-4 (b).

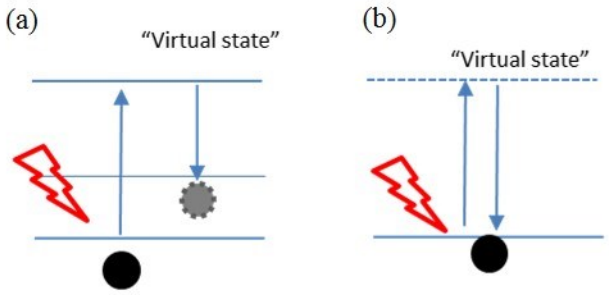

Figure 3-4: The different of (a) Raman Scattering) (b) Rayleigh scattering

Raman spectra of AC is used to analyze the graphitization of ACs by examining types of bonding and arrangement of carbon [36, 39, 43]. In this study, the Raman spectra of AC samples were recorded on Renishaw's inVia Raman microscope as shown in Figure 3-5. The samples were excited with 514nm Argon ion laser wavelength (green) employing 10% of 20mW with 10scans, 10s person on the sample. Further analysis and data fitting of the obtained spectra was done using OriginLab, data analysis, and graphing software.

Figure 3-5: Renishaw inVia Raman microscope

3.2.6 X-ray Photoelectron Spectroscopy (XPS)

XPS is a technique to determine the surface chemistry and to quantify the elemental composition on a sample surface by irradiating a surface area of the sample from the top 1-10nm with x-rays and measuring the energy spectrum of photo electrons emitted. The analysis is conducted under an ultra-high vacuum condition, to prevent interference from gas molecules with photoelectrons. The result displayed as spectra which recorded by counting the rejected electrons over a range of kinetic energies, with elements and bonding environments emitting electrons of a characteristic energy.

In this work, XPS analysis was conducted using a Thermo Scientific Al-K alpha surface analyzer. Element analysis and data fitting were carried out using CASA XPS software. Relative Sensitivity Factors (RSF) (Table 3-1) from element library of CASA XPS software was applied to convert the XPS signal and further measure the quantification of the XPS spectra peak area. The XPS peak area was further normalized with total C 1s with an arbitrary number of 100 to determine the ratio of chemical elements and species.

Table 3-1: RSF used to scale the XPS raw peak areas

Element	Relative Sensitivity Factor
C	1
O	2.93

3.2.7 Karl-Fischer Titration

Karl Fisher (KF) coulometric titration is an effective analytical technique to determine the water content of non-aqueous electrolytes. The moisture content of all involved non-aqueous electrolytes in this project was determined using Karl Fischer titration. KF899 Coulometer Metrohm with generator electrode without diaphragm was used for the Karl Fischer titration. The Karl Fisher reaction is based on the Sulfordioxide only reacts in the presence of water with iodine (Equation 3-4):

$$2H_2O + I_2 + SO_2 \rightarrow SO_4^{2-} + 2I^- + 4H^+ \qquad \textbf{Equation 3-4}$$

The Karl Fischer titration consists of two electrodes: (a) the working electrode where the Iodine is produced, and the charge is monitored. (b) an indicator electrode to measure the amount of produced iodine. The sensitivity of this coulometric Karl Fisher titrators allows determining water content in the range of 0.001% to 1%. Iodine is generated electrochemically in the titration cell. Amount of charge needed to produce I_2 until the indicator electrode recognizes the end point of titration (visible in a sudden drop in Voltage). Water and iodine are consumed in a 1:1 mole ratio in KF reaction. The coulometric titrator measures how much charge has passed through the generator electrode to produce the iodine (I_2) needed to stoichiometrically react with the water (H_2O) contained in the sample. So a strictly quantitative relationship exists between the amount of electric charge and the amount of iodine generated and therefore to the amount of water determined[136, 137].

3.3 Carbonization and CO_2 activation

3.3.1 Carbonization

About 10 g of biomass was transferred in a ceramic boat and placed in the center of a tube furnace (Carbolite model 2408) as in Figure 3-6. The end seals of the tube furnace were secured and purged with argon atmosphere for an hour at constant flow rate prior to heating for carbonization. This is to ensure the tube furnace is in argon condition for carbonization to prevent any oxidation occurs. To study the effect of the heating rate, the temperature of the tube furnace was then increased from room temperature to 950^0C with three different heating rates of $5^{\circ}Cmin^{-1}$, $10^{\circ}Cmin^{-1,}$ and $15^{\circ}Cmin^{-1}$ as shown in Figure 3-7. The sample was heated for a duration of 3 hours at 950°C to remove the volatile content of the sample. The samples were let to cool down to room temperature in Argon condition. Afterward, the carbon materials were ball milled for 10mins (details at section 3.3.2). The carbonized materials were then transferred to a glass jar and stored in a vacuum oven at a temperature of 120°C before use.

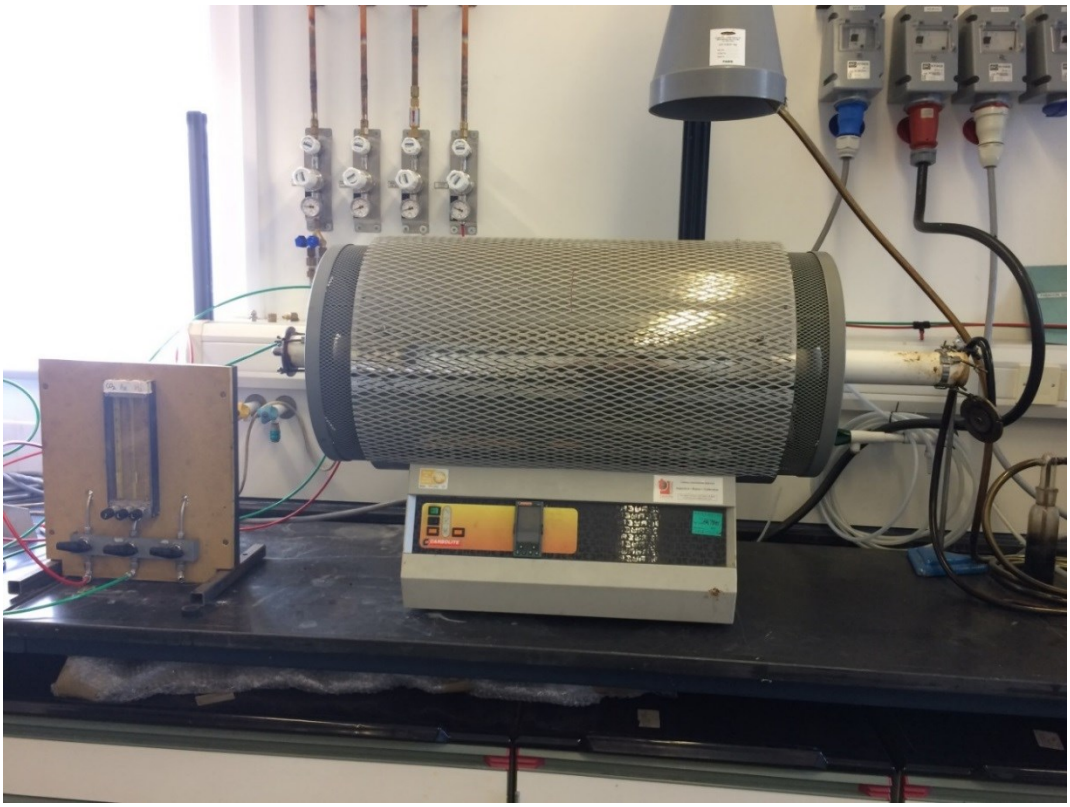

Figure 3-6: Carbolite model 2408 tubular furnace

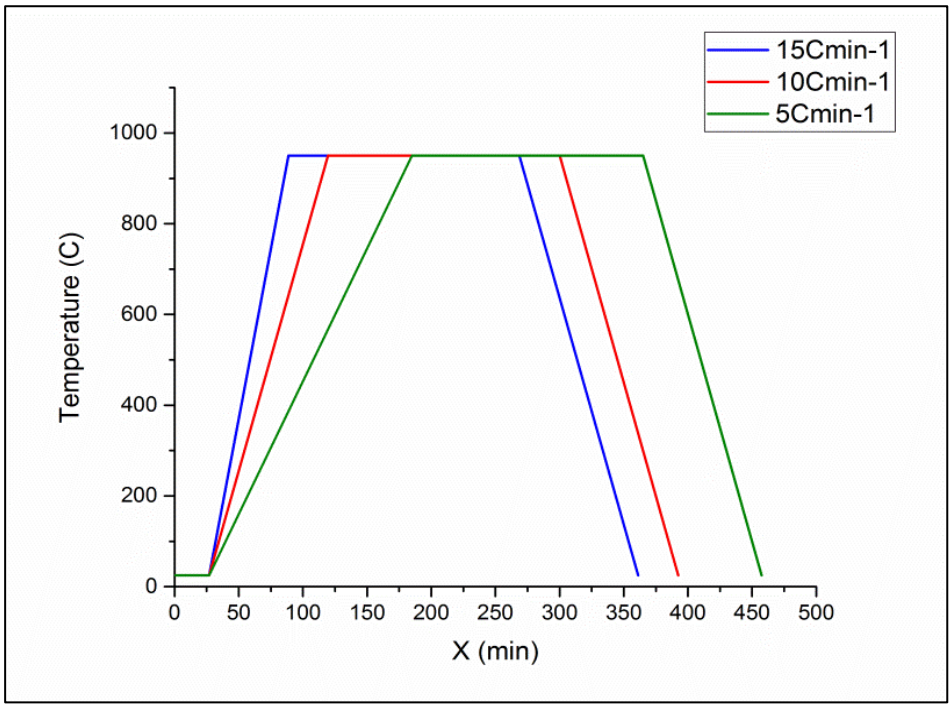

Figure 3-7: Temperature flow profile with different hearting rate

3.3.2 Ball Milling of Carbon Materials

Prior to the activation process, ball milling on the carbonized materials was aimed to increase the surface area and as well as uniform the particle size of the carbonized materials. The ball milling preparation step was carried out as according to the procedure elsewhere. [138] with minor modification. The carbonized material from vacuum-oven was transferred to a glovebox antechamber and allowed to cool down under inert atmosphere. The glovebox antechamber was evacuated and purged at least 3 times before transferring the carbonized material into the glovebox (MBraun MB200MOD). The carbonized material was then added to the ball mill vial under Ar atmosphere and sealed with parafilm before discharging from the glovebox. This step is to prevent any oxidation of the carbon materials during high-energy milling. The ball mill vial was locked in a high energy ball mill (SPEX SamplePrep 8000 M). The sample was ball milled for 10 minutes and left to cool for 30mins before storing in a glass vial.

3.3.3 Physical Activation- CO_2

For the activation process, the carbonized materials were placed in a cleaned tubular furnace (Carbolite model 2408) as seen in Figure 3-6 and purged with argon for an hour. The temperature of the tube furnace was increased from room temperature to 950^{o}C with heating rates of 10^{o}Cmin^{-1}. Next, the carbons were heated at 950^{o}C for 2 hours. Carbon dioxide (99.8%, CO2 (g)) was chosen as the oxidizing agent. The activation temperature profile for 80mins activation is shown as Figure 3-8. During the activation duration, the carbons were purged with CO_2 for different activation holding times of 20, 40, 60, 80 and 100 mins and then switched back to Argon condition for cooling purpose. The activated carbon was transferred to a glass jar and stored under vacuum at a temperature of 120^{o}C before use. The ACs were labeled according to the used biomass represented by M=Marabú; E=palm oil empty fruit bunch pellets; C= spent ground coffee; R= rubberwood with carbonization heating rates (5^{o}Cmin^{-1}, 10^{o}Cmin^{-1} or 15^{o}C/min), followed by activation holding time (20mins = V2; 40mins= V4 and so on). For instance, Marabú derived activated carbon with carbonization heating rate of 10^{o}Cmin^{-1} and followed by 80mins activation time is labeled as M10V8.

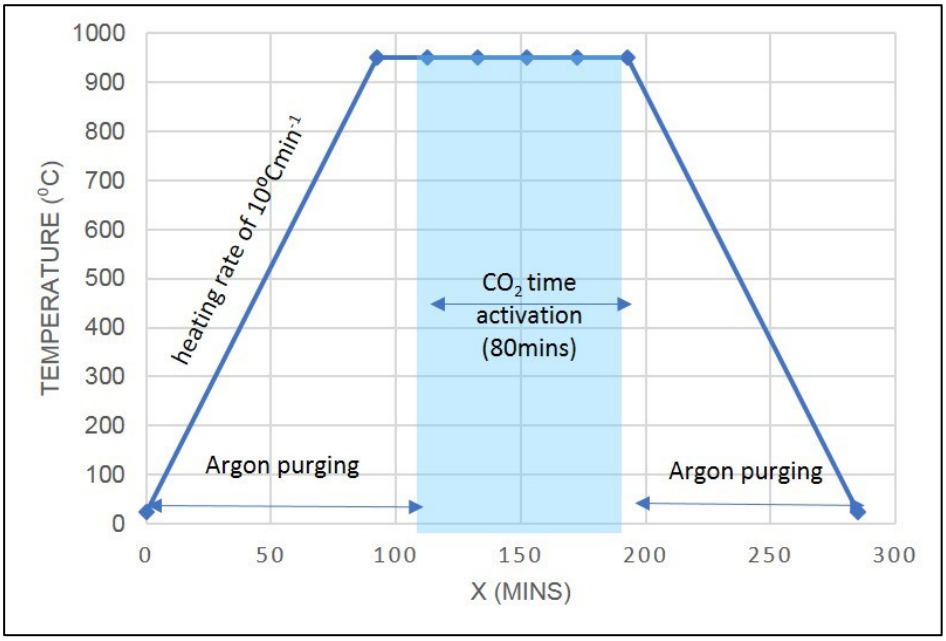

Figure 3-8: Temperature profile of CO_2 activation process for 80mins CO_2 activation time.

3.4 EDLC cell preparation

3.4.1 Electrodes Materials and Electrolytes

In this project, biomass-derived activated carbons are used as activated carbon materials to prepare supercapacitor electrodes. Commercial activated carbon (YP80F, Kuraray Chemical, Japan) was mixed with carbon black and polymer binder as a model electrode (the selection of polymer binder is depending on the selected electrolyte for the cell). The properties of carbon black and YP80F given by supplier are summarized as in Table 3-2.

Table 3-2: Properties of carbon materials used for supercapacitor electrodes

	Surface area (m^2g^{-1})	Ash content (%)	Particle size (µm)
Super C-45 (CB)	45[1]	0.0025[1]	20-45[1]
YP80F (AC)	2084[2]	<1[1]	5-20[3]

[1] According to a datasheet from the suppliers.

[2] Experimentally determined using nitrogen adsorption isotherm

[3] Determined from the literature [74]

EDLCs using AC derived from wastes biomass as electrode material were assembled with two different types of electrolyte, which are organic electrolyte and ionic liquid (only for AC derived Marabú) to test

their electrochemical performance. Prior to the assembly the EDLC, electrolytes were prepared under an Argon filled glove box (H_2O < 0.1 ppm, O_2 < 0.1 ppm). Although $TEABF_4$/AN is commonly using in commercial EDLC[33], 1molL^{-1} $TEABF_4$ in anhydrous PC was prepared as an organic electrolyte for all the electrochemical analysis of EDLC. AN is highly toxic, PC is much environment-friendly and a higher flash point (132°C) to create an environment-friendly and safety performance of an electrolyte.

For ionic liquid (IL) electrolyte, $EMImBF_4$ which is a standard IL was employed. $EMImBF_4$ was stirred and heated up to 100°C overnight. The moisture content of electrolytes was determined to be less than 10ppm by Karl Fischer titration (KF899 Coulometer, Metrohm).

3.4.2 EDLC Electrode fabrication

For organic electrolyte, EDLC electrodes were fabricated by mixing the biomass-derived carbon with the conductive carbon (Super C45) and a polymer binder (PVDF, KynarFlex 2801) in a mass ratio of 80/10/10. A small amount of *N-Methyl-2-Pyrrolidone* (NMP) was added as a solvent in the slurry to ensure the slurry is well combined. The mixture slurries were spread on aluminum foils on vacuum bed coater (MSK-AFA-L800BH, MTI Corporation) with a thickness of 150 μm using macrometer adjustable gap paint applicator. The sheet was then vacuum-oven dried and punched into individual carbon electrodes in 12 mm diameter.

In this project, the electrochemical stability window (ESW) of EDLCs with [EMIM][BF_4] electrolyte was found narrowed using PVDF binder (refer to subsection 5.2 for detail explanation). For ionic liquid, polymer binder, PTFE (Teflon 30-N, Alfa Aesar) was used in electrode fabrication. To prepare the electrode for ionic liquid ($EMIMBF_4$), activated carbon with PTFE and carbon black (Super C45) in an 80/10/10 mass ratio was mixed in ethanol in a vial until the dough formed. The thickness of the dough was rolled to form a sheet and controlled with a thickness of 150μm using the HR01 hot rolling machine. The sheet was punched into individual electrodes 12 mm in diameter for EDLC electrode. The electrodes were vacuum dried overnight. All the electrodes were then transferred to glovebox directly without exposing to air.

3.4.3 EDLC Cell construction

The symmetric two-electrode button cells (2016) were constructed with stainless steel spacers, paired electrodes of symmetric weight mass, size, and a disc of glass fiber filter paper with a diameter of 16mm as the separator (Whatman GF/F). Few drops of electrolytes were applied to wet the electrode surface

and the separator was then placed on top of the wetted electrode. The surface of the separator was moistened by a few drops of selected electrolytes under this study and further layered with another symmetric electrode and topped with a stainless-steel spacer. Cells were then sealed tight inside the argon-filled glovebox. Each sample was tested with 4 assembled cells to verify the performance. The structure of the cell is shown in Figure 3-9.

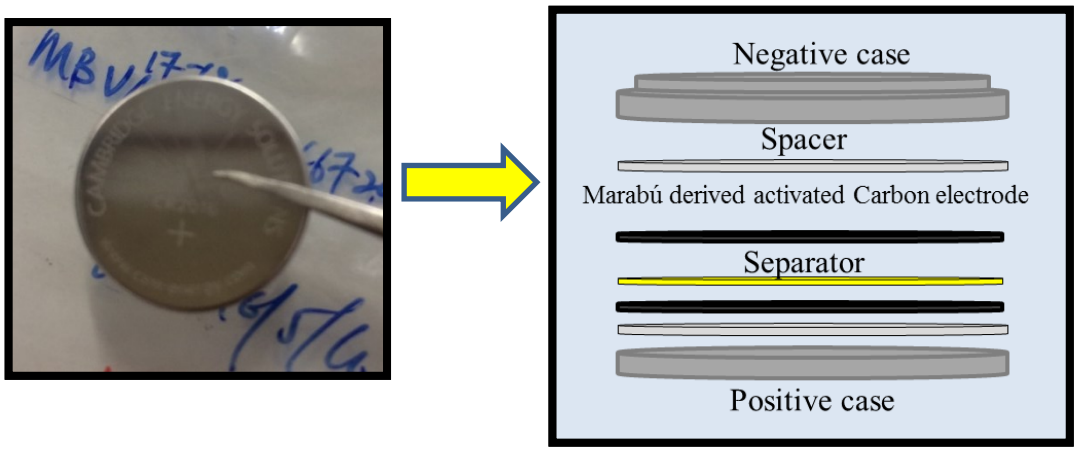

(a) (b)

Figure 3-9: Cell structure of two-electrode button EDLC cells (2016). (a) the size 2016 two-electrode button cell (b) the overall of the 2016 button cell structure

3.5 Electrochemical Measurement

3.5.1 Electrochemical Stability Window (ESW) measurement and analysis of Electrolytes

Electrochemical stability window (ESW) is the potential range limit of electrolytes for energy storage systems, in which an electrode can be polarized in an electrolyte without hindered by the electrolyte decomposition during the operation [139]. The overall performance of EDLC is greatly affected by the type of electrolyte used, as different types of the electrolyte has different ESW. Generally, aqueous electrolytes are operating not more than 1V, organic electrolytes operate in a range of 2-3 V and ionic liquids operate 3-5V. [10]

In this work, CV technique was used to measuring the ESW of the electrolyte by measuring the current at the working electrode during the potential scans. The experiments for ESW evaluation testing of EDLCs was conducted as described elsewhere [31, 32] with some modifications. The CV measurements were performed with IL, $EMIMBF_4$ by Solartron Analytical 1470E multichannel Potentiostat/

Galvanostat. The working electrode was prepared using commercial activated carbon YP80F, conductive carbon black (Super C45, Imerysys G&C) and PTFE polymer binder (Teflon 30-N, Alfa Aesar) with a mass ratio of 80-10-10 as described for IL in section3.4.2. Each cell has a counter electrode with the same composition as the working electrode. The counter electrode is at least the mass 20 times greater than the working electrode was used in this work[31, 32]. This is to ensure the potential differences are equal in both electrodes[21] and it will not be the limiting factor in the kinetics of the electrochemical process.

To study the effect of the binder on ESW of IL, another working electrode was prepared with a polymer binder (PVDF) as described section 3.4.2A fresh counter electrode that prepared using PTFE binder as described above was used to repeat the study in $EMIMBF_4$.

The CV was carried out according to the procedure conducted by Rennie et al. [32]. Before any ESW analysis, 8 hr holding step was applied to the cell to ensure the equilibrium condition between electrodes and electrolyte. The CV was carried out on asymmetric cells from the OCP to 0.5V at $5mVs^{-1}$ for two times. The window was then raised in 0.1V increments to the maximum potential of 3.6V. This was repeated using new cells for a cathodic limit from 0 to -1V and gradually reduced in 0.1V to maximum -3V for 2 cycles in each potential window. Two fresh cells were prepared for anodic and cathodic limit studies respectively.

The data were further evaluated based on Weingarth el.al [140] and Xu et. al. [141] to determine the ESW of EDLC with different polymer binders. The S-value was calculated according to Xu et. al [139] as displayed in Equation 3-2 and 3-3.

$$\boldsymbol{S_{pos} = \frac{Q_{+ve}}{Q_{-ve}} - 1} \qquad \textbf{Equation 3-5}$$

$$\boldsymbol{S_{neg} = \frac{Q_{-ve}}{Q_{+ve}} - 1} \qquad \textbf{Equation 3-6}$$

Q_{+ve} and Q_{-ve} values are calculated from positive and negative currents of one sweep respectively. A graph of S-value versus potential range was plotted and S value below 0.1 is used as an indication for the stability criterion of the electrolyte. However, there are few limitations for this method as the S-value could not reflect the stability at different temperatures. Thus the S vs potential plot was further analysed by evaluating $\frac{d^2S}{dV^2} < 0.05$, which indicates that the system is only considered in stable condition with faradaic current contribution increment not more than 5%[140]. In addition, the changes of S-value between two successive points should not be more than 0.005. The ESW of the electrolyte is further determined by subtraction of the anodic and cathodic potential limit.

3.5.2 Cyclic Voltammetry (CV) measurement

Cyclic voltammetry (CV) is an electrochemical technique to measure the current of EC by cycling the potential sweep between two values at a fixed rate as illustrated in Figure 3-10. This technique is simple and very useful to provide information about the electrochemical behavior of EC such as ESW, capacitance and life cycle. Cyclic Voltammogram is a plot of current density versus potential, which is obtained by measuring the current at a working electrode during the potential scans. Figure 3-11 illustrates a rectangular shape voltammogram of an ideal EDLC without any redox reaction or a sharp peak which represents a pseudocapacitance behavior. This technique has also been used to investigate the electrode transfer kinetics of EDLC by changing the scan rates (mVs^{-1}) and to determine the ESW of an electrolyte by gradually increasing the potential range at a very low scan rate.

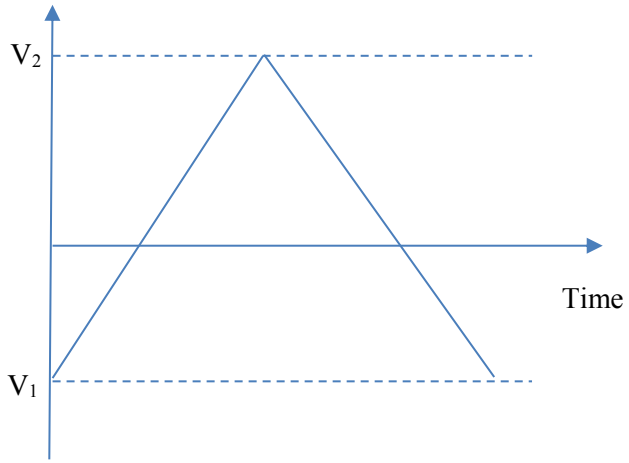

Figure 3-10: Potential is swept between V1 and V2 for CV measurement

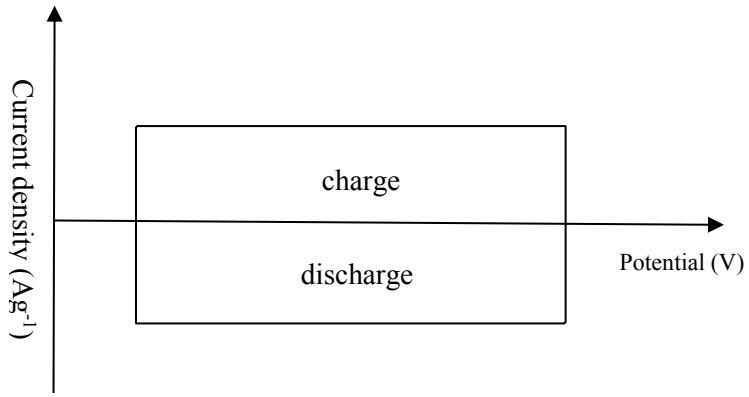

Figure 3-11: Cyclic Voltammograms for an ideal EDLC without faradaic reaction

In this case, electrochemical evaluations were performed using a symmetrical two-electrode system without a reference electrode. The CV was carried out using Solartron Analytical 1470E multichannel Potentiostat/ Galvanostat between 0 - 2.2V at sweep rates from 5-500mVs^{-1}. The cells were kept in a temperature control chamber at 25^{0}C.

For cyclic voltammetry measurements, the specific capacitance, C (Fg^{-1}), was obtained from Equation 3-7.

$$\boldsymbol{C = \frac{\int i.dt}{U.m}} \qquad \textbf{Equation 3-7}$$

Where $\int i.dt$ (C) is referring to the charge delivered during the discharge, U (V) is the operating potential window, and m (g) the mass of activated carbon in both electrodes.

3.5.3 Galvanostatic Charge/ Discharge (GC) measurement

Galvanostatic charge/ discharge (GC) is referred to replicate the charge and discharge current in a fixed charge/discharge time. The current is applied and draw on the working electrode at a constant value and the potential versus time is recorded within the operating potential of the cell. The charge and discharge current are commonly expressed in C-rate. A 1C discharge is referred to the rated 1A drained from an energy storage system in an hour. Ideally, potential changes with time linearly when the cell is discharged at a constant current as shown in Figure 3-12 (a). The three major parameters of EDLC, the total cell capacitance, operating potential and ESR can be determined. The time constant, power densities and energy densities can be further derived from the core parameters [30]. The cycling stability of an EDLC is also commonly studied using GC test. The internal resistance also can be evaluated through the GC test from the potential drop (iR drop) on the current peak at the initiation of the discharge. The losses during the charging and discharging of an EDLC is related to the movement of ions in the electrolyte across the separator to the electrodes and into the porous structure of active materials, which is also measured as internal direct current (DC) resistance. This should not be confused with the ESR, which measured as AC internal resistance using electrochemical impedance spectroscopy (EIS) in a low frequency of 1kHz. Generally, the IR drop in the GC curves is much higher than ESR. Ohmic potential drop (IR drop) is common appear in potential response during Galvanostatic cycling as displayed in Figure 3-12 (b). IR drop is the potential drop reflecting the equivalent series resistance (ESR) in EDLC. ESR exhibited in EDLC is commonly due to the electrolyte resistance, construction, impurities or low surface area in the electrode materials.

The ESR of an EDLC can be determined based on the Equation 3-8

$$ESR = \frac{\Delta V_{iR}}{I} \qquad \textbf{Equation 3-8}$$

In this work, GC of the EDLCs was evaluated using a Maccor 4000M cell test system between 0-2.2V at various rates of current density from 0.1 to 10Ag^{-1} for ten charges/ discharge cycles. The work was conducted using the Maccor is due to the availability of a number of channels (more than 50 channels as compared to only less than 10 channel in the Solatron). the Gravimetric capacitance was determined from the applied current, I (A) and the slope of the discharge curve (dV/dt) after any "iR drop" was observed as shown in Equation 3-9 below,

$$C = \frac{i}{\left(\frac{dV}{dt}\right)} \qquad \textbf{Equation 3-9}$$

The value of cell capacitance was evaluated based on the tenth discharge cycle for each rate. The stability of the symmetric cells was then further tested at a constant current density of 0.1Ag^{-1} over 30000 cycles at room temperature.

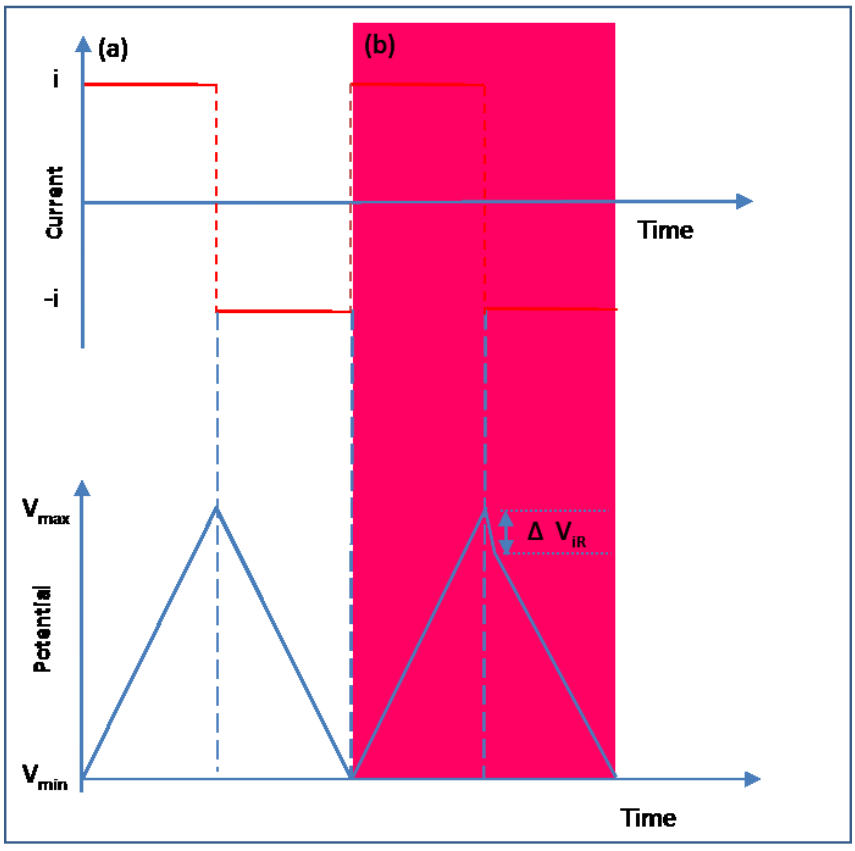

Figure 3-12: Changes in current and response in the potential for an EDLC with time (a) ideal (b) with ESR

3.5.4 Electrochemical Impedance Spectroscopy

Electrochemical impedance spectroscopy (EIS) is a technique to study the behavior of potential perturbations when different frequencies applied (mHz to MHz) at a constant AC signal or open circuit potential. This technique is commonly applied to determine capacitance, resistance, frequency-dependent and also to study the ion mobility in the ECs.

The EIS data are normally illustrated as a Bode plot with the phase angle as a function of frequency or Nyquist plot to show the imaginary and real impedances of a cell. A simple equivalent circuit model is normally designed to fit the actual EIS data generated from an experiment to evaluate the equivalent series resistance (ESR) and describe the operating characteristics of EDLCs. Randles circuit is the simplest and most common model used to describe the electrolyte resistance (R_s), double-layer capacitance (C_{dl}) and charge-transfer resistance (R_{ct}) as shown in Figure 2-6. More detail models are introduced to understand clearly the electrochemical process of an EDLC [142-144].

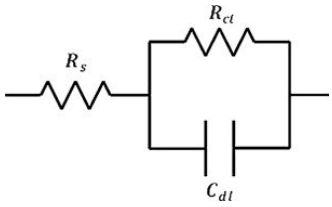

Figure 3-13: The Randles circuit [145]

The EIS spectra, Nyquist plot is often used to present the results from EIS with the real and imaginary part of impedance on x and y-axis respectively. The Nyquist plot is divided into three frequency regions. Solution resistance, Rs with a small semicircle appears in the high-frequency region for EDLCs. The semicircle corresponds to the electron transfer-limited process [146]. In this case, the EDLC is not associated with any redox reaction, thus it mainly attributes to the resistance for electrolyte ions to access narrow pores in the electrode and the motion of ions inside pores [31]. Warburg line in the intermediate frequency, followed by a transition to linearity at low frequency. The Warburg line represents the ion diffusion from the electrolyte to the electrode surface. The slope of Warburg closer to 90° suggested that the pure capacitive behavior and also fast ion transfer to the electrode surface [37].

A simple equivalent circuit model, with circuit elements such as resistance (R), capacitance (C), constant phase element (CPE), Warburg coefficient (W) and inductance (L) is normally used to fit the actual EIS data generated from an experiment.

The CPE which represents an impure double-layer capacitance, a CPE with impedance can be calculated using

$$Z_{(w)=}Q(j\omega)^{-n} \qquad \textbf{Equation 3-10}$$

Where j is equal to -1 when n in the range of $0<n<-1$ and Q is a constant with dimension Fs^{n-1}. When n=1 or 0, the CPE acts as an ideal capacitor. The imperfect double-layer behavior appears when n is 0.5 and this is also called as a Warburg element.

Kang et. al.[142] proposed an equivalent circuit which well observes the capacitive and resistive characteristics of a practical EDLC by considering the electrolyte resistance, bulk electrolyte, diffusion layer and Helmholtz layer impedances (Figure 3-13) based on Graham's theory (2.1.1). The circuit model is designed to understand the electrochemical process at double layer interface and the effects of the nature of electrolytes on the capacitance performance of a practice EDLC in aqueous and non-aqueous electrolytes. R1 represents the electrolyte resistance. The bulk process occurs only at high frequencies and is valid when the electric current overcomes the bulk impedance, thus leading to a CPE (CPE-1) modeled in parallel with bulk resistance (R2). Bulk resistance (R2) is irrespective of resistance to form the diffusion layer with excess electrolyte ions. The CPE for the bulk electrolyte is expressed as in the form in Equation 3-11[147].

$$Z_{CPE=}\frac{1}{T_{bulk}(j\omega)^{p_{bulk}}} \qquad \textbf{Equation 3-11}$$

Where T_{bulk} is referring to the CPE coefficient of bulk electrolyte (CPE-T in zview), p_{bulk} is the exponential factor of the bulk resistance (CPE-P in Z View).

Helmholtz layer is related to ions adsorption (CPE-3) (without charge transfer) on the electrode surface and Helmholtz layer formation by electrostatically attracted ions (CPE-2).
The impedance expression for the ion adsorption of CPE is as in Equation 3-12.

$$Z_{CPE=}\frac{1}{T_{ads}(j\omega)^{p_{ads}}} \qquad \textbf{Equation 3-12}$$

The CPE parameters, T_{ads} and p_{ads} are represents the CPE coefficient of ion adsorption (CPE2-T in Z view) and exponential factor of ion adsorption (CPE2-P in Z view).

The formula for CPE-3 (without charge transfer) can be expressed as in Equation 3-13.

$$Z_{CPE=}\frac{1}{T_H(j\omega)^{pH}} \qquad \textbf{Equation 3-13}$$

The T_H (CPE3-T in Z View) is referring to the coefficient of Helmholtz layer and p_H (CPE3-P in Z view) the exponential factor of Hethe lmholtz layer.

Diffusion impedance is represented by Warburg coefficient (W). The Warburg impedance can be expressed as in Equation 3-14[142].

$$\boldsymbol{Z_W = \frac{R_W}{Qw\sqrt{jw}} coth\left(B\sqrt{jw}\right)} \qquad \textbf{Equation 3-14}$$

The parameter R_W is referring to the diffusion resistance, $\boldsymbol{B}$ is corresponding to the transit time of ions[142], the diffusion time constant [142]. In Z View, W-R is referring R_W, W-T is representing $\boldsymbol{B}$ and W-P is referring to Warburg coefficient.

Since EDLC is not associated with any transfer of charge, thus R3 represents adsorption resistance and electrostatically ions attraction. This circuit was verified by Kamugai et. al. [147] to study the effects of porosity on the electrochemical performance of ACs in an IL-based EDLC. Moreover, the detail behaviors of ions electrolytes in the pores of AC based on the diffusion layer, the double layer, and the bulk electrolyte was discussed based on the circuit model.

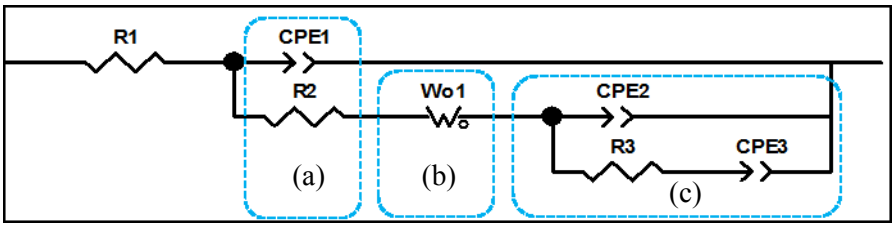

Figure 3-14: An EDLC equivalent circuit proposed by Kang et. al. [142] by involving (a) bulk electrolyte (b) diffusion layer (c) Helmholtz layer.

The capacitance of an EDLC is commonly calculated using

$$\boldsymbol{C_{EIS} = \frac{-1}{2\pi f Z'' m}} \qquad \textbf{Equation 3-15}$$

Where f (Hz) is the perturbation frequency, Z'' (Ω) is an imaginary component of impedance and m is the active mass (g) in the electrode.

In this work, the impedance of the cell was tested using a Modulab XCM (Solartron) over a frequency range from 100 kHz to 10 mHz in an environmental chamber (Maccor MTC-010) at 25°C. Nyquist plots and equivalent circuits were evaluated using Z View software (Scribner Associates, Inc).

4 Materials Preparation and Characterisation- Results and Discussion

This chapter presents the results and discussion for the properties of the five selected biomass and the characterizations of biomass-derived activated carbons. Five selected biomass wastes (Marabú wood (M), Malaysia wood pellets (MSW), palm oil empty fruit bunch pellets (EFB), Spent coffee ground (CG), Rubber wood (RW) were characterized to determine their suitability as carbon electrode materials for supercapacitors. First, section 4.1 discusses the characterization of carbon precursors, the carbonization temperature for each biomass were determined using DTG analysis. The effectiveness of the selected carbonization temperature was studied by comparing the chemical composition of the carbonized samples with the raw biomass to ensure most of the moisture and volatile removed prior to the activation process. In section 4.2, the discussion focuses on the impact of the carbonization heating rates and the activation holding time from 40-80mins on the properties of Marabu derived ACs. Next, the effects of CO_2 activation temperatures on the properties of the CG derived ACs was explained in section 4.3. Lastly, the fixed carbonization heating rates of $10^0 C min^{-1}$ with the effect of CO_2 activation holding time on the properties of MSW and EFB was compared and studied in section 4.4. The chemical composition, specific surface area and porosity of the samples were studied associated with the morphologies, Raman analysis and XPS spectra of the ACs. This is the essential screening stage to shortlist the potential AC precursors for supercapacitors applications.

4.1 Characterization of Carbon Precursors

4.1.1 CHN Analysis

The CHN analysis of Marabú, Spent Coffee ground and EFB pellets were measured using a CHNS analyzer (Vario MICRO cube CHN/S analyzer) to determine the elemental composition of carbon (C), Hydrogen (H) and Nitrogen (N) in samples. The average value of the results from duplicate tests is summarized and presented in Table 4-1. The CHN analysis data of the MSW and RW were obtained from the literature review as they used from the same source materials [148].

The obtained results of Marabú were comparable with the study conducted by Fernández, M. et. al. [126] to investigate the potential energy use of Marabú (Marabou weed). The level of C, H, and N of Marabú is 46.5%, 6.2%, and 0.7% respectively. The nitrogen (N) level of the Marabú analyzed in this project is slightly low at only 0.36%.

Table 4-1: CHN Analysis of Selected Carbon Precursors

CHN	Marabú	CG	EFB	MSW[148]	RW[148]
Carbon (wt.% (a.r))	46.7	57.7	47.0	44.606±0.98	45.002±0.37
Hydrogen (wt.% (a.r))	6.3	7.3	6.2	0.175±0.004	0.222±0.01
Nitrogen (wt.% (a.r))	0.4	1.7	ND[b]	7.72±0.34	7.62±0.49
Oxygen[a] (wt.% (a.r))	46.6	33.3	46.8	47.505	47.16

[a] by difference [b] ND- non-detected

Colombia Spent Coffee ground (CG) contains the highest carbon content, C (57.72%) among other selected biomass since it was roasted and processed for beverage production. The similar composition was reported for CG in the study by Vardon et. al [149] to investigate the potential utilization of coffee waste in energy use as Biodiesel, Bio-Oil, and Biochar. In the published work, CG contains 56.1% of carbon, 7.2% of hydrogen, 2.4% of nitrogen content respectively with a trace amount of sulfur, S (0.14%) and phosphorus, P (0.18%).

The EFB pellets from the literature [150] contain 45.14% C, 6.05% H, 0.54% N, 0.2% of S.As compared to the current work in Table 4-1, the C and H contents of EFB pellets are comparable with the literature [150] but there was no any N content detected.

The coconut shells which is widely used by supercapacitor manufacturers to produce active materials[17], contains a similar range of C as compared to the wastes biomass used in this work. Based on Tsamba et. al.[151], coconut shells contain ~47.6% of C, 6.4% of H, only 0.1% of N and about 45% of O. Similar CHN percentage of coconut shells was reported in the work of Irawan et. al.[152] that the precursors contain 48% of C, 6.5% of H, 0.1% of N, a trace amount of sulfur (0.01%) and the remaining of 44.64% of O detected.

Among all the selected biomass, CG contains the highest carbon content (57%), even higher than the coconut shells. Marabú and EFB contain similar carbon content (46-47%) as compare to coconut shells. On the other hand, MSW and RW contain slightly lower carbon content (44.6-45%). This indicated that the five selected biomass has sufficient carbon content as carbon precursor as compare to coconut shells.

4.1.2 Thermogravimetric analysis/ Proximate Analysis

The thermogravimetric analysis (TGA)/ proximate analysis on the selected biomass was performed and was repeated for ten times to ensure the accuracy. Figure 4-1 shows the TGA profiles for the studied biomass. From the TGA profile, all the carbon precursors experienced a weight loss at 127°C, denoting the moisture removed from the carbon precursors. After all the moisture removed from the biomass, EFB and CG's weight reduced gradually until the temperature at ~180°C. Marabú, RW and MSW's weight continued to decrease slowly until the furnace temperature has reached up to 250°C.

At the temperature range of 180- 350°C, a sharp weight loss profile for EFB and RW was observed. While the weight loss profile for MSW, CG, and Marabú is located at the temperature range of 180-380°C. Finally, all the samples were heated up until the temperature of 950°C until a constant weight of samples were observed at this stage.

A study by Mezerette and Girard [153] reviews the overall wood pyrolysis to five stages: moisture in wood was completely removed at temperature up to 200°C; less thermally stable hemicellulose in the wood breakdown at a temperature between 200-280°C and turns to acetic acid, formic acid, CO, CO_2, and methanol in temperature range of 280°C to 350°C is mainly lighter tars appear with some acetic acid, formic acid, methanol, and acetone. Some of the disordered carbon (cellulose) breakdown to CO_2 and charcoal and some heavier tars appear at the temperature range of 350-500°C. Hence higher temperature above 500°C is needed to remove the heavy tar. Thus, this review agrees well with the pattern of decomposition observed for wood-based agriculture by-products, Marabú, RW, and MSW in the TGA result in Figure 4.1.

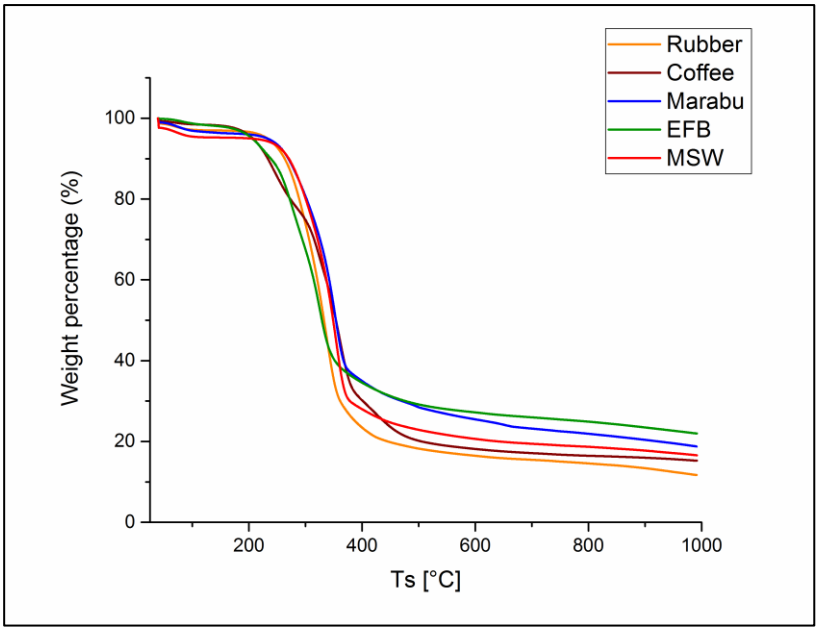

Figure 4-1: Weight loss percentage (%) versus temperature applied for biomass using proximate analysis method

The TGA results were interpreted and analyzed to determine the fixed carbon, volatile and ash content of biomass as shown in Figure 4-2, which shows that five selected waste biomass has moisture content levels under 10% which is recommended for biomass combustion [148]. CG shows a low moisture content (3.5%) as it was dried after the beverage production process. The higher moisture content in the biomass, more energy is needed to evaporate the water in the biomass during the carbonization. From the data obtained for volatile matter, one can observe that all samples are in the range of 70-80%. The volatile value lies within the typical range (up to 80%) for all the biomass[154].

The comparison made in Figure 4-2 revealed that CG, MSW, and rubber have less ash content, less moisture and but richer in the volatile matter than Marabú and EFB. EFB presented the highest fixed carbon content (~17.2%) among all the waste biomass and comparable to coconut shell (17.6%) [152]. Marabú shows larger variation data in fixed carbon content. This is due to the properties of the raw biomass. MSW, RW, EFB, and Marabú are categorized as wood samples. The fixed carbon content of MSW and RW are slightly lower than the values reported by Halim & Swithenbank [148]. Nevertheless, the fixed carbon content of all the wood samples in this is in good agreement with the carbon content or various wood samples as reported by Telmo et. al. [155] is within the range from 14 to 18%.

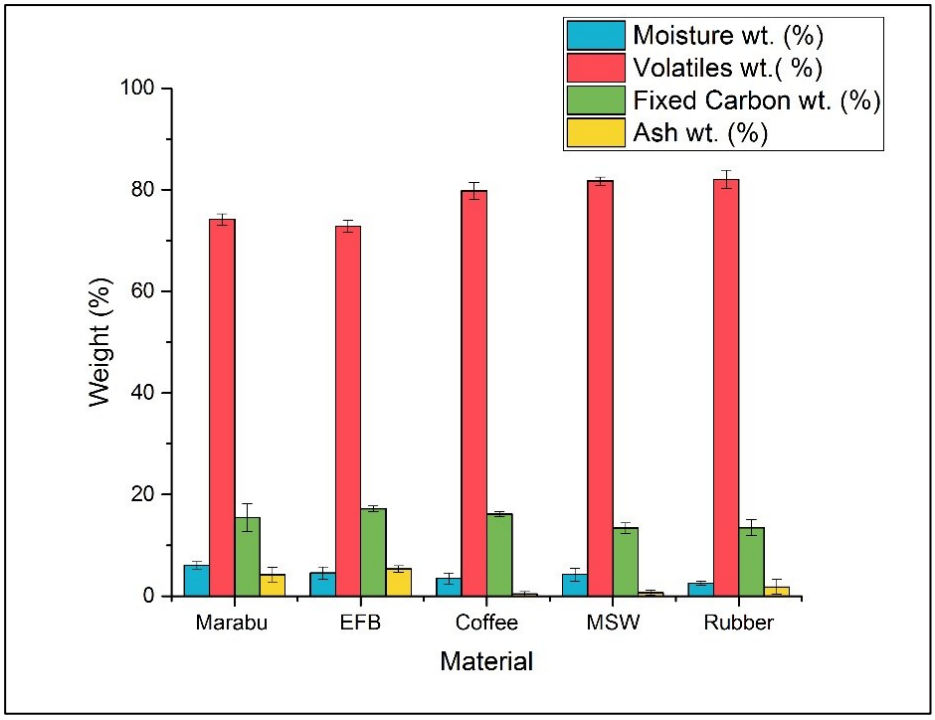

Figure 4-2: Composition of Moisture content, fixed carbon, volatile and ash content (wt%) of biomass on a dry basis determined by proximate analysis.

Based on Figure 4-2, most analyzed samples have ash contents between 0.0054 and 6.1%. Ash contains all the mineral elements that were in the biomass. Water rinsing or also called as water leaching is commonly used to demineralize and remove the ash content from samples[156, 157]. CG has the lowest ash content with a value of 0.46% as it was rinsed and treated during the beverage process before collecting as a sample for this work. the Marabú and RW are untreated, hence they have wider spread data, Marabú wood has an average ash content of 4.25% wt. and RW contains 1.1%wt.

4.1.3 Derivative Thermogravimetric analysis (DTG)

The biomass samples are then further analyzed with Derivative Thermogravimetric analysis (DTG) curve. The DTG curve of each biomass reveals clearly the decomposition temperature of each component in biomass. This step is important to improve the carbonization process in order to ensure carbon from the biomass samples is free from any other impurities. Samples were heated up from 25°C to 950°C with a heating rate of 10°Cmin^{-1} under nitrogen condition. The DTG curves of each biomass are overlapped. With some adjustment, the DTG curves of each biomass are clearly shown in Figure 4-3. Each biomass has its unique DTG curve. The DTG of all the biomass samples exhibited the maximum rate a maximum rate of weight loss at a temperature range of 260°C - 370°C. This is the temperature range that hemicellulose and cellulose are decomposed [158]. The moisture of biomass is associated with the peak at a temperature range of 110°C. For Marabú, there are additional two small peaks appear

at a temperature of 500°C and 650°C. For MSW, additional two tiny peaks appear at a temperature of 695°C and 920°C. There is one tiny peak for EFB pellets at 510°C. There is a peak at a temperature range of 200-260°C appears in CG and a shoulder peak at 400°C- 500°C. Based on the DTG analysis of biomass samples, the temperature of 950^{0}C is chosen for the carbonization process for all the selected biomass.

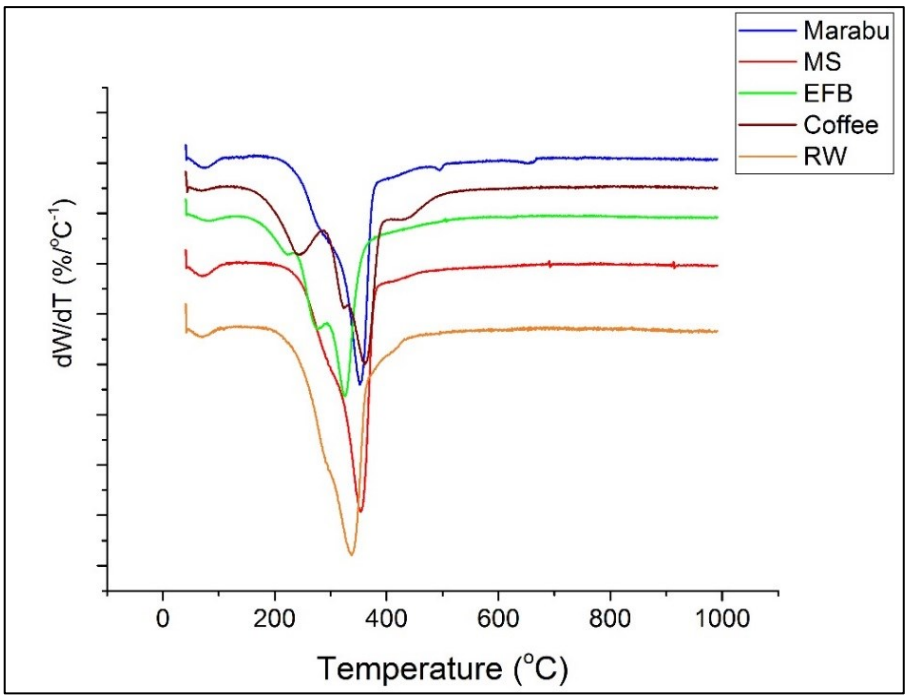

Figure 4-3: Derivative Thermogravimetric analysis (DTG) curve of waste biomass samples.

Based on the above discussion, all of the selected biomass has comparable carbon content (44.6-57%) as coconut shells which are the major source of carbon electrode material for supercapacitor applications [17]. The low moisture content below 10% and the reasonable range of fixed carbon content of all the selected biomass as compared to the wood and coconut shells suggested that all the biomass is potential as the carbon precursors. Thus, the impact of carbonization heating rates with physical activation holding time on the properties of Marabú derived ACs were further studied and discussed in section 4.2

4.2 Preparation and Characterization of Marabú derived Activated Carbon

4.2.1 The Effect of Heating Rate on the Marabú derived Carbonized Materials

Heating rate in a carbonization process is playing an important role to remove volatiles, moisture content, and impurities from biomass. In the preparation of activated carbon (AC), the development of the surface area and porosity depends on various parameters such as carbonization heating rate [81] and activation holding time[101, 113]. In this study, the effect of carbonization heating rates on yield, ash and carbon contents of carbonized samples derived from Marabú (M) were studied. The effect of heating rate on carbonization of Marabú has been studied with three different heating rates of 5°Cmin^{-1} (M5), 10°Cmin^{-1} (M10) and 15°Cmin^{-1} (M15), carbonization temperature of 950°C for the duration of 3 hours under Argon condition.

4.2.1.1 Carbonized Products Yield

The percentage yield of carbonized samples was calculated from the weight of the resultant carbonized carbon divided by the weight of dried raw biomass. In this work, the results show that thecarbonized samples yield decreases when increasing the heating rate at the temperature of 950°C. The carbonized Marabú yield decreases from 29.5% to 24.5% when the heating rate increases from 5 to 15^{0}Cmin^{-1}. The yield is 27.8% at carbonization heating rate of 10^{0}Cmin^{-1}. This is agreed well with finding for the carbonized products yield from eucalyptus [84] that the yield of the carbonised sample decreases when a higher heating rate applied at 900°C. The is due to higher and stronger molecular disruption t higher heating rates, thus accelerates the release of volatiles. In contrast, there are only weak chemical bonds in the carbon removed with low heating rate, thus slow release of volatile and resulting in a higher yield of carbonized samples [84, 159, 160].

4.2.1.2 Proximate Analysis

The carbonized Marabú samples were further analyzed using proximate analysis and the result as displayed in Table 4-2. It is nothing that most of the volatile has been removed after the high-temperature carbonization. The volatile content (VC) of Marabú reduced from ~75% to less than 10%. Higher content of the remaining VC was found in carbonized samples at higher heating rate. This contradicts as reported in the pyrolysis of sugar cane bagasse with higher yield and VC of thecarbonized sample at a lower heating rate applied[161]. In this work, this could be explained by referring to Figure 4-4, biomass was treated with longer heating time in total with a lower heating rate. It took more than

450 minutes to complete the carbonization process with 5^0Cmin^{-1} (M5). For the heating rate of 15^0Cmin^{-1} (M15), there were only 360 minutes in total to complete the process. Although a higher heating rate promotes the release of volatile, the short period to complete the carbonization could be insufficient for the release of VC. Thus, this resulting in higher VC and lower yield for samples treated at a higher heating rate at 950^0C.

Table 4-2: Proximate analysis of carbonized Marabú samples at different heating rates

Heating rate (^0C/min)	Proximate Analysis (%)			
	MC	VC	FC	Ash
5	0.7	4.9	89.5	4.9
10	1.6	5.6	88.2	4.6
15	1.9	7.6	87.5	3.0

*MC= moisture content, VC= volatile content, FC= Fixed carbon

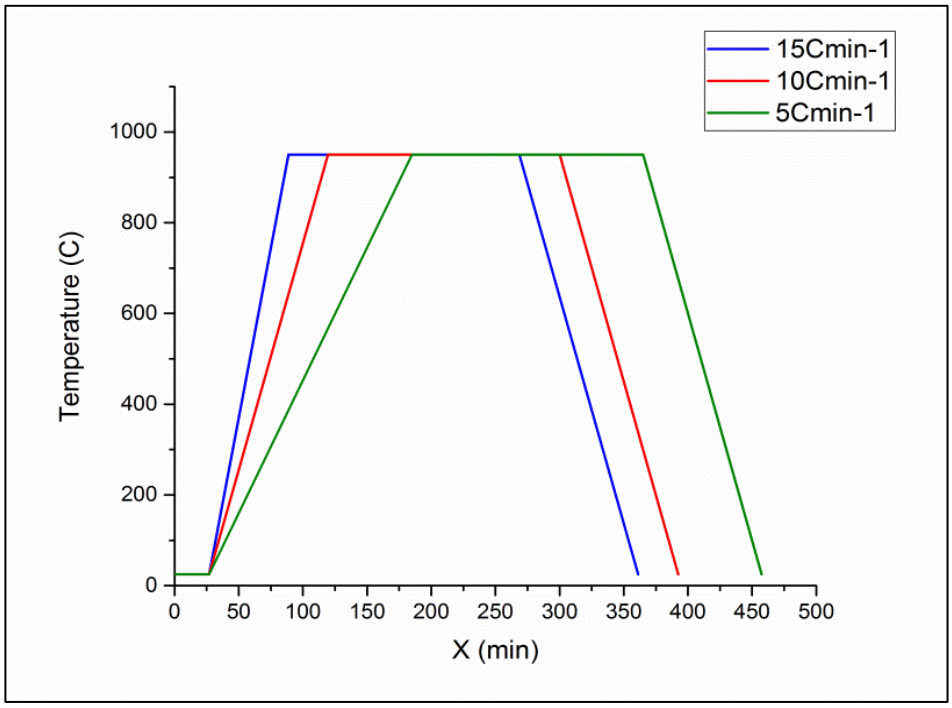

Figure 4-4: Temperature flow profile with different hearting rate

4.2.2 The Effect of Activation Holding Time on Marabú derived Activated Carbon

Activation holding time is one of the key parameters in preparation of ACs, which significantly affects the yield, surface area, and porous characteristics. The effect of CO_2 activation holding time on preparation AC using different biomass precursors was studied by various researchers [14, 15, 102,

162]. In this project, the Marabú derived AC samples were further prepared from carbonized samples of M5, M10, and M15 at activation temperature of 950°C with a constant heating rate of 10°Cmin^{-1}.

4.2.2.1 Burn-off

Figure 4-5 compares the evolution of burn-off of AC with the influence of CO_2 activation holding times (40, 60 and 80 min). The samples were labeled as M=Marabú with carbonization heating rate of 10 ^{0}C/min and followed by activation time. For instance, Marabú derived activated carbon with carbonization heating rate of 10^{0}C/min and followed by 80mins activation time is labeled as M10V8.

With the increase of activation holding time from 40 to 80mins, the burn-off of prepared AC was increased from 35.5% to 67%, 32.3% to 69.8% and 39% to 60% for M5, M10, and M15 respectively. Likewise, a similar scenario was observed by Al-khalid et. al. [162] where the burn-off of AC derived from olive oil seed increased as the activation time increase from 15 mins to 120 mins at activation temperature of 850°C. This could be explained by the CO_2 activation mechanism using endothermic Baudouard reaction as in Equation. 4-1

$$\mathbf{CO2 + C \leftrightarrow 2CO} \qquad \mathbf{\Delta H=172\ kJ/mol} \qquad \textbf{Equation 4-1}$$

This reaction favors to CO formation as heat supplied, carbon atoms were removed when the temperature above 700°C applied [102]. As the activation holding time increase, this results in the increase of burn-off. The difference in burn-off for AC from M5, M10, and M15 was relatively small for activation time below 40mins, the profile curve changes thereafter. The burn-off profile for AC from M5 increases linearly as longer activation time applied. The burn-off for AC from M15 slightly reduced after 40mins activation holding time. M10V6 is showing a slight reduction of burn-off at 60mins holding time and reached to the highest burn-off at 80 mins holding time (M10V8) as compared to AC prepared using carbonized samples of M5 & M15. In addition, activation holding time of 100mins was carried out for M10. The carbon material was burned off and there was only ash being recovered at the end of the activation process.

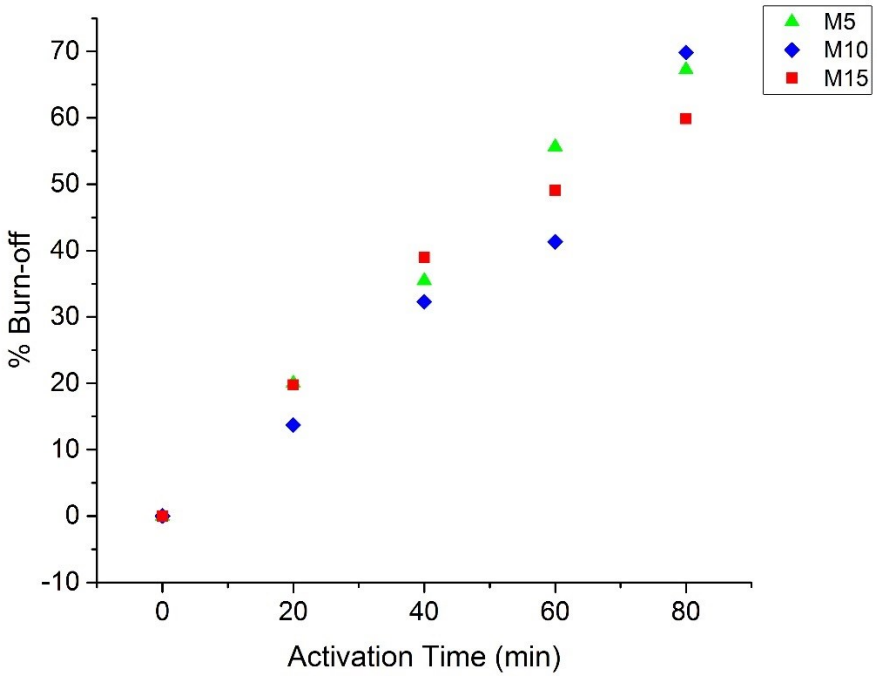

Figure 4-5: Percentage Burn-off (%) of Marabú derived AC Samples with an activation time

4.2.2.2 Proximate Analysis

Proximate analysis of samples was further carried out to reveal the effect of activation holding time on the FC and ash content in the AC samples. As seen in Figure 4-6, an increase of activation holding times leads to a decrease in fixed carbon content in AC. This is attributed by the higher volatile release and loss of fixed carbon due to the carbon-CO_2 reaction as mentioned in Equation 4-1. After 40mins activation holding time, there is about 88% of FC remaining in AC of M5; FC reduced to 78% for additional 40mins of activation holding time. For AC of M10, there was 82% of FC after 40mins holding time (M10V4) and FC in the AC reduced continuously until only 72% remaining of FC for 80mins activation time (M10V8). ACs of M15 contains the lowest FC. There is about 82% of FC in the AC after 20mins activation holding time (M15V4); the FC decrease gradually till 60mins activation holding time applied and a sharp decrease at 80mins activation holding time.

The ash content increases for both samples treated with different carbonized heating rates; the most significant increment can be seen for AC of M5. For AC of M5 and M10, the ash content increases exponentially from 5 to 10% and 3 to 8% in the range of 20 to 80 mins holding time respectively. This could be explained with the high burn-off with longer activation holding time and thus showing an increment of ash content in overall. The pore structure and surface area of Marabú derived prepared AC samples were further analyzed using N_2 adsorption/desorption isotherms.

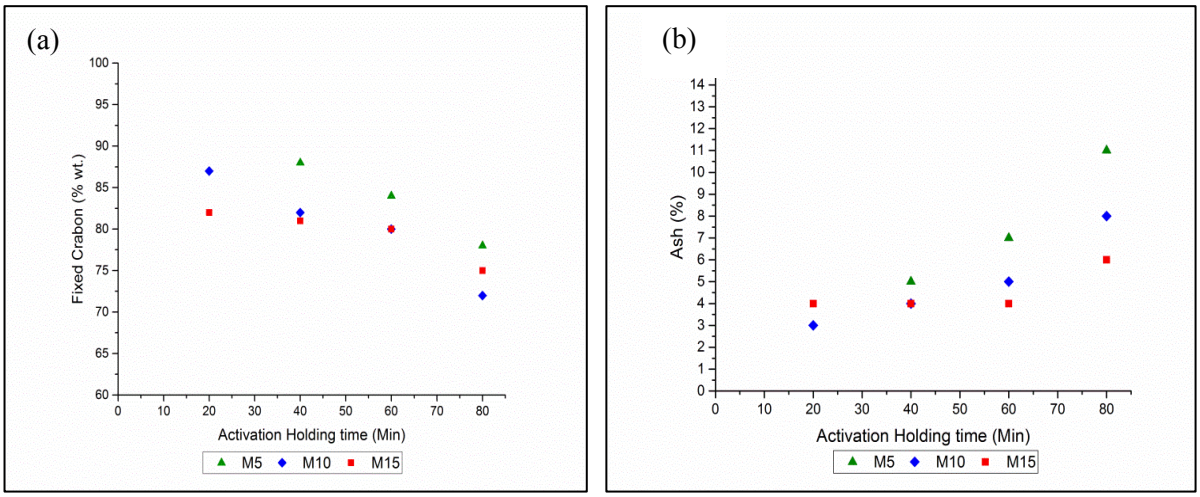

Figure 4-6: Proximate Analysis (a) Fixed carbon (b) Ash content for Marabú derived Actived carbon at 950°C under CO_2 activation.

4.2.2.3 CHN Analysis

Table 4-3 shows the elemental analysis of the ACs derived from Marabú produced with activation holding time from 40-80mins at 950°C. The reduction of carbon was observed from 75.48% (M10V4) to 70.31% (M10V8). Lower carbon content was observed with longer activation time. The result is consistent as compared to Figure 4-6 (a). This could be explained by the carbon-CO_2 reaction as stated in Equation 4-1 thus resulting in a lower yield of fixed carbon content and confirmed by the element analysis in Table 4-3.

Similar results were observed by Smets et. al. [163] when they studied the effect of physical activation condition on AC derived from rapeseed cake. The burn-off increases and elemental analysis indicated the carbon content for AC derived from rapeseed cake reduced at a temperature of 900°C for 120mins holding time using both steam and CO_2 activation method.

Table 4-3: CHN Analysis of Marabú derived Activated carbon

Material		Run 1	Run 2	Average
M10V4	C (wt.% (a.r))	75.48	75.47	75.48
	N (wt.% (a.r))	2.44	2.42	2.43
	H (wt.% (a.r.))	0.54	0.43	0.49
	O (wt.%)		**By difference* 21.61	
M10V6	C (wt.% (a.r))	78.01	77.90	77.96
	N (wt.% (a.r))	1.98	2.01	2.00
	H (wt.% (a.r.))	0.55	0.59	0.57
	O (wt.%)		**By difference* 19.48	
M10V8	C (wt.% (a.r))	69.92	70.69	70.31
	N (wt.% (a.r))	2.10	2.07	2.09
	H (wt.% (a.r.))	0.74	0.77	0.76
	O (wt.%)		**By difference* 26.86	

4.2.2.4 Porous Structure and Surface Area

The nitrogen gas adsorption-desorption measurements were conducted to study the porous characteristics of ACs. The effect of holding time on the N_2 adsorption and desorption isotherms of Marabú derived AC prepared with M5 can be observed in Figure 4-7. The AC samples categorized as a combination of type I /IV isotherms according to the IUPAC classification of adsorption isotherms with narrow hysteresis loops, which is indicative of the presence of mesoporous and microporous in AC samples. The adsorbed volume of AC samples inclines sharply under relatively low pressure ($P/P_0<0.1$) and a hysteresis observed at a higher relative pressure ($P/P_0>0.4$). The quantity of adsorption-desorption isotherm is greatly reflecting the specific surface area of each AC samples. A noticeable hysteresis loop confirms the mesoporosity at a great extent in M10V8 among other AC samples.

The pore size distribution (PSD) of Marabú derived AC was determined by Density Functional Theory (DFT) model and presented in Figure 4-7 (b). Most of the pore width of the AC samples are not more than 3.8nm. The combination of microporous and mesoporous in Marabú derived AC was confirmed and agreed with the DFT as displayed in Figure 4-7(a).

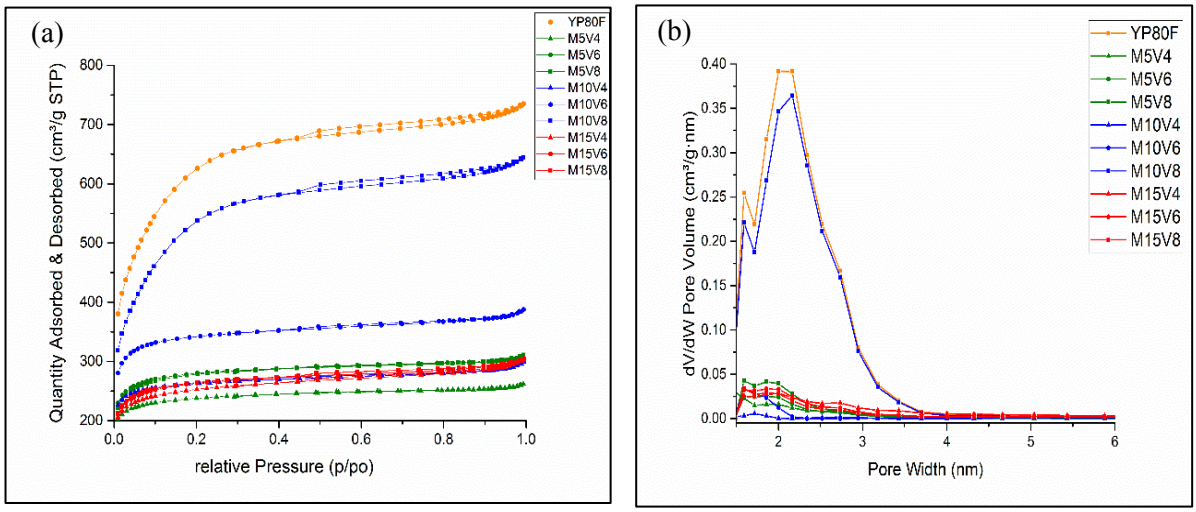

Figure 4-7: (a)N_2 gas adsorption/ desorption isotherm (at 77K) and (b) Particle size distributions of Marabú derived AC prepared with M5, M10, and M15 at different activation holding times.

AC with low ash content with high surface area is beneficial to the capacitance of EDLCs. Hence, BET analysis was carried out to investigate the specific surface area and pore volume of ACs. Summary of surface area and porosity are presented in Table 4-4. As the activation holding time increases, the specific surface area of ACs increase. As expected, surface area and porosity of samples M5 and M15 are lower than those for active samples of M10, this could be clearly explained with the lower quantity adsorption-desorption isotherm for M5 and M15 as shown in Figure 4-7(a). Among all the samples, AC with carbonization heating rates of $10^0 Cmin^{-1}$ (M10) shows higher BET surface area. The BET surface area of the active samples is a sequence of M10 > M5> M15. The specific surface area of active materials increases from $1031 m^2g^{-1}$ (M10V4) to $1977 m^2g^{-1}$ (M10V8). Although the specific surface area of M10V8 is slightly lower than YP80F (2084 m^2g^{-1}), M10V8 has the highest mesoporous volume (0.173 cm^3g^{-1}) and mesoporous surface area (153 m^2g^{-1}) among all the carbon materials. S_{meso} of M10V8 has increased about four times of M10V4 ($39.9 m^2g^{-1}$). This indicates that the activation holding time has greatly improved the mesoporous of AC samples. Based on the Equation 4-1, it can be suggested that the longer activation holding time promotes the process of gasification thus develops porosity by removing some of the fixed carbon from carbonized samples. Some of the microporous formed during carbonization was opened due to the extensive carbon burn-off with long activation holding time. This leads to widening pores and thus increases mesoporosity in M10V8. Besides, the microporous surface area of M10V8 (1861 m^2g^{-1}) is double of M10V4 (981 m^2g^{-1}). Samples M10V6 has a microporous surface area of 1243 m^2g^{-1} and BET surface area, 1324 m^2g^{-1}. Total pore volume (V_{tot}) and mesopore volume (V_{meso}) also increase significantly from M10V4 to M10V8. Micropore volume (V_{mic}) of M10V6 is $0.538 cm^3g^{-1}$. The specific surface area of AC slightly decreased while

increasing the activation time up to 80mins. This can be attributed by the carbon structure ordering and some of the micropore coalescence[84].

Table 4-4: Surface area and Porosity Characteristics of Marabú derived Activated Carbon and Commercial carbon (YP-80F)

Material	S_{BET}[a] ($m^2 g^{-1}$)	S_{mic}[b] [$m^2 g^{-1}$]	S_{meso}[c] [$m^2 g^{-1}$]	V_{tot}[d] [$cm^3 g^{-1}$]	V_{mic}[e] [$cm^3 g^{-1}$]	V_{meso}[f] [$cm^3 g^{-1}$]
M5V4	917	864	36.8	0.3142	0.365	0.0406
M5V6	1065	1026	43.5	0.3760	0.435	0.051
M5V8	1065	1025	44.8	0.375	0.431	0.0541
M10V4	1031	981	39.9	0.3619	0.408	0.055
M10V6	1324	1243	56.6	0.6	0.538	0.073
M10V8	1977	1861	153	0.998	0.719	0.173
M15V4	917	802	30.2	0.388	0.332	0.071
M15V6	952	1042	16.2	0.433	0.371	0.077
M15V8	932	880	15.2	0.343	0.365	0.039
YP80F	2084	1979	40	0.90	0.855	0.121

[a] Specific surface area calculated using the BET method.[b] micropore surface area determined using the t-plot method. [c] mesopore surface area determined from the adsorption branch of the isotherm using the BJH method. [d] total pore volume calculated at $P/P_0 > 0.99$.[e] Micropore volume determined using the Dubinin- Radushkevich (DR) method. [f] mesopore volume determined using the BJH method

4.2.2.5 Morphologies analysis

Based on the BET analysis, AC samples prepared with M10 has the highest surface compared to M5 and M15. AC samples of M10 were further examined by Scanning Electron Microscope (SEM) to analyze the surface and morphology of the sample. The morphology of Marabú derived activated materials was imaged as in Figure 4.8 (a) – (c). It can be clearly seen that the particle size of active materials reduces when increasing the activation time. The carbon sample turns into random shapes, various particle sizes, and porous size.

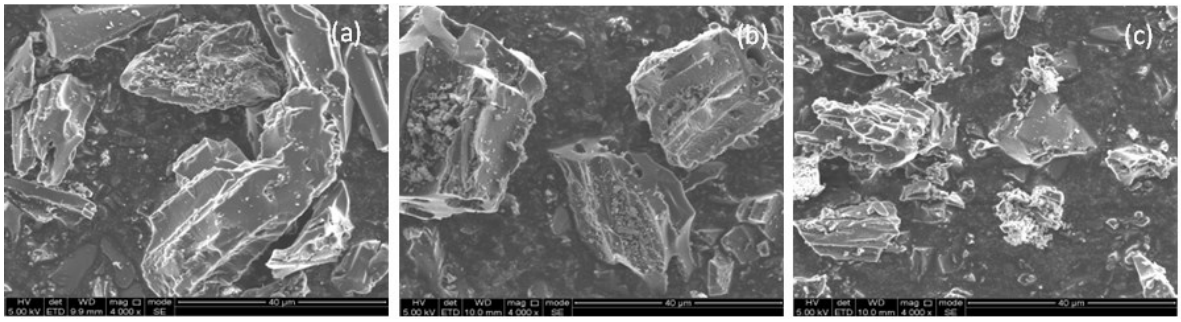

Figure 4-8: Morphology analysis using SEM for Marabú derived activated carbon under the effect of carbonization heating rates and holding times (a) M10V4, (b) M10V6, (c) M10V8

4.2.3 Raman Spectroscopy

Investigation on the structure of the active materials was conducted using Raman analysis. Figure 4-9 shows the Raman spectra of the prepared activated carbon, M10V4, M10V6, M10V8 and the selected commercial activated carbon, YP80F, and the fitting parameters are listed in Table 4-5.

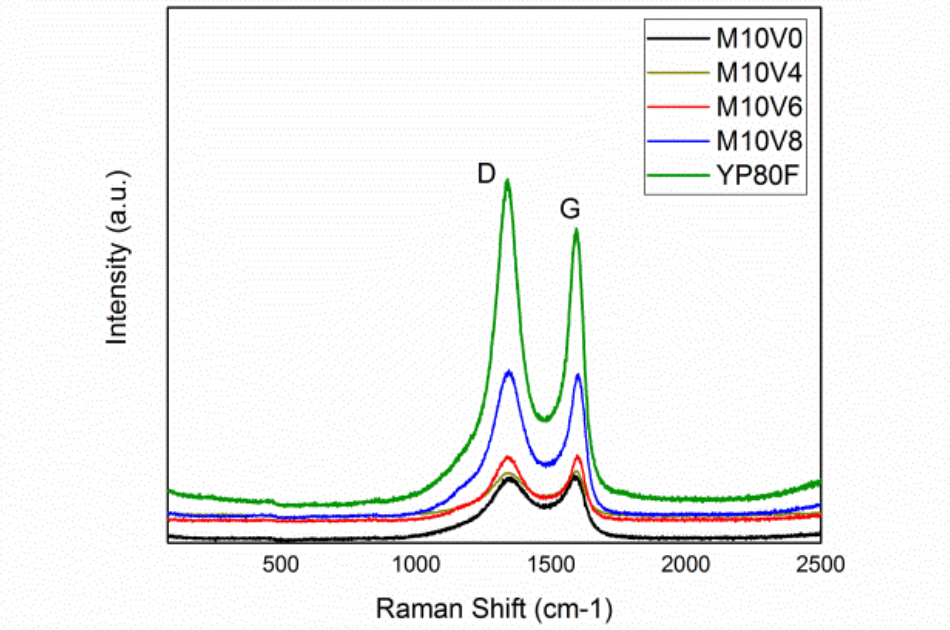

Figure 4-9: Raman spectra for Marabú derived active materials and YP80F

The Raman spectrum depicted in Figure 4-9 shows two intense Raman peaks, which located at ~ 1341cm^{-1} (D-band) and ~1600cm^{-1} (G-band). Curve fitting was performed by setting the position of bands D & G according to the values from the literature review for carbonaceous materials [164-166] with boundary tolerance of 5% (Appendix A). The position of the Raman band of each AC derived from Marabú is listed in Table 4-5. The assignments of bands are summarized in Table 4-6. The curve fitting clearly indicates that five bands (D1, D2, D3, D4, and G) were observed using Voigt lineshape (convolution of Gaussian & Laurentzian lineshapes).

Table 4-5: Position of the Raman band of Marabú derived carbon samples

Peak	Position (cm-1)	YP80F	M10V8	M10V6	M10V4
D4	~1200	1185	1185	1182	1165
D1	~1350	1339	1344	1341	1341
D3	~1500	1530	1533	1501	1549
G	~1580	1595	1597	1594	1594
D2	~1620	-	1613	1603	1608

The basic peaks of observed in Raman spectrum of graphitic materials [164, 167] are G mode, which designated at approximately 1580cm^{-1} and the other four-order peaks found between ~1200 cm^{-1} (D4), ~1340-1350 cm^{-1} (D1), ~1620 cm^{-1} (D2) and ~1500 cm^{-1} (D3). Peaks appearing of D4, D3 and D2, which are related to impurities [164], amorphous[166] and disordered carbons[168], respectively.

Table 4-6: Summary of position Raman bands assignments and bond type

Peak	Position (cm^{-1})	Possible interpretation	Bond type	Reference
D4	~1200	• C–C and C=C stretching vibrations of polyene-like structures	$sp^2 – sp^3$	[164]
D1	~1350	• D peak of microcrystalline graphite • D peak due to aromatic clusters of benzene rings	sp^2	[165, 166]
D2	~1620	• Disordered graphitic lattice	sp^2	[165, 169]
D3	~1500	• Amorphous carbon • Typical fingerprint of polymeric a-CH		[164, 166]
G	~1580	• Graphite; aromatic ring quadrant breathing; alkene C=C	sp^2	[165, 170]

Table 4-7: Area and height value of Raman Peak D1 and G for Marabú derived carbon samples and YP80F

	Peak D1		Peak G		ID1/IG
	FWHM	height	FWHM	height	ratio height
M10V8	138	8309	65	5584	1.48
M10V6	142	3633	85	1103	1.516
M10V4	174	2518	106	1638	1.537
YP80F	103	18130	107	13550	1.337

The G-band is related to the vibration of sp2-hybridized carbon atoms in a two-dimensional hexagonal lattice [39]. D1 is commonly attributed to the disordered graphitic lattice [164] or the number of defect sites[36, 171]. Some work correlated D1 to aromatic clusters of benzene rings [165, 166]. Recently, D1 is correlated to the oxygen functional groups on the samples[171].

D1 & G bandwidth could be characterized by the disordered degree for carbon materials [167, 171, 172]. The FWHM of G band reduced with a longer activation holding time applied (Table 4-7). This suggested that the increase of bond-angle ordering at sp2 sites. Similarly, the FWHM of the D1 band for M10V8 band decreased as compared to M10V4 and M10V6, which suggested the reduction of degree disordered [172].

The relative intensity of D1/G peaks is one of the conventionally used to characterize the degree of structural order of carbons [167]. In this case, ID1/IG of M10V4 is 1.537, reduced to 1.516 for M10V6 and only 1.48 for M10V8. The ID1/IG ratio drops as longer activation holding time applied, which indicates that longer holding time promotes the removal of disordered carbon thus the graphitization degree has improved [40]. Lower ID1/G ratio also represents a lower oxygen functional group [171], which is well agreed with the reduction of the O composition by using XPS analysis.

4.2.4 X-ray photoelectron spectroscopy (XPS)

Surface functional groups of ACs have greatly influenced the performance as electrode materials in supercapacitor owing to its effects on the wettability and Faradaic reaction in the cell [41, 173]. XPS spectra of AC derived Marabú were further studied to understand the elemental composition and surface functional groups in the AC samples. The elemental composition of the ACs surface layer was determined from the XPS spectra.

Figure 4-10 presents the high- resolution XPS survey spectra of Marabú derived ACs (M10V4, M10V6, and M10V8). All the activated carbon samples exhibit four peaks with binding energy of ~285 eV (C 1s), ~350eV (Ca 2p), ~400 eV (N 1s), 532eV (O 1s). C1s and O 1s are showing as high binding energy peak, which indicates the presence of C, O. It is noticed that the C atomic percentage decreases as longer holding time applied, where M10V4 achieves 88.16%, M10V6 achieves 88.13% and reduced to 87.84% for M10V8. O atomic percentage increases from 11.32% (M10V4) to 11.87% (M10V6) and 11.3% for M10V8. There is a trace of N composition of 0.52% and 0.62% was found in M10V4 and M10V8, respectively. Ca composition (0.93%) was only detected in M10V8. The Ca and N content might be due to the mineral from the soil that the plants grow. Although the carbon composition determined by XPS has the same agreement trend as that found in CHN analysis, it is noticeable that there are some differences between the value obtained using CHN analysis and XPS spectra. The composition was determined by XPS is based on the surface layer of samples in atomic percentage, while CNH analysis is based on bilk combustive. There is some limitation for both technique as the CHN analysis is unable

to determine the oxygen content of samples, thus the oxygen content is assumed as the balance from the composition. While XPS is not able to ascertain the hydrogen content.

The high- resolution C 1s spectrum of M10V4, M10V6 and M10V8 can be resolved in several peaks centred (Figure 4-11), respectively referring to C 1s-A(283.89eV) and C 1s-B (284.8eV), C 1s-C (285.5eV), C 1s-D (286.8eV), C 1s- E (287.5eV), C 1s-F (288.5eV) and C1s-G (289.5eV). For the peak at a binding energy of 283.5eV, there are still ongoing discussions which could represent CH_3-[174] or -CH_2-[175]. There is also a study claimed that this is due to the sp hybridized carbon [176, 177]. Similarly, the O 1s spectrum was further deconvoluted in three peaks centered (Figure 4.12) at 531.58eV, 533.04e, and 535.39eV, corresponding to O1s-A, O1s-B and O1s-C, respectively. The results of deconvoluted C 1s and O1s spectra and the data fitting are listed in Table 4-8.

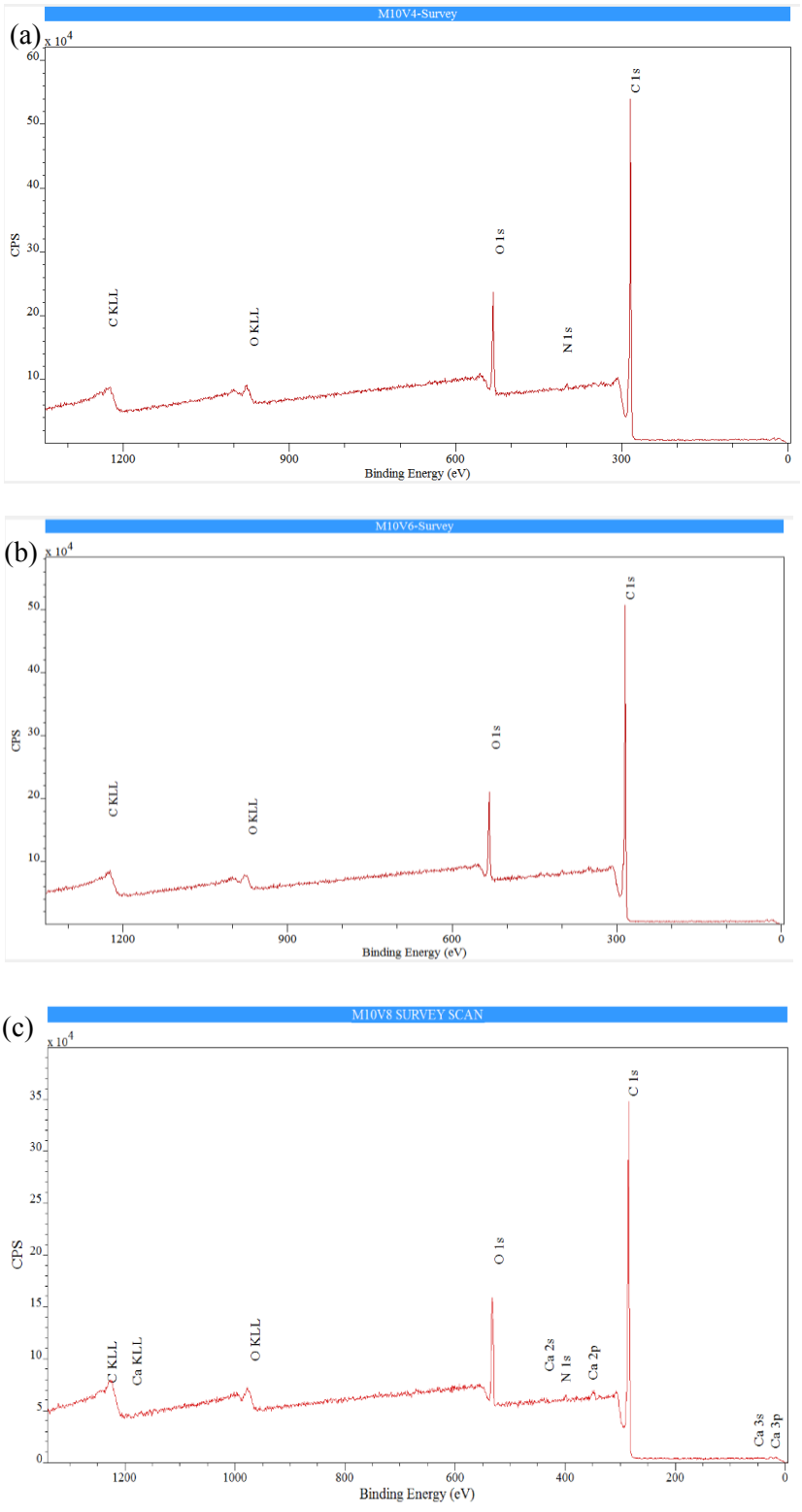

Figure 4-10: XPS survey scan of Marabú derived ACs samples of (a)M10V4, (b) M10V6 and (c) M10V8

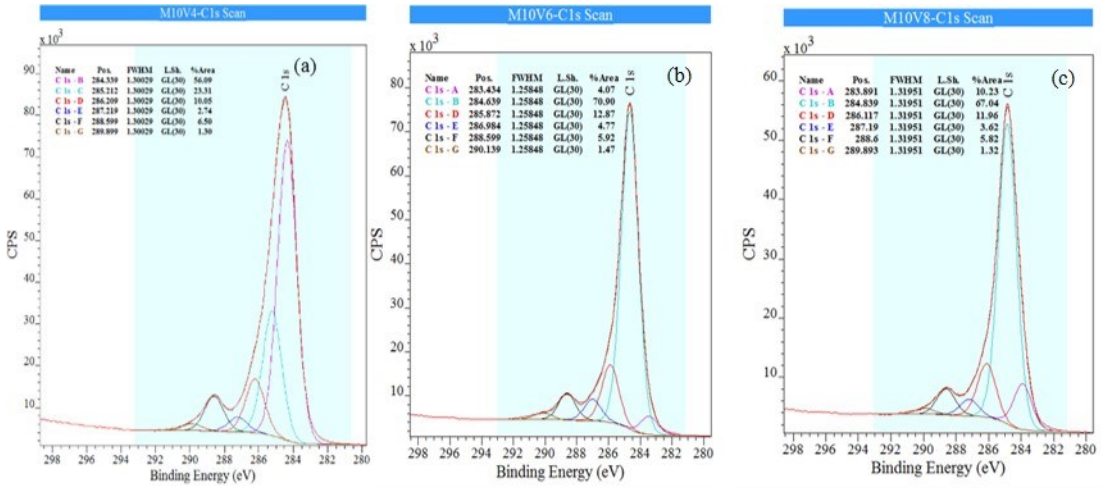

Figure 4-11: C1s XPS spectra for (a) M10V4, (b) M10V6 and (c) M10V8 with deconvolution analysis

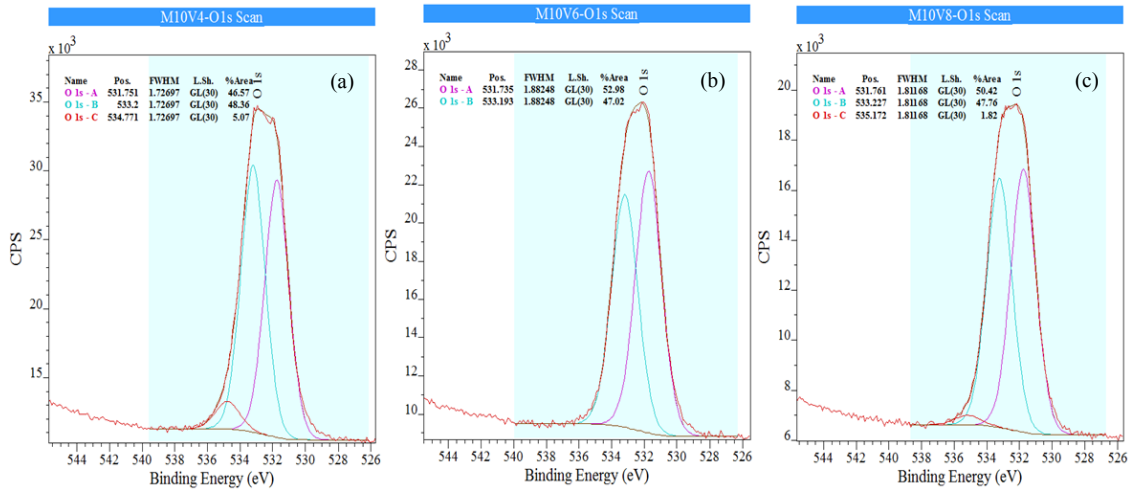

Figure 4-12: O1s XPS spectra for (a) M10V4 (b) M10V4 (B) M10V6 (C) M10V8 with deconvolution analysis

Table 4-8: XPS peak fitting results for Marabú derived AC samples carbonized with 10^0Cmin^{-1} (M10)

Region	Name	BE (eV)	Assigned to	Reference
C 1s	C1s- A	283.5	CH_3- / -CH_2-	[174] [175]
	C1s- B	284.5	C=C	[36, 178, 179]
	C1s- C	285.5	C-C	[179, 180]
	C1s- D	286.8	C-O-	[178, 179]
	C1s- E	287.5	C-O-C	[181]
	C1s- F	288.5	C=O	[36, 178, 179]
	C1s- G	289.5	O-C=O	[179]
O 1s	O1s-A	531.58	O=C	[41]
	O1s-B	533.04	O-C	[41]
	O1s-C	535.39	Chemisorbed oxygen or H_2O	[182]

Based on Figure 4-11, the dominant peaks for M10V4 is C1s- B (56%), C1s-C (23%), which are assigned as C=C and C-C respectively. C1s-D (10.05%), C1s-E (2.74%), C1s-F (6.5%) and C1s-G (1.3%), which attributed as oxygen functional groups (Table 4-8) is observed in low percentage from the C1s spectra.

It is noticed that the peak of C1s-C was disappeared and C1s-A, as a weak peak was detected in both M10V6 and M10V8. It is clearly seen in Figure 4-11 that peak C1s-B is the dominant peak in M10V6 and M10V8, which is 70.9% and 67%, respectively. The peak of C1s-E (286.9eV), C1s-F (288.6eV) and C1s-G (290.1eV) which are attributed as oxygen functional groups are detected for M10V6 and M10V8. For O 1s spectra (Figure 4-12), there is no significant effect of activation on the O1s. All the AC samples have equal percentage area for O1s-A (~531eV) and O 1s-B (~532eV), which corresponding to O=C and O-C respectively.

4.2.5 Summary

Marabú weed, invasive hardwood plant in Cuba, is a potential activated carbon precursor to produce low-cost and high surface area carbon for energy storage systems applications. Based on the discussion above, the chemical compositions and the porous structure of Marabú derived AC samples are greatly influenced by the carbonization heating rates and the activation time. In this work, AC was prepared using three different carbonization heating rates: M5, M10, and M15. ACs which prepared from M5. A lower heating rate requires a longer duration to complete the carbonization process promotes the loss of the fixed carbon and devolatilization. The longer carbon-CO_2 reaction delivered a lower yield AC due to the carbon loss in the process. Among all the ACs, M10V8 shows the highest specific surface area (1977 $m^2 g^{-1}$) with a mixture of microporous and mesoporous. The ID1/IG ratios of Marabú derived AC decrease from 1.537 (M10V4) to 1.48 (M10V8) with a longer activation time applied from 40-80mins. This indicating the improvement in the degree of graphitic crystalline structure and lower oxygen functional groups on the surface of ACs.

4.3 Preparation and Characterization of Spent Coffee Ground (CG) Pellets derived Activated Carbon

4.3.1 The Effect of Activation Temperature

Activation temperature is one of the most influencing factors for the development porosity of AC either through chemical or physical activation process [36, 39, 44, 45, 93, 105]. Based on the effect of carbonization heating rates and activation holding time on Marabú derived activated carbon in section 4.2, higher surface area with lower ash content of AC achieved with carbonization heating rate of $10^{o}Cmin^{-1}$. Hence, carbonization condition with the temperature of 950°C and fixed heating rate of $10^{o}Cmin^{-1}$ is selected to prepare carbon prior to prepare activated carbon Spent Coffee Ground (CG). In this section, the effect of activation temperature of 950^{0}C (C10V) and 1000^{0}C (C10W) and activating holding times (40, 60, 80 and 100mins) on the production of spent Coffee ground (CG) derived activated carbon are studied. The influence of activation temperature on AC yield, burn-off, ash and fixed carbon content of CG derived activated carbon samples are discussed. The explanation on surface properties and porosities of the AC under the effect of activation temperature are also included.

4.3.1.1 Burn-Off

Figure 4-13 represents the carbon burn-off of CG under the effect of CO_2 activation temperature of 950°C and 1000°C. It can be clearly seen that the activation temperature greatly affects the burn-off of CG. With the increase of activation holding time from 40 mins to 100 mins, the burn-off increase from 19% to 48% and 30% to 81% for activation temperature 950°C (C10V) and 1000°C (C10W) respectively. The observation agrees well with work by Demiral *el al.* [111]. Higher burn-off was observed as activation temperature increase from 750°C to 900°C with longer holding time to prepare olive bagasse derived activated carbon using CO_2 activation. Chang *et. al*.[110] has prepared activated carbon from corn cob, higher burn-off was observed either in steam or CO_2 activation at higher activation temperature from 800°C to 900°C.

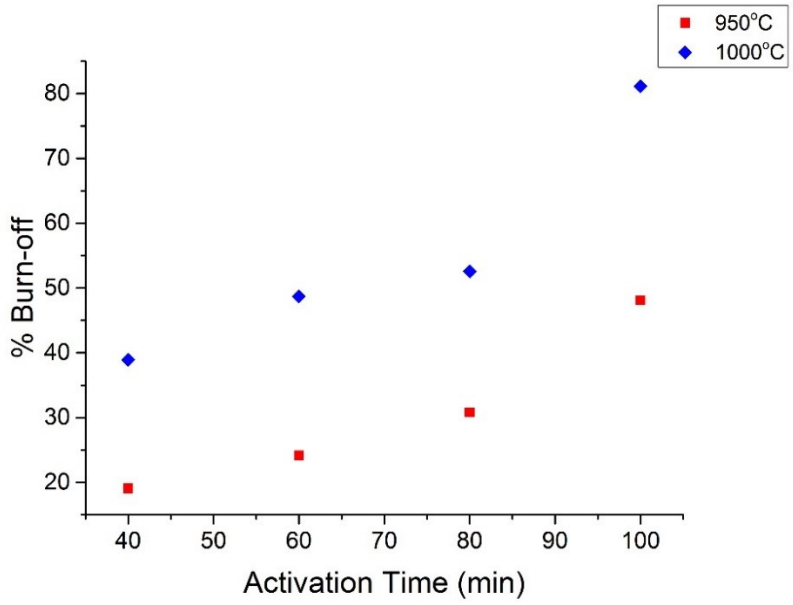

Figure 4-13: Effect of CO_2 activation temperature on the burn-off of prepared AC derived from Coffee

4.3.1.2 Proximate Analysis

Table 4-9 shows the proximate analysis results for the CG derived AC samples obtained at 950°C (C10V) and 1000°C (C10W) activation temperature with holding time from 40mins to 100mins at a constant heating rate of 10°Cmin^{-1}. As referred to Table 4-9, an increase of activation temperature with longer activation holding time leads to a reduction of carbon content in the AC produced. For AC produced at 950°C, the fixed carbon reduced from 93.38% to 86.63%. At 1000°C, the fixed carbon dropped from 93.76% to 88.08%. According to Molina- Sabio et. al.[183], the activation rate could be calculated based on the relationship between burn-off and activation time. By comparing the slopes of the two activation temperatures in Figure 4-13, the rate of the activation at 1000°C is higher for CG. This could be explaining that an increase in activation rate at 1000°C and thus favor the reactivity of carbon with CO_2 oxidizing gas agent[103]. This could enhance the total pore volume[110] and removal of some disordered carbon and thus leading to the increase of ash proportion.

Table 4-9: Proximate analysis of CG derived AC under the effect of CO_2 activation temperature

	Proximate Analysis, %			
	Moisture Content	**Volatile Matter**	**Fixed Carbon**	**Ash**
C10V4	1.24	5.79	93.38	0.41
C10V6	1.17	4.97	90.63	3.23
C10V8	1.91	8.81	85.97	3.34
C10V10	0.32	6.18	86.63	7.02
C10W4	1.08	2.98	93.76	2.56
C10W6	0.84	4.33	91.45	3.36
C10W8	0.84	4.23	91.74	3.20
C10W10	0.47	5.75	88.08	6.18

4.3.1.3 Morphologies of CG derived Activated Carbon analysis

Morphology of the CG derived AC samples were further analyzed using Scanning electron microscopy (SEM). This could provide a comprehensive understanding of the morphological changes of the prepared AC samples under the impact of carbon dioxide activation temperatures. Prior to the activation process, the escape of volatile materials during the carbonization has created the fundamental pore structure on the CG carbonized materials. Hence pores of the carbon have further enlarged and widen during the CO_2 activation process. As referred to Figure 4-14 (b), irregular cavities with obstructed small pits distributed over C10V8. This could be due to blockage by that condensed volatiles which release during the gasification process. Wider pores and with larger pits could be found in C10V10 as longer activation time applied, some obstructed pits still visible as shown in Figure 4-14 (c). As the activation temperature increased from 950 to 1000°C, the development of unobstructed pore structure as shown in Figure 4-14 (d). Small pits, large porous with different shapes could be seen clearly from the photograph, this could be accounted for the higher specific surface area and total pore volume.

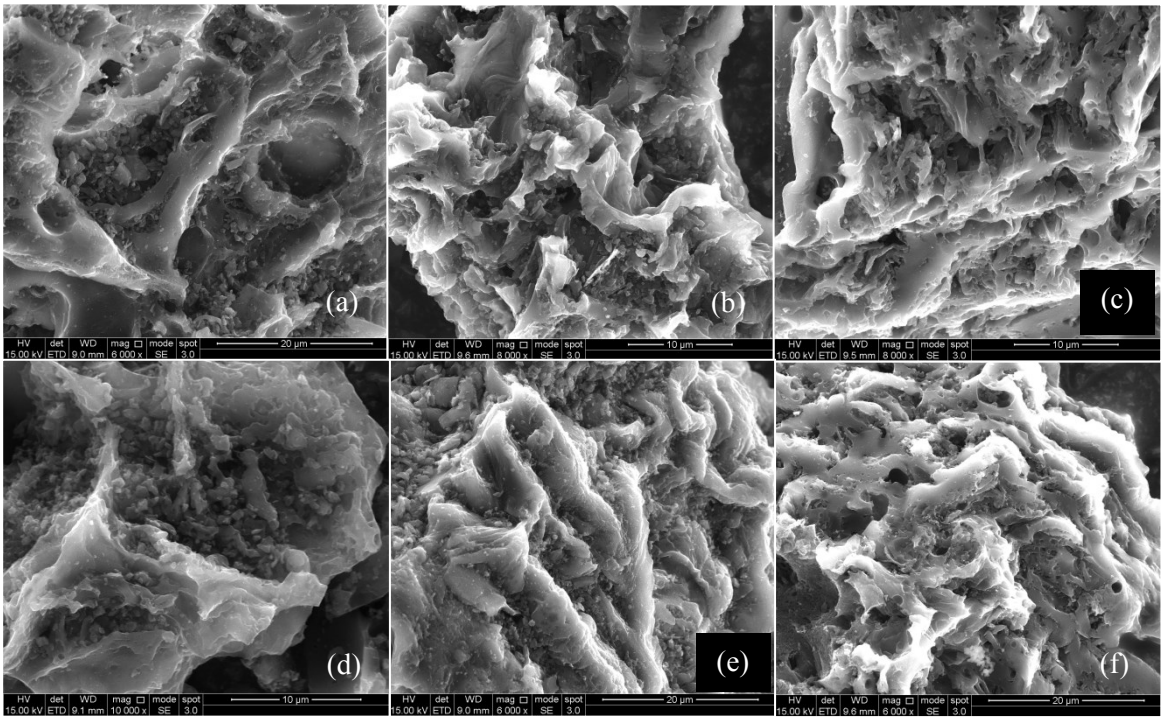

Figure 4-14: SEM of CG derived ACs (a) C10V6 (b) C10V8 (c) C10V10 (d) C10W6 (e) C10W8 (f) C10W10

4.3.1.4 The porous structure of CG derived Activated carbon

The porosity characteristics of CG, including BET surface area (S_{BET}), and pore volumes were determined and are summarized in Table 4-10 shows that the porosities of AC are greatly influenced the activation holding time and the activation temperature.

The S_{BET} of AC is higher with an activation temperature of 1000°C. S_{BET} of AC prepared at 950°C and 1000°C increased from 396m^2g^{-1} to 1082 m^2g^{-1} and from 791m^2g^{-1} to 1473 m^2g^{-1}, respectively with the increase of holding time ranging from 40mins to 100mins. On other hands, total pore volume increases with longer holding time at higher activation temperature of 1000°C. With the increase of holding time, the V_{tot} of AC prepared at 950°C were gradually increased from 0.15 cm^3g^{-1} to 0.39 cm^3g^{-1}. The V_{tot} of AC prepared at 1000°C was increase from 0.337 cm^3g^{-1} to 0.54 cm^3g^{-1}. This indicates that a higher activation temperature with longer holding time helps to develop a porous structure with a higher S_{BET} and V_{tot}. By comparing the V_{tot} value for two different temperatures, the V_{tot} value of C10W4 is two times higher than the V_{tot} value of C10V4. As the holding time increases, the V_{tot} value difference between these two activation temperatures is gradually reduced as shown in Figure 4-15.

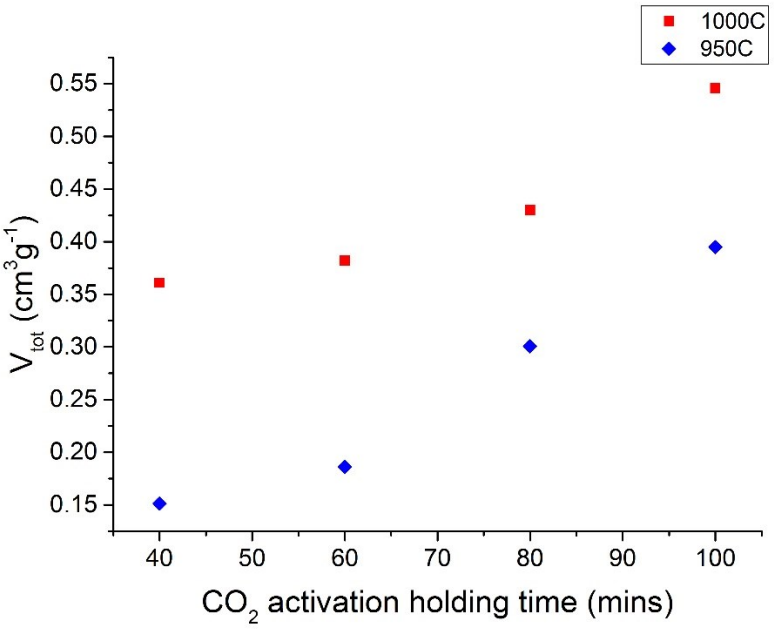

Figure 4-15: Effect of activation temperature with holding time range from 40-100mins on total pore volume of CG derived ACs

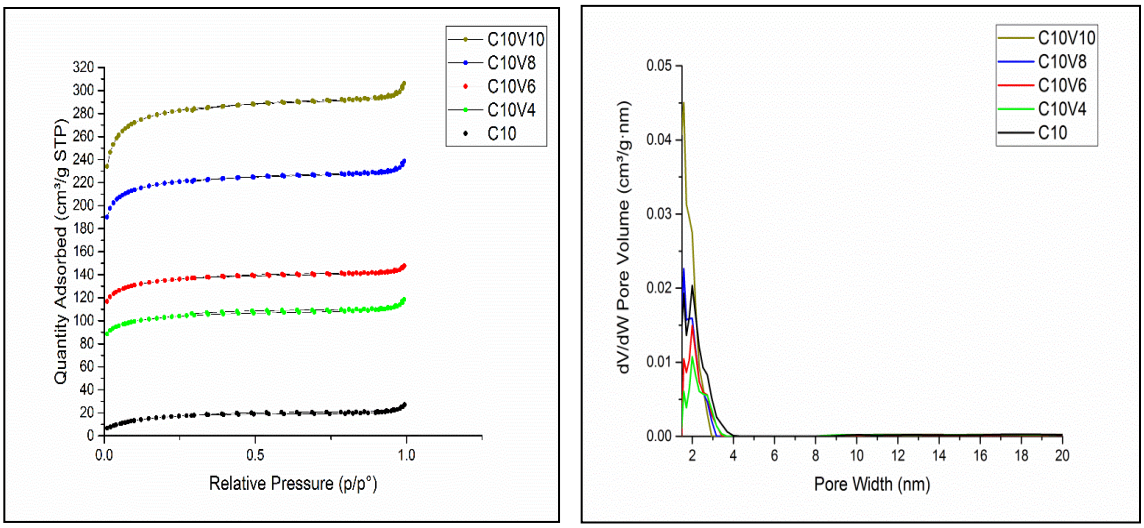

Figure 4-16: (a) N_2 gas adsorption-desorption of CG derived AC and (b) PSD of CG derived ACs for activation holding time from 40-100mins at activation temperature of 950^{o}C

Figure 4-16 illustrates the adsorption isotherm and pore size distributions of the prepared ACs by CO_2 activation with an activation temperature of 950^{o}C and activation holding time from 40mins to 100mins. The general form of the isotherms is the same for all the ACs although the initial uptake at low relative pressure increases with longer holding time. A narrow degree of hysteresis exists in C10 indicated that there are some microspores in the carbonized samples. CG derived AC with 100 mins activation holding time is the optimum N_2 adsorption capacity value. The shapes of isotherm with narrow hysteresis loops

exhibit typical features of Type-1 in IUPAC classification of adsorption isotherms, which suggests that the prepared AC mainly consist of microporous with a little amount of mesoporous. This is reflected in Figure 4-16(b) that the pore widths of ACs are not more than 4nm. It is noted that the pore size range slightly reduced as longer activation time applied to produce AC at 950°C. The pore size of carbonized materials is not more than 4nm; the pore size of the ACs further reduced to maximum 3nm for C10V10. As referred to Table 4-9, the remaining volatile content in AC samples which treated in 950°C is higher than treated at 1000°C. This indicated that the temperature of 950°C is insufficient for CG to achieve an optimum gasification process. This confirmed by the morphology of carbon with clearer pits in C10W10 as shown in Figure 4-14(f).

Table 4-10: Surface area and pore volume of CG derived AC prepared under activation temperature of 950°C and 1000°C

Material	S_{BET} $[m^2g^{-1}]^a$	S_{mic} $[m^2g^{-1}]^b$	S_{meso} $[m^2g^{-1}]^c$	V_{tot} $[cm^3g^{-1}]^d$	V_{mic} $[cm^3g^{-1}]^e$	V_{micro}/V_{tot}	V_{meso} $[cm^3g^{-1}]^f$	V_{meso}/V_{tot}
C10	58.3	-	1.94	0.0381	-	-	0.0092	0.241
C10V4	396	326	3.15	0.1514	0.128	0.845	0.0145	0.096
C10V6	523	439	3.85	0.1861	0.171	0.919	0.0125	0.067
C10V8	856	741	6.6	0.3008	0.289	0.961	0.0219	0.073
C10V10	1082	912	9.3	0.3948	0.3593	0.91	0.0292	0.081
C10W4	791	651	8.2	0.361	0.337	0.93	0.0247	0.068
C10W6	1058	865	9.5	0.382	0.343	0.897	0.0248	0.065
C10W8	1169	914	12.2	0.430	0.366	0.851	0.0313	0.073
C10W10	1473	1050	20.6	0.546	0.43	0.787	0.0525	0.096

[a] Specific surface area calculated using the BET method.[b] micropore surface area determined using the t-plot method. [c] mesopore surface area determined from the adsorption branch of the isotherm using the BJH method. [d] total pore volume calculated at $P/P_0 > 0.99$. [e] Micropore volume determined using the t-plot method. [f] mesopore volume determined using the BJH method

The nitrogen adsorptions for CG derived materials prepared at 1000°C are shown in Figure 4-17 (a). Similar adsorption isotherm form of the type-I category is observed for most of the ACs prepared at 1000°C excepted C10W10. An obvious hysteresis can be observed in C10W10 indicated the higher micropore in the sample. The N_2 adsorption capacity of the samples increased and reach a maximum at 100mins.

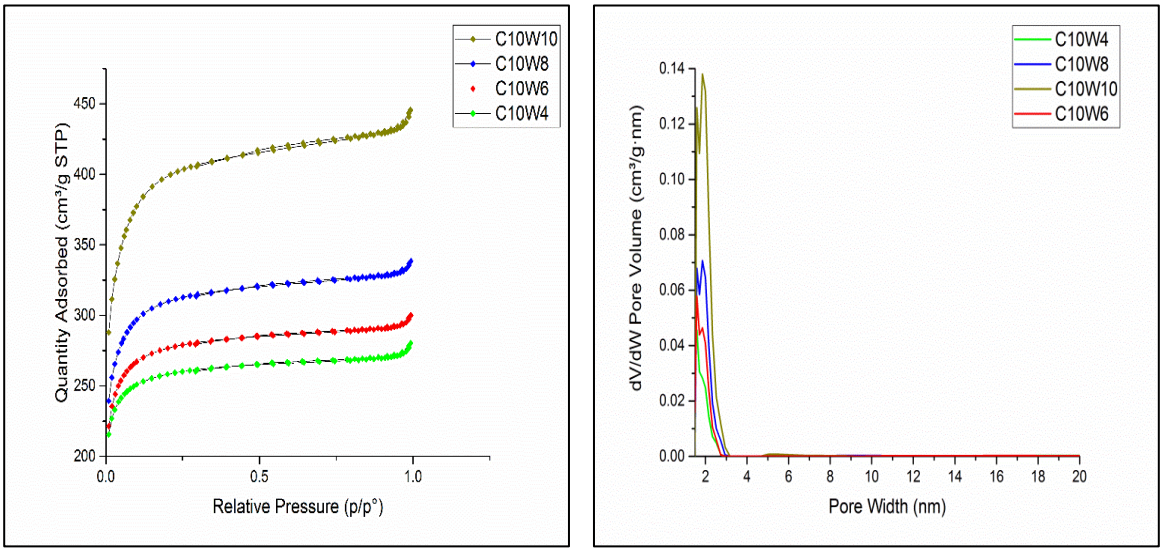

Figure 4-17: (a) N_2 gas adsorption-desorption of CG derived AC and (b) PSD of CG derived ACs for activation holding time from 40-100mins at an activation temperature of 1000°C.

The PSD of the sample of the AC prepared at 1000°C are shown in Figure 4-17(b). In contrast with AC prepared at 950°C (Figure 4-16), the pore size range slightly widens as longer holding time applied to produce AC. The pore size of C10W4 is not more than 2.8nm while maximum pore size for sample C10W10 is 3.2nm.

4.3.1.5 Raman Spectroscopy

By considering the high specific surface area among the AC samples, C10W10 and C10V10 samples which were treated at different temperature but with the same activation holding time are selected to further study the effect of activation temperature on the structure properties of samples. The Raman spectrum of C10W10 and C10V10 displayed in Figure 4-18 shows two intense Raman peaks, located at ~ 1341cm^{-1} (D-band) and ~1600cm^{-1} (G-band). Curve fitting of the Raman spectra was conducted with five Voigt bands. Voigt is a convolution of Gaussian and Laurentzian line shapes (Appendix A). The position of the five peaks position is listed in Table 4-11 and the assignments of each peak are clearly summarised in Table 4.6.

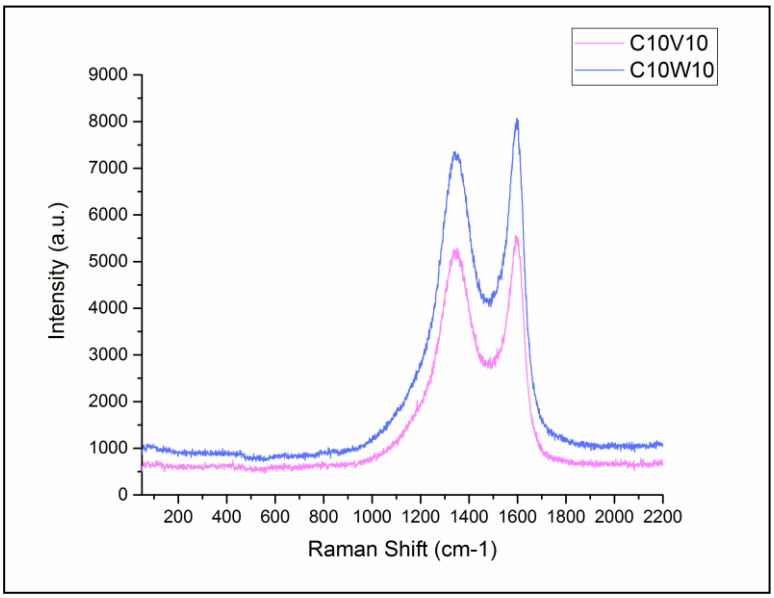

Figure 4-18: Raman spectra for CG derived active materials: C10W10 and C10V10

As referring to Table 4-12, the ID1/IG ratio of C10W10 (1.51) is lower than C10V10 (1.96). The decreasing of the ratio suggests that the lower oxygen functional groups bonded to the edge carbon atoms when the higher activation temperature applied[171, 184]. The width of G peak is often used to evaluate the graphitization of ordered carbons. In this case, the FWHM of G peak of C10W10 is larger than C10V10 (Table 4-12), suggesting the non-uniform distribution of the sp^2 carbon cluster [185, 186]. This lead to a higher bond-angle disorder[186].

Among all the samples, C10W10 showing a wider FWHM in D1 bands. This suggested that there are higher defects in the carbon samples. This is consistent with the finding by Xia et. al. [187] that the higher CO_2 activation temperature introduces more defects to the graphene plane of the hierarchical porous graphene-based carbons.

Table 4-11: Position of the Raman band of the Raman spectra of CG derived carbon samples

Peak	Position (cm-1)	YP80F	C10W10	C10V10
D4	~1200	1185	1211	1225
D1	~1350	1339	1348	1346
D3	~1500	1530	1474	1507
G	~1580	1595	1578	1588
D2	~1620	-	1600	1603

Table 4-12: Area and height value of Raman Peak D1 and G for CG derived carbon samples

	Peak D1		Peak G		Peak D2	Peak D3	ID1/IG
	FWHM	height	FWHM	height	height	height	
C10W10	151	5804	128	3823	3058	1153	1.51
C10V10	136	4187	86	2675	2137	1535	1.96

4.3.1.6 X-ray photoelectron spectroscopy (XPS)

The survey spectra of C10W10 and C10V10 (Figure 4.19) confirmed the existence of C, O, and N. The quantification of element composition as an atomic percentage of top 1-2nm of the carbon particles from survey scan indicated C is the major component for C10W10 and C10V10, which are 97.35% and 96.48%, respectively. A low percentage of O is observed in both samples, where C10W10 has a slightly lower amount of O (1.75%) and 2.23% for C10V10. The lower amount of oxygen suggesting the lower oxygen functional groups as expected in Raman spectrum analysis. It is interesting that C10W10 has some trace amount of N (0.8%) and *Ca* (0.1%). While C10V10 is containing only some N (1.19%) without any *Ca* is detected. Quantification of the weak and broad peak of *Ca* in XPS spectra could correspond to the ash content in C10W10 determined by proximate analysis in Table 4-13. Although slightly high ash content was detected for C10V10, there is no Ca detected in its XPS spectra.

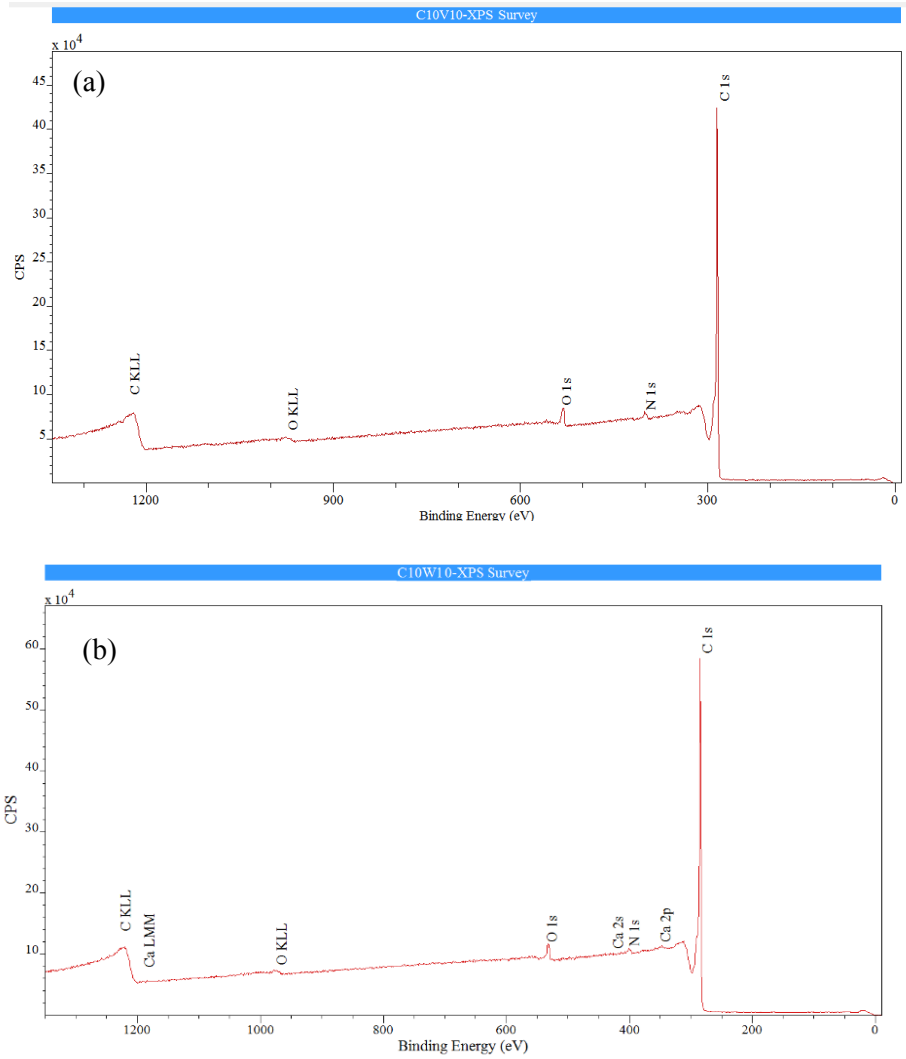

Figure 4-19: XPS survey scan of CG derived ACs samples of (a) C10V10 and (b) C10W10

Deconvolution of the C1s spectra was resolved by fitting eight peaks as displayed in Figure 4-20. C1s-A, C1s-B, and C1s-C are attributed to different types of the carbon-carbon bonding, while C1s-D, C1s-E, C1s-F and C1s-G are centered on the binding energy of oxygen bound to carbon in, which represents the oxygen functional groups on the carbon surface. Overall, there are no significant changes in the composition for both samples. The O1s region was fitted by three components, which corresponding to O=C(O1s-A), O-C (O1s-B) and the moisture (O1s-C) on the carbon. It is noticed that the O=C appears higher and the O-C slightly reduced in C10W10 samples (Figure 4-21).

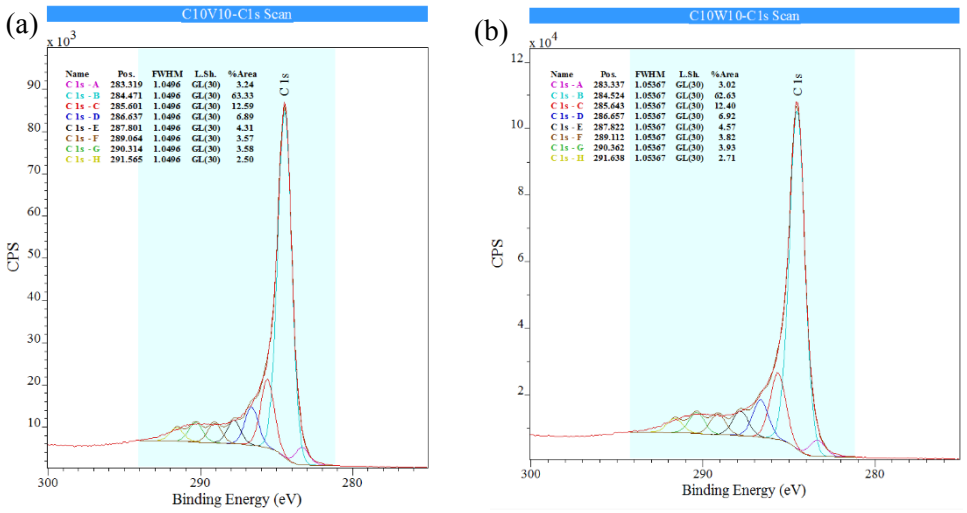

Figure 4-20: C1s XPS spectra for (a) C10V10 (b) C10W10 with deconvolution analysis

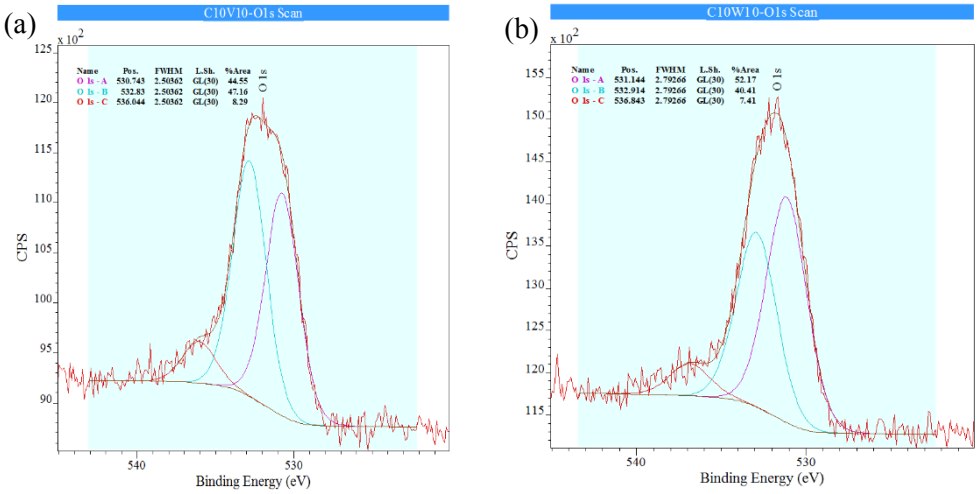

Figure 4-21: O1s XPS spectra for (a) C10V10 and (b) C10W10 with deconvolution analysis

4.3.2 Summary

The effect of CO_2 activation temperatures with 950°C and 1000°C on the properties of AC derived from CG was studied in section 4.3. As expected, at a higher activation temperature promotes the CO_2-C reaction as stated in Equation 4-1 thus leads to a higher burn-off with a longer activation time applied. The specific surface area of AC treated with 950°C is in range of 396-1082m^2g^{-1} while C10W10 achieves the highest specific surface area (1473m^2g^{-1}) among all the ACs. The lower specific surface area of the sample treated with 950°C concluded that the lower temperature is insufficient to activate in the depth of the fiber in order to open the pores structure of the carbon. However, a higher V_{mic}/V_{tot} ratio is observed in the samples. At the lower activation temperature, there are lots of new porous are

created, whereas at a higher temperature the pore in the samples was deepened and broaden and thus reduce the V_{mic}/V_{tot} and lead to the increase of mesoporous[188]. By comparing the ID1/IG, the oxygen functional groups are lower in C10W10 and this is verified by the XPS analysis with lower O composition in the elemental composition. However, a higher defect for C10W10 was suggested based on the interpretation from the Raman spectrum.

4.4 Preparation and Characterization of Malaysia Agriculture by-products derived Activated Carbon

Malaysia is rich in agro-biomass resources and booming in agriculture industries, thus abundant of agriculture by-products are generated annually. In this project, three Malaysia agriculture by-products, Malaysian Wood Pellets (MSW), Palm Oil Empty Fruit Bunch Pellets (EFB) and Rubberwood (RW) are selected to investigate the potential to be used as activated carbon precursors for supercapacitor electrode materials. Based on the study on the effect of carbonization heating rate as explained in section 4.2.1 and the thermal analysis of biomass in section 4.1.2 & 4.1.3, all the selected biomass were first carbonized at 950^0C with a heating rate of $10^0 Cmin^{-1}$. The carbonized samples were then activated with CO_2 at 950°C with activation holding time from 40-80mins. Comparison of burn-off, proximate analysis of ACs and the porosity and surface area of the prepared ACs are discussed in this section.

4.4.1 Burn-off

Figure 4-22 represents the effect of activation holding time on burn-off of ACs derived from EFB, RW, and MSW. The burn-off increased linearly with the increase of holding time at 950°C. With the increase of holding time from 40mins to 80mins, the burn-off increased from 24.4% to 46.7%, 45.7 to 75.5%, 58.68 to 93.21% for MSW, EF, and RW, respectively. Activation with CO_2 at high temperature and longer holding time promote C-CO_2 reactions, resulting in the removal of carbon atoms and causing the weight loss of AC[110]. Activation of olive bagasse using CO_2 physical activation technique also has a similar burn-off pattern, with burn-off increased linearly as activation time increases at various activation temperatures [111].

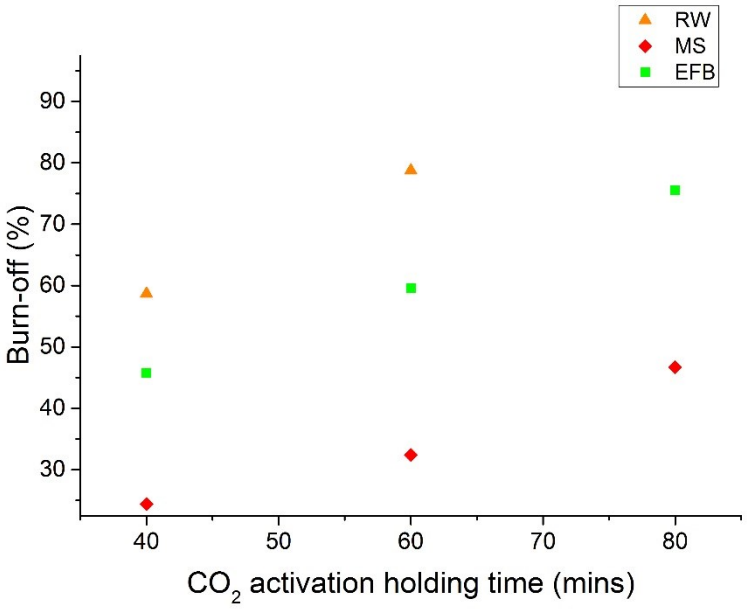

Figure 4-22: Percentage burn-off of EFB, RW and MSW pellets derived AC during the activation process

4.4.2 Proximate Analysis

Figure 4-23 – 4-25 show the proximate analysis results of the prepared AC samples from EFB, MSW, and RW, respectively. As refer to Figure 4.23, the ash content of EFB has increased from 26.3% (E10V4) to 63.9% (E10V8). Similarly, the ash content increase for MSW (Figure 4-24) and RW derived AC samples (Figure 4-25) as longer holding time applied. For MSW derived AC samples, ash content increase from 8% (MS10V4) to 13.38% (MS10V8). For RW derived AC samples, about 7% and 23.3% of ash for the sample treated with 40 mins and 60 mins holding time, respectively. It is interesting that the AC sample treated with 80 mins holding time shows burn-off up to 93.3% (R10V8) and only ash remaining in the sample. The increasing of the activation holding time promote the C-CO_2 reaction and thus increase the carbon burn-off, therefore there is an increasing trend of the ash content of overall mass in the samples.

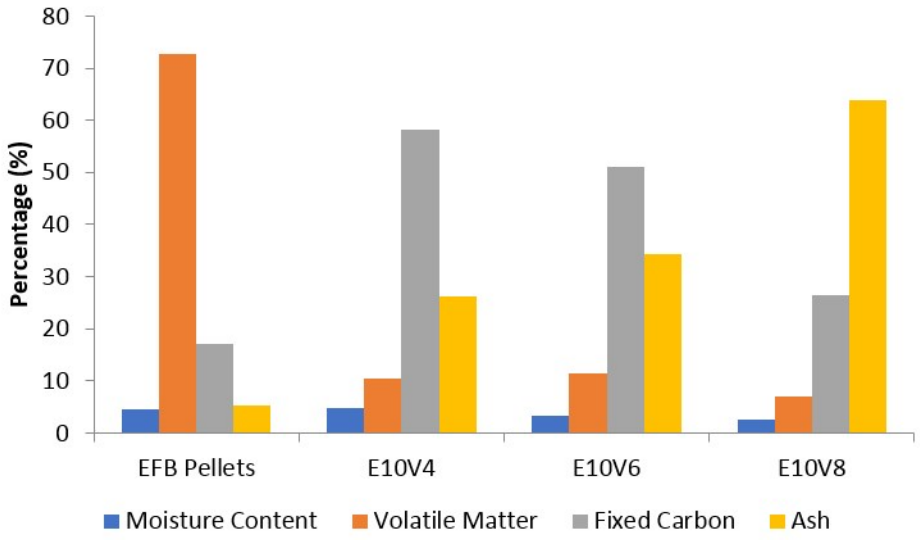

Figure 4-23: Proximate analysis of EFB Pellets & EFB derived AC samples

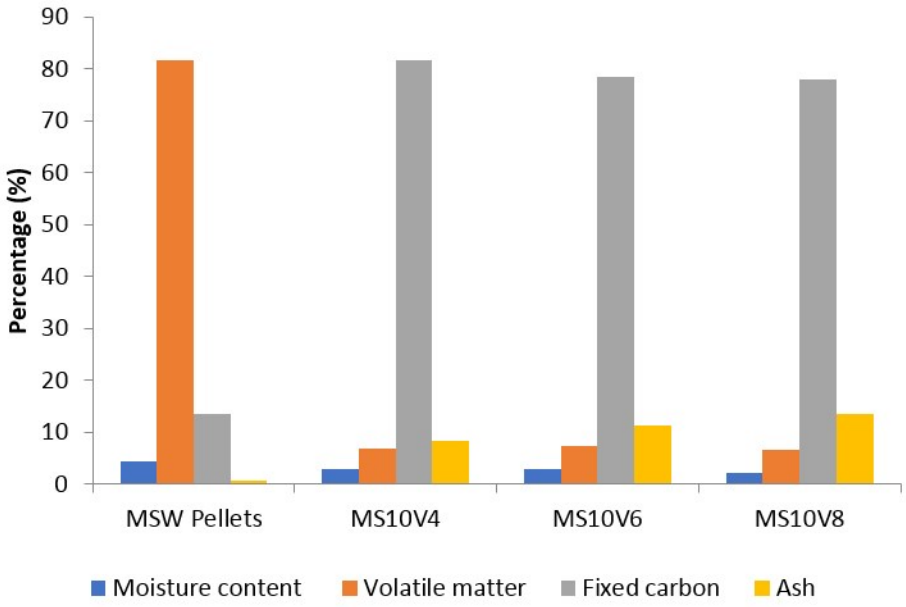

Figure 4-24: Proximate analysis of MSW and MSW derived AC samples

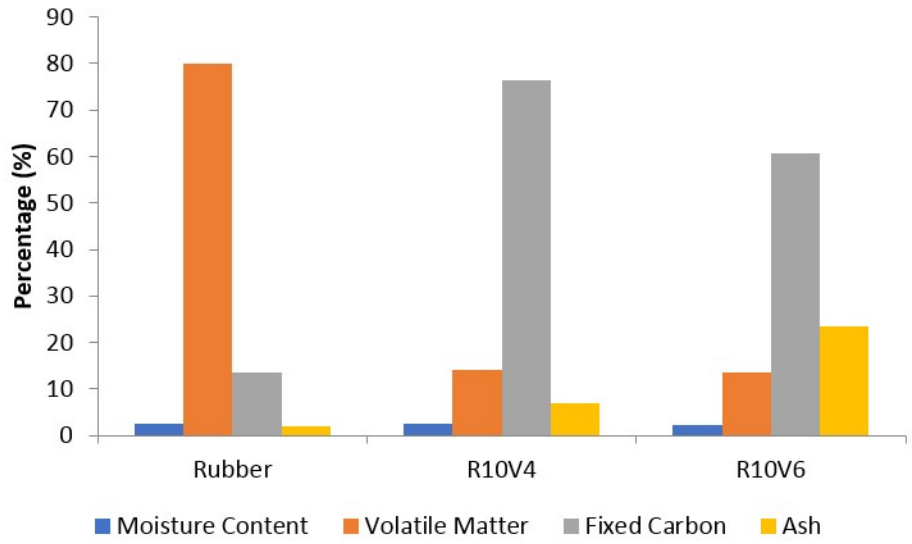

Figure 4-25: Proximate analysis of RW and rubber wood-derived AC samples

Impurities such as mineral content, ash in activated carbon which used as electrode materials could provide negative influential factor exist on the supercapacitor cycle life, narrow the potential window of the cells and also high leakage currents [189]. Ash on the surface of ACs could clog some of the porous and this restricted the optimum performance of the electric double-layer capacitor. The gas produced due to the reaction of impurities on the surface of the AC[190]. Nevertheless, an additional step to demineralize ACs is essential in this case to remove the impurities and thus leading to increases in production costs.

On the other hand, the fixed carbon content has the opposite trend for all the Malaysia agriculture biomass wastes. The fixed carbon content of AC samples decreased from 58% (E10V4) to 26.43% (E10V8), 81.6% (MS10V4) to 77.9% (MS10V8) for EFB and MSW respectively. For RW, the fixed carbon decreased from 76.53% (R10V4) to 60.77% (R10V6). It is also interesting that self-ignition was observed for sample R10V6 although after overnight cooling down in argon condition. This could be due to depletion of volatiles from the sample thus leads to the increment of surface active sites for oxidation or self-heating [191]. Pore phenomenon is also might be one of the possible factors for the self-heating due to the high overall surface area in the samples[192]. Further study and explanations on the surface area and porosity of biomass-derived AC is discussed in section 4.4.3.

4.4.3 Morphologies Analysis Carbon

The results for scanning electron micrograph (SEM) of AC derived from EFB pellets for activation at 950°C and 2 hours are shown in Figure 4-26. It can be observed that there are various particle size AC appear in E10V4, some large particle with a typical honeycomb structure with the pore of different size formed on the EFB derived AC. Some spheres appear and cling on the surface of the AC sample of E10V4. The particle size of E10V6 was observed, there are no spheres appear on the large particle as seen in E10V4. As longer activation time applied, impurities on the surface reduced, sphere detached on the AC was disappeared in E10V8. However, some unknown spheres objects have still appeared in the sample E10V8. Based on the EDX analysis, those unknown sphere objects are in high Si content, which is favorable as ash content in the ACs (Appendix B).

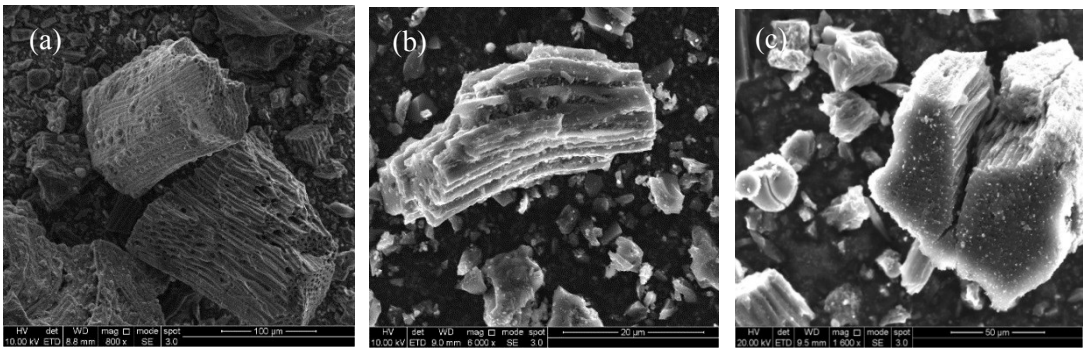

Figure 4-26: SEM of EFB derived ACs (a) E10V4 (b) E10V6 (c) E10V8

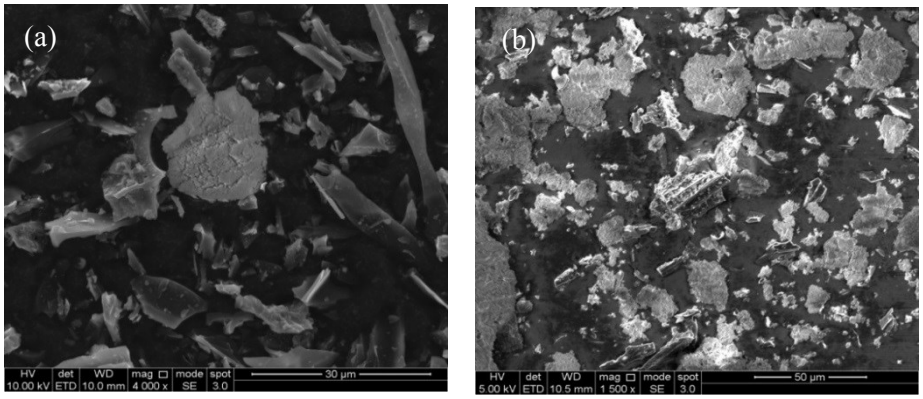

Figure 4-27: SEM of Rubber Wood derived AC (a) R10V6 and (b) R10V8

As refer to Figure 4-27, there are lots of white spots appeared in the SEM samples of R10V6 and R10V8. There is not much porous carbon visible in the samples. Thus, further EDX analysis confirmed that the actual compositions of the white spots are consist of Ca, K, P and Mg (Please refer to Appendix B). This suggested that the RW samples are containing high ash or impurities.

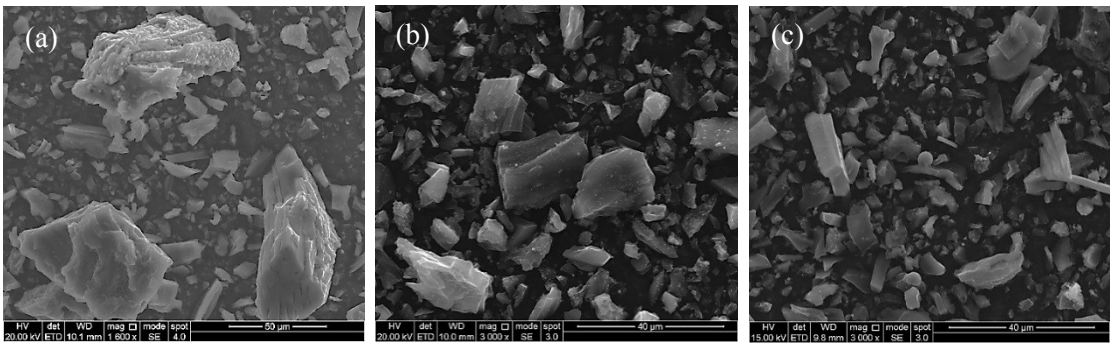

Figure 4-28: SEM of MSW pellet derived AC (a) MSW10V4 (b) MSW10V6 (c) MSW10V8

The morphology of the MSW derived ACs was displayed as in Figure 4-28. It can be seen that MSW-ACs have irregular shapes with numerous particle size. For AC samples of MS10V4, there are some sphere-like micro-particles on cling on the surface of larger particles, which suggested that it could be some of the impurities still present in the MS10V4 residues. The EDX analysis suggested that the sphere-like micro-particles could be Ca components. As longer activation time applied, the sphere-like micro-particles disappeared in MS10V6 and MS10V8.

4.4.4 Surface area and Porous structure

The porosity and surface area of AC samples greatly affecting the capacitance performance when used for electrode materials in supercapacitors. As refer to Table 4-13, activation at 950°C with holding time from 40 to 80 mins is greatly influence the surface area and porosity of all the biomass-derived ACs.

For the AC derived from EFB, the BET surface area is 789 m^2g^{-1} for E10V4 and slightly reduced to 645m^2g^{-1} for E10V6 and raised up to the highest BET surface area of 845m^2g^{-1} for E10V8. The pore volume of the AC samples is in range of 0.263 -0.34 cm^3g^{-1}. The EFB derived AC exhibit adsorption isotherm of type-I/IV with a hysteresis (Figure 4-29(a), which is commonly represents a mixture of micropores and mesopores in the AC. As refer to Table 4-13, the V_{mic}/V_{tot} ratio is in range of 0.805-0.96, thus this indicates microporous as predominant with some mesoporous in the total pore in the EFB carbon. When compared with the AC prepared from EFB fibers by Farma et. al. [193], a slightly lower V_{mic}/V_{tot} ratio (0.81) and S_{meso}/S_{micro} ratio of 0.14 with BET surface area of 448 m^2g^{-1} was reported.

Table 4-13: Surface area and Porosity characteristics of EFB, MSW, and RW derived AC samples

Material	S_{BET} (m^2g^{-1})[a]	S_{mic} [m^2g^{-1}][b]	S_{meso} [m^2g^{-1}][c]	V_{tot} [cm^3g^{-1}][d]	V_{mic} [cm^3g^{-1}][e]	V_{micro}/V_{tot}	V_{meso} [cm^3g^{-1}][f]	V_{meso}/V_{tot}
YP80F	2084	1979	40	0.90	0.855	0.95	0.121	0.134
E10V4	789	595	52.7	0.318	0.256	0.805	0.086	0.27
E10V6	645	595	20.6	0.319	0.263	0.824	0.0448	0.14
E10V8	845	780	27.0	0.34	0.328	0.964	0.0598	0.176
MS10V4	776	687	34.7	0.328	0.239	0.728	0.0744	0.227
MS10V6	784	659	58	0.379	0.235	0.62	0.135	0.356
MS10V8	1003	882	124	0.456	0.306	0.671	0.155	0.34
R10V4	838	760	14.5	0.3131	0.31	0.99	0.00277	0.0088
R10V6	963	742	19.2	0.3731	0.297	0.796	0.0413	0.11
R10V8	44	-	1.64	0.0228	-	-	0.00432	0.189

[a] Specific surface area calculated using the BET method.[b] micropore surface area determined using the t-plot method. [c] mesopore surface area determined from the adsorption branch of the isotherm using the BJH method. [d] total pore volume calculated at $P/P_0 > 0.99$. [e] Micropore volume determined using the t-plot method. [f] mesopore volume determined using the BJH method

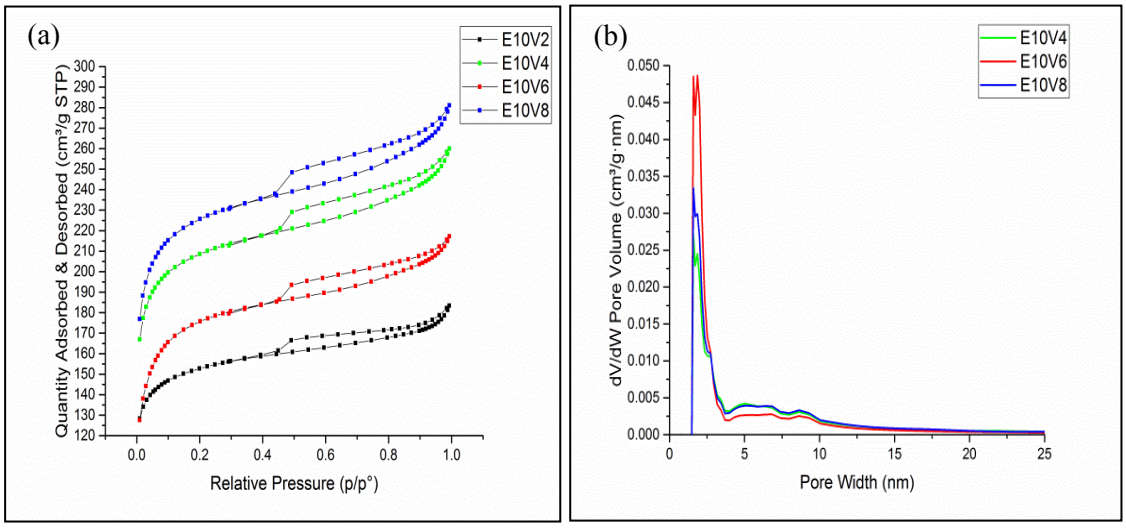

Figure 4-29: (a) N_2 adsorption isotherm at 77K and (b) pore size distributions of EFB derived AC samples

The BET surface area of MSW derived ACs was slightly higher than the ACs that produced from EFB and RW. The BET surface area of AC derived from MSW is in range of 776-1003 m^2g^{-1}. The BET surface area rose from 776m^2g^{-1} for MS10V4, 784m^2g^{-1} for MS10V6 and further increased up to 1003m^2g^{-1} for MS10V8. An adsorption isotherm of type-I/IV with a narrow hysteresis was observed for MSW- AC as seen in Figure 4-30. This is well agreed with the low ratio in $V_{meso}/V_{tot,}$ although there is an increasing trend from 0.226, 0.356, to 0.340 for MS10V4, MS10V6, MS10V8 respectively. The V_{micro}/V_{tot} ratio of MS10V6 (0.62) is lower than MS10V4 (0.728) and the value further decreases to 0.67 for MS10V8.

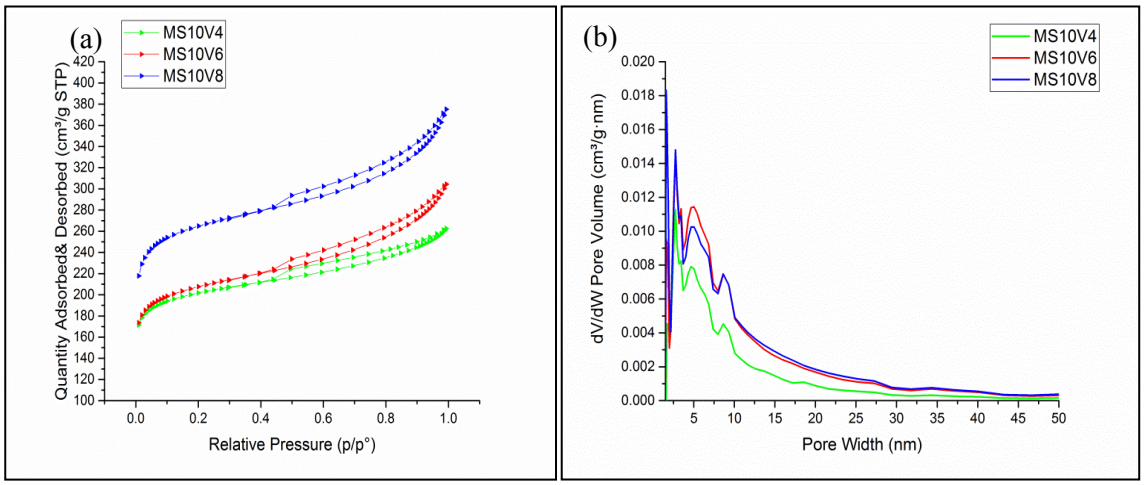

Figure 4-30: N_2 adsorption isotherm at 77K and (b) pore size distributions of MSW derived AC samples

From the results shown in Table 4.13, it can be observed that the surface area and pore volume of AC derived from RW increased with the increasing of activation holding time from 40 to 60mins. The BET surface area of R10V4 is 838 m^2g^{-1} and R10V6 is 963m^2g^{-1} with a very high V_{mic}/V_{tot} ratio of 0.99 and 0.796, respectively. The surface area of R10V8 is very low (44 m^2g^{-1}) due to the high ash content as shown in Figure 4.14 and also high burn-off as shown in Figure 4.25. Taer et. al [194] also prepared AC from rubberwood sawdust as supercapacitor electrode and the maximum BET surface area of the prepared AC (913 m^2g^{-1}) was achieved with 2 hr activation time at 900°C using CO_2 as activating agent. However, a much lower surface area (300-465 m^2g^{-1}) and total pore volume (0.15- 0.239 m^3g^{-1}) of AC derived from rubberwood sawdust which prepared with lower activation temperature at 700°C was reported[195].

S_{BET} of AC derived from EFB, MSW, and RW as a function of burn-off percentage was further discussed. It can be seen in Table 4.13, E10V4 (789m^2g^{-1}) has a similar S_{BET} value as MS10V6 (784m^2g^{-1}). However, the burn-off between these two samples is very different, E10V4 obtained 45.7% and

MS10V6 has only 32.4% burn-off. The V_{micro}/V_{tot} of MS10V6 (0.62) is much lower than the V_{micro}/V_{tot} of E10V4 (0.805). In another hand, the V_{meso}/V_{tot} of E10V4 (0.27) is lower than MS10V6 (0.356).

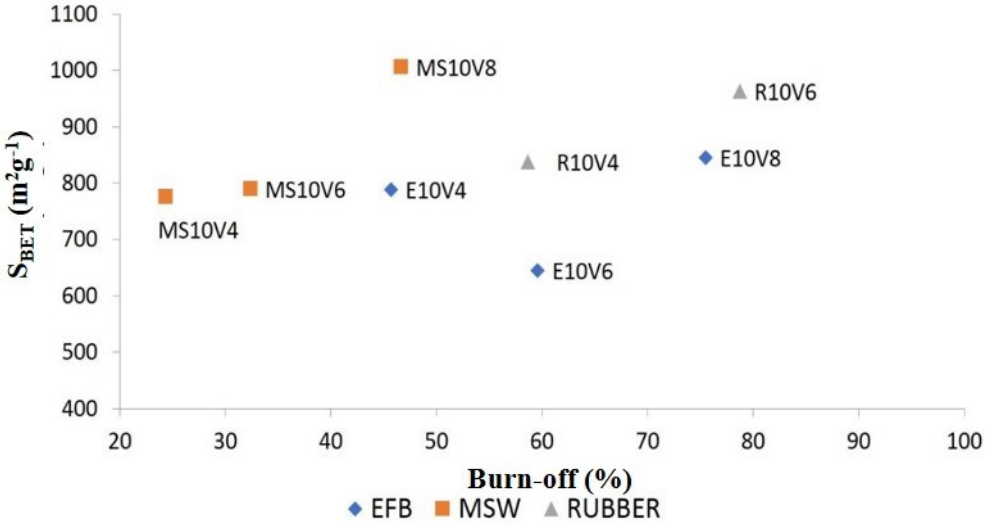

Figure 4-31: S_{BET} of AC derived from EFB, MSW, and Rubber as a function of the burn-off percentage

As referred to Figure 4.31, the S_{BET} of MS10V8 (1006m^2g^{-1}) is much higher than E10V4 (789m^2g^{-1}) although these two AC samples have a similar percentage of burn-off (46-47%). The V_{micro}/V_{tot} of MS10V8 (0.671) is lower than the V_{micro}/V_{tot} of E10V4 (0.805). In contrast, the V_{meso}/V_{tot} of MS10V6 is higher (0.356) than E10V4. The S_{BET} of R10V4 (838m^2g^{-1}) is much higher than E10V6 (645m^2g^{-1}) although R10V4 (58.68%) and E10V6 (59.6%) have a similar percentage of burn-off. Based on the evaluations, the S_{BET} is greatly depended on the type of biomass. This finding shows that there is no correlation between the specific surface area and the burn-off a percentage of biomass-derived ACs. This finding is agreed well as reported by Schöder *et. al.*[196] that the increase in the surface area of AC depends on different waste biomass.

4.4.5 Raman Spectrometry

Raman spectra of ACs are illustrated in Figure 4.32 for (a) EFB pellets and (b) MS wood pellets. There are two peaks which locate at ~1345cm^{-1} (D-band) and ~1599 cm^{-1} (G-band) were observed in Raman spectra of MS wood pellets and EFB. It is noticed that the two intense Raman peaks are slightly overlapping with each other. Thus, the Raman spectra were further deconvoluted by using five Voigt lineshape (convolution of Gaussian & Laurentzian lineshapes). The curve fitting clearly indicates that five bands: D1 (~1350cm^{-1}), D2 (~1620cm^{-1}), D3(~1500cm^{-1}), D4 (~1200cm^{-1}) and G (~1580cm^{-1}) were

observed in the region from 200 to 2200cm^{-1} (Appendix A). The assignments of bands are summarized in Table 4.6 and the positions of peaks for each sample are listed as in Table 4.14.

The width and intensity of peaks could deliver information about the degree of graphitization and the structured bond carbon of the sample. D1 is often related to the defect or disorder by measuring the presence of 6-fold rings structure in Raman spectra of a sample[186]. The reduction in the FWHM of the D1 band is observed from E10V4 to E10V8, suggesting that the improvement in the degree of disorder. The broadening of FWHM of G band is observed, suggests the bond-angle disorder at sp^2 sites[185] and hence increase the sp^3 content. In contrast, the FWHM of G band for MS-AC decreased after 80mins activation time, which suggests the oxidation of the sp3 content and bond-angle ordering at sp2 site[171]. The narrowing of the FWHM of D1 band was observed for AC derived from MS pellets, suggesting the AC has a higher degree of structural order.

In contrary to observation for AC derived from Marabú (Section 4.2.3), the relative intensity of D1 and G band (ID1/IG) grows when the activation holding time increases from 40mins to 80mins for AC derived from EFB and MS (Table 4.11). Chernyak et. al. [171] correlated the increase of ID1/IG ratio to the increase of oxygen functional groups bonded to the edge carbon atoms. XPS analysis of the carbon was further investigated and discussed in section 4.4.6.

The presence of D2 (~1620cm^{-1}) peak was correlated to the disordered graphitic lattice on the surface layer [164, 168]. It also considered as vibration arises from aromatic ring stretching due to the existence of oxygen functional groups on the surface or crystalline edges[197]. Shimodaira et. al.[198] labeled this peak as G1 and ~1580cm^{-1} as G2, the ratio of G2/G1 was used to explain relative content of bond angle disorder to order in the AC samples. In this case, the ratio of G2/G1 is interpreted as IG/ID2. The IG/ID2 is apparently smaller for AC derived from EFB with longer activation holding time. The same trend is observed from AC derived from MS, which indicates that the structure changes to higher bond angle order as longer activation holding time applied.

Table 4-14: Position of the Raman band of the Raman spectra of EFB derived carbon samples

Peak	Position (cm^{-1})	E10V8	E10V6	E10V4	MS10V8	MS10V6	MS10V4
D4	~1200	1205	1210	1200	1194	1238	1190
D1	~1350	1347	1349	1349	1345	1344	1346
D3	~1500	1502	1504	1503	1485	1481	1480
G	~1580	1584	1584	1586	1579	1580	1580
D2	~1620	1605	1603	1619	1602	1604	1601

Table 4-15: Fitting Parameters obtained from Voigt deconvolution based on maximum peak height.

	Peak D1		Peak G		Peak D2	ID1/IG	IG/ID2
	FWHM	height	FWHM	height	height		
E10V8	142	13429	97	5528	7745	2.42	0.71
E10V6	151	7214	76	4058	3912	1.77	1.04
E10V4	152	6413	72	5284	2063	1.21	2.56
MS10V8	104	539	54	194	348	2.77	0.56
MS10V6	116	821	56	314	56	2.61	5.61
MS10V4	140	2707	133	1099	55	2.46	19.98

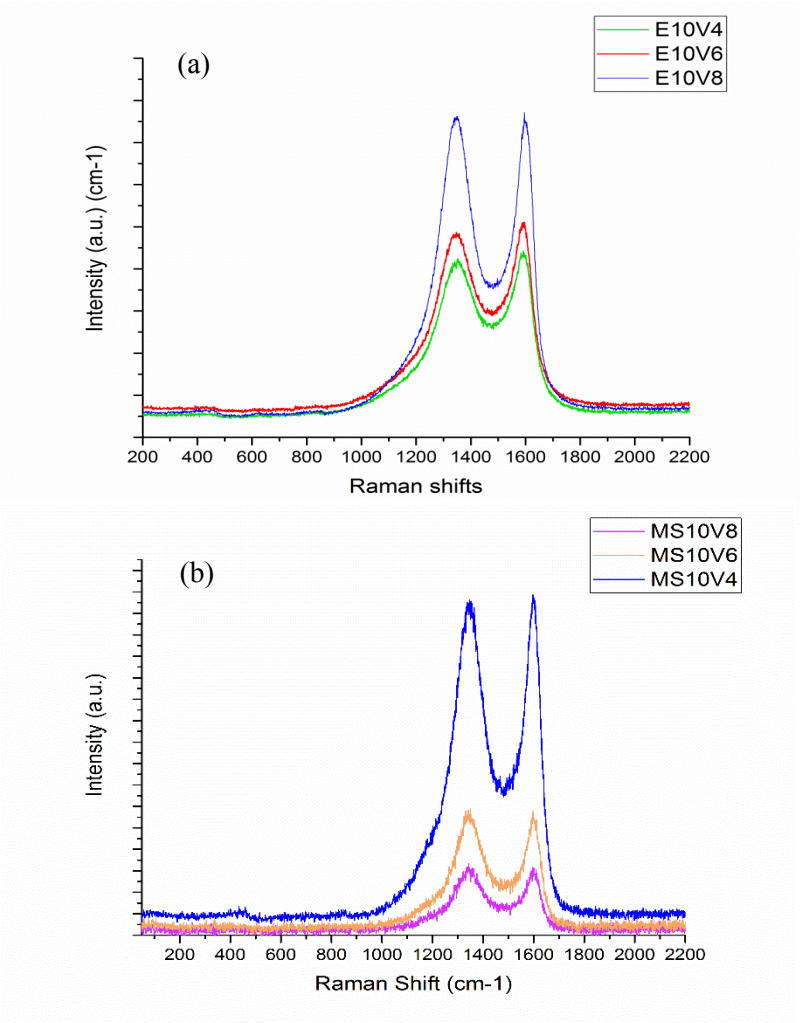

Figure 4-32: Raman spectra for AC derived from (a) EFB pellets and (b) MS wood pellets.

4.4.6 X-ray photoelectron spectroscopy (XPS)

Figure 4-33 illustrated the XPS survey spectra obtained for AC derived from EFB pellets. The element composition based on atomic percentage was from the survey spectrum indicated that C and O are the major composition for AC from EFB pellets. Four compositions were detected in E10V4, there are C (87.18%), O (12.26%) with a small amount of N (0.28%) and Ca (0.28%). E10V6 containing high C (87.02%) and 12.27% of O, there is no N was detected in E10V6. E10V8 consist of 84.74% of C, 14.24% of O, and a small amount of N. the carbon content is slightly lower (84.74%) with higher O content (14.24%). The carbon composition of MS10V6 (88.98%) is lower than MS10V4 (90.27%) and slightly rise at MS10V8 (89.78%). The composition of O for MS10V6 (11.02%) is slightly higher than MS10V4 (9.73%) and then further reducing MS10V8 (9.84%). Among these three samples, there is a very low composition of N was detected for MS10V8 only.

The high- energy resolution C1s spectra of E10V4, E10V6 and E10V8 were resolved in several peaks (Figure 4-34), which referring to C 1s-A(283.89eV) and C 1s-B (284.8eV), C 1s-C (285.5eV), C 1s-D (286.8eV), C 1s- E (287.5eV), C 1s-F (288.5eV) and C1s-G (289.5eV). The assignment of each peak was summarized as in Table 4-8. There is no C1s-A detected for E10V4 and E10V8. The peak of C1s-B (C=C) and C 1s-C (C-C) are high were observed in all the EFB-AC samples. The deconvoluted peak of C 1s-D, C1s-E, C 1s-F, and C1s- G are relating to C-O-, C-O-C, C=O and O-C=O are appearing in all the samples, which indicates that there are oxygen functional groups present in the carbon samples. A satellite peak is also detected at ~292eV, which is due to sudden changes in coulombic potential as the electron passes through the valence band.

The O1s spectrum was also deconvoluted in three peaks centered: O 1s-A (~531.58eV), O 1s- B (~533eV) and O1s – C (~535.39eV) as displayed in Figure 4-35. The O 1s-B is higher than O1s-A in E10V4 and E10V8, which is consistent as finding in C1s with a higher percentage of C-O. In contrast, O1s- A is higher than O 1s-B for E10V6.

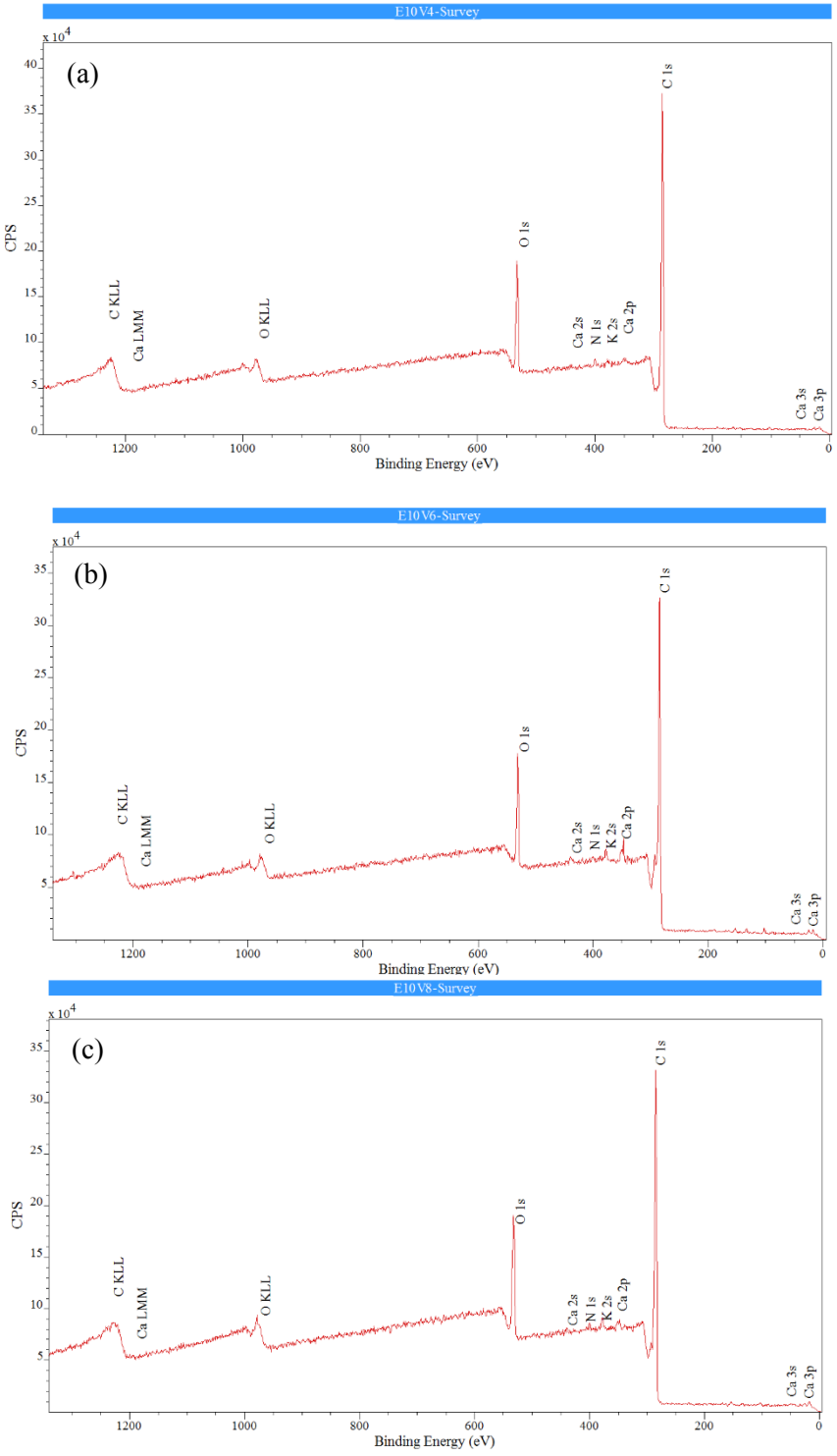

Figure 4-33: XPS survey scan of EFB derived ACs samples of (a) E10V4, (b) E10V6 and (c) E10V8

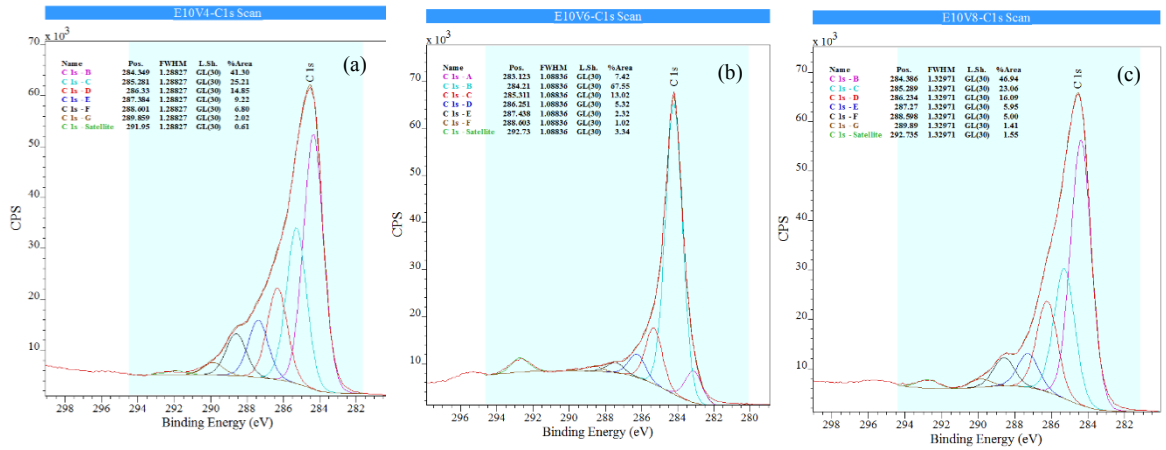

Figure 4-34: C1s XPS spectra for (a) E10V4 (b) E10V6 (C) E10V8 with deconvolution analysis

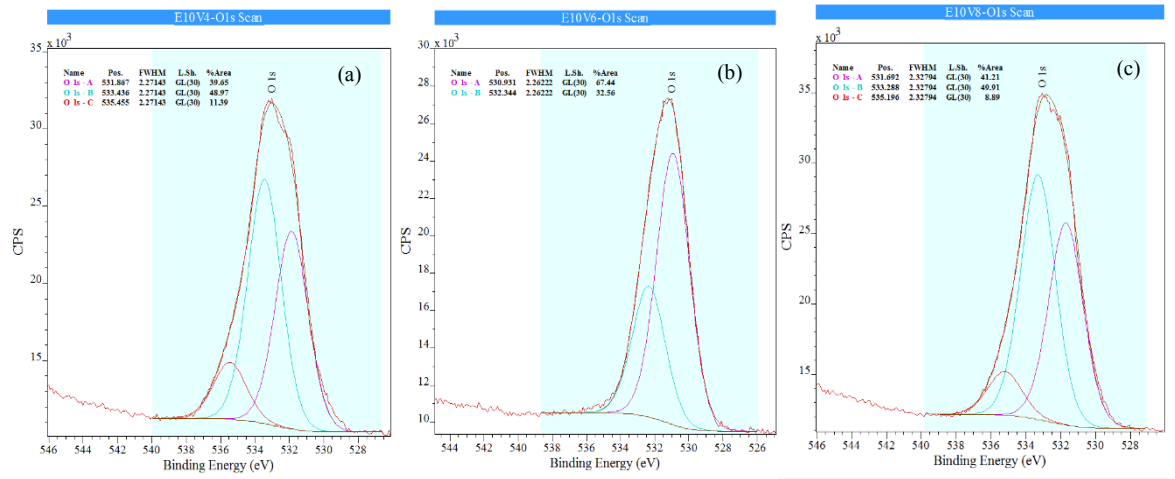

Figure 4-35: O1s XPS spectra for (a) E10V4 (b) E10V6 (C) E10V8 with deconvolution analysis

The XPS spectra of the AC derived from MS pellets are shown in Figure 4-36. C 1s and O 1s are intense peaks in the spectrum with other elements with low concentration, N and Ca. Ca peak is observed lower in the XPS spectrum of sample MS10V8. Figure 4-37 represents the C1s core level spectrum of AC derived from MS were resolved in several peaks as EFB-AC. The majority of carbon species contained C=C and C-C which represented by C 1s-B and C1s-C respectively. C1s-B gradually reduced as longer activation holding time applied, from 66.6% (MS10V4) to 62.04% (MS10V8). In contrast, C1s- C increased from 14.7% (MS10V4), 17.38% (MS10V6) to 18.7% (MS10V8). There is no significant changes were observed in all ACs for C1s-D which represents the C-O- bond. C1s-E, C1s-F, and C1s-G which referring to the C-O-C, C=O, and O-C=O respectively are relatively low. The C 1s-E is only less than 3% obtained for all the AC samples. Around 5% of C1s- F and not more than 1.1% of C1s-G was observed in all the samples. There are two resolved peaks for O 1s spectra as in Figure 4.38, which attributed to the O=C and O-C respectively. The O1s-A (~52%) has a slightly higher percentage as

compared to Os1-B (~48%) for all the MS-AC. This results summarised that there is no significant effect of activation holding time on the oxygen functional groups in the MS-AC samples.

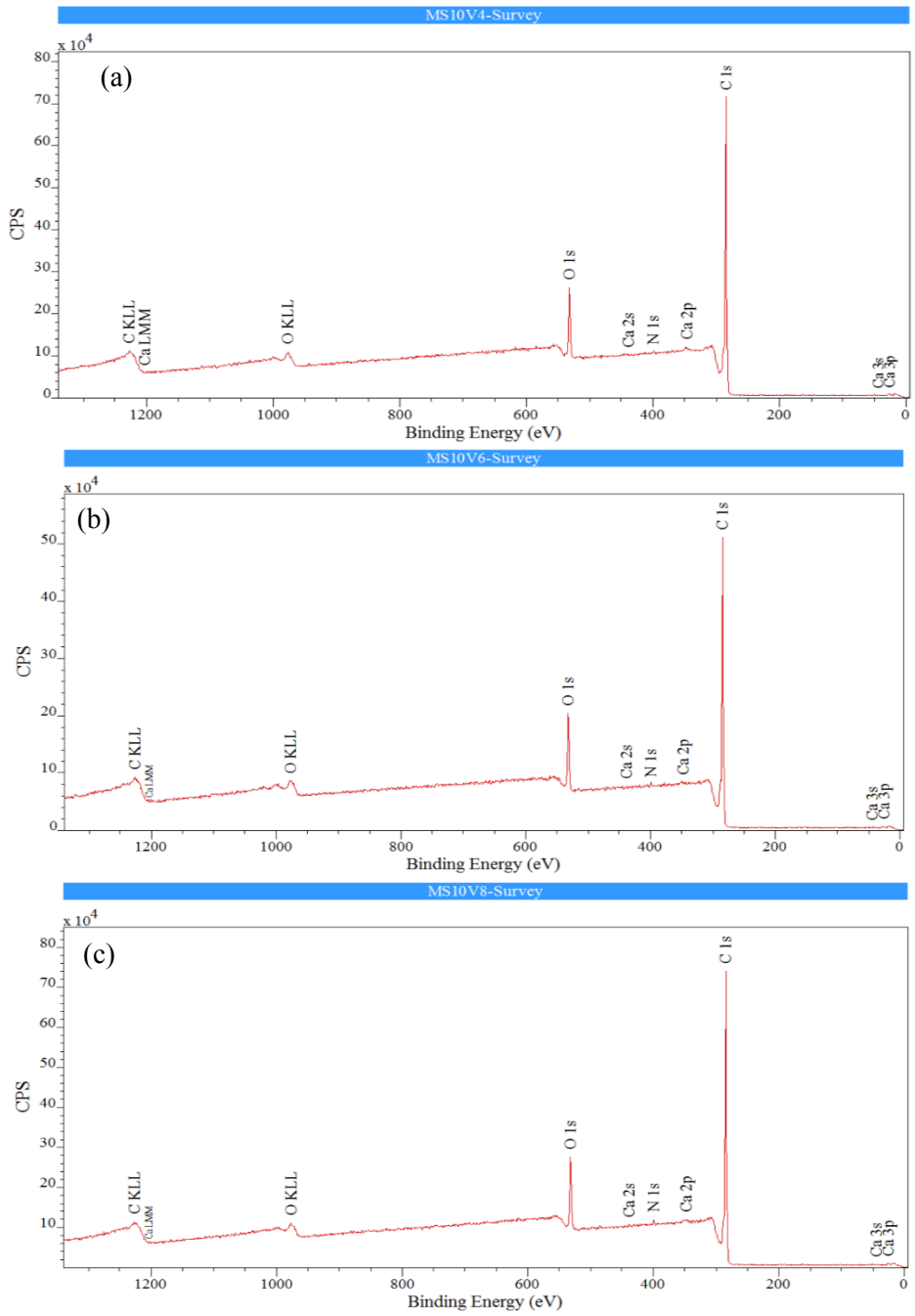

Figure 4-36: XPS survey scan of MSW derived ACs samples of (a) MS10V4, (b) MS10V6 and (c) MS10V8

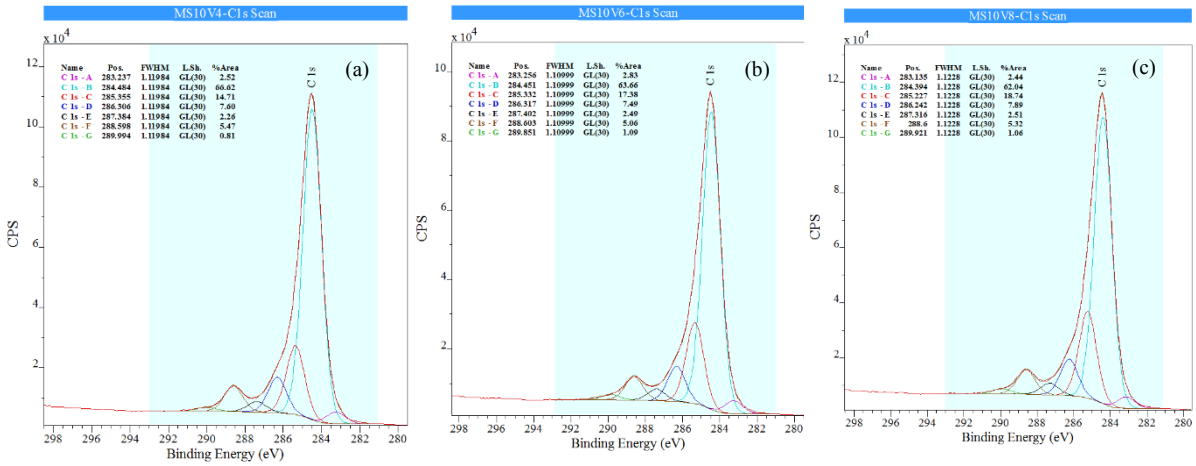

Figure 4-37: C1s XPS spectra for (a) MS10V4 (b) MS10V6 (C) MS10V8 with deconvolution analysis

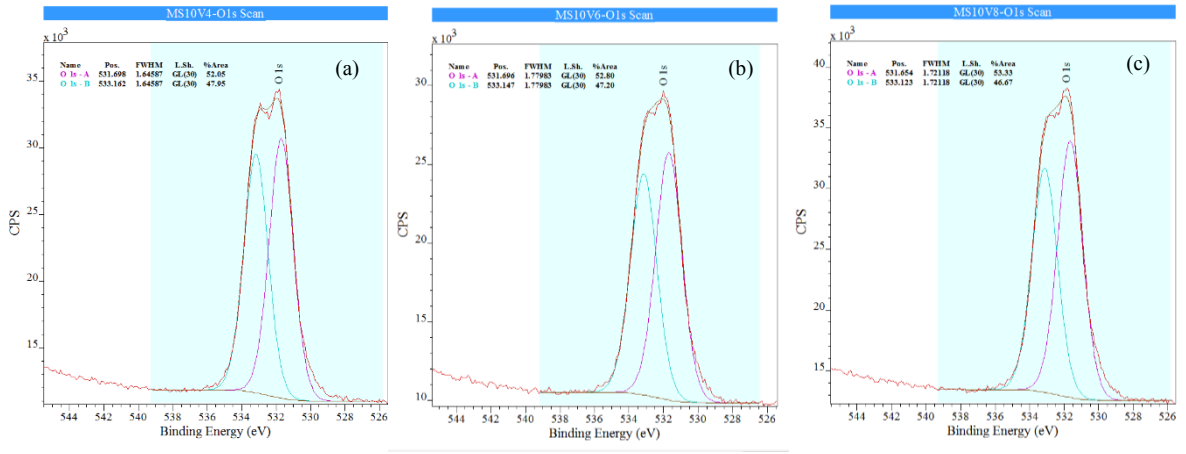

Figure 4-38: O1s XPS spectra for (a) MS10V4 (b) MS10V6 (C) MS10V8 with deconvolution analysis

4.4.7 Summary

Three agriculture by-products: rubberwood (RW), EFB pellets and MS pellets were selected to study the potential as carbon electrode materials in supercapacitor applications. High burn-off and self-ignition of R10V6 was detected even though an overnight cooling under argon condition. Due to the thermal sensitivity of RW, thus this hinders the possibility of RW as stable carbon electrode material. Although a very high ash content was spotted in ACs derived EFB, reasonable high surface area (789-845m^2g^{-1}) with high V_{mic}/V_{tot} were observed in AC derived from EFB pellets. The ID1/IG for ACs derived from EFB pellets increased, indicating the increase of oxygen functional groups on the carbon samples. However, there is no significant effect of activation holding time on the oxygen functional groups in the MS-AC samples by XPS analysis with increasing of O composition in AC as longer activation holding time applied. Among all the ACs, MS10V8 achieves the highest specific surface area of 1003m^2g^{-1} with a higher ratio of V_{meso}/ V_{total}.

5 Electrochemical performance of Marabú Derived Activated Carbon as electrode material for Electrical Double-Layer Capacitors using Ionic Liquid Electrolyte and Organic Electrolyte

This chapter presents the electrochemical performance of ELDC using Marabú derived AC as the electrode material with two different types of electrolytes, organic electrolyte, and Ionic liquid electrolyte. A simple symmetrical EDLC was demonstrated to understand the fundamental investigation on the correlations between the operating principle of an EDLC system and the properties of the prepared carbon samples in the organic electrolyte and ionic liquid. The impact of carbonization heating rate and the activation holding time range on the properties of AC as electrode material for the electrochemical performance of EDLCs in the organic electrolyte and ionic liquid were investigated. Electrochemical performance of the EDLC was evaluated using Galvanostatic cycling (GC) and Cyclic Voltammetry (CV). The interpretations of electrochemical impedance spectroscopy (EIS) for the EDLC was studied. The cycle stability of cells was further tested over 30000 cycles to investigate the real application lifetime.

5.1 The Electrochemical Performance of EDLC using Marabú derived activated carbon as electrode material with Organic Electrolyte

5.1.1 The Effect of heating rate

5.1.1.1 Cycle Voltammetry

The cyclic voltammograms (CV) obtained at 200mVs^{-1} for Marabú derived active materials and commercial carbon (YP80F) in the organic electrolyte is shown in Figure 5-1. Although low, weak and broad peaks of oxygen functional groups have been detected as explained in XPS analysis in section 4.2.4, typical supercapacitor rectangular shapes of CV curves were observed without any redox peaks for all the Marabú derived electrode cells. This indicates there is mainly coulombic interactions in the cells. Although the CV curve of M10V8 is slightly lower than the commercial carbon, YP80F, M10V8 exhibits the biggest rectangular CV curve and highest specific capacitance among all the Marabú derived AC. This is reasonable that YP80F has higher BET surface area (2084m^{2}g^{-1}) than M10V8 (1977m^{2}g-1). The rectangular CV curves show the quick response of the electrode materials to the current change with the sudden reversing potential sweep. This also suggests that the ion in the electrolyte can interact efficiently with the carbon electrode of M10V8 in the cell. M5V8 exhibits the

second largest area of CV with a BET surface area of 1065m^2g^{-1}. M15V8 exhibit the smallest rectangular CV due to a lower surface area of 1031m^2g^{-1}.

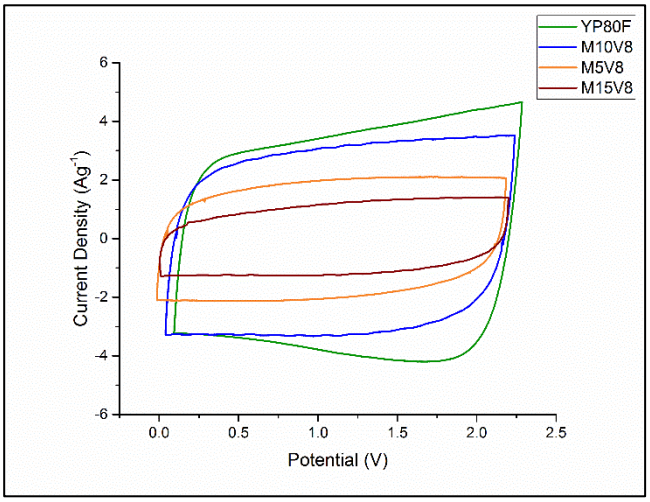

Figure 5-1: CV of commercial carbon and Marabú derived AC under different carbonization heating rates as a carbon electrode

Cyclic voltammograms with a different scan rate of 5, 50, 100 and 200mVs^{-1} for M5V8, M10V8 and M15V8 were further analyzed and displayed as in Figure 5-2. At a low scan rate of 5mVs^{-1}, all the samples retain rectangular shapes without any redox peak. It is clear that some noises are visible for M5V8 at 50mVs^{-1}. Although M5V8 has high BET surface area up to 1065m^2g^{-}1, this could be due to the high ash content of 11% as analyzed using proximate analysis and displayed at Figure 4-6. Noises were observed in the CV of all the scan rates for M15V8. This scenario could be due to the lower surface area of the AC samples and the S_{meso} of M15V8 (15.2 m^2g^{-1}) is only one-third of M5V8 (44.8m^2g^{-1}) as summarized in Table 4-4.

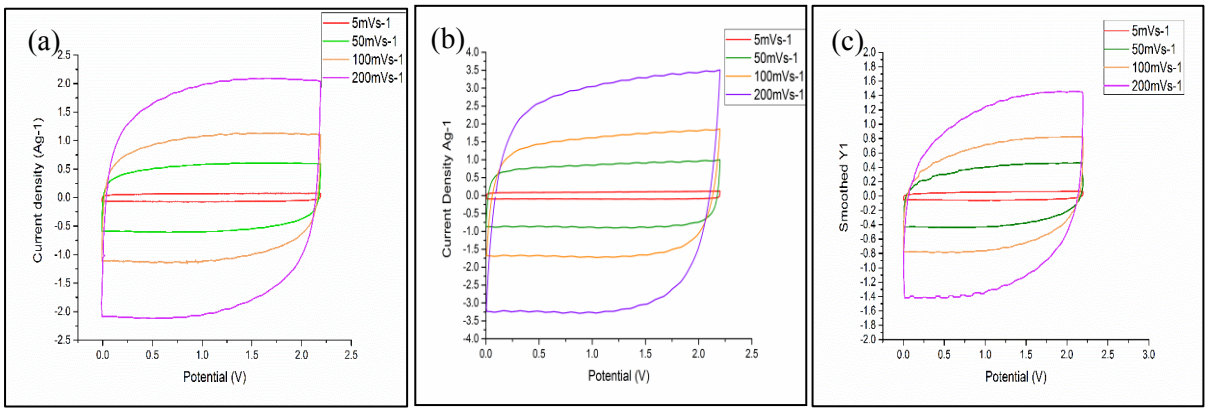

Figure 5-2: CV measurement at various scan rate for (a) M5V8, (b) M10V8 (c) M15V8

The relationship of specific capacitance of M5V8, M15V8, and M10V8 electrodes on various potential sweep rates from 5mVs^{-1} to 500mVs^{-1} is depicted in Figure 5-3. The specific capacitance of all AC samples shows a declining trend as the potential sweep rate increases. Among all the active materials, the commercial YP80F has achieved the highest specific capacitance, which nearly 28Fg^{-1} at 5 mV s^{-1}. The specific capacitance is closely related to the BET surface area and the purity of AC samples. The higher BET surface area of samples exhibits the larger area of CV curves and contributes a higher specific capacitance. Among all the Marabú derived ACs, M10V8 has the highest BET surface area (1977 m^{2}g^{-1}) delivers the highest specific capacitance up to 20Fg^{-1} at 5mVs^{-1}. M5V8 achieved specific capacitance up to 13.3Fg^{-1} at 5mVs^{-1}. M15V8 (932 m^{2}g^{-1}) exhibits the lowest low specific capacitance of 7 Fg^{-1} at 5mVs^{-1}.

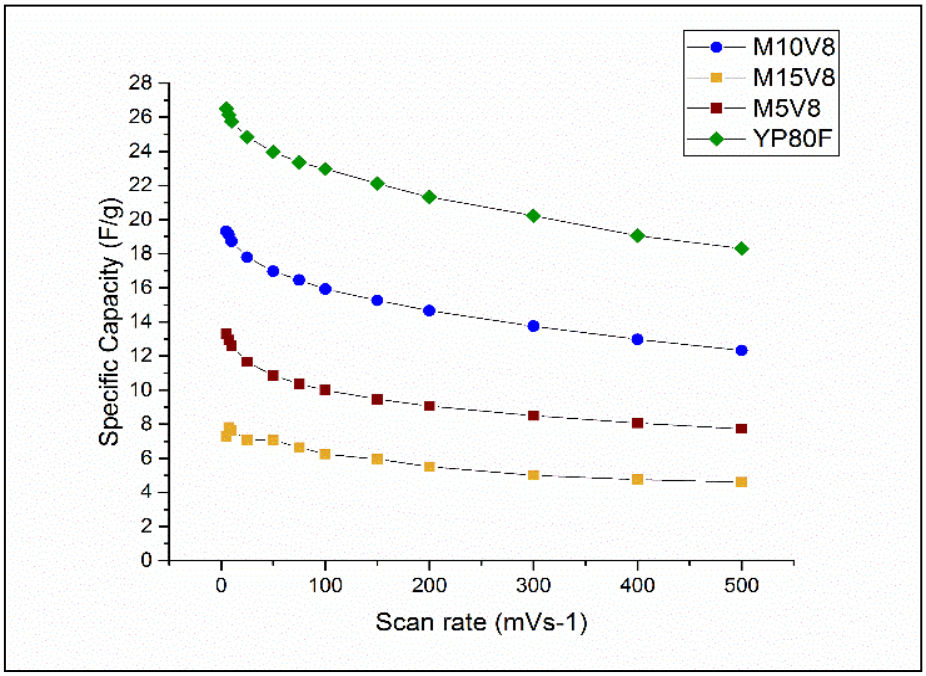

Figure 5-3: Specific capacitance of cell with sweep rate (5mVs^{-1}- 500mVs^{-1}) using cyclic voltammetry

At a very high scan rate, the adsorption of electrolyte ion could only occur on the surface of the carbon electrode. The specific capacitance remains at 12Fg^{-1} (~60%, M10V8), 7.7Fg^{-1} (58%, M5V8) and 4Fg^{-1} (57%, M15V8), respectively at high scan rate of 500mVs^{-1}. The high retain capacitance at a high scan rate suggests that the AC sample could deliver in a fast ionic transportation rate and the relatively high conductivity properties[15]. Based on the specific capacitance of EDLC with the prepared AC as electrode materials (Figure 5-3) and the observation from CV under various scan rates, M10V4, M10V6 and M10V8 are selected for further evaluation to study the effect of activation holding time of AC to the electrochemical performance in EDLC.

5.1.2 The Effect of CO_2 activation holding time

5.1.2.1 Cycle Voltammetry

Among the three AC samples, M10V8 shows the largest symmetrical rectangular CV curves without any faradaic peaks (Figure 5-4). Cyclic voltammograms with different scan rates of 5, 50, 100 and 200mVs^{-1} for M10V4, M10V6 and M10V8 were further analyzed and displayed as in Figure 5-5. As refer to Figure 5-5, the CV of M10V6 (Figure 5-5 (b)) shows larger rectangular curves than the CV of M10V4 (Figure 5-5 (a)). Some noises are visible in the CV of M10V4. This could be due to the lower BET surface area of M10V4 (1031m^{2}g^{-1}) than M10V6 (1324m^{2}g^{-1}) and M10V8.

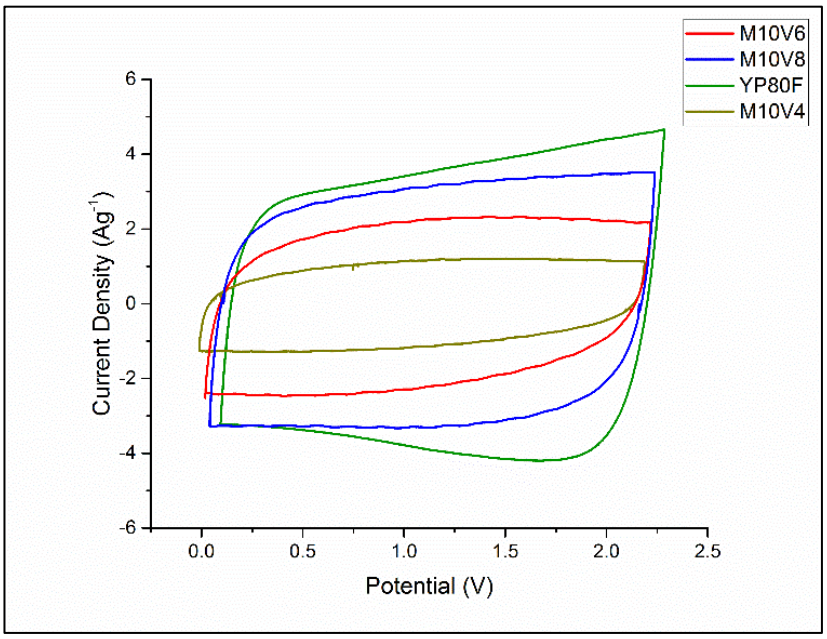

Figure 5-4: CV of commercial carbon, YP80F and Marabú derived ACs under various activation holding times.

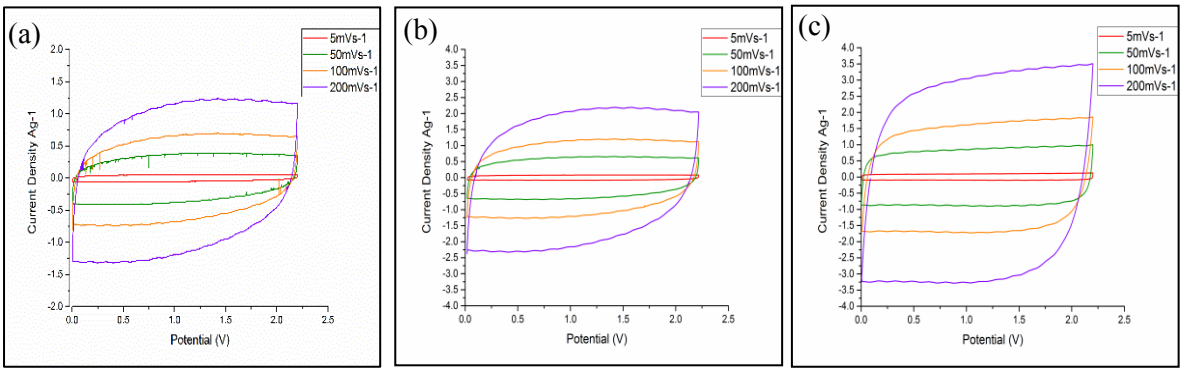

Figure 5-5: CV measurement at various scan rate for (a) M10V4 and (b) M10V6 (c) M10V8

5.1.2.2 Galvanostatic charge-discharge

The galvanostatic charge-discharge measurements were further conducted between the potential range of 0 to 2.2V at a current density of $1Ag^{-1}$. AC derived from Marabú and commercial carbon YP80F exhibit symmetrical triangular shapes with small IR drop for YP80F and M10V8 (Figure 5-6), typically represent a non-Faradaic system[21]. it is because there is some energy loss in the EDLC due to the internal resistance, thus IR drop illustrated along with the reversible ion adsorption mechanism. Smaller IR drop was found for M10V8 (0.0191V) as compared to M10V4 (0.0613V) and M10V6 (0.0177V) at a current density of $1Ag^{-1}$. The IR drop for commercial carbon, YP80F is 0.0143V. The specific capacitance was calculated based on the slope of the galvanostatic discharge curve (excluded the IR drop) at the same current density of $1Ag^{-1}$. Although EDLC with AC derived from Marabú shows lower the specific capacitance value as compared to YP80F ($25.9Fg^{-1}$), the cell capacitance value for EDLC increase from $5.3Fg^{-1}$ for M10V4, $11.5Fg^{-1}$ for M10V6, and up to $\sim 17Fg^{-1}$ for M10V8. It is noticed that the cell capacitance value has similar values as observed in a CV at a low scan rate of $25mVs^{-1}$ as seen in Figure 5-3.

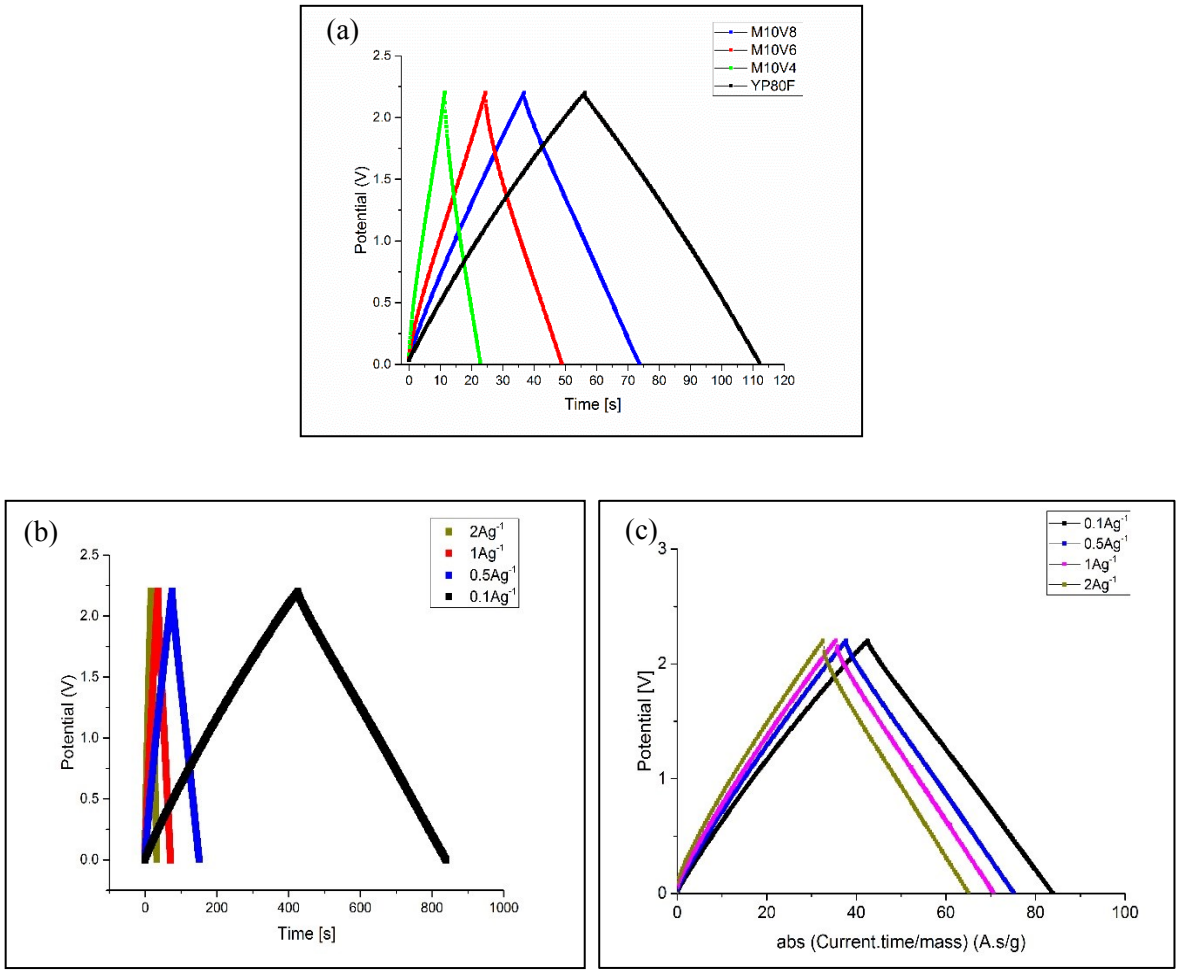

Figure 5-6: Electrochemical performance of EDLC in the organic electrolyte, 1 mol L^{-1} $TEABF_4$/PC (a) Galvanostatic charge-discharge curves at a current density of $1Ag^{-1}$, (b) Galvanostatic charge-discharge curve vs time of M10V8 at various current densities. (c) Galvanostatic charge-discharge curve of M10V8 vs abs [current.time/mass] at various current densities.

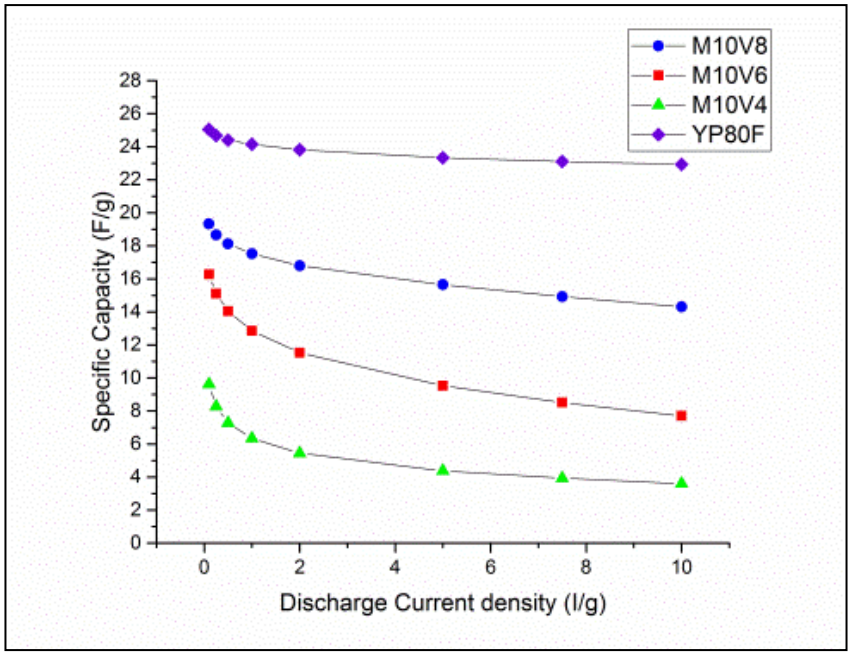

Figure 5-7: Specific capacitance of cell using AC derived from Marabú and YP80F respectively in organic electrolyte using various current density (0.1-10Ag^{-1})

Galvanostatic charge-discharge of M10V8 with various current densities from 0.1Ag^{-1} to 10Ag^{-1} was further examined and displayed in Figure 5-6(b). M10V8 presents similar symmetrical triangle charge-discharge curve at various specific currents densities with non-overt potential decrease as the current density increased. The linear characteristic indicates M10V8 electrode has reversible ion transport without redox reaction occurs [36, 115]. There is an increasing profile of IR drop in M10V8 with increasing of the specific current density in Figure 5-6(b), could be due to the resistance of the electrolyte ion [15, 199].

Figure 5-7 shows the specific capacitance of ACs with current density ranged from 0.1Ag^{-1} to 10Ag^{-1}. The specific capacitance of Marabú derived ACs decrease gradually with the increase of current density. A similar trend of cell capacitance was observed in CV (Figure 5-4) in scan rate range of 5 to 200mVs^{-1}. At high current density (10Fg^{-1}), the capacitance of M10V8 remains of 73.9% of initial capacitance. M10V6 retains of 47.3% while M10V4 only retain of 37.4%. The internal resistance in an EDLC shows a great significant effect on the cell capacitance as higher scan rates, which is likely happening as in real devices[138].

5.1.3 Electrochemical Impedance Spectra (EIS)

The electrochemical behavior of the samples was further investigated by electrochemical impedance spectra (EIS) analysis (frequencies from 0.01 Hz to 1MHz). The Nyquist plots of M10V4, M10V6, M10V8, and the commercial YP80F electrodes after galvanostatic cycling are shown in Figure 5-8. A semicircle appears in high-frequency region, Warburg diffusion line in the intermediate frequency region and followed by a transition to linearity at low frequencies for all the samples. Warburg diffusion lines show a slope about 45^0 from the real axis and followed by a transition to linearity with a slope closer to 90^0 at low frequencies suggested that the pure capacitive behavior and fast ion transfer to the electrode surface [37].

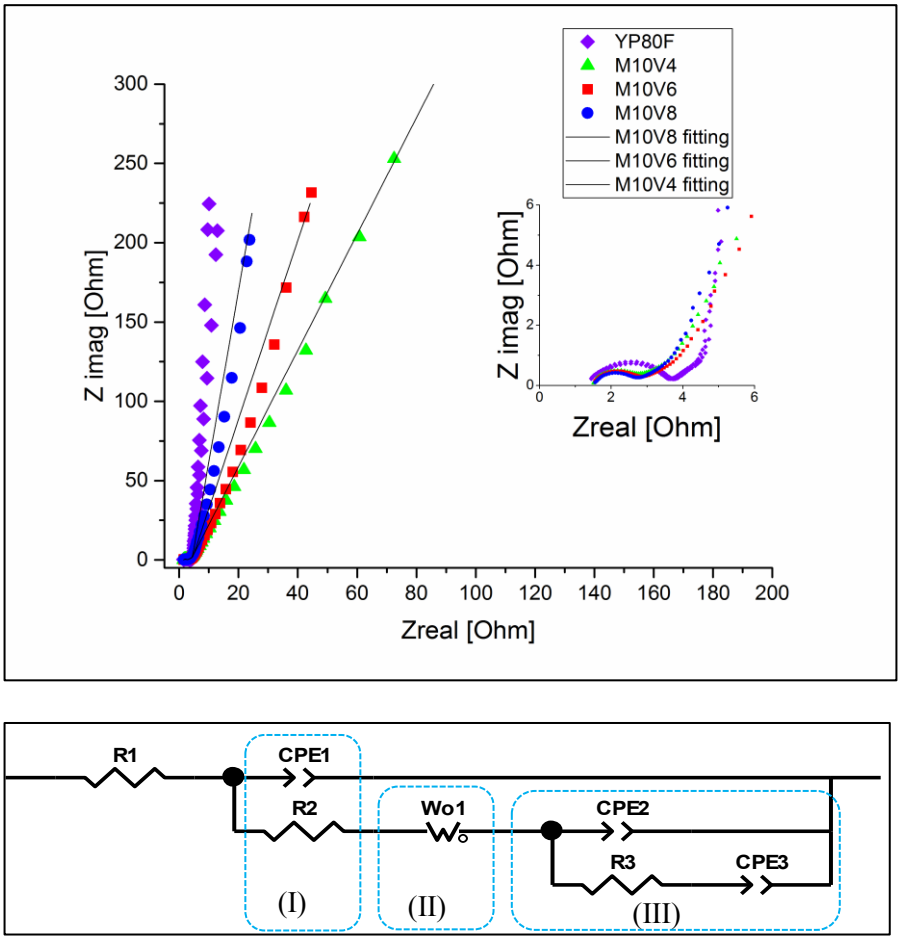

Figure 5-8: (a)Nyquist plot of Marabú derived AC samples as electrode materials in the organic electrolyte at a current density of $1Ag^{-1}$. (b) Kang's completed equivalent circuit modeling of (I) bulk electrolyte (II) diffusion layer (III) Helmholtz layer.

The straight line in low-frequency region was more parallel to the imaginary axis with an increase of activation holding time, indicating that M10V8 reflects a better capacitive behavior of the EDLC as compared to M10V4 and M10V6.

The EIS of the EDLCs in the organic electrolyte was analyzed with Kang's equivalent circuit model [142]. A circuit modeling of (I) bulk electrolyte, (II) diffusion layer and (III) Helmholtz layer in an EDLC are taken into account in the circuit model as shown in Figure 5.8. The fitting parameters of the designed equivalent circuit for Marabú derived AC samples are summarized in Table 5-1. The constant phase element (CPE) can be interpreted to two parameters: CPE-T and CPE-P, where CPE-T is the coefficient of bulk electrolyte [142] and CPE-P is the CPE exponential factor. CPE-P is referring to Q and CPE-T is referring to n as referred to as Equation 3-10. There are three parameters that related to Warburg impedance, W-T, W-P and W-R. W-R is referred to as Ohmic resistance, W-T is diffusion time constant and W-P is an exponential factor for Warburg [200]. Kumagai *et. al.* [147] has further summarized the elements and impedance applied in Kang's model.

The R1 represents the electrolyte resistance and some external circuit resistance. Same organic electrolyte and the same materials were used for cell fabrication, thus R1 value (~1.51 Ω) was observed for all the three AC samples. The bulk process is effective only at high frequency when the current overcomes the bulk impedance[142]. The CPE coefficient of bulk electrolyte (CPE1-T) is very low ($<\sim10^{-4}$) as compared to the other two CPE coefficients in the model (CPE2 and CPE3). A similar value of R2 under three samples (1.1-1.15) was found in the organic electrolyte-based systems. The R2 represents the bulk resistance, which explained as the resistance to create the double-layer capacitance by supplying excess ion to the diffusion layer [147].

The ion diffusion is represented by Warburg impedance. A shorter Warburg line for M10V8 is observed as compared to M10V6 and M10V4. This indicates the ion diffusion in M10V8 is more fluent than M10V6 and M10V4. In other words, the activation holding time has improved the surface of AC, ion diffusion occurs between the electrolyte and the surface of M10V8 has improved and faster. Therefore, the EIS data indicate the ion diffusion is greatly improved by the Marabú derived AC treated with longer activation holding time, leading improvement in electrochemical performance.

According to Kang's circuit model, the Helmholtz layer capacitance was interpreted as the ion adsorption (CPE2) and ion transportation due to the different of the ion concentration between the bulk and the interfacial electrolyte (CPE3) and with an interfacial resistance (R3) [147]. The R3 for M10V4, M10V6, and M10V8 are 1.5Ω, 1.4 Ω and 0.8 Ω respectively. The lower R3 for M10V8 suggested that there is a reduction of the ion resistance to access the porous of the electrode[31]. The value of CPE2-T for M10V8 (0.65) was found higher than M10V6 (0.54) and M10V4 (0.35). It was found that the value of CPE3-T of M10V4 is small (0.04) when compared to M10V6 (0.35) and M10V8 (0.4). Thus, this suggesting that the M10V6 and M10V8 is contributed by the adsorption capacitance and double-layer capacitance. However, the capacitance of M10V4 is attributed mainly to the adsorption

capacitance only. These results were consistent with the lower specific capacitance of M10V4 as compared to M10V6 and M10V8 as shown in Figure 5-4.

An attractive aspect of the present results is that there is a great improvement in the specific capacitance of the EDLC and lower interfacial resistance (R3), higher contribution in Helmholtz layer capacitance by adsorption and ion diffusion is observed for longer activation holding time treated samples. The capacitance calculated from the lowest frequency using Equation 3-14 for both AC samples, there are 15.4Fg^{-1}, 12.8 Fg^{-1} and 7.42Fg^{-1} for M10V8, m10V6 and M10V4 respectively. These values are close to the capacitance which determined using CV at 25mVs^{-1}.

Table 5-1: Fitting parameters for an equivalent circuit for M10V4, M10V6, and M10V8 in 1M $TEABF_4$/PC

Element	Note	Unit	M10V8	M10V6	M10V4
R1	Electrolyte resistance	Ω	1.51	1.51	1.51
CPE1-T	Coefficient of CPE (bulk electrolyte)		5.7E-4	5.3E-5	3.5E-4
CPE1-P	The exponential factor of CPE (bulk electrolyte)		0.78	0.91	0.87
R2	Bulk electrolyte resistance	Ω	1.1	1.1	1.15
Wo1-R	Diffusion resistance	Ω	2.4	4.3	3.5
Wo1-T	Diffusion time constant		1.63	2.5	0.65
Wo1-P	The exponential factor for W		0.48	0.465	0.435
CPE2-T	Coefficient of CPE (Helmholtz layer formation)		0.65	0.54	0.35
CPE2-P	The exponential factor of CPE (Helmholtz layer formation)		0.33	0.49	0.55
R3	Interfacial resistance	Ω	0.8	1.4	1.5
CPE3-T	Coefficient of CPE (ion adsorption)		0.4	0.35	0.04
CPE3-P	The exponential factor of CPE (ion adsorption)		0.98	0.98	0.98

5.1.4 Ragone Plot

Ragone plot is an important graph to relate the energy-power characteristic of an energy storage system. The performance of the Marabú derived active materials as electrode material for EDLC is presented in Figure 5-9, which reflects the relationship between the energy and the power density of the materials in the EDLC. The specific energy and power of an EDLC cell were calculated from galvanostatic charge/ discharge curves and based on the mass of the activated carbon in the cell. M10V8, M10V6 and M10V4 exhibit energy densities of 12, 7.5, and 5 Wh/kg at 4W/kg, respectively. Among all the prepared samples, the maximum energy and power density of 12 $Whkg^{-1}$ and 385Wkg^{-1} were obtained for M10V8. Although there is no published work reported using physically activated carbon derived from biomass and organic electrolyte in EDLC, the present work is comparable to some published works in EDLC using KOH activated biomass-derived AC as summarized in Table 2-2. Xu et. al. [116] reported that

KOH activated carbon derived from Pistachio shell which showed the energy density of 39Whkg^{-1} and 286Wkg^{-1} in an organic-based symmetrical EDLC. Recently, Wang et. al. [10] prepared KOH activated carbon derived from pine tree sawdust powder achieved about 18Whkg^{-1} of energy density and ~200Wkg^{-1} of power density. These results reveal the possibility of Marabú based AC in energy storage to fulfill the energy demands.

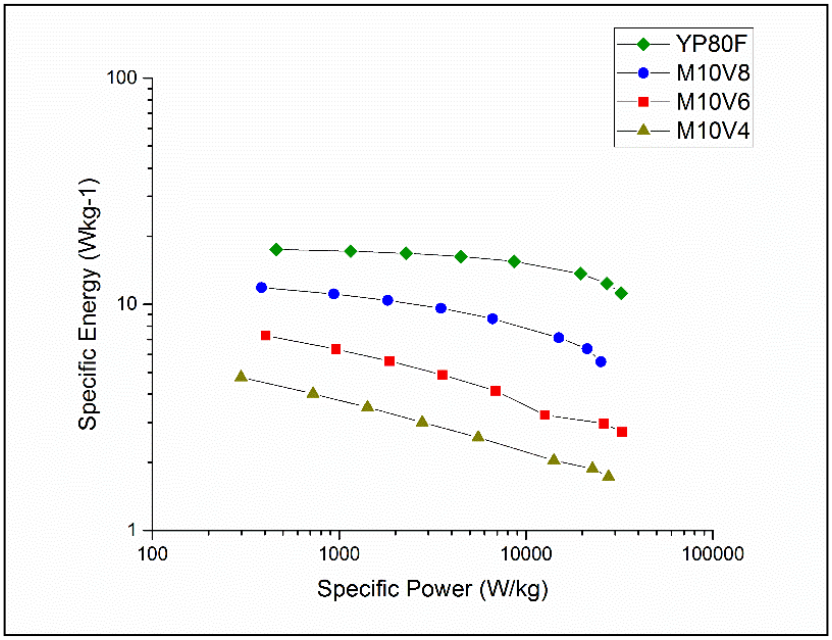

Figure 5-9: Ragone plot of symmetric capacitors with Marabú active materials and YP80F as electrode materials.

5.1.5 Cyclic stability

Furthermore, long term cyclic stability performance of AC was tested at a current density of 5Ag^{-1} within the potential range from 0 to 2.2V in 1 M $TEABF_4$/PC electrolyte in room temperature. Figure 5-10 shows that all the samples have completed 30000 of charge-discharge cycle. This indicating that all the Marabú derived ACs exhibit a stable behavior in the long-term cycle.

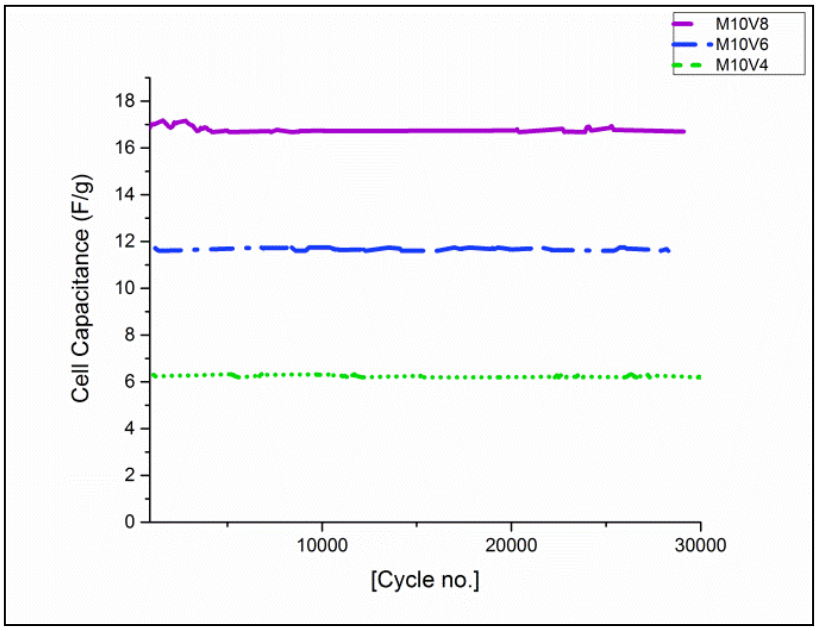

Figure 5-10: The cycling stability of EDLCs with Marabú active materials as electrode materials in the organic electrolyte at a current density of $1Ag^{-1}$.

5.2 The Effect of Binder on the Electrochemical Stability of Ionic Liquid electrolyte

It is important to determine the widest ESW of electrolytes for EDLC devices to achieve optimum energy. The selection of electrolytes and the electrode materials are often as the major consideration to determine the widest ESW for an EDLC. In addition, Abbas *et. al.* [201] reported that a binder in carbon electrode indeed greatly affects the potential window and electrochemical performance of an EDLC.

In this work, the ESW of EMIMBF4, IL was studied using commercial carbon (YP80F) with two different polymer binders, there are PVDF and PTFE. The stability criterion with an S-value limit of 0.1 which was introduced by Xu et. al. [139] to determine electrochemical stability of electrolyte. Figure 5-1 shows the S-value vs potential plots for IL $EMIMBF_4$ using commercial carbon (YP80F) with (a) PVDF and (b) PTFE as a binder. The ESW of $EMIMBF_4$ using PTFE as a binder in carbon electrode is more stable than using PVDF as a binder. The system using PVDF as binder exhibits a lower potential range as referring to Figure 5-1(a). A wider region of electrochemical stability was observed using a carbon electrode with PTFE as a binder as shown in Figure 5-1(b).

The ESW of the systems were further evaluated using the new stability criterion which was introduced by Weingarth et. al. [140]. The second derivate of S-value was further evaluated with the limitation of not more than 0.05. A narrower potential range of $EMIMBF_4$ using PVDF as a binder was observed as in Figure 5-2 (a), which is less than 2 V. The potential range of $EMIMBF_4$ using PTFE as binder exhibits

a wide potential range of 4.4V, which well agreed as reported by [202]. This can be clearly revealed that the selection binder in carbon electrode fabrication is greatly affected by the electrochemical stability of $EMIMBF_4$ IL in this work. Therefore, PTFE is selected and applied as a binder in the carbon electrode for $EMIMBF_4$.

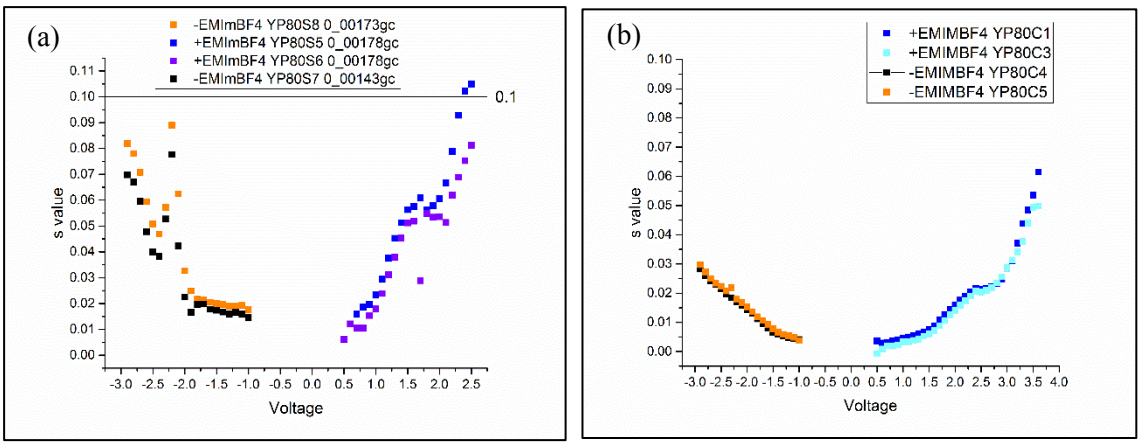

Figure 5-11: S-value vs potential plot for IL EMIMBF4 using (a) PVDF and (b) PTFE as a binder in carbon electrode

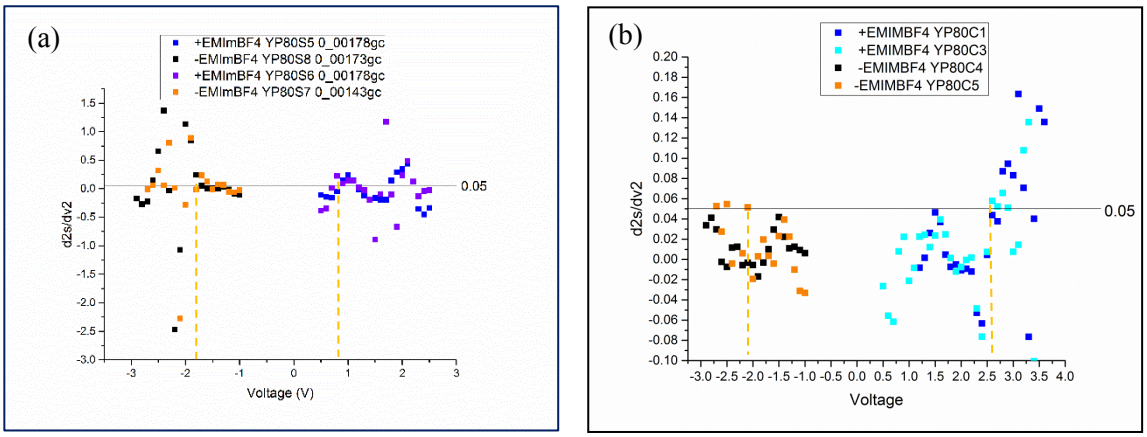

Figure 5-12: The second derivative of S-value vs potential using (a) PVDF and (b) PTFE as a binder in carbon electrode

5.3 The Electrochemical Performance of EDLC using Marabú derived carbon as electrode material with Ionic Liquid electrolyte

5.3.1 Cycle Voltammetry

In order to extend the potential range of Marabú based EDLC, the electrochemical performance of EDLCs with two-symmetric electrodes using M10V4, M10V6 and M10V8 as the carbon electrode ingredient were further tested in EMIMBF4, IL. The potential range of 3.5V is selected to avoid any electrolyte decomposition occurs. Figure 5-13 shows almost rectangular CV curves without any apparent faradaic peaks present at the scan rate of 5mVs^{-1}. Besides, there is no significant redox peaks appear on the CV curves at scan rates from 5 to 200mVs^{-1}, displayed in Figure 5-14. This confirmed that there is only physical ion charge and discharge occur in the cells. There are CV distorted at switching potential in CV scans was observed, Jiang and Kucernak [203] and Yang et. al. [204] suggested this could be due to the effect from the inner resistance between the electrode and electrolyte and scan rates.

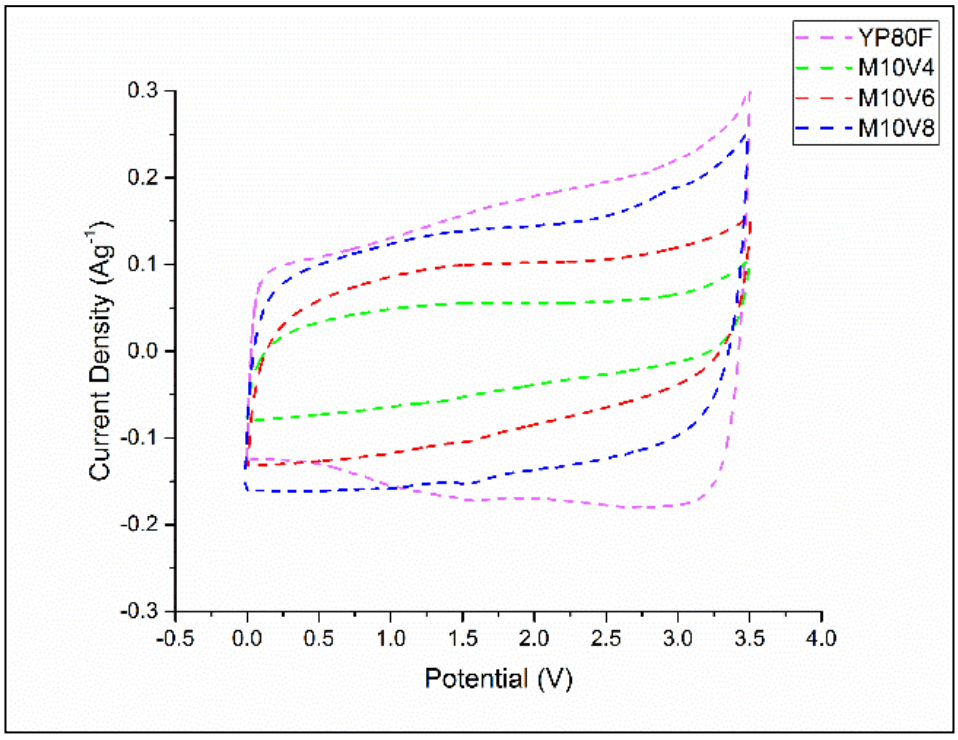

Figure 5-13: CV curves of the symmetric two-electrode cell using M10V4, M10V6, M10V8 and YP80F as electrode materials in Ionic liquid, EMIMBF$_4$ at a scan rate of 5mVs-1.

The specific capacitance at different scan rates is illustrated in Figure 5-15. It is clearly seen that the specific capacitance decreases as a function of scan rate. The initial specific capacitance of M10V8 is 25.5Fg^{-1} at 5mVs^{-1} and started to decrease to 7Fg^{-1} at 200mVs^{-1}. The initial specific capacitance is 17Fg^{-}

^{1} and 9.5Fg^{-1}, further dropped to 4.8Fg^{-1} and 3Fg^{-1} for M10V6 and M10V4, respectively. The reason for the sharp reduction of specific capacitance is due to the limitation of the ions adsorption to the electrode surface. At high scan rates, the inner porous of the carbon electrodes are unreachable by ions in the electrolyte, thus charge/discharge performance of the cell is not fully operated.

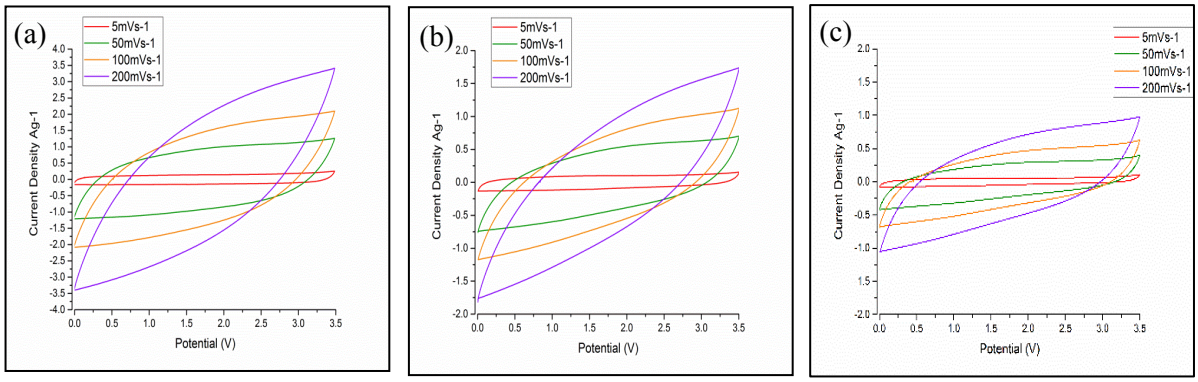

Figure 5-14: CV measurements at different scan rates for (a) M10V8 and (b) M10V6. (c) M10V4

On the other hand, a higher specific surface capacitance was observed in IL as compared to the organic electrolyte. Considering the diameter of ions $EMIM^{+}$ (0.6nm) and $BF4^{-}$ (0.46nm) in IL [147] and diameter of TEA^{+} (0.68nm), $BF4^{-}$ (0.46nm) and PC (0.55nm) in organic electrolyte [10], smaller ions in IL promotes the ion diffusion on the electrode surface with high specific surface area at initial stage. However, the viscosity of $EMIMBF_4$ is much higher than 1 molL^{-1} $TEABF_4$/PC. In-room temperature of 25°C, the viscosity of 1 molL^{-1} $TEABF_4$/PC, an organic electrolyte is about 4mPa s [205], while the viscosity of $EMIMBF_4$ is about 37cP [206]. Thus, this could hinder the ion diffusion of IL into the inner porous of the carbon electrodes [207].

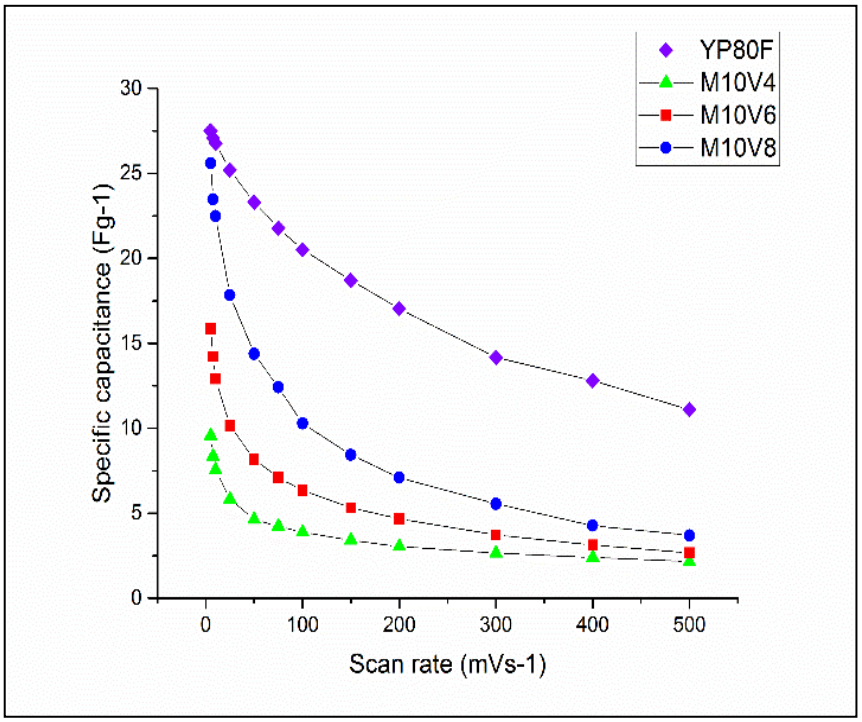

Figure 5-15: Specific capacitance of cell using AC derived from Marabú in EMIMBF4 using various current density (0.1-10Ag^{-1})

5.3.2 Galvanostatic charge-discharge

The kinetic reversibility by the quick response to the potential switching is an ideal behavior for an EDLC. The Galvanostatic charge-discharge (GCD) curves of the EDLC at a fixed current density of 1Ag^{-1} is analyzed as illustrated in Figure 5.16 (a). As compared to cells in the organic electrolyte (Figure 5-6), the IR drop is much higher in $EMIMBF_4$. It is interesting that the IR drop of commercial carbon, YP80F exhibits slightly higher value (0.5292Ω) than M10V8 (0.5086Ω). The GCD curves for M10V8 is further evaluated under various current densities ranging from 0.1Ag^{-1} to 2Ag^{-1}, as illustrated in Figure 5-16(b). The shape of charge/ discharge curves is very similar to each other with visible IR drop are observed at 0.5-2Ag^{-1}.

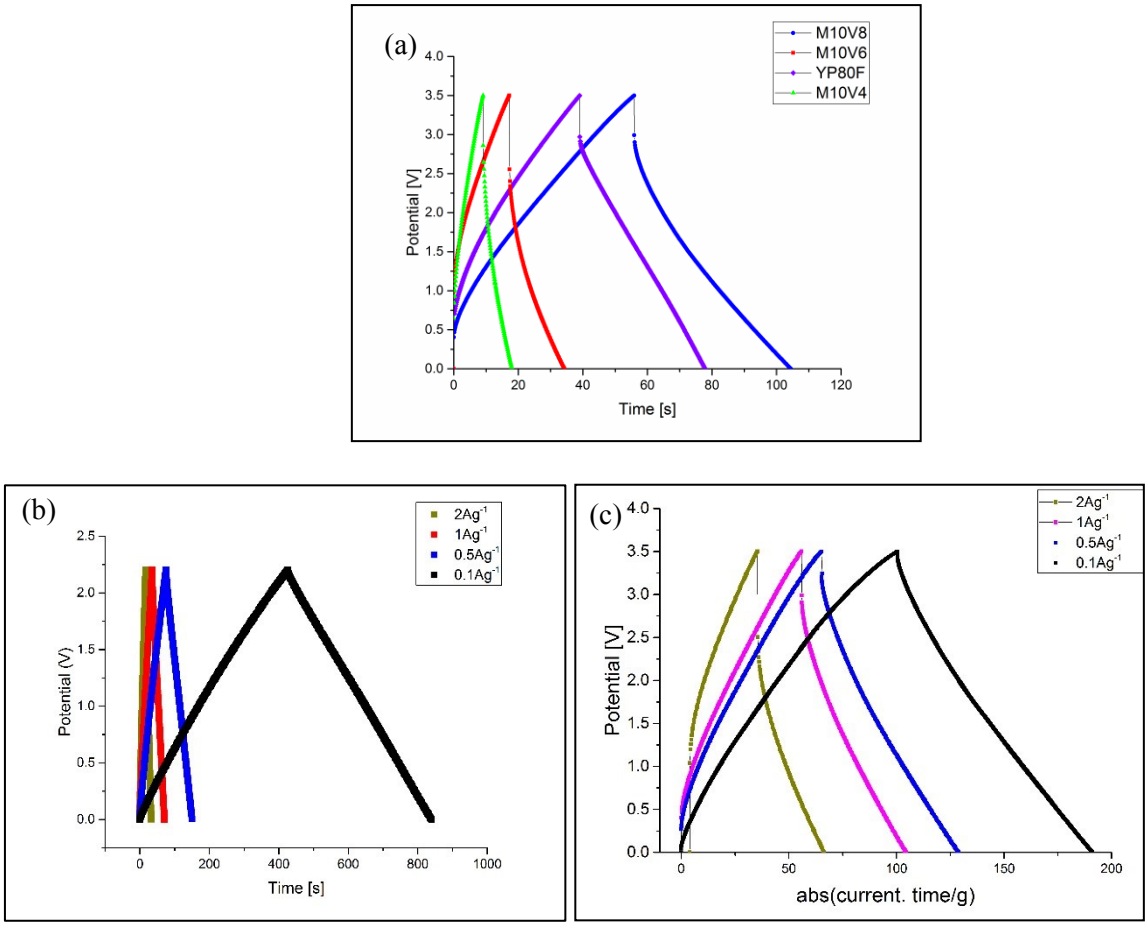

Figure 5-16: Electrochemical performance of EDLC in $EMIMBF_4$, IL (a) Galvanostatic charge-discharge curves at a current density of $1Ag^{-1}$ for all the AC samples, (b) Galvanostatic charge-discharge curve of M10V8 at various current densities.

5.3.3 Cyclic stability

The cycling stability of Marabú based AC in $EMIMBF_4$ was studied at a current density of $1Ag^{-1}$ (Figure 5-17). There is some degradation in capacitance value was observed for all the samples. The initial capacitance value of M10V8, M10V6, and M10V4 are $20Fg^{-1}$, $10Fg^{-1}$ and ~$5Fg^{-1}$ respectively. The capacitance retained about 77% for YP80F ($21Fg^{-1}$), ~50% for M10V8 ($10Fg^{-1}$), ~28% for M10V6 (~$3.5Fg^{-1}$) and ~30% for M10V4 (~$1.6Fg^{-1}$) after 30000cycles. The degradation in the cyclic stability test consistent with the observation in the reduction of specific capacitance as an increase of scan rate (Figure 5-15) and the high IR drop in GCD curve (Figure 5-16).

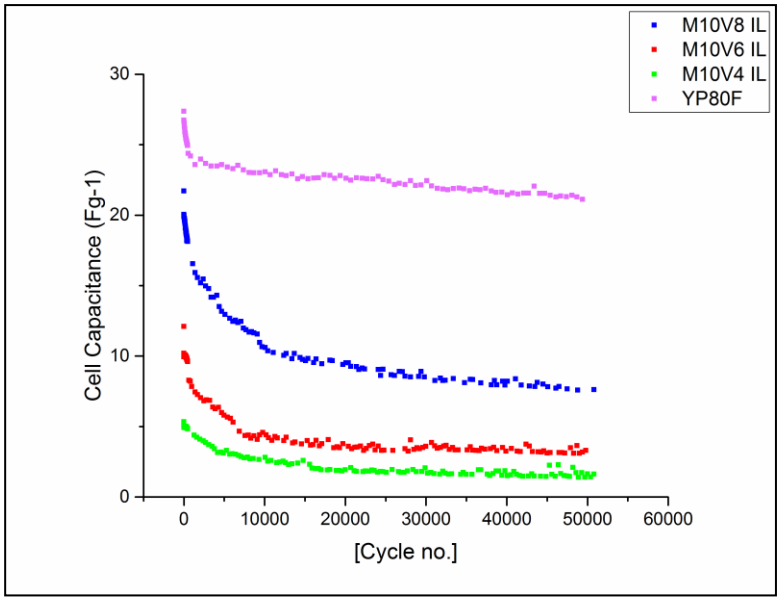

Figure 5-17: The cycling stability of EDLC in $EMIMBF_4$ at a current density of $1Ag^{-1}$

5.3.4 Ragone Plot

The Ragone plot for the Marabú derived active materials as electrode material for EDLC using IL system is presented in Figure 5.18, which reflects the relationship between the energy and the power density of the materials in the EDLC. The specific energy and power of an EDLC cell were calculated from galvanostatic charge/ discharge curves and based on the mass of the activated carbon in the cell. M10V8, M10V6 and M10V4 exhibit energy densities of 37, 16.8, and 7.8 $Whkg^{-1}$ at 4W/kg, respectively. Among all the prepared samples, the maximum energy and power density of 37 $Whkg^{-1}$ and $697Wkg^{-1}$ were obtained for M10V8. As compared to Figure 5.9 that Marabú in EDLC organic electrolyte system, IL systems achieve a much higher value of energy density. However, the energy density profile drops dramatically at higher power density. This is consistence with the poor cycle stability observation in Figure 5.17 and also the increment of the IR drop value as higher current densities applied as shown in Figure 5.16 (c).

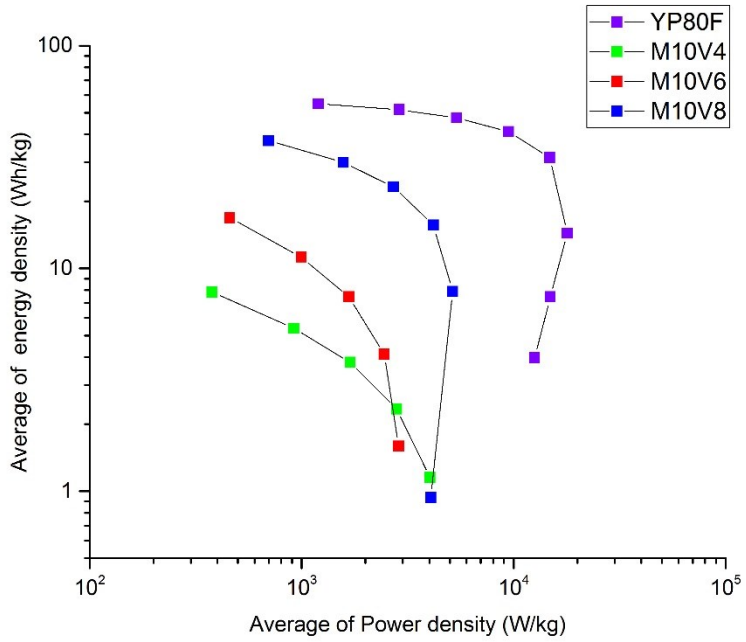

Figure 5-18: The Ragone plot of symmetric capacitors with Marabú active materials and YP80F as electrode materials.

5.3.5 Electrochemical Impedance Spectra (EIS)

A typical EIS Nyquist plot with a semicircle, Warburg diffusion line and followed by a transition to linearity was observed for all the samples (Figure 5-19). The same value of R1 (1.78Ω) was observed for all the samples due to the same electrolyte and fabrication technique applied to each EDLC. It is noticed that the value of R1 is higher than organic electrolyte due to the lower conductivity of IL (~0.01Scm^{-1}) than most of the common organic electrolyte(~0.02Scm^{-1}) [208]. In this case, CPE1 coefficient of bulk electrolyte (T_{bulk}) for IL-based system is very low (<~10^{-4}) as in organic-based EDLC. The bulk resistance, R2 is much higher than as reported in organic electrolyte-based systems in section 5.2.3. The increasing trend of R2 is observed, which are 0.0001 (M10V4), 0.51 (M10V6) and 5.15 (M10V8). Likewise, similar findings were observed by Seiji et. al. [147], where higher bulk resistance was reported for a sample with high mesoporous. M10V8 has a higher mesoporous surface area and mesoporous volume among others as listed in Table 4.4 and as presented in Figure 4-7 9(b). Thus, this could be explained by the low movement of ion $EMIM^+$ and BF_4^- to approach the mesoporous surface thus a greater resistance hinders the diffusion layer formed on the surface of the electrode. In contrast to the observation in 1molL^{-1} $TEABF_4$ in PC, the organic electrolyte in section 5.2.3, R3 is relatively high in $EMIMBF_4$, which are 6Ω, 10Ω to 16Ω for M10V4, M10V6, and M10V8 respectively (Table 5-2). The increase of R3 suggests that increasing interfacial resistance on the surface of the carbon electrode. In addition, the diffuse resistance (W-R) of M10V8 is lower in IL. The difference between

R3 and W-R reflect the diffusion and double-layer formation are greatly associated with the type of electrolyte applied in EDLC.

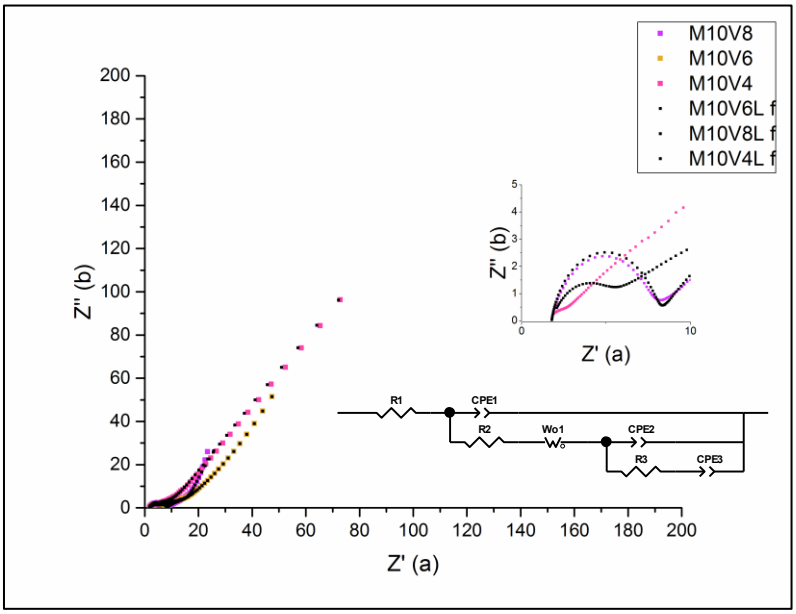

Figure 5-19: Nyquist plot of Marabú derived active materials as electrode materials in EMIMBF$_4$ at a current density of 1Ag^{-1}

Table 5-2: Fitting parameters for equivalent circuit for M10V4, M10V6 and M10V8 in IL system

Element	Note	M10V8 IL	M10V6 IL	M10V4 IL
R1	Electrolyte resistance	1.78	1.78	1.78
CPE1-T	Coefficient of CPE (bulk electrolyte)	0.00015	0.00025	0.025
CPE1-P	Exponential factor of CPE (bulk electrolyte)	0.85	0.65	0.59
R2	Bulk electrolyte resistance	5.15	0.5	0.0001
Wo1-R	Diffusion resistance	0.9	3.65	4.65
Wo1-T	Diffusion time constant	0.1	0.0025	2.8
Wo1-P	Exponential factor for W	0.002	0.065	0.1
CPE2-T	Coefficient of CPE (Helmholtz layer formation)	0.22	0.25	0.005
CPE2-P	Exponential factor of CPE (Helmholtz layer formation)	0.53	0.63	0.3
R3	Interfacial resistance	16	10	6
CPE3-T	Coefficient of CPE (ion adsorption)	1.6	0.35	0.25
CPE3-P	Exponential factor of CPE (ion adsorption)	0.88	0.71	0.71

5.4 Summary

In this chapter, an overview of EDLC based on two symmetrical electrodes derived from Marabú in the organic electrolyte and ionic liquid has been presented. In EDLCs, the capacitance is obviously depending on the specific surface area. However, the pore size, degree of graphitization, functional group on the surface carbon and the impedance in the cell could be important to affect the electrochemical performance of an EDLC. A longer CO_2 activation holding time of 80mins promotes a higher specific surface area, lower carbon defects, and lesser functional groups. Thus, this helps the interaction between the electrolyte ions and the porous network and charges storage on the carbon electrode. Although the performance of EDLC is slightly lower than the commercial carbon as the electrode material, The EDLC in organic electrolyte shows a high specific capacitance value of $20Fg^{-1}$ at $5mVs^{-1}$ and maximum energy and power density of 12 $Whkg^{-1}$ and $385Wkg^{-1}$ were obtained for M10V8 with BET surface area (1977 m^2g^{-1}) as carbon electrode material. Even though an EDLC in IL electrolyte resulted in a higher specific capacitance. However, significant degradation of specific capacitance was observed in the CV and the cycle stability test in IL. Based on the EIS evaluation, the is due to the low mobility of ion $EMIM^+$ and BF4- approaching the surface electrode and thus create high internal resistance in the system and higher IR drop as compared the system in organic electrolyte. The results demonstrate the potential of AC derived from Marabú as suitable and promising electrode material with comparable specific capacitance and energy density in EDLC application. The enhancement of the electrochemical performance of an EDLC so far can be further optimized by removing the ash content in the AC in order to boot the energy density and the specific capacitance of the system.

6 Electrochemical Performance of Activated Carbon derived from Spent Coffee Ground as the electrode material for EDLC

This chapter discusses the electrochemical performance of EDLC using spent coffee ground (CG) derived activated carbon (AC) as the electrode material in an organic electrolyte, 1 M triethylmethylammonium-tetrafluoroborate ($TEABF_4$)/propylene carbonate (PC). The ACs prepared under two activation temperatures, 950^{o}C and 1000^{o}C were used as the electrode material of EDLC. The electrochemical performance of the EDLC was discussed and compared with the commercial carbon (YP80F). The electrochemical performance of EDLCs was evaluated and discussed based on galvanostatic charge-discharge (GC), cyclic voltammetry (CV) and electrochemical impedance spectroscopy (EIS). The cycle stability of the cells was further tested to run over 30,000 cycles. The Ragone plot was plotted to reflect the energy-power characteristic of the cells.

6.1 Cyclic Voltammetry

The cyclic voltammograms (CV) at 200mVs^{-1} for EDLC using AC derived from CG as electrode material are illustrated in Figure 6-1. It is clearly seen that the CV curves for AC prepared with an activation temperature of 1000^{o}C (Figure 6-1 (a)) are close to an ideal rectangular shape. This indicates that AC derived from CG activated at higher temperature show a better capacitive nature. Among all the ACs, C10W10 showing the largest CV curve. This indicating the fast diffusion kinetics of electrolyte ions in the cell using C10W10 due to the low inner resistance[115]. Although distorted CV with some noises was observed for AC treated with an activation temperature of 950^{o}C, there are no significant faradic peaks observed in the CV as displayed in Figure 6-1(b).

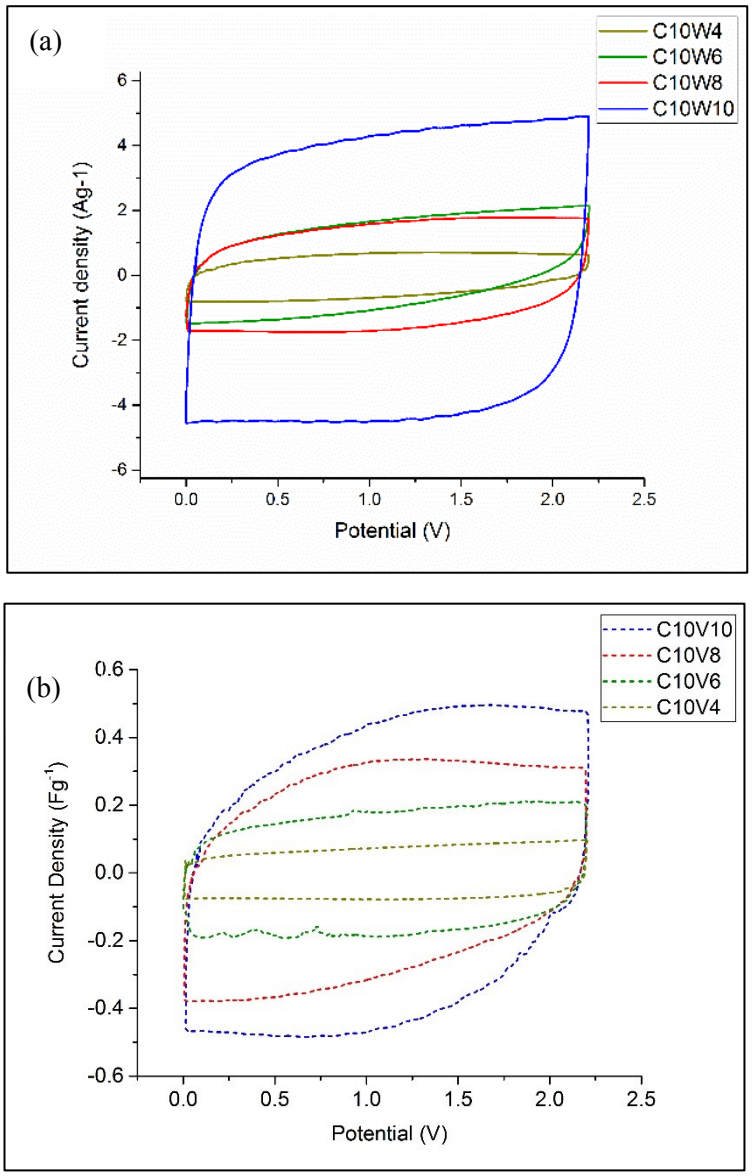

Figure 6-1: CV curves of spent coffee ground derived ACs, which prepared with activation temperature of (a) 1000^{o}C (b) 950^{o}C as electrode materials in the organic electrolyte, 1 mol L^{-1} TEABF$_4$/PC at a scan rate of 200mVs^{-1}

The CV curves of ACs were further analyzed at various scan rates from 5mVs^{-1} to 500mVs^{-1} to study the charge storage mechanism as illustrated in Figure 6-2. At low scan rates, a perfect rectangular CV curve is observed for C10W10, there is no distort shape on the CV was observed even at a high scan rate of 200mVs^{-1}. This evincing that C10W10 is showing a good conductivity and quick response as an electrode material to the current change with a sudden reversing potential sweep. The ion in the electrolyte interacts efficiently with C10W10 in an organic-based EDLC. The rectangular shape was observed for C10W6 and C10W8, and the CV curves were slightly distorted at higher scan rates. While on the contrary, noises were observed at a low scan rate of 5mVs^{-1} and the CV curve shape distorted with further increases scan rate to 200mVs^{-1}for C10V10 and C10V8.

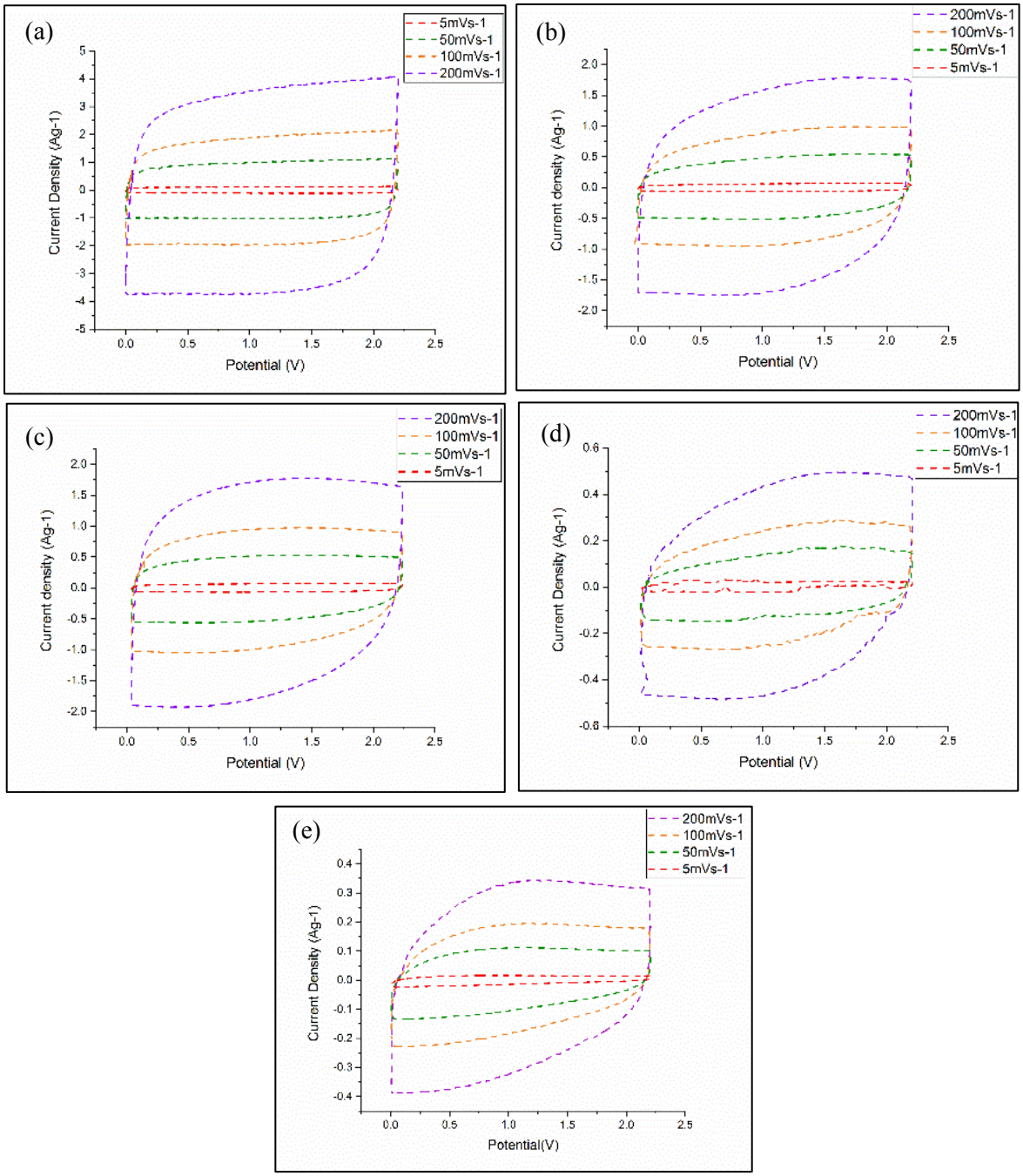

Figure 6-2: Specific capacitance of cell with sweep rate ($5mVs^{-1}$- $500mVs^{-1}$) using cyclic voltammetry for (a) C10W10, (b) C10W8, (c) C10W6, (d) C10V10 and (e) C10V8

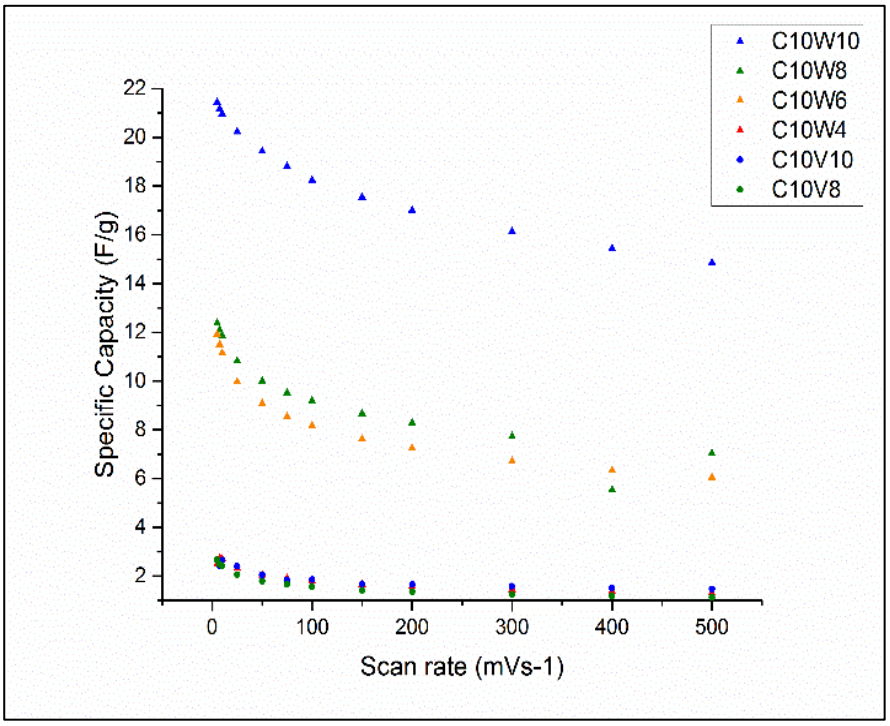

Figure 6-3: Specific capacitance of EDLC with sweep rate ($5mVs^{-1}$- $500mVs^{-1}$) using cyclic voltammetry

Figure 6-3 shows the specific capacitance of EDLCs with sweep rate range in $5mVs^{-1}$ - $500mVs^{-1}$, the value was calculated by using the integral area of the discharge as referred to Figure 6-2. As expected, C10W10 with the largest CV curve delivered the highest specific capacitance of up to $21.44Fg^{-1}$. C10W10 has the highest specific surface area of $1003m^2g^{-1}$as referred to Table 4-10 with a combination of microporous and mesoporous as illustrated in Figure 4-17(b). The high specific capacitance could be attributed to the large accessible surface area and good network path between microporous and mesoporous for ion transportation in the electrode. C10W8 with a specific surface area of $1169m^2g^{-1}$ could achieve only half of the specific capacitance of C10W10, $12.38Fg^{-1}$ and follow by C10W6 ($1058m^2g^{-1}$) with $11.91Fg^{-1}$. Although C10V10 and C10W6 have similar BET surface areas and S_{mic} (Table 4.10), the specific capacitance of C10V10 (less than $3Fg^{-1}$) is much lower than the specific capacitance of C10W6. The different performance of both samples could be due to the difficulty of accessibility of narrow micropores for ions in the electrolyte. Higher activation temp of 1000°C promotes the porous structure formation and removes the impurities in the carbon. Lower volatile content and lower ash content in C10W10 (Table 4-9) reduces the obstacle to ions in the electrolyte to access to the surface of the electrode. Besides, C10W10 shows lower functional groups based on XPS analysis in section 4.3.16 and a higher graphitization as observed in the Raman analysis (Table 4-12). By considering the specific capacitance, C10W10, C10W8, C10W6, and C10V10 are further analyzed in symmetric 2 electrode EDLC using Galvanostatic charge-discharge technique.

6.2 Galvanostatic charge-discharge

The galvanostatic charge-discharge (GCD) measurements were conducted in an organic electrolyte, 1molL^{-1} $TEABF_4$/PC at a fixed current density of 1Ag^{-1} is illustrated in Figure 6-4. Symmetric triangle with linear characteristics which agreed well with the CV analysis in Figure 6-1 that there is quick reversible ion transport with no faradaic reaction in an organic electrolyte based EDLCs. There is no significant IR drop observed in both samples at a fixed current density of 1Ag^{-1}. The specific capacitance was calculated based on the slope of the GDC curve using Equation 3-9 and displayed in Figure 6-5. Based on the Equation 3-9, the EDLC with C10W10 as carbon electrode achieved the highest cell capacitance of 19.5 Fg^{-1}. C10W8 and C10W6 achieve 8.3Fg^{-1} and 8.29Fg^{-1} respectively, which is only half of the performance of C10W10. While C10V10 and C10V8 only delivered 1.75Fg^{-1} and 1.5Fg^{-1} respectively. The specific capacitance trend for all the samples is consistent as observed in a CV at the low scan rates in Figure 6.3. Overall, the specific capacitance of EDLC is much outstanding using AC at a higher activation temperature of 1000°C.

The higher value of specific capacitance attributed to the higher mesoporous (Table 4-10) and wider PSD of the AC at the activation temperature of 1000°C (Figure 4-6). As refer to Table 4-10, AC with an activation temperature of 1000°C shows lower V_{mic}/V_{tot} at the same time the high activation temperature broadens some of the bottle-neck micropores and increases mesoporous. Mesopores provide channels for ions in the electrolyte to reach micropores. Besides, ACs under the higher CO_2 activation temperature introduce more defects to the graphene plane of the CG derived ACs (section 4.3.1.5). Defects within carbon could affect the carbon capacitance [209]. In addition, oxygen functional groups on the surface of AC which could hinder the ions diffuse into micropores [210] are relatively low was observed in XPS analysis with an activation temperature of 1000°C.

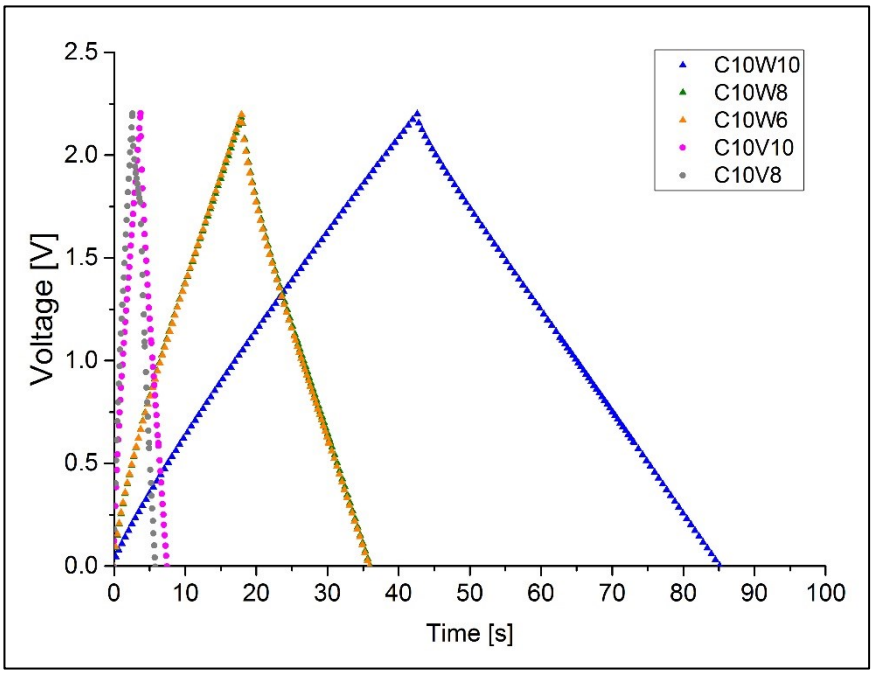

Figure 6-4: Galvanostatic charge-discharge curves at a current density of $1Ag^{-1}$ for EDLC in the organic electrolyte, 1 mol L^{-1} $TEABF_4$/PC

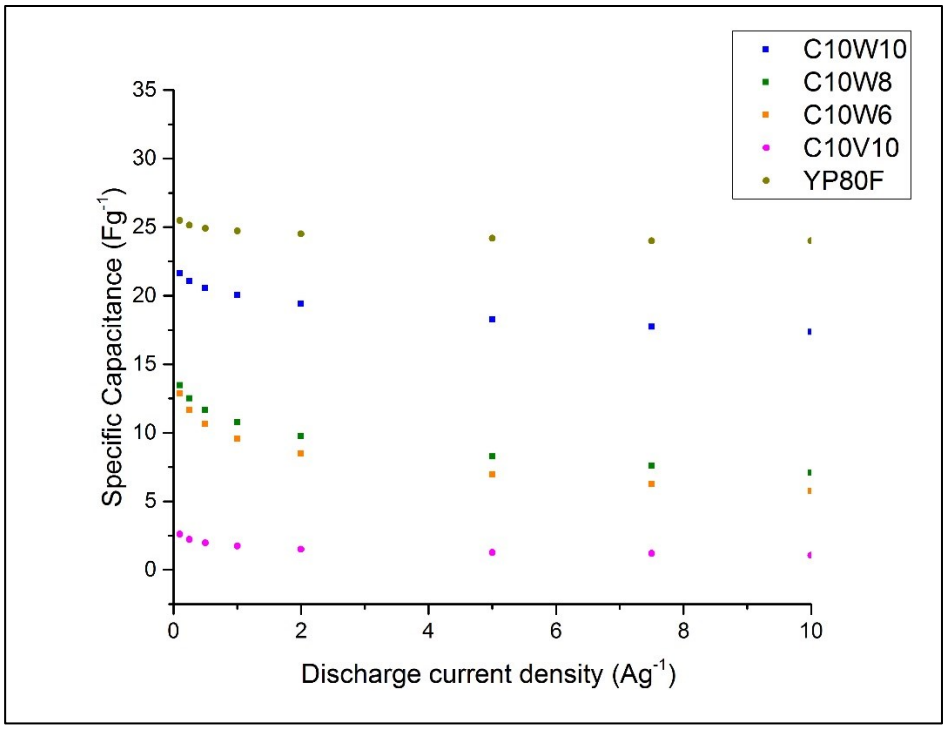

Figure 6-5: Specific capacitance of cell using AC derived from CG and YP80F respectively in organic electrolyte using various current density ($0.1\text{-}10Ag^{-1}$)

Figure 6-5 shows the relationship between the specific capacitance with current density ranged from 0.1Ag^{-1} to 10Ag^{-1}. A similar trend of cell capacitance was observed in CV (Figure 6-3) in scan rate range from 5 to 200mVs^{-1}. Although the specific capacitance of C10W10 is slightly lower than the commercial carbon, YP80F (25.5Fg^{-1}), C10W10 achieves the highest specific capacitance (21.7Fg^{-1}) among all the AC derived from CG. C10V10 shows a very low specific capacitance (below 3Fg^{-1}) as compared to any AC with higher activation temperature.

6.3 Cyclic stability

Figure 6-6 illustrates the stability of the electrode material by cycling at a constant current density of 1Ag^{-1} over 30,000cycles. All AC samples have completed 50,000 cycles. There is significant energy loss found in the commercial carbon YP80F from 25.1 Fg^{-1} to 23.18 Fg^{-1} and it remained stable at 23.2Fg^{-1} for the rest of the cyclic test. Although C10W10 achieves a lower cell capacitance (20.5Fg^{-1}) than YP80F, there is no significant energy loss even after the 10,000 cycles. There is no temperature control on the cyclic stability test. Hence, there is a slight fluctuation in the specific capacitance.

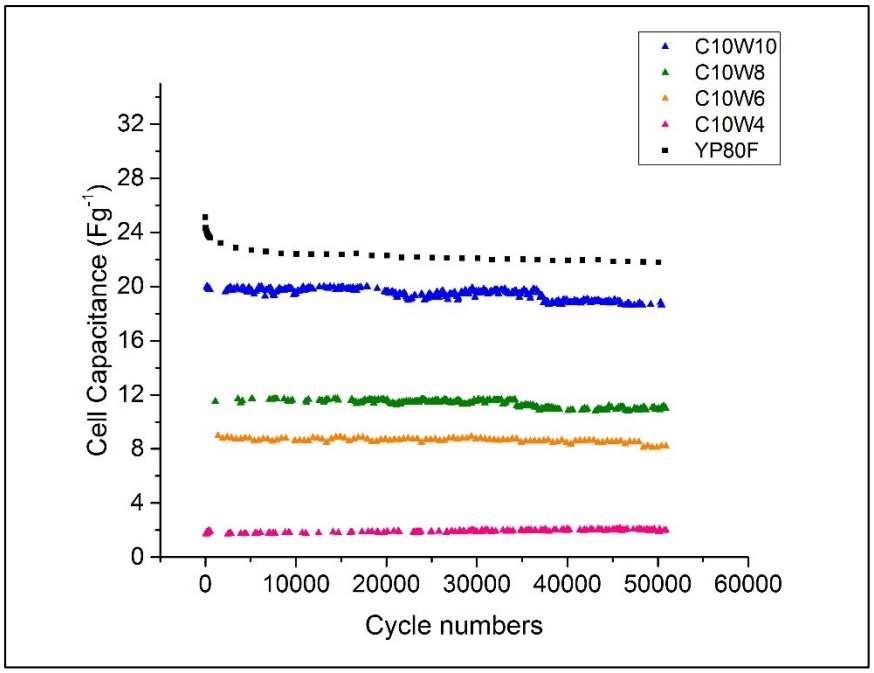

Figure 6-6: The cycling stability of EDLCs with Spent coffee ground which prepared with an activation temperature of 1000^{0}C as electrode materials in organic electrolyte at a current density of 1Ag^{-1}

6.4 Electrochemical Impedance Spectra (EIS)

By considering the electrochemical performance of each AC, C10W10 with the highest specific capacitance was selected to further study the ion transport mechanism using EIS. The Nyquist plot of C10W10 is displayed in Figure 6-7. The EIS plot shows a small flattened semi-circle at high frequency and a nearly straight line at the low-frequency region. As there is no redox reaction was observed in CV and GC, the small flattened semi-circle is attributed to some bottle-neck micropores that hinder the accessibility of ions in the electrolyte. Few papers suggested the oxygen functional groups on the carbon materials (section 4.3.1.6) could cause the blockage pore volume of micropores and thus hinder the ions access into microporous[67, 210]. The deviation from the vertical axis represents a common of inhomogeneous double layer formation due to the uniform porous structure of the carbon [138].

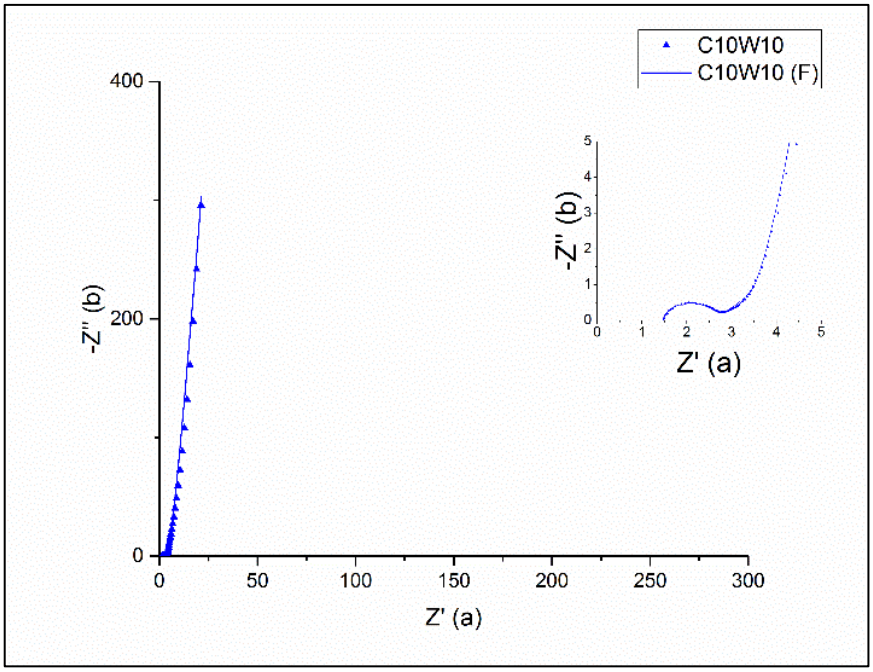

Figure 6-7: Nyquist plot of C10W10 as electrode materials in 1molL^{-1} $TEABF_4$ in PC at a current density of 1Ag^{-1}

EIS circuit model simulation was further conducted using Kang's equivalent circuit [142] to investigate the electrolyte's resistive and capacitive behaviors of EDLC. Fitting parameters of an equivalent circuit for C10W10 is listed in Table 6-1. Same electrolyte (1molL^{-1} $TEABF_4$/PC) and EDLC fabrication were applied as in section 5-2, thus the value of R1 of C10W10 (1.48 Ω) is close to the R1 of AC derived Marabú was observed for C10W10 (1.51 Ω). The CPE coefficient of bulk electrolyte (CPE1-T) is very

low (<~10^{-4}) as compared to the other two CPE coefficients. It is noticed that the value R2 (1.12Ω) is within the range as in organic electrolyte based EDLC for Marabu-AC.

R3 is the crucial factor that influences the ESR in the equivalent circuit. In this case, as compared to a lower R3 (0.3Ω) is observed for C10W10 as compared to M10V8 (0.8Ω) which suggested a lower ion resistance to access the porous of the electrode. The value of CPE2-T for C10W10 (0.95) is higher than M10V8 (0.65), and it was noticed that CPE3-T of C10W10 has the same value of CPE3-T as M10V8 (0.4). This explained the higher specific capacitance of C10W10 as compared to M10V8. In addition, this indicates that the capacitance in an EDLC is mainly attributed to CPE_2 (double layer capacitance) and adsorption capacitance (CPE_3). The capacitance of C10W10 is also calculated from EIS using Equation 3.14 at the lowest frequency (0.01Hz), which is 17.88Fg^{-1}. The value is very close to the capacitance which determined from CV at 100mVs^{-1}.

Table 6-1: Fitting parameters of the equivalent circuit for C10W10

Element	Note	Unit	C10W10
R1	Electrolyte resistance	Ω	1.48
CPE1-T	Coefficient of CPE (bulk electrolyte)		0.0004
CPE1-P	The exponential factor of CPE (bulk electrolyte)		0.88
R2	Bulk electrolyte resistance	Ω	1.12
Wo1-R	Diffusion resistance	Ω	2.15
Wo1-T	Diffusion time constant		1
Wo1-P	The exponential factor for W		0.485
CPE2-T	Coefficient of CPE (Helmholtz layer formation)		0.95
CPE2-P	The exponential factor of CPE (Helmholtz layer formation)		0.38
R3	Interfacial resistance	Ω	0.3
CPE3-T	Coefficient of CPE (ion adsorption)		0.4
CPE3-P	The exponential factor of CPE (ion adsorption)		0.98

6.5 The Ragone Plot

The Ragone plot for C10W10 which commonly represents the energy-power characteristic of electrode material in EDLC is illustrated in Figure 6.8. EDLCs with C10W10 in the organic electrolyte, 1molL^{-1} $TEABF_4$/PC stores about ~15Whkg^{-1} when operating at 400Wkg^{-1}. This value is comparable to the commercial carbon YP80F with a specific energy of 17.4Fg^{-1} at 460Wkg^{-1}and Maxwell EDLC with a potential window of 2.7V [211]. In addition, it is also noticed that the energy density of C10W10 is slightly higher than KOH activated carbon derived from CG by Kikuchi et. al. [69]. The KOH-AC with a surface area of 1852m^{2}g^{-1} and majority micropores of 1.5nm stored energy density of ~ 12 Whkg^{-1} when operating at a similar power density in 1 molL^{-1} $TEABF_4$/PC.

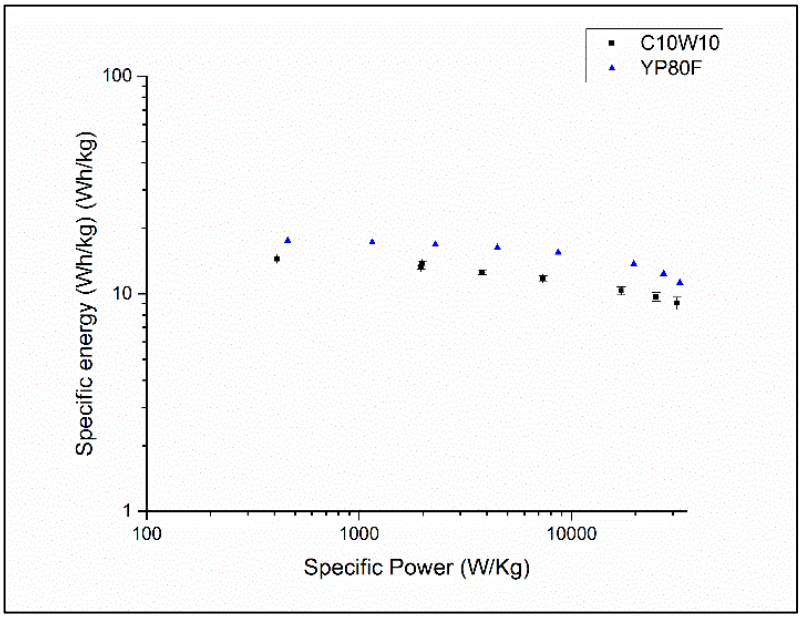

Figure 6-8: The Ragone plot of symmetric capacitors with C10W10 and YP80F as electrode materials

6.6 Summary

In this chapter, the electrochemical performance of AC derived from CG used as the electrode material in a two symmetric electrodes EDLC with organic electrolyte was presented. A better specific capacitance (8-21.8Fg^{-1}) obtained with AC which activated with a higher activation temperature of 1000°C. AC with an activation temperature of 950°C only achieves specific capacitance not more than 3Fg^{-1}. It is clear that the AC properties are greatly depending on the CO_2 activation temperature applied. In this case, the higher activation temperature of 1000°C promotes the removal of impurities (lower volatiles content) thus improving the degree of graphitization (lower I_D/I_G). This could reduce the internal resistance in EDLC, further reduce the energy loss of the cell and improve the cyclic stability. It also promotes the CO_2 to further deepen into the pores to open and broaden some of the micropores of AC, improving the surface area and create the combination of meso- and microporous. A well-balanced meso- and microporous creates a good network for ion diffuse on the surface of the electrode to create the double-layer capacitance. In addition, higher activation temperature reduces the oxygen functional groups of AC which could hinder ions access into microporous and creates resistance in EDLC. In this work, C10W10 with a surface area of 1003m^2g^{-1} exhibited the highest specific capacitance of ~22Fg^{-1}. CV and GC analysis evidence that the C10W10 provides quick reversible ion transport with no faradaic reaction in the EDLC system and good cyclic stability. EDLCs with C10W10 in the organic electrolyte of 1molL^{-1} $TEABF_4$/PC store about ~15$Whkg^{-1}$ when operating at 400Wkg^{-1}. Based on the EIS analysis, the capacitance in an EDLC is mainly attributed to CPE_2 (double layer capacitance) and adsorption capacitance (CPE_3). The results reveal the potential of AC derived from CG as suitable and promising electrode material with comparable specific capacitance and energy density in EDLC application.

7 Electrochemical Performance based on Activated Carbon derived from Malaysia agriculture by-products

By considering the rapid growth of the global market and huge demand in energy storage devices, various attempts are in progress to reduce the cost of these energy storage systems. The development in the production of activated carbon derived from abundant and sustainable biomass as an alternative electrode material has received much attention to reducing the production cost and improving the specific density. Malaysia wood pellets (MS pellets) and Palm oil empty fruit bunch pellets (EFB pellets) are commonly used as fuel combustion for the reactor in industries. However, there are no studies on the use of AC from EFB pellets or MS wood pellets for supercapacitor applications. ACs derived from EFB pellets and MS pellets were prepared under CO_2 activation time range of 40-80mins as described in chapter 3. The prepared ACs were used as the electrode material in a simple symmetrical EDLC coin cell with organic electrolyte, 1 M triethylmethylammonium-tetrafluoroborate (TEA-BF_4)/propylene carbonate (PC). The electrochemical properties of the EDLC were evaluated by cyclic voltammetry (CV), galvanostatic charge/discharge (GDC) and electrochemical impedance spectroscopy (EIS). The cycle stability of the EDLCs was tested by running over 30000 cycles at $1Ag^{-1}$.

7.1 Cyclic Voltammetry

The CV obtained at $200mVs^{-1}$ for ACs derived from EFB pellets and MS pellets are displayed in Figure 7-1. The rectangular CV curves of all the prepared ACs exhibit good electrical conductivity in the selected organic electrolyte, 1 $molL^{-1}$ $TEABF_4$/PC. At $200mVs^{-1}$, MS10V8 has the largest rectangular CV curve among all the AC samples with the highest BET surface area of ($1003m^2g^{-1}$). Although E10V8 has very high ash content (~63%), E10V8 with BET surface area of $845m^2g^{-1}$ exhibits the second largest area of CV. The specific capacitance was further calculated based on the discharge of CV with a sweep rate of $5mVs^{-1}$- $500mVs^{-1}$. It is clearly seen that the specific capacitance decreased with higher scan rates applied. At a low scan rate of $5mVs^{-1}$, MS10V8 shows the highest specific capacitance of $14.3Fg^{-1}$ and followed by E10V8 with a specific capacitance of $11Fg^{-1}$. E10V6, MS10V6, E10V4, and MS10V4 with the surface area below $800m^2g^{-1}$ show specific capacitance below $8Fg^{-1}$.

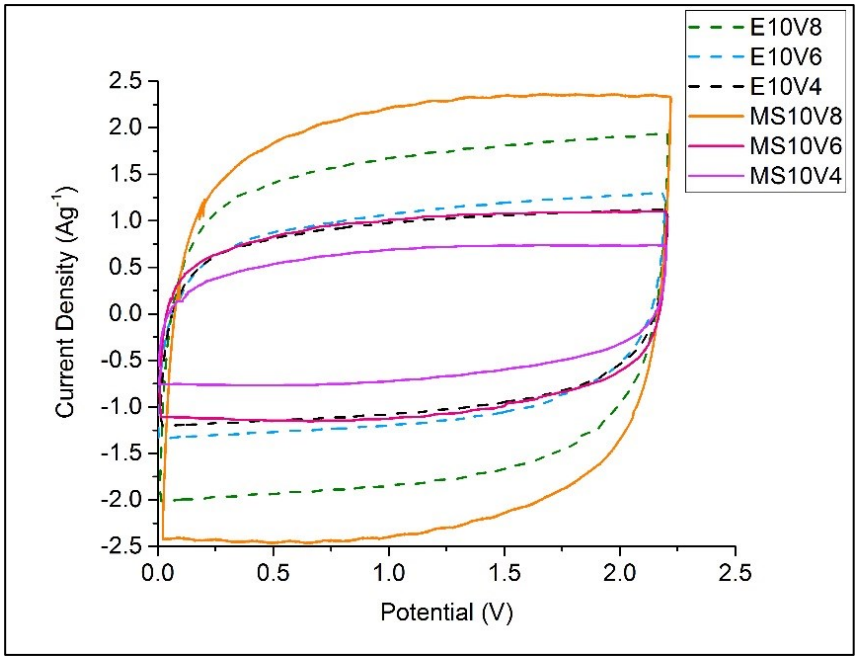

Figure 7-1: CV curves of EFB pellets and MS pellets derived ACs in an organic electrolyte, 1 mol L^{-1} $TEABF_4$/PC at a scan rate of 200mVs^{-1}.

Besides the improvement in S_{BET} from 776m^2g^{-1} to 1003m^2g^{-1}, S_{meso} of AC derived from MS pellets has improved significantly from 34.7m^2g^{-1} to 124m^2g^{-1} with the activation holding time increased from 40mins to 80mins. This has enhanced the specific capacitance from 4Fg^{-1} for MS10V4, 7Fg^{-1} for MS10V6 and up to 14.3Fg^{-1} for MS10V8. The improvement in specific capacitance suggested that activation holding time has played an important impact on the properties of AC and thus show a significant impact on the specific capacitance of EDLC. A shorter activation holding time could be insufficient to remove some of the impurities such as volatiles, disorder carbon in the carbon structure and hence hinder the material to reveal the optimum performance in EDLC. At scan rate of 500mVs^{-1} applied, the specific capacitance retains about 61.1% (8.7Fg^{-1}) for MS10V8, 58.2% (4Fg^{-1}) for MS10V6, and 64.9% (2.7Fg^{-1}) for MS10V4 (Figure 7-2).

AC samples from EFB pellets achieve specific capacitance from 4.16Fg^{-1} for E10V4, 7.8Fg^{-1} for E10V6 and up to 11Fg^{-1} for E10V8. Although E10V8 containing high ash content of 63%, the specific capacitance of E10V8 shows higher specific performance than MS10V6 and MS10V4. However, at high scan rates of 500mVs^{-1}, the significant reduction of specific capacitance for AC sample from EFB pellets is observed by only retaining about 56% (6.1Fg^{-1}) for E10V8, 54% (4.3Fg^{-1}) for E10V6, and 51.1% (3.7Fg^{-1}) for E10V4. The low retain capacitance suggested that the ash content in the ACs disturb and hinder the ionic transportation between the surface electrode and the electrolyte. Hence, additional ash removal for AC from EFB pellets is necessary to improve the performance of electrode material in EDLC applications.

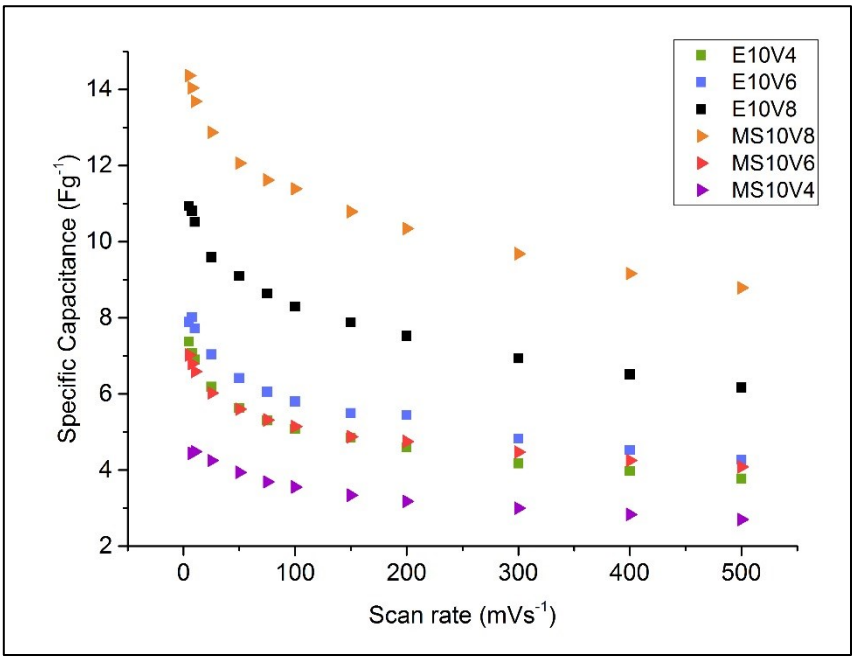

Figure 7-2: Specific capacitance of cell with sweep rate ($5mVs^{-1}$- $500mVs^{-1}$) using cyclic voltammetry

7.2 Galvanostatic charge-discharge

The GCD measurement of symmetrical EDLCs using ACs derived from MS10V8, MS10V6, E10V8, E10V6 and E10V4 at $1Ag^{-1}$ is displayed in Figure 7-3. Symmetric triangle of charge and discharge plot was observed for all the sample with a small IR drop. MS10V8 shows the smallest IR drop with only 0.0494V and E10V8 shows an IR drop of 0.0579V. MS10V6 shows an IR drop of 0.0722V. A higher IR drop was observed for AC sample from EFB pellets with shorter activation holding time, where 0.09184V for E10V6 and 0.0939V for E10V4.

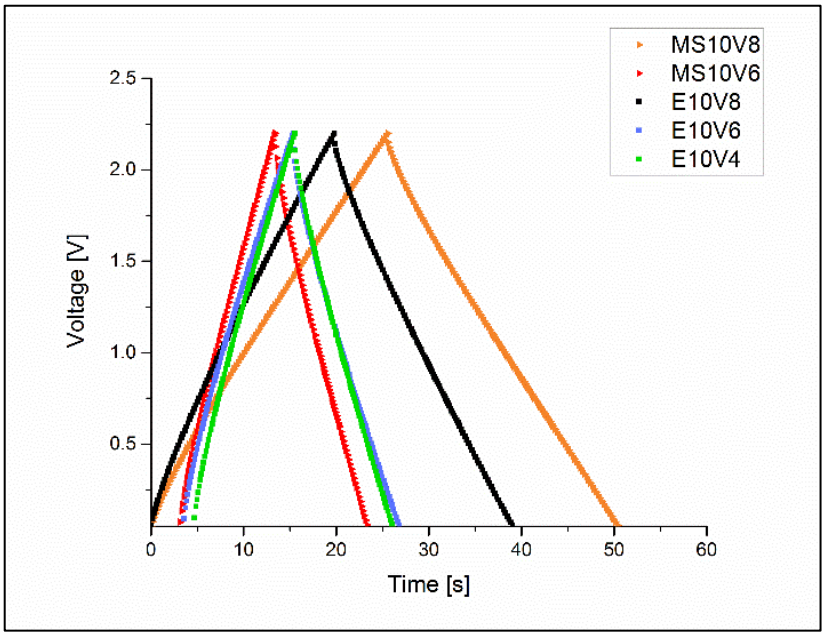

Figure 7-3: Galvanostatic charge-discharge curves of EDLC in the organic electrolyte, 1 mol L^{-1} $TEABF_4$/PC at a current density of $1Ag^{-1}$

The specific capacitance was calculated based on the slope of the GDC curve (excluded the IR drop) at the same current density of $1Ag^{-1}$. The cell capacitance value for EDLC with MS10V8 as carbon electrode obtained the highest value of $11.8Fg^{-1}$, E10V8 achieves $9.2Fg^{-1}$, $5.57\ Fg^{-1}$ for E10V6, $5.12Fg^{-1}$ for E10V4 and $4.8Fg^{-1}$ for MS10V6. The specific capacitance trend for all the samples is consistent as observed in CV as seen in Figure 7-2. Although MS10V6 shows higher specific surface area than E10V6 and E10V4, the specific capacitance of MS10V6 is much lower. This suggested that not all the surface area of MS10V6 has contributed to charge storage. MS10V6 might contain bottle-necks microporous which are smaller than the ions in the electrolyte and thus cause the difficulty for ion in the electrolyte to access those micropores. As refer to Table 4-9 that the S_{mic} and V_{mic}/V_{tot} of MS is lower than E10V4 and E10V6. The presence of microporous in an AC promotes the charge storage, while mesopores in an AC helps in transport ions to the micropores [212]. Thus, higher V_{mic}/V_{tot} of E10V6 and E10V4 encourages the energy storage in an EDLC. Although, E10V6 and E10V4 obtained a higher specific capacitance than MS10V6, the internal resistance of both AC samples is much higher. However, the IR drop value for E10V8 is relatively low although higher ash content is observed from the proximate analysis in Figure 4-23.

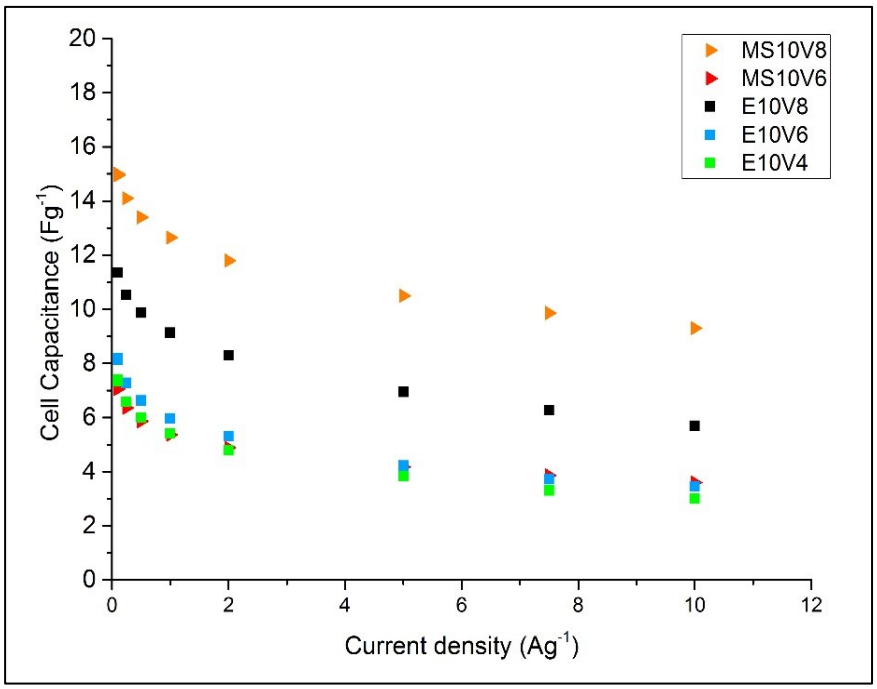

Figure 7-4: Specific capacitance of cell using AC derived from EFB pellets and MW pellets in organic electrolyte using various current density (0.1-10Ag^{-1})

Figure A-The relationship between the specific capacitance under galvanotactic cycling currents between 0.1 to 10Ag^{-1} is plotted in Figure 7-4. The specific capacitance is slightly higher than the values that measured from CV with the same sequence as seen in Figure 7-2. From the electrochemical analysis using cyclic voltammetry and galvanotactic charge-discharge presented in Figure 7-2 and Figure 7-4, there are few key differences of using EFB pellets and MS pellets as electrode materials for EDLC: (a) AC derived from MS pellets has higher specific surface area but much lower V_{mic}/V_{tot} than AC derived from EFB pellets, MS10V8 showing the highest capacitance however the capacitance of MS10V4 and MS10V6 is significantly lower than E10V6 and E10V4, (b) Lower retention of energy was observed for AC derived from EFB pellets and (c) Although E10V4 and E10V6 has higher capacitance, yet the IR drops are significantly higher were observed in the cells.

EFB pellets have a higher ash content than MS pellets (Figure 4-23-4-24) and higher burn-off was observed in the activation process (Figure 4-22), thus resulting in high levels of ash in AC production. XPS analysis shows peaks at low binding energy, which attributed to Ca and N. By considering the specific capacitance of the materials, MS10V8 and E10V8 were selected to further study in cyclic stability.

7.3 Cyclic Stability

Figure A-The impurities of EFB electrodes has a significant impact on the energy loss during the charge-discharge cycling as clearly seen in Figure 7-5. There was about 7.4% of capacitance reduction for AC MS10V8 after 5000 cycles and further reduction up to 15% capacitance drop after 30,000 cycles life testing cycle. The E10V8 shows capacitance reduction up to 16.9%, while further capacitance drops by more than 20% were observed after 30,000cycles. A similar scenario was reported by Rufford et. al. [213] where bagasse carbon with high ash content decreases more than 20% after 5000 cycles. Although some trace Ca and N also observed in MS10V8 (Figure 4-24(c)), the peaks are weak as compare to E10V8 (Figure 4-23(c)) and thus there is no much significant effect on the life cycling test of EDLC with MS10V8.

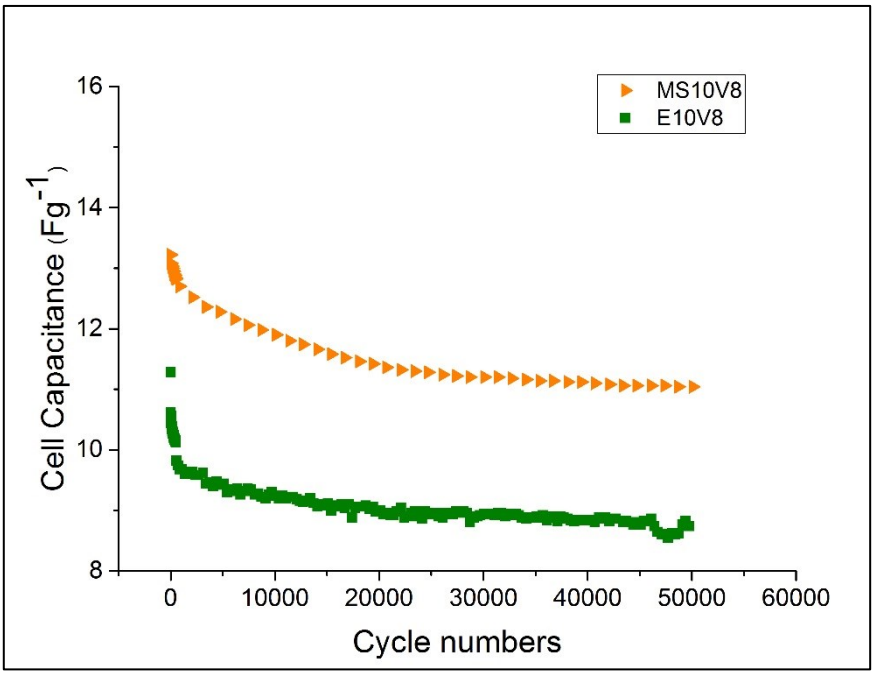

Figure 7-5: The cycling stability of EDLCs with MS10V8 and E10V8 as electrode materials in the organic electrolyte at a current density of $1Ag^{-1}$.

7.4 Electrochemical Impedance Spectra (EIS)

The EIS spectra of E10V8 and MS10V8 are illustrated in Figure 7-6. The Nyquist plot shows a flattening small semi-circle in the high-frequency region and a sloping line in the low-frequency region. As refer to Figures 7-1 and 7-2, there is no any significant Faradaic peaks observed in the CV curve and the GCD curve showing a linearity slop after any IR-drop. Thus, this can conclude that the semi-circle is not associated with any charge transfer, but it could be due to the resistance that happens with a larger

ion of the electrolyte to access small pores of AC in the electrode. The sloping line for MS10V8 is shorter and more parallel to the imaginary axis, indicating that MS10V8 is better in capacitive behavior and ion diffusion is more fluent as compared to E10V8. The EIS of the EDLCs was further analyzed with Kang's equivalent circuit model and the fitting parameters of the designed equivalent circuit are summarized in Table 7-1.

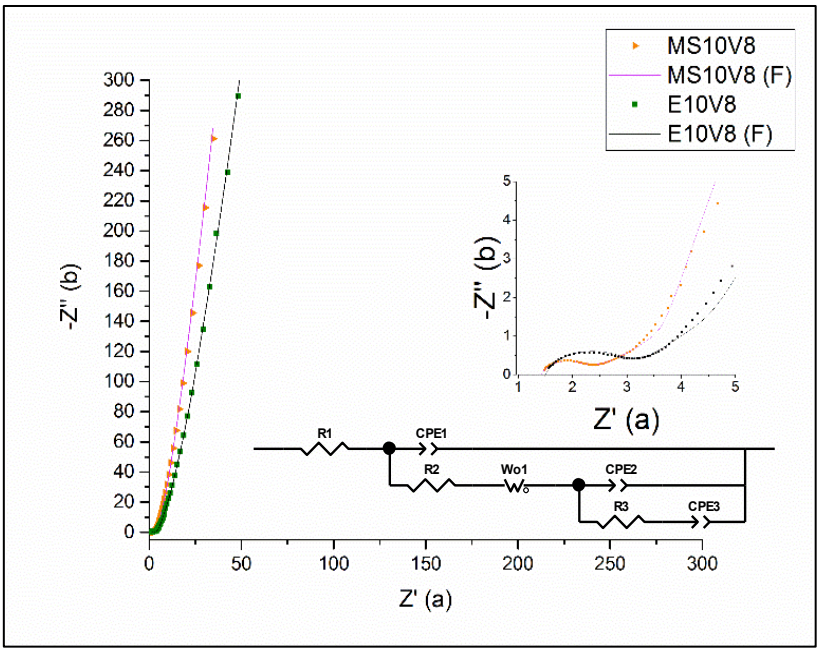

Figure 7 6: Nyquist plot of MS10V8 and E10V8 as electrode materials in 1molL^{-1} TEABF$_4$ in PC at a current density of 1Ag^{-1}

The same electrolyte was used for EDLC fabrication and hence the same value of R1 (1.5Ω) is observed. R2 of MS10V8 is lower than E10V8, which suggested that a lower resistance create the double-layer capacitance by using MS10V8 as an electrode material. The Helmholtz layer capacitance was interpreted as the double layer on the electrode surface (CPE2) and ion transportation due to the difference of the ion concentration between the bulk and the interfacial electrolyte (CPE3) [147]. MS10V8 has a higher value of CPE2 and CPE3, which explain the higher capacitance in performance. This suggesting that the of MS10V8 is contributed by the ion adsorption capacitance and ion diffusion (double layer capacitance). Helmholtz layer capacitance of E10V8 is attributed mainly to the ion diffusion as the value of CPE2 is much lower.

Table 7-1: Fitting parameters for equivalent circuit for E10V8 and MS10V8

Element	Note	Unit	E10V8	MS10V8
R1	Electrolyte resistance	Ω	1.5	1.5
CPE1-T	Coefficient of CPE (bulk electrolyte)		0.00078	0.0005
CPE1-P	The exponential factor of CPE (bulk electrolyte)		0.8	0.85
R2	Bulk electrolyte resistance	Ω	1.1	0.77
Wo1-R	Diffusion resistance	Ω	3	3
Wo1-T	Diffusion time constant		0.8	1.5
Wo1-P	Exponential factor for W		0.468	0.478
CPE2-T	Coefficient of CPE (Helmholtz layer formation)		0.05	0.4
CPE2-P	The exponential factor of CPE (Helmholtz layer formation)		0.01	0.38
R3	Interfacial resistance	Ω	0.5	0.9
CPE3-T	Coefficient of CPE (ion adsorption)		0.35	0.4
CPE3-P	The exponential factor of CPE (ion adsorption)		0.6	0.98

7.5 The Ragone plot

The Ragone plot of ACs derived from MS pellets and EFB pellets as the electrode material for EDLC is displayed in Figure 7-7. EDLC using the commercial carbon, YP80F exhibited the maximum of average energy density, 17.5Whkg^{-1}. While MS10V8 and E10V8 achieved the maximum value if average energy density, 8.2Whkg$^{-1,}$ and 6.8Whkg^{-1}, respectively. Although the two prepared biomass-derived ACs delivered lower density than the commercial carbon, YP80F, the present work is comparable with the performance of EDLC using KOH- AC derived from lotus delivered the energy density range of 10-14Whkg^{-1} in an aqueous electrolyte[40]. The energy densities of the present work are within the range of organic EDLCs in the Ragone plot of Gu & Gleb [61]. This reveals the potential of MS pellets and EFB pellets as electrode material for energy storage to overcome the energy demands in the future.

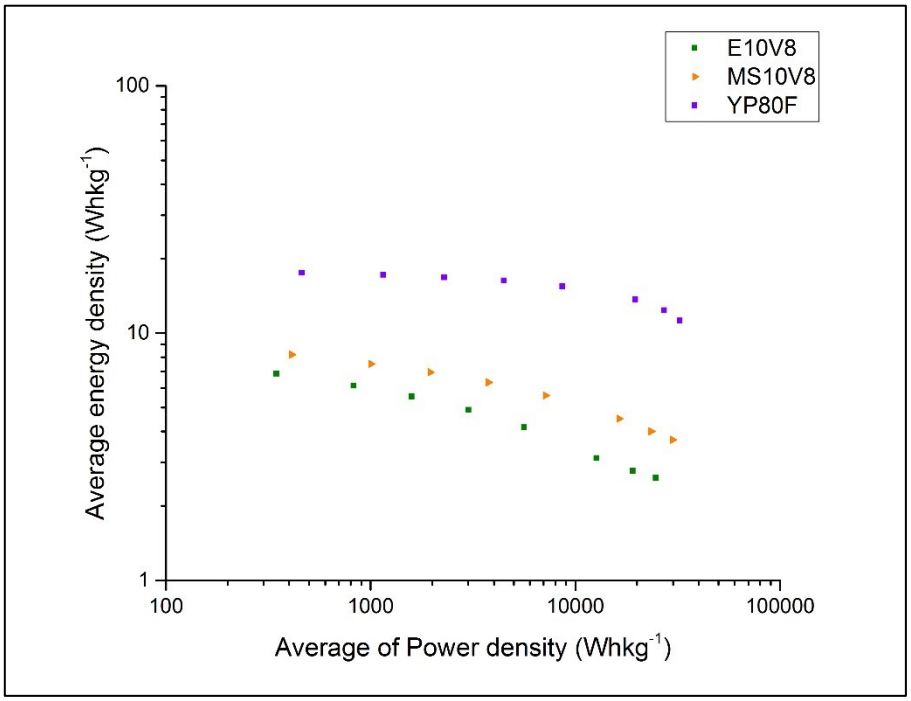

Figure 7-7: The Ragone plot of MS10V8, E10V8, and YP80F as electrode materials in 1molL^{-1} TEABF$_4$/ PC

7.6 Summary

The EDLC behavior of using AC derived from MS pellets and EFB pellets was successfully demonstrated and studied. ACs was prepared under carbonization heating rate of $10^{\circ}Cmin^{-1}$ and CO_2 activation temperature of $950^{\circ}C$ with a range of activation holding time from 40-80mins. Activation holding time of 80mins creates ACs with the highest specific surface area of $845m^2g^{-1}$ and $1003m^2g^{-1}$ for EFB pellets and MS pellets, respectively. Although the same activation condition was applied to produce ACs from MS pellets and EFB pellets, porosities, and surface area of ACs highly depends on the selection of biomass as the activated carbon precursors. Symmetric triangle of charge and discharge and the typical rectangular CV curve indicates AC derived from EFB pellets and MS pellets showing the EDLC behavior without redox reactions. Among all the AC samples, MS10V8 with the highest specific surface area of $1003m^2g^{-1}$ showing the highest specific capacitance of $13.2Fg^{-1}$ at a current density of $1Ag^{-1}$. Despite that E10V8 has high impurities, the high specific surface area and high V_{mic}/V_{tot} (>0.9) promotes the specific capacitance up to $11.3Fg^{-1}$ at a current density of $1\ Ag^{-1}$. However, the impurities accelerate energy loss during the charge-discharge cycle was observed thus this creates the aging problem to the EDLC system. Higher specific capacitance was observed with electrode materials of E10V4 and E10V6 as compared to MS10V6 and MS10V4 with the slightly higher specific surface area, suggesting high V_{mic}/V_{tot} greatly contribute to the capacitance. Demineralization or carbon rinsing to remove the impurities in the AC is recommended for AC derived from MS pellets and E10V8 to further optimize the energy storage of E10V8 and to achieve a stable performance.

8 Overall Discussion

In this work, the study has been focused on the AC derived from wastes biomass as carbon electrode materials for EDLC applications. AC derived from five different wastes biomass (Marabú, oil palm empty fruit bunch pellets (EFB), Malaysia wood pellets (MS), spent coffee ground (CG) and rubberwood) were prepared using carbonization and CO_2 activation method.

First, thermal analysis was carried out to determine the carbon and ash content of all the wastes biomass. The fixed carbon content of MS, EFB, Marabú, and RW agree well within the range from 14-18% in most of the wood samples[155]. While CG contains about 16.25% of fixed carbon. From the graph of the Derivative Thermogravimetric (DTG) analysis (Figure 4-3), there is a reduced peak for each wastes biomass appears at the temperature range of 350-410°C. However, there are few small reduced peaks were observed from the DTG curves at the temperature range of 450-920°C (Section 4.1.3), which indicates that a higher temperature is needed to ensure carbon from the wastes biomass is free from any impurities. Therefore, the temperature of 950°C was selected to treat all the wastes biomass during the carbonization process.

The effect of carbonization heating rates (5°min^{-1}, 10°min^{-1}, and 15°min^{-1}) and the activation holding times (40-100°C) on the properties of AC was studied using Marabú as a precursor. CG was employed to produce AC under the effect of CO_2 activation temperatures (950^{0}C and 1000^{0}C). The suitability of AC derived from EFB pellets, MS pellets and rubberwood, which categorized as Malaysia agriculture wastes biomass, were explored under a fixed carbonization heating rate of 10°Cmin^{-1} at carbonization and activation temperature of 950°C. All the ACs were applied as carbon electrodes for EDLCs in the symmetric two-electrode configuration. The electrochemical performance of ACs was studied in 1 M $TEABF_4$ in PC electrolyte. The performance of Marabú wood as electrode materials was further investigated in ionic liquid $EMIMBF_4$.

High fixed carbon, low ash content and high surface area are some of the key factors for AC to work as good electrode material in EDLC. Among all the AC derived from Marabú, M10V8 achieved the highest specific surface area (1977m^2g^{-1}) with the combination of the meso-and microporous surface of AC. The ACs under carbonization rate of 10^{0}Cmin^{-1} has a higher specific surface area in between 1031-1977m^2g^{-1}. A lower surface area was observed for ACs treated at 5°min^{-1} and 15°min^{-1}. The specific surface area of ACs with mostly microporous is between 917-1065 m^2g^{-1} and 917-932 m^2g^{-1} for carbonization heating rate of 5°min^{-1} and 10°min^{-1}, respectively. According to Marcilla et. al[214], carbon/ chars treated at high carbonization heating rate showed a higher gasification reactivity and

produce AC with a higher surface area. The same observation was reported in the work of eucalyptus carbonization as fuel [84]. However, in this work carbonization heating rate of 15^0Cmin^{-1} could be too fast and insufficient time for the reaction to create the fundamental carbon structure and remove all the volatiles from the carbon structure. Whereas, lower carbonization heating rate at 5^0Cmin^{-1} shows lower reactivity and longer duration time to complete the carbonization process (Figure 4-4). Therefore, the carbonized sample with lower VC and higher FC is obtained with a heating rate at 5^0Cmin^{-1} and 10^0Cmin^{-1}.

As referring to the double-layer capacitance Equation 8.1, AC with higher specific surface areas is expected to deliver a higher specific capacitance.

$$C = \frac{\varepsilon_r \varepsilon_0 A}{d_{dl}} \qquad \textbf{Equation 8-1}$$

where ε_r is the relative permittivity, ε_0 is the permittivity of vacuum, A is the surface area of the electrode and d_{dl} is the distance between the two electrodes. Among all the Marabú derived ACs, M10V8 contains the highest specific surface area (1977m^{2}g^{-1}) and high mesoporous (158m^{2}g^{-1}). EDLC with M10V8 as electrode material is expected to exhibit the highest specific capacitance of ~20Fg^{-1} at a current density of 1Ag^{-1}. Mesoporous in AC is playing an important role in promotes fast ion transportation and assist the electrolyte ions to diffuse and accumulate on the micropores electrode surface[215]. M5V8 has a slightly higher specific surface area of 1065m^{2}g^{-1} with double amount mesoporous surface area than M15V8 (932m^{2}g^{-1}) delivered specific capacitance of 13.3Fg^{-1}. Whereas, M15V8 could achieve only 7Fg^{-1}.

Among three carbonization heating rates, ACs treated under carbonization heating rate of $10^{\mathbf{o}}$min^{-1} delivered the highest specific capacitance range in EDLC using organic electrolyte of 1M $TEABF_4$/PC. Although the commercial carbon YP80F shows a higher (25.9 Fg^{-1}) specific capacitance, ACs derived from Marabú increases from 10Fg^{-1} (M10V4) to 20Fg^{-1} (M10V8) with activation holding time from 40-80mins. This could be attributed to the increase of specific surface area and high in mesopores in ACs when a longer activation holding time applied. In addition, both EDLCs with ACs derived from Marabú show great cyclic stability over 30,000 cycles at a current density of 1Ag^{-1}. A smaller IR drop was observed in M10V8 as compared to M10V4 and M10V6, this could be due to the improvement in the interaction between the electrolyte ions, the porous network and thus increase charge storage on the carbon electrode. The maximum energy and power density of 12 Whkg^{-1} and 385Wkg^{-1} were obtained for M10V8 in the organic electrolyte system.

Although C10W10 has a much lower specific surface area (1473m^2g^{-1}) than M10V8 (1977m^2g^{-1}), C10W10 achieves the highest specific capacitance of ~22Fg^{-1} at a current density of 1Ag^{-1} among all the wastes biomass-derived AC in 1 M $TEABF_4$ in PC. C10W10 delivers a high energy density of ~15$Whkg^{-1}$ when operating at 400Wkg^{-1}. This value is comparable to the commercial carbon YP80F with a specific energy of 17.4Fg^{-1} at 460Wkg^{-1}. This indicates the specific surface area of AC is not only the factor that affects the electrochemical performance of an EDLC. C10W10 was found in higher fixed carbon content (88.08%) with lower ash (6.18%) and volatile content (5.75%). Whereas, M10V8 has a lower fixed carbon content of 72%, higher ash content of 8%, and 16% of volatile matter. M10V8 has higher impurities than C10W10, could be the reason restricted the optimum performance of M10V8. In the literature, current leakage and the unstable in the cycling stability test were reported with AC in higher impurities [35]. Besides, a higher ESR is observed for M10V8 with higher impurities using Kang's equivalent circuit model.

On the other hand, C10V10 which activated at a temperature of 950^{0}C with the specific surface area (1082m^2g^{-1}) could only achieve specific capacitance not more than 3Fg^{-1}. Although C10V10 has a specific surface area that similar to M5V8 (1065 m^2g^{-1}), the specific capacitance of C10V10 is much lower than M5V8. Macro and mesopores served as ions buffering reservoir and allow ions to diffuse fast to the surface of the electrode[216, 217]. By comparing the porosity of both AC samples, the lower specific capacitance of C10V10 can be explained with the much lower mesoporous surface area (9.3 m^2g^{-1}) of C10V10 than M5V8 (44.8 m^2g^{-1}), thus limited the ion transportation and charges accumulate on the electrode surface. Besides, the micropore in C10V10 could be mostly in narrow pore neck (ink-bottle pore), which inaccessible for solvated ions[218]. This is agreed well with the high IR drop of C10V10 (0.1696V) as compared to C10W10 (0.0177V). This suggested that the activation temperature of 950^{0}C is insufficient to open the pore structure of C10V10.

Three selected Malaysia agriculture by-products: MS, EFB Pellets and RW were carbonized with a heating rate of 10^{0}Cmin^{-1} at 950^{o}C and further CO_2 activated at 950^{0}C with activation holding time from 40-80mins. The high thermal sensitivity of RW has restricted the possibility of rubberwood as a stable electrode material for EDLC applications. For EFB, the specific surface area of ACs in range of 789- 845m^2g^{-1} was achieved with high ash content (26-63.9%). Little is known about the influence of impurities on the performance of EDLC. Thus, electrochemical performance was further carried out. Although high ash content was found in AC derived from EFB pellets as increasing the activation holding time, an ideal EDLC behavior was shown in a CV without any redox reaction. However, the impurities accelerate the energy loss during the charge-discharge cycle and the life cycle test was observed. The cycling stability of an EDLC is also greatly affected by the impurities in the electrode materials. This is well agreed as the work reported by Zhou et.al. [35] that impurities accelerated the current leakage and cause an unstable condition during cycling stability test. In addition, a high IR drop

(0.0579V) was obtained in GC and a high ESR for E10V8 was determined in Kang's equivalent circuit model. AC derived from MSW exhibited the specific surface area in the range of 776- 1003m^2g^{-1} with a mixture of meso- and micropores. Among all the AC derived from the selected Malaysia agriculture by-products, MS10V8 with the highest specific surface area of 1003m^2g^{-1} showing the highest specific capacitance of 11.8Fg^{-1} at a current density of 1Ag^{-1}. The specific capacitance of MS10V8 is much higher than C10V10 which has similar specific surface area due to the high mesopore surface area (124m^2g^{-1}). A large IR drop was found in C10V10 (0.1696V) as compared to the MS10V8 (0.05V). This was confirmed by a higher value of ESR in C10V10 than MS10V8.

A carbon with a higher degree of graphitization accelerate the ion diffusion[219], thus the degree of graphitization of AC is also one of the factors that influence the specific capacitance[220]. In this work, there are two overlapping intense Raman peaks which locate at ~1345cm^{-1} (D-band) and ~1600 cm^{-1} (G-band) were observed in Raman spectra of all the AC samples. ID/IG is commonly applied to characterize the defectiveness of carbon samples [171]. Raman analysis was commonly applied to the overlapping bands, the peaks deconvolution allowed to clearly describe all peaks with an excellent good fit[164]. The Raman spectra were deconvoluted to five bands using Voigt function (convolution of Gaussian & Laurentzian lineshapes). There are only 4 bands observed for YP80F. The D1 band (~1350cm^{-1}) is commonly attributed to the number of defect sites, the increase ratio of D1/G elucidates the number of edge carbon atoms bonded to functional groups[171]. The lower ratio of D1/G of AC derived Marabú was observed when the longer holding time applied, represents the lower oxygen functional groups in the AC. This is well agreed with the reduction of the O composition in the XPS analysis. In contrary to the observation for AC derived from Marabú, the ID1/IG grows when the longer activation holding time applied for AC derived from EFB and MS, there are oxygen functional groups present was observed in XPS analysis. However, there is no significant correlation with the activation holding time at this time. On the other hand, the ratio of ID1/IG for C10W10 is lower than C10V10 and this is verified by the XPS analysis with lower O composition in the elemental composition. However, a higher defect for C10W10 was suggested based on the interpretation of the Raman spectrum. This agreed well with Xia et al [187] that suggesting the higher activation temperature introduce more defects to the graphene plane.

To increase the energy density of an EDLC, the performance of AC derived from Marabú wood as electrode materials in a symmetric two-electrode cell was further investigated in the ionic liquid $EMIMBF_4$ with wider ESW. A narrower potential range was observed using PVDF as a binder for a carbon electrode in the EDLC. Thus, PTFE was employed to prepare a carbon electrode for the $EMIMBF_4$ system. Initially, the symmetrical two-electrode cell achieved a higher value of specific capacitance of 32Fg^{-1} in $EMIMBF_4$ at a current density of 1Ag^{-1}. This can be explained by the smaller diameter of desolvated ions $EMIM^+$ (0.6nm) and $BF4^-$ (0.46nm) in IL and thus promotes the diffusion

of the ions on the electrode surface. However, significant degradation of specific capacitance was observed in the CV and the cycle stability test. This could be due to the larger diameter of solvated ions in electrolyte hinders the contact of electrolyte ions to the pores of the electrode and the high viscosity of IL [206] causes the low mobility of ion $EMIM^+$ and $BF4^-$.This was supported by the high internal resistance & higher IR drop in $EMIMBF_4$ as compared to 1 M $TEABF_4$ in PC. Besides, the pore size distribution of Marabú could be too narrow for those solvated ions $EMIM^+$ and $BF4^-$ which could be bigger in diameter than the desolvated ions TEA^+ (0.68nm), $BF4^-$ (0.46nm) and PC (0.55nm) in organic electrolyte.

The data energy performance of available commercial supercapacitors [18] and the present work was marked in the Ragone plot by Gu and Gleb[61] as shown in Figure 8-1. Most of the ACs in the present work show comparable performance as those available commercial EDLCs, C10W10 and M10V8 even show much higher performance than those available commercial EDLC. This indicated there is a potential for ACs in energy storage performance using ACs derived from wastes biomass in the present work.

In summary, this research has proven the potential of physical activation to prepare high surface area AC derived from wastes biomass. The properties of ACs are greatly affected by carbonization heating rates, activation temperature and holding time. This research work has helped to understand the effect of properties of AC derived from biomass on the electrochemical behavior of EDLC.

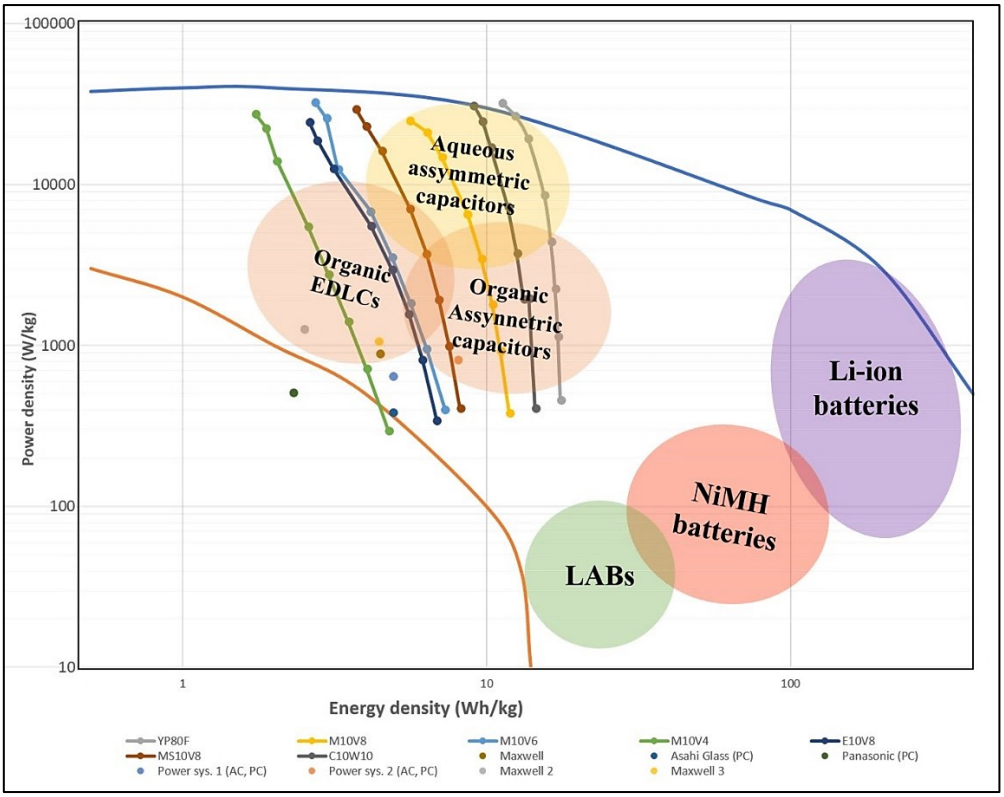

Figure 8-1: The comparison in energy and power density of the commercial supercapacitors and the EDLC using ACs in the present work in the Ragone plot by Gu and Gleb [61]**.**

9 Conclusion, Key Contributions and Recommendations

This study has been concentrated on the suitability of activated carbon which generated from a series of selected wastes biomass as carbon electrode materials for EDLC applications. AC derived from five different wastes biomass (Marabú weed, oil palm empty fruit bunch pellets (EFB), Malaysia wood pellets (MS), spent coffee ground (CG) and rubberwood) were prepared using CO_2 activation method. The novel Marabú wood source was explored to produce AC under the impact of the carbonization heating rates and the activation holding times. Based on the specific surface area and porosity of the samples, the selected carbonization heating rate of $10^0 Cmin^{-1}$ was applied to treat the rest of the waste biomass during the carbonization process. CG was employed to produce AC under the effect of CO_2 activation temperatures (950^0C and 1000^0C). Three different types of Malaysia agriculture by-products (EFB pellets, MS pellets, and rubberwood) were explored to prepare ACs at a fixed carbonization heating rate of $10^o Cmin^{-1}$ with the carbonization and activation temperature of 950^oC. All the ACs were applied as carbon electrodes for EDLCs in a symmetric two-electrode configuration. The electrochemical performance of all the ACs samples was studied in 1 M $TEABF_4$ in PC. The performance of ACs derived from Marabú wood as electrode materials were further investigated in ionic liquid $EMIMBF_4$. Through this study, the following conclusions can be drawn:

1) High surface area ACs derived from biomass precursor can be produced using CO_2 activation technique. The high surface area is comparable as prepared using chemical activation technique. There are many factors that influence the properties of AC derived from wastes biomass. A suitable carbonization heating rate promotes the gasification reactivity to prepare the fundamental carbon structure without generating much ash in the samples. M10V8 which generated at carbonization heating rates of $10^0 Cmin^{-1}$ with 80mins of activation holding time achieved the highest specific surface area ($1977 m^2 g^{-1}$) with the combination of meso- and microporous. Among all the AC derived from Marabú, M10V8 delivered the highest specific capacitance of ~$20 Fg^{-1}$ at a current density of $1 Ag^{-1}$ in 1 M $TEABF_4$ in PC.

2) The ESW of IL, $EMIMBF_4$ was evaluated with two different binders, PVDF and PTFE in carbon electrode. The EDLC using PVDF as binder exhibits a lower potential range. Thus, PTFE was utilized to prepare a carbon electrode for the IL. A higher value of specific capacitance of $32 Fg^{-1}$ was delivered using M10V8 in $EMIMBF_4$ at a current density of $1 Ag^{-1}$. However, there is a significant degradation of specific capacitance observed in a CV and in the cycle stability test

due to the high viscosity of IL and thus cause low mobility of ion $EMIM^+$ and $BF4^-$. This was supported by the high internal resistance using the Kang's equivalent model circuit and higher IR drop as compared with the organic electrolyte system. Besides, the pore size distribution of Marabú could be too narrow for the solvated ions $EMIM^+$ and $BF4^-$ and thus hinder the ion diffusion on the carbon electrode surface.

3) Although C10W10 has a lower specific surface area than M10V8, C10W10 exhibited the highest specific capacitance (~22Fg^{-1}) among all the AC derived from wastes biomass. Whereas, C10V10 only achieved a specific capacitance not more than 3Fg^{-1}. This suggested that the activation temperature of 950°C is not sufficient to open the up the pore structure of AC, thus some of the micropores could be narrow pore neck and thus inaccessible for ions to diffuse on the surface electrode. In addition, this also indicated that the specific surface area is not the only factor that influences the electrochemical performance of an EDLC. A higher volatile and ash content was detected M10V8 as compared to C10W10, this could be the factor that limited the optimum performance of M10V8.

4) Although AC derived from MS and EFB contain in high ash content, an ideal EDLC CV curve without any Faradaic reaction was observed. However, the impurities in the AC samples accelerate energy loss and disturbed the cycling stability of the cell. On the other hand, the high thermal sensitivity has restricted the possibility of RW as a stable electrode material for EDLC applications.

5) Raman analysis and XPS analysis of the AC samples were conducted to understand the correlation of the oxygen functional groups and carbon structure to the electrochemical performance. The ratio of ID1/IG grow with a higher activation temperature and the oxygen functional groups reduced on the surface AC derived from CG, which resulted in a better electrochemical performance. On the other hand, the ID1/IG drop with longer activation holding time and the oxygen functional groups reduced for AC derived from Marabú. However, there is no significant correlation for AC derived from EFB and MS pellets. Hence, more studies are needed to further understand the relationship of the carbon structure and the oxygen functional group to the electrochemical performance of an EDLC.

6) Although the overall performance of waste biomass in this work shows a lower specific capacitance as compared to the commercial YP80F with a higher specific surface area and a high ratio of meso-micropores. Despite that, M10V8 and C10W10 show comparable performance as

those available commercial EDLCs [18]. C10W10 delivers a high energy density of ~15Whkg^{-1} when operating at 400Wkg^{-1}. This value is comparable to the commercial carbon YP80F with a specific energy of 17.4Fg^{-1} at 460Wkg^{-1} in an organic electrolyte.

In this work, it has proven that the potential of physical activation to prepare a high specific surface area AC derived from wastes biomass. The properties of ACs are greatly affected by carbonization heating rates, CO_2 activation temperature and the CO_2 activation holding time. This research work has helped to understand the effect of properties of AC derived from biomass on the electrochemical behavior of an EDLC.

9.1 Recommendations

Based on the present work, there are few recommendations to improve the electrochemical performance of an EDLC:

1) Based on the literature review, the viscosity of IL, [EMIM][BF4] could be reduced at a higher temperature and thus this could improve the mobility of ions diffusion. In this work, the performance of the EDLC in IL is much higher than in an organic electrolyte at the beginning of the cyclic stability test, a great degradation was observed due to the high viscosity and poor mobility of the IL. Thus, the effect of operating temperature (above room temperature) on the performance of an EDLC with M10V8 in IL is recommended to improve the mobility of ions diffusion and also to determine the best temperature to achieve optimum performance.

2) Utilizing different types of electrolytes to study the electrochemical performance with AC derived from CG as electrode carbon material. This could provide a clear understanding of the correlation of the porosity of AC and the electrolyte ions size to the performance of an EDLC.

3) Selection of polymer binders in the electrode fabrication affects the ESW electrolyte. Thus, exploration of the different polymer binders in the carbon electrode to the ESW of an electrolyte is recommended. This is ensuring the EDLC is operating in an optimum ESW and thus improve the energy density and the specific capacitance of the cell. This step is also highly recommended to apply to the novel electrolyte for optimum electrochemical performance.

4) Based on the DTG curve, a lower carbonization temperature range of 600- 900°C is recommended for EFB to produce AC to reduce the ash content of the samples. The fixed carbonization temperature of 950°C could be too high for the low-density EFB and thus lead to

a high ash content in the samples. The volatile content of the carbonized samples is needed to be monitored to ensure all the impurities reduced.

5) Hybrid physical activation by combining CO_2 and steam activation could be another research aspect to produce a high surface area AC in a lower activation temperature. This could save some energy and production cost and at the same time enlarge the pore size of the AC. The reactivity, the carbonization, and the activation temperature could be determined in the TGA using the combination of CO2 and steam. Exploration of the potential of other wastes biomass to produce porous AC using physical activation as electrode materials in EDLC.

6) Although there is no redox reaction was observed in the CV with high ash content AC derived EFB as an electrode material, further understanding the effect of the ash content and the volatile matter on the electrochemical performance in a different type of electrolytes is recommended.

References

1. BP p.l.c., *BP's Energy Outlook 2017 eddition*. 2017.
2. World Energy Council, *World Energy Scenarios: Composing energy futures to 2050*. 2013: England.
3. DECC, *Digest of United Kingdom Energy Statistics 2016*. 2016.
4. Eurostat, *Renewable statistics*. 2018.
5. EREC, *Renewable Energy Target by Europe by 2020*. 2013, European Renewable Energy Council.
6. Conway, B.E., *Electrochemical Supercapacitors: Scientific Fundamentals and Technological Applications*. 1999: Springer US.
7. Gonzalez, F., *Electrochemical Double Layer Capacitors: Supercapacitors 2014-2024* 2014.
8. Yu, G., et al., *Hybrid nanostructured materials for high-performance electrochemical capacitors.* Nano Energy, 2013. **2**(2): p. 213-234.
9. Holmberg, S., et al., *3-D Micro and Nano Technologies for Improvements in Electrochemical Power Devices.* Micromachines, 2014. **5**(2): p. 171.
10. Wang, X., et al., *Enhancing capacitance of supercapacitor with both organic electrolyte and ionic liquid electrolyte on a biomass-derived carbon.* RSC Advances, 2017. **7**(38): p. 23859-23865.
11. Yu, A., V. Chabot, and J. Zhang, *Electrochemical Supercapacitors for Energy Storage and Delivery: Fundamentals and Applications*. 2017: CRC Press.
12. Zhang, L.L. and X.S. Zhao, *Carbon-based materials as supercapacitor electrodes.* Chemical Society Reviews, 2009. **38**(9): p. 2520-2531.
13. Dubal, D.P., et al., *Hybrid energy storage: the merging of battery and supercapacitor chemistries.* Chemical Society Reviews, 2015. **44**(7): p. 1777-1790.
14. Abioye, A.M. and F.N. Ani, *Recent development in the production of activated carbon electrodes from agricultural waste biomass for supercapacitors: A review.* Renewable and Sustainable Energy Reviews, 2015. **52**: p. 1282-1293.
15. Jin, Y., et al., *Hierarchical porous microspheres of activated carbon with a high surface area from spores for electrochemical double-layer capacitors.* Journal of Materials Chemistry A, 2016. **4**(41): p. 15968-15979.
16. Zhang, T., et al., *Preparation of activated carbon from forest and agricultural residues through CO2 activation.* Chemical Engineering Journal, 2004. **105**(1–2): p. 53-59.
17. Weinstein, L. and R. Dash, *Supercapacitor carbons.* Materials Today, 2013. **16**(10): p. 356-357.
18. Burke, A., *R&D considerations for the performance and application of electrochemical capacitors.* Electrochimica Acta, 2007. **53**(3): p. 1083-1091.
19. Jäckel, N., et al., *Comparison of carbon onions and carbon blacks as conductive additives for carbon supercapacitors in organic electrolytes.* Journal of Power Sources, 2014. **272**: p. 1122-1133.
20. Beguin, F. and E. Frackowiak, *Carbons for Electrochemical Energy Storage and Conversion Systems*. 2009: CRC Press.
21. Stoller, M.D. and R.S. Ruoff, *Best practice methods for determining an electrode material's performance for ultracapacitors.* Energy & Environmental Science, 2010. **3**(9): p. 1294-1301.
22. Jong H., K., et al., *The effect of Nickel Foam current collector in carbo electrode baed electric double layer capacitor.* Electrochemistry - Tokyo, 2001. **69**(11): p. 5.
23. Gu, W. and G. Yushin, *Review of nanostructured carbon materials for electrochemical capacitor applications: advantages and limitations of activated carbon, carbide-derived carbon, zeolite-templated carbon, carbon aerogels, carbon nanotubes, onion-like carbon, and graphene.* Wiley Interdisciplinary Reviews: Energy and Environment, 2014. **3**(5): p. 424-473.
24. Saito, M., et al., *Strategies for fast ion transport in electrochemical capacitor electrolytes from diffusion coefficients, ionic conductivity, viscosity, density and interaction energies based on HSAB theory.* RSC Advances, 2017. **7**(24): p. 14528-14535.

25. Jäckel, N., et al., *Increase in Capacitance by Subnanometer Pores in Carbon.* ACS Energy Letters, 2016. **1**(6): p. 1262-1265.
26. Kashkooli, A.G., et al., *Effects of structural design on the performance of electrical double layer capacitors.* Applied Energy, 2015. **138**: p. 631-639.
27. Zhang, Y., et al., *Progress of electrochemical capacitor electrode materials: A review.* International Journal of Hydrogen Energy, 2009. **34**(11): p. 4889-4899.
28. Rennie, A., et al., *Nitrogen-enriched Carbon Materials for High-power Electrochemical Capacitors*. 2011: University of Strathclyde.
29. Smith, T.J. and K.J. Stevenson, *4 - Reference Electrodes A2 - Zoski, Cynthia G*, in *Handbook of Electrochemistry*. 2007, Elsevier: Amsterdam. p. 73-110.
30. Zhang, S. and N. Pan, *Supercapacitors performance evaluation.* Advanced Energy Materials, 2015. **5**(6).
31. Martins, V.L., et al., *Ionic liquids containing tricyanomethanide anions: physicochemical characterisation and performance as electrochemical double-layer capacitor electrolytes.* Physical Chemistry Chemical Physics, 2017. **19**(25): p. 16867-16874.
32. Rennie, A.J.R., et al., *Ionic Liquids Containing Sulfonium Cations as Electrolytes for Electrochemical Double Layer Capacitors.* The Journal of Physical Chemistry C, 2015. **119**(42): p. 23865-23874.
33. Zhong, C., et al., *A review of electrolyte materials and compositions for electrochemical supercapacitors.* Chemical Society Reviews, 2015. **44**(21): p. 7484-7539.
34. Zeller, M., et al., *Relationship Between Structural Properties and Electrochemical Characteristics of Monolithic Carbon Xerogel-Based Electrochemical Double-Layer Electrodes in Aqueous and Organic Electrolytes.* Advanced Energy Materials, 2012. **2**(5): p. 598-605.
35. Zhou, S.-Y., et al., *Effect of activated carbon and electrolyte on properties of supercapacitor.* Transactions of Nonferrous Metals Society of China, 2007. **17**(6): p. 1328-1333.
36. Bello, A., et al., *Renewable pine cone biomass derived carbon materials for supercapacitor application.* RSC Advances, 2016. **6**(3): p. 1800-1809.
37. Peng, C., et al., *Promising activated carbons derived from waste tea-leaves and their application in high performance supercapacitors electrodes.* Electrochimica Acta, 2013. **87**: p. 401-408.
38. Qian, W., et al., *Human hair-derived carbon flakes for electrochemical supercapacitors.* Energy & Environmental Science, 2014. **7**(1): p. 379-386.
39. Wang, K., et al., *Promising biomass-based activated carbons derived from willow catkins for high performance supercapacitors.* Electrochimica Acta, 2015. **166**: p. 1-11.
40. Wang, X., et al., *Low-cost, green synthesis of highly porous carbons derived from lotus root shell as superior performance electrode materials in supercapacitor.* Journal of Energy Chemistry, 2016. **25**(1): p. 26-34.
41. Zhan, C., et al., *Flour food waste derived activated carbon for high-performance supercapacitors.* RSC Advances, 2016. **6**(92): p. 89391-89396.
42. Ferrero, G.A., A.B. Fuertes, and M. Sevilla, *From Soybean residue to advanced supercapacitors.* Scientific Reports, 2015. **5**: p. 16618.
43. Ruan, C., K. Ai, and L. Lu, *Biomass-derived carbon materials for high-performance supercapacitor electrodes.* RSC Advances, 2014. **4**(58): p. 30887-30895.
44. Sudhan, N., et al., *Biomass-Derived Activated Porous Carbon from Rice Straw for a High-Energy Symmetric Supercapacitor in Aqueous and Non-aqueous Electrolytes.* Energy & Fuels, 2017. **31**(1): p. 977-985.
45. Adinaveen, T., et al., *Surface and porous characterization of activated carbon prepared from pyrolysis of biomass (rice straw) by two-stage procedure and its applications in supercapacitor electrodes.* Journal of Material Cycles and Waste Management, 2015. **17**(4): p. 736-747.
46. Pandolfo, A.G. and A.F. Hollenkamp, *Carbon properties and their role in supercapacitors.* Journal of Power Sources, 2006. **157**(1): p. 11-27.
47. Kötz, R. and M. Carlen, *Principles and applications of electrochemical capacitors.* Electrochimica Acta, 2000. **45**(15): p. 2483-2498.

48. Wessells, C., et al., *Investigations of the Electrochemical Stability of Aqueous Electrolytes for Lithium Battery Applications.* Electrochemical and Solid-State Letters, 2010. **13**(5): p. A59-A61.
49. Dai, Z., et al., *Cell voltage versus electrode potential range in aqueous supercapacitors.* Scientific Reports, 2015. **5**: p. 9854.
50. Tomiyasu, H., et al., *An aqueous electrolyte of the widest potential window and its superior capability for capacitors.* Scientific Reports, 2017. **7**: p. 45048.
51. Zhong, C., et al., *Electrolytes for Electrochemical Supercapacitors*. 2016: CRC Press.
52. Dincer, I., *Comprehensive Energy Systems*. 2018: Elsevier Science.
53. Kim, M., I. Oh, and J. Kim, *Effects of different electrolytes on the electrochemical and dynamic behavior of electric double layer capacitors based on a porous silicon carbide electrode.* Physical Chemistry Chemical Physics, 2015. **17**(25): p. 16367-16374.
54. Armand, M., et al., *Ionic-liquid materials for the electrochemical challenges of the future.* Nature Materials, 2009. **8**: p. 621.
55. Wasserscheid, P. and T. Welton, *Ionic Liquids in Synthesis.* Organic Process Research & Development, 2003. **7**(2): p. 223-224.
56. Kumar, V. and S.V. Malhotra, *Ionic Liquids as Pharmaceutical Salts: A Historical Perspective*, in *Ionic Liquid Applications: Pharmaceuticals, Therapeutics, and Biotechnology*. 2010, American Chemical Society. p. 1-12.
57. Rodriguez Castillo, A.S., et al., *Physicochemical properties of some hydrophobic room-temperature ionic liquids applied to volatile organic compounds biodegradation processes.* Journal of Chemical Technology & Biotechnology, 2017. **93**(1): p. 215-223.
58. Noofeli, A., P.J. Hall, and A.J.R. Rennie, *Ionic liquid based EDLCs: influence of carbon porosity on electrochemical performance.* Faraday Discussions, 2014. **172**(0): p. 163-177.
59. Martins, V.L., et al., *Improved Performance of Ionic Liquid Supercapacitors by using Tetracyanoborate Anions.* ChemElectroChem: p. n/a-n/a.
60. Pohlmann, S., et al., *The influence of pore size and surface area of activated carbons on the performance of ionic liquid based supercapacitors.* Physical Chemistry Chemical Physics, 2013. **15**(40): p. 17287-17294.
61. Gu, W. and G. Yushin, *Review of nanostructured carbon materials for electrochemical capacitor applications: advantages and limitations of activated carbon, carbide‐derived carbon, zeolite‐templated carbon, carbon aerogels, carbon nanotubes, onion‐like carbon, and graphene.* Wiley Interdisciplinary Reviews: Energy and Environment, 2014. **3**(5): p. 424-473.
62. Hall, P.J., et al., *Energy storage in electrochemical capacitors: designing functional materials to improve performance.* Energy & Environmental Science, 2010. **3**(9): p. 1238-1251.
63. Koh, A.R., et al., *The effect of the ionic size of small quaternary ammonium BF4 salts on electrochemical double layer capacitors.* Physical Chemistry Chemical Physics, 2014. **16**(29): p. 15146-15151.
64. Huang, M.-M., et al., *Static relative dielectric permittivities of ionic liquids at 25 C.* Journal of Chemical & Engineering Data, 2011. **56**(4): p. 1494-1499.
65. Kim, D., P.K. Kannan, and C.-H. Chung, *High-Performance Flexible Supercapacitors Based on Ionogel Electrolyte with an Enhanced Ionic Conductivity.* ChemistrySelect, 2018. **3**(7): p. 2190-2195.
66. Wang, G., L. Zhang, and J. Zhang, *A review of electrode materials for electrochemical supercapacitors.* Chem Soc Rev, 2012. **41**(2): p. 797-828.
67. Lozano-Castelló, D., et al., *Influence of pore structure and surface chemistry on electric double layer capacitance in non-aqueous electrolyte.* Carbon, 2003. **41**(9): p. 1765-1775.
68. He, Y., *Capacitive Mechanism of Oxygen Functional Groups on Carbon Surface in Supercapacitors.* arXiv preprint arXiv:1704.08405, 2017.
69. Kikuchi, K., et al., *Double Layer Properties of Spent Coffee Grounds-derived Carbon Activated with Potassium Hydroxide (KOH).* Electrochemistry, 2013. **81**(10): p. 828-832.
70. Shi, H., *Activated carbons and double layer capacitance.* Electrochimica Acta, 1996. **41**(10): p. 1633-1639.

71. Wang, J. and S. Kaskel, *KOH activation of carbon-based materials for energy storage.* Journal of Materials Chemistry, 2012. **22**(45): p. 23710-23725.
72. Yang, H., et al., *Achieving Both High Power and Energy Density in Electrochemical Supercapacitors with Nanoporous Graphene Materials.* arXiv preprint arXiv:1311.1413, 2013.
73. Zhang, L.L., R. Zhou, and X.S. Zhao, *Graphene-based materials as supercapacitor electrodes.* Journal of Materials Chemistry, 2010. **20**(29): p. 5983.
74. Quintero, R., et al., *Carbon nanotube 3D current collectors for lightweight, high performance and low cost supercapacitor electrodes.* RSC Advances, 2014. **4**(16): p. 8230-8237.
75. Kurig, H., et al., *Electrochemical Characteristics of Titanium Carbide Derived Carbon|1-Ethyl-3-Methylimidazolium Tetrafluoroborate Electrical Double Layer Capacitors.* ECS Transactions, 2010. **25**(23): p. 15-23.
76. Song, W.-L., X. Li, and L.-Z. Fan, *Biomass derivative/graphene aerogels for binder-free supercapacitors.* Energy Storage Materials, 2016. **3**: p. 113-122.
77. Bryan, A.M., et al., *Conducting polymers for pseudocapacitive energy storage.* Chemistry of Materials, 2016. **28**(17): p. 5989-5998.
78. Augustyn, V., P. Simon, and B. Dunn, *Pseudocapacitive oxide materials for high-rate electrochemical energy storage.* Energy & Environmental Science, 2014. **7**(5): p. 1597-1614.
79. Lee, G., C.V. Varanasi, and J. Liu, *Effects of morphology and chemical doping on electrochemical properties of metal hydroxides in pseudocapacitors.* Nanoscale, 2015. **7**(7): p. 3181-3188.
80. Liu, M., et al., *Nitrogen-doped graphene nanoribbons as efficient metal-free electrocatalysts for oxygen reduction.* ACS Appl Mater Interfaces, 2014. **6**(6): p. 4214-22.
81. Ioannidou, O. and A. Zabaniotou, *Agricultural residues as precursors for activated carbon production—A review.* Renewable and Sustainable Energy Reviews, 2007. **11**(9): p. 1966-2005.
82. Low, L.W., et al., *Carbonization of Elaeis guineensis frond fiber: Effect of heating rate and nitrogen gas flow rate for adsorbent properties enhancement.* Journal of Industrial and Engineering Chemistry, 2015. **28**: p. 37-44.
83. Zeng, K., et al., *The effect of temperature and heating rate on char properties obtained from solar pyrolysis of beech wood.* Bioresource Technology, 2015. **182**: p. 114-119.
84. Guerrero, M., et al., *Pyrolysis of eucalyptus at different heating rates: studies of char characterization and oxidative reactivity.* Journal of Analytical and Applied Pyrolysis, 2005. **74**(1–2): p. 307-314.
85. Li, A., et al., *Effects of Temperature and Heating Rate on the Characteristics of Molded Bio-char*. 2016. Vol. 11. 2016.
86. Mermoud, F., et al., *Influence of the pyrolysis heating rate on the steam gasification rate of large wood char particles.* Fuel, 2006. **85**(10–11): p. 1473-1482.
87. Ponrouch, A., et al., *In search of an optimized electrolyte for Na-ion batteries.* Energy & Environmental Science, 2012. **5**(9): p. 8572-8583.
88. Shi, L., et al., *Effect of heating rate on the electrochemical performance of MnO X @CNF nanocomposites as supercapacitor electrodes.* Chinese Science Bulletin, 2014. **59**(16): p. 1832-1837.
89. Yu, J., J.A. Lucas, and T.F. Wall, *Formation of the structure of chars during devolatilization of pulverized coal and its thermoproperties: A review.* Progress in Energy and Combustion Science, 2007. **33**(2): p. 135-170.
90. Zhang, Z., et al., *Effect of Temperature and Heating Rate in Pyrolysis on the Yield, Structure and Oxidation Reactivity of Pine Sawdust Biochar*, in *Proceedings of Chemeca 2013: Challenging Tomorrow*. 2013, Engineers Media Pty Ltd. p. 7pp.
91. Fu, P., et al., *Evaluation of the porous structure development of chars from pyrolysis of rice straw: Effects of pyrolysis temperature and heating rate.* Journal of Analytical and Applied Pyrolysis, 2012. **98**: p. 177-183.
92. Cetin, E., R. Gupta, and B. Moghtaderi, *Effect of pyrolysis pressure and heating rate on radiata pine char structure and apparent gasification reactivity.* Fuel, 2005. **84**(10): p. 1328-1334.
93. Kim, D.-W., et al., *Structural elucidation of physical and chemical activation mechanisms based on the microdomain structure model.* Carbon, 2017. **114**: p. 98-105.

94. Lozano-Castelló, D., et al., *Preparation of activated carbons from Spanish anthracite: I. Activation by KOH.* Carbon, 2001. **39**(5): p. 741-749.
95. Zhou, W., et al., *Carbon Materials for Supercapacitors*, in *Nanomaterials in Advanced Batteries and Supercapacitors*, K.I. Ozoemena and S. Chen, Editors. 2016, Springer International Publishing: Cham. p. 271-315.
96. Wang, J., et al., *Biomass derived carbon for energy storage devices.* Journal of Materials Chemistry A, 2017.
97. Deng, J., M. Li, and Y. Wang, *Biomass-derived carbon: synthesis and applications in energy storage and conversion.* Green Chemistry, 2016. **18**(18): p. 4824-4854.
98. Rodríguez-Reinoso, F. and M. Molina-Sabio, *Textural and chemical characterization of microporous carbons.* Advances in Colloid and Interface Science, 1998. **76**: p. 271-294.
99. Calo, J.M. and M.T. Perkins, *A heterogeneous surface model for the "steady-state" kinetics of the boudouard reaction.* Carbon, 1987. **25**(3): p. 395-407.
100. Hunt, J., et al., *Microwave-Specific Enhancement of the Carbon–Carbon Dioxide (Boudouard) Reaction.* The Journal of Physical Chemistry C, 2013. **117**(51): p. 26871-26880.
101. González, J.F., et al., *Porosity Development in Activated Carbons Prepared from Walnut Shells by Carbon Dioxide or Steam Activation.* Industrial & Engineering Chemistry Research, 2009. **48**(16): p. 7474-7481.
102. Jung, S.-H. and J.-S. Kim, *Production of biochars by intermediate pyrolysis and activated carbons from oak by three activation methods using CO2.* Journal of Analytical and Applied Pyrolysis, 2014. **107**: p. 116-122.
103. Ngernyen, Y., C. Tangsathitkulchai, and M. Tangsathitkulchai, *Porous properties of activated carbon produced from Eucalyptus and Wattle wood by carbon dioxide activation.* Korean Journal of Chemical Engineering, 2006. **23**(6): p. 1046-1054.
104. Sulaiman, K.S., A. Mat, and A.K. Arof, *Activated carbon from coconut leaves for electrical double-layer capacitor.* Ionics, 2016. **22**(6): p. 911-918.
105. Seixas F., et al., *Activated Carbon from Sugarcane Bagasse Prepared by Activation with CO2 and Bio Oil Recuperation.* CHEMICAL ENGINEERING TRANSACTIONS, 2017. **57**: p. 139-144.
106. Wei, L. and G. Yushin, *Electrical double layer capacitors with sucrose derived carbon electrodes in ionic liquid electrolytes.* Journal of Power Sources, 2011. **196**(8): p. 4072-4079.
107. Valente Nabais, J.M., J.G. Teixeira, and I. Almeida, *Development of easy made low cost bindless monolithic electrodes from biomass with controlled properties to be used as electrochemical capacitors.* Bioresource Technology, 2011. **102**(3): p. 2781-2787.
108. Yu, M., et al., *CO2-activated porous carbon derived from cattail biomass for removal of malachite green dye and application as supercapacitors.* Chemical Engineering Journal, 2017. **317**(Supplement C): p. 493-502.
109. Nabais, J.M.V., et al., *Production of activated carbons from coffee endocarp by CO2 and steam activation.* Fuel Processing Technology, 2008. **89**(3): p. 262-268.
110. Chang, C.-F., C.-Y. Chang, and W.-T. Tsai, *Effects of Burn-off and Activation Temperature on Preparation of Activated Carbon from Corn Cob Agrowaste by CO2 and Steam.* Journal of Colloid and Interface Science, 2000. **232**(1): p. 45-49.
111. Demiral, H., et al., *Production of activated carbon from olive bagasse by physical activation.* Chemical Engineering Research and Design, 2011. **89**(2): p. 206-213.
112. Olivares-Marín, M., et al., *Preparation of activated carbon from cherry stones by physical activation in air. Influence of the chemical carbonisation with H2SO4.* Journal of Analytical and Applied Pyrolysis, 2012. **94**(Supplement C): p. 131-137.
113. Román, S., et al., *Control of pore development during CO2 and steam activation of olive stones.* Fuel Processing Technology, 2008. **89**(8): p. 715-720.
114. Ruiz-Fernández, M., et al., *Development of activated carbon from vine shoots by physical and chemical activation methods. Some insight into activation mechanisms.* Adsorption, 2011. **17**(3): p. 621-629.
115. Chang, J., et al., *Activated porous carbon prepared from paulownia flower for high performance supercapacitor electrodes.* Electrochimica Acta, 2015. **157**: p. 290-298.

116. Xu, J., et al., *Preparing two-dimensional microporous carbon from Pistachio nutshell with high areal capacitance as supercapacitor materials.* Scientific Reports, 2014. **4**: p. 5545.
117. Blomquist, N., et al., *Metal-free supercapacitor with aqueous electrolyte and low-cost carbon materials.* Scientific Reports, 2017. **7**: p. 39836.
118. Wei, L. and G. Yushin, *Nanostructured activated carbons from natural precursors for electrical double layer capacitors.* Nano Energy, 2012. **1**(4): p. 552-565.
119. Wei, L., et al., *Hydrothermal Carbonization of Abundant Renewable Natural Organic Chemicals for High-Performance Supercapacitor Electrodes.* Advanced Energy Materials, 2011. **1**(3): p. 356-361.
120. Wang, D.-W., et al., *3D Aperiodic Hierarchical Porous Graphitic Carbon Material for High-Rate Electrochemical Capacitive Energy Storage.* Angewandte Chemie International Edition, 2007. **47**(2): p. 373-376.
121. He, X., et al., *Efficient preparation of biomass-based mesoporous carbons for supercapacitors with both high energy density and high power density.* Journal of Power Sources, 2013. **240**(Supplement C): p. 109-113.
122. Si, W.-J., et al., *Bagasse-based Nanoporous Carbon for Supercapacitor Application.* Journal of Inorganic Materials;, 2011. **26**(1): p. 107-113.
123. Zhang, L., et al., *High-Performance Supercapacitor Electrode Materials Prepared from Various Pollens.* Small, 2013. **9**(8): p. 1342-1347.
124. Biswal, M., et al., *From dead leaves to high energy density supercapacitors.* Energy & Environmental Science, 2013. **6**(4): p. 1249-1259.
125. Global Invasive Species Database *Species profile: Dichrostachys cinerea.* 2017.
126. Fernández, M., et al., *Energy use of Marabou weed (Dichrostachys cinerea L.) as an aid to mechanical control*. 2013, Universitat Politècnica de València: València. p. 103-107.
127. Szenthe, A. *Top Coffee Producing Countries*. 2017; Available from: http://www.worldatlas.com/articles/top-coffee-producing-countries.html.
128. Chin, K.L., et al., *Production of glucose from oil palm trunk and sawdust of rubberwood and mixed hardwood.* Applied Energy, 2011. **88**(11): p. 4222-4228.
129. Biofuel Resource *EFB Pellet*. 2017 [cited 2017 10-7]; Available from: http://www.biofuelresource.com/efb-pellet/.
130. Elementar, *The Elemental Analyzer Vario macro cube*. 2014: GmbH.
131. Lowell, S. and J.E. Shields, *Powder Surface Area and Porosity*. 2013: Springer Netherlands.
132. Barrett, E.P., L.G. Joyner, and P.P. Halenda, *The Determination of Pore Volume and Area Distributions in Porous Substances. I. Computations from Nitrogen Isotherms.* Journal of the American Chemical Society, 1951. **73**(1): p. 373-380.
133. Thomson, W., *LX. On the equilibrium of vapour at a curved surface of liquid.* The London, Edinburgh, and Dublin Philosophical Magazine and Journal of Science, 1871. **42**(282): p. 448-452.
134. Lippens, B.C. and J.H. de Boer, *Studies on pore systems in catalysts: V. The t method.* Journal of Catalysis, 1965. **4**(3): p. 319-323.
135. Halsey, G., *Physical Adsorption on Non‐Uniform Surfaces.* The Journal of Chemical Physics, 1948. **16**(10): p. 931-937.
136. Margreth, M., *Fundamentals of Karl Fischer Titration*. 2016.
137. Peter Bruttel and R. Schlink, *Water determination by Karl Fischer Titration (Monograph)*.
138. Rennie, A.J.R., et al., *Influence of Particle Size Distribution on the Performance of Ionic Liquid-based Electrochemical Double Layer Capacitors.* Scientific Reports, 2016. **6**: p. 22062.
139. Xu, K., S.P. Ding, and T.R. Jow, *Toward Reliable Values of Electrochemical Stability Limits for Electrolytes.* Journal of The Electrochemical Society, 1999. **146**(11): p. 4172-4178.
140. Weingarth, D., et al., *A reliable determination method of stability limits for electrochemical double layer capacitors.* Electrochimica Acta, 2013. **103**: p. 119-124.
141. Xu, K., M.S. Ding, and T. Richard Jow, *A better quantification of electrochemical stability limits for electrolytes in double layer capacitors.* Electrochimica Acta, 2001. **46**(12): p. 1823-1827.

142. Kang, J., et al., *Development of an equivalent circuit model for electrochemical double layer capacitors (EDLCs) with distinct electrolytes.* Electrochimica Acta, 2014. **115**(Supplement C): p. 587-598.
143. Niu, R. and H. Yang. *Modeling and identification of electric double-layer supercapacitors*. in *2011 IEEE International Conference on Robotics and Automation*. 2011.
144. Yuan, X.Z., et al., *Electrochemical Impedance Spectroscopy in PEM Fuel Cells: Fundamentals and Applications*. 2009: Springer London.
145. Randles, J.E.B., *Kinetics of rapid electrode reactions.* Discussions of the Faraday Society, 1947. **1**(0): p. 11-19.
146. Yu, L., et al., *3D porous gear-like copper oxide and their high electrochemical performance as supercapacitors.* CrystEngComm, 2013. **15**(38): p. 7657-7662.
147. Kumagai, S., M. Hatomi, and D. Tashima, *Electrochemical performance of microporous and mesoporous activated carbons in neat and diluted 1-ethyl-3-methylimidazolium tetrafluoroborate.* Journal of Power Sources, 2017. **343**(Supplement C): p. 303-315.
148. Halim, S.A. and J. Swithenbank, *Characterisation of Malaysian wood pellets and rubberwood using slow pyrolysis and microwave technology.* Journal of Analytical and Applied Pyrolysis, 2016. **122**: p. 64-75.
149. Vardon, D.R., et al., *Complete Utilization of Spent Coffee Grounds To Produce Biodiesel, Bio-Oil, and Biochar.* ACS Sustainable Chemistry & Engineering, 2013. **1**(10): p. 1286-1294.
150. Bemgba Bevan Nyakuma, et al., *EVALUATING THE THERMOCHEMICAL FUEL PROPERTIES OF OIL PALM WASTE USING ELEMENTALANALYSIS*, in *3rd Conference on Emerging Energy and Process Technology*. 2014: Port Dickson, Malaysia.
151. Tsamba, A.J., *Fundamental study of two selected tropical biomasses for energy: coconut and cashew nut shells*. 2008, KTH.
152. Irawan, A. *Effect of torrefaction process on the coconut shell energy content for solid fuel*. in *AIP Conference Proceedings*. 2017. AIP Publishing.
153. Mezerette, C. and P. Girard, *Environmental Aspects of Gaseous Emissions from Wood Carbonisation and Pyrolysis Processes*, in *Biomass Pyrolysis Liquids Upgrading and Utilization*, A.V. Bridgwater and G. Grassi, Editors. 1991, Springer Netherlands: Dordrecht. p. 263-287.
154. Quaak, P., H. Knoef, and H.E. Stassen, *Energy from Biomass: A Review of Combustion and Gasification Technologies*. 1999: World Bank.
155. Telmo, C., J. Lousada, and N. Moreira, *Proximate analysis, backwards stepwise regression between gross calorific value, ultimate and chemical analysis of wood.* Bioresource Technology, 2010. **101**(11): p. 3808-3815.
156. Jiang, L., et al., *Influence of different demineralization treatments on physicochemical structure and thermal degradation of biomass.* Bioresource Technology, 2013. **146**: p. 254-260.
157. Stefanidis, S.D., et al., *Optimization of bio-oil yields by demineralization of low quality biomass.* Biomass and Bioenergy, 2015. **83**: p. 105-115.
158. Chaula, Z., et al., *Modelling the Suitability of Pine Sawdust for Energy Production via Biomass Steam Explosion.* Smart Grid and Renewable Energy, 2014. **Vol.05No.01**: p. 7.
159. Collard, F.-X. and J. Blin, *A review on pyrolysis of biomass constituents: Mechanisms and composition of the products obtained from the conversion of cellulose, hemicelluloses and lignin.* Renewable and Sustainable Energy Reviews, 2014. **38**(Supplement C): p. 594-608.
160. Shen, J., et al., *Effects of particle size on the fast pyrolysis of oil mallee woody biomass.* Fuel, 2009. **88**(10): p. 1810-1817.
161. Katyal, S., K. Thambimuthu, and M. Valix, *Carbonisation of bagasse in a fixed bed reactor: influence of process variables on char yield and characteristics.* Renewable Energy, 2003. **28**(5): p. 713-725.
162. Al-Khalid, T.T., et al., *Activation of olive-seed waste residue using CO2 in a fluidized-bed reactor.* Fuel Processing Technology, 1998. **57**(1): p. 55-64.
163. Smets, K., et al., *Rapeseed and Raspberry Seed Cakes as Inexpensive Raw Materials in the Production of Activated Carbon by Physical Activation: Effect of Activation Conditions on Textural and Phenol Adsorption Characteristics.* Materials, 2016. **9**(7): p. 565.

164. Sadezky, A., et al., *Raman microspectroscopy of soot and related carbonaceous materials: Spectral analysis and structural information.* Carbon, 2005. **43**(8): p. 1731-1742.
165. Schwan, J., et al., *Raman spectroscopy on amorphous carbon films.* Journal of Applied Physics, 1996. **80**(1): p. 440-447.
166. Ferrari, A. and J. Robertson, *Resonant Raman spectroscopy of disordered, amorphous, and diamondlike carbon.* Physical Review B, 2001. **64**(7): p. 075414.
167. Gomez Sanz, S., et al., *A new perspective on catalytic dehydrogenation of ethylbenzene: the influence of side-reactions on catalytic performance.* Catalysis Science & Technology, 2015. **5**(7): p. 3782-3797.
168. Seong, H.J. and A.L. Boehman, *Evaluation of Raman Parameters Using Visible Raman Microscopy for Soot Oxidative Reactivity.* Energy & Fuels, 2013. **27**(3): p. 1613-1624.
169. *<supplement data for [An].pdf>*.
170. Zhao, Y., et al., *Effect of pyrolysis temperature on char structure and chemical speciation of alkali and alkaline earth metallic species in biochar.* Fuel Processing Technology, 2016. **141**: p. 54-60.
171. Chernyak, S.A., et al., *Oxidation, defunctionalization and catalyst life cycle of carbon nanotubes: a Raman spectroscopy view.* Physical Chemistry Chemical Physics, 2017. **19**(3): p. 2276-2285.
172. Cuesta, A., et al., *Raman microprobe studies on carbon materials.* Carbon, 1994. **32**(8): p. 1523-1532.
173. Ruiz, V., et al., *Effects of thermal treatment of activated carbon on the electrochemical behaviour in supercapacitors.* Electrochimica Acta, 2007. **52**(15): p. 4969-4973.
174. Lee, A.F., et al., *A Fast XPS study of the surface chemistry of ethanol over Pt{1 1 1}.* Surface science, 2004. **548**(1-3): p. 200-208.
175. Kravets, L.I., et al., *Structure and electrochemical properties of track membranes with a polymer layer obtained by plasma polymerization of acetylene.* Journal of Physics: Conference Series, 2014. **516**(1): p. 012006.
176. Rybachuk, M. and J.M. Bell, *Electronic states of trans-polyacetylene, poly(p-phenylene vinylene) and sp-hybridised carbon species in amorphous hydrogenated carbon probed by resonant Raman scattering.* Carbon, 2009. **47**(10): p. 2481-2490.
177. Zhang, L., et al., *Growth and field electron emission properties of nanostructured white carbon films.* Journal of Vacuum Science & Technology B: Microelectronics and Nanometer Structures Processing, Measurement, and Phenomena, 2007. **25**(2): p. 545-547.
178. Wu, X.-L., et al., *Biomass-Derived Sponge-like Carbonaceous Hydrogels and Aerogels for Supercapacitors.* ACS Nano, 2013. **7**(4): p. 3589-3597.
179. Chua, C.K. and M. Pumera, *Renewal of sp2 bonds in graphene oxides via dehydrobromination.* Journal of Materials Chemistry, 2012. **22**(43): p. 23227-23231.
180. Dave, K., K.H. Park, and M. Dhayal, *Two-step process for programmable removal of oxygen functionalities of graphene oxide: functional, structural and electrical characteristics.* RSC Advances, 2015. **5**(116): p. 95657-95665.
181. Huang, Y.-L., et al., *Effect of extended polymer chains on properties of transparent graphene nanosheets conductive film.* Journal of Materials Chemistry, 2011. **21**(45): p. 18236-18241.
182. Wu, M., et al., *Rice (Oryza sativa L) plantation affects the stability of biochar in paddy soil.* Scientific Reports, 2015. **5**: p. 10001.
183. Molina-Sabio, M., et al., *Development of porosity in combined phosphoric acid-carbon dioxide activation.* Carbon, 1996. **34**(4): p. 457-462.
184. Jiang, J., et al., *Highly ordered macroporous woody biochar with ultra-high carbon content as supercapacitor electrodes.* Electrochimica Acta, 2013. **113**: p. 481-489.
185. Ferrari, A.C. and J. Robertson, *Interpretation of Raman spectra of disordered and amorphous carbon.* Physical review B, 2000. **61**(20): p. 14095.
186. Paul, R., et al., *Synthesis of DLC films with different sp2/sp3 ratios and their hydrophobic behaviour.* Journal of Physics D: Applied Physics, 2008. **41**(5): p. 055309.
187. Xia, K., et al., *Hierarchical porous graphene-based carbons prepared by carbon dioxide activation and their gas adsorption properties.* International Journal of Hydrogen Energy, 2014. **39**(21): p. 11047-11054.

188. Wigmans, T., *Industrial aspects of production and use of activated carbons.* Carbon, 1989. **27**(1): p. 13-22.
189. Dietz, S., *Production Scale-Up of Activated Carbons for Ultracapacitors*. 2017: TDA research.
190. Kim, J.-A.P., In-Soo; Seo, Ji-Hye; Lee, Jung-Joo, *A Development of High Power Activated Carbon Using the KOH Activation of Soft Carbon Series Cokes.* Transactions on Electrical and Electronic Materials 2014. **15**.
191. Cruz Ceballos, D.C., K. Hawboldt, and R. Hellleur, *Effect of production conditions on self-heating propensity of torrefied sawmill residues.* Fuel, 2015. **160**(Supplement C): p. 227-237.
192. Wang, H., B.Z. Dlugogorski, and E.M. Kennedy, *Analysis of the mechanism of the low-temperature oxidation of coal.* Combustion and Flame, 2003. **134**(1): p. 107-117.
193. Farma, R., et al., *Preparation of highly porous binderless activated carbon electrodes from fibres of oil palm empty fruit bunches for application in supercapacitors.* Bioresource technology, 2013. **132**: p. 254-261.
194. Taer, E., et al., *Preparation of a highly porous binderless activated carbon monolith from rubber wood sawdust by a multi-step activation process for application in supercapacitors.* Int. J. Electrochem. Sci, 2011. **6**(8): p. 3301-3315.
195. Mazlan, M.A.F., et al., *Activated Carbon from Rubber Wood Sawdust by Carbon Dioxide Activation.* Procedia Engineering, 2016. **148**(Supplement C): p. 530-537.
196. Schröder, E., et al., *Activated carbon from waste biomass*. 2011: INTECH Open Access Publisher.
197. Nakamizo, M. and K. Tamai, *Raman spectra of the oxidized and polished surfaces of carbon.* Carbon, 1984. **22**(2): p. 197-198.
198. Shimodaira, N. and A. Masui, *Raman spectroscopic investigations of activated carbon materials.* Journal of Applied Physics, 2002. **92**(2): p. 902-909.
199. Jaidev, et al., *Polyaniline-MnO2 nanotube hybrid nanocomposite as supercapacitor electrode material in acidic electrolyte.* Journal of Materials Chemistry, 2011. **21**(44): p. 17601-17605.
200. Jana, M., et al., *Non-covalent functionalization of reduced graphene oxide using sulfanilic acid azocromotrop and its application as a supercapacitor electrode material.* Journal of Materials Chemistry A, 2015. **3**(14): p. 7323-7331.
201. Abbas, Q., et al., *Effect of binder on the performance of carbon/carbon symmetric capacitors in salt aqueous electrolyte.* Electrochimica Acta, 2014. **140**: p. 132-138.
202. Kurig, H., et al., *Electrical Double Layer Capacitors Based on Two 1-Ethyl-3-Methylimidazolium Ionic Liquids with Different Anions.* Electrochemical and Solid-State Letters, 2011. **14**(8): p. A120-A122.
203. Jiang, J. and A. Kucernak, *Electrochemical supercapacitor material based on manganese oxide: preparation and characterization.* Electrochimica Acta, 2002. **47**(15): p. 2381-2386.
204. Yang, H., et al., *Rapidly annealed nanoporous graphene materials for electrochemical energy storage.* Journal of Materials Chemistry A, 2017. **5**(45): p. 23720-23726.
205. Rennie, A.J.R., et al., *Ether-Bond-Containing Ionic Liquids as Supercapacitor Electrolytes.* The Journal of Physical Chemistry Letters, 2013. **4**(17): p. 2970-2974.
206. Nishida, T., Y. Tashiro, and M. Yamamoto, *Physical and electrochemical properties of 1-alkyl-3-methylimidazolium tetrafluoroborate for electrolyte.* Journal of Fluorine Chemistry, 2003. **120**(2): p. 135-141.
207. Liu, W.-w., et al., *Flexible and conductive nanocomposite electrode based on graphene sheets and cotton cloth for supercapacitor.* Journal of Materials Chemistry, 2012. **22**(33): p. 17245-17253.
208. Frąckowiak, E., P. Ratajczak, and F. Béguin, *Electrochemical Capacitors Based on Carbon Electrodes in Aqueous Electrolytes*, in *Electrochemistry of Carbon Electrodes*. 2015, Wiley-VCH Verlag GmbH & Co. KGaA. p. 285-312.
209. Moon, J.S., et al., *Increasing Capacitance of Zeolite-Templated Carbons in Electric Double Layer Capacitors.* Journal of The Electrochemical Society, 2015. **162**(5): p. A5070-A5076.
210. Nian, Y.-R. and H. Teng, *Influence of surface oxides on the impedance behavior of carbon-based electrochemical capacitors.* Journal of Electroanalytical Chemistry, 2003. **540**: p. 119-127.

211. Acznik, I., K. Lota, and A. Sierczyńska, *Improvement of power–energy characteristic of the lithium-ion capacitor by structure modification of the graphite anode.* MRS Communications, 2017. **7**(2): p. 245-252.
212. Barzegar, F., et al., *Effect of conductive additives to gel electrolytes on activated carbon-based supercapacitors.* AIP Advances, 2015. **5**(9): p. 097171.
213. Rufford, T.E. and E. Fiset, *Biomass-Derived Carbon Electrodes for Electrochemical Double-Layer Capacitors*, in *Green Carbon Materials: Advances and Applications*, T.E. Rufford and D. Hulicova-Jurcakova, Editors. 2014, Pan Stanford Publishing Pte Ltd: Singapore.
214. Marcilla, A., M. Asensio, and I. Martín-Gullón, *Influence of the carbonization heating rate on the physical properties of activated carbons from a sub-bituminous coal.* Carbon, 1996. **34**(4): p. 449-456.
215. Yang, W., et al., *Fabrication of microporous and mesoporous carbon spheres for high‐performance supercapacitor electrode materials.* International Journal of Energy Research, 2015. **39**(6): p. 805-811.
216. Li, Y., et al., *A top-down approach for fabricating free-standing bio-carbon supercapacitor electrodes with a hierarchical structure.* Scientific Reports, 2015. **5**: p. 14155.
217. Xu, F., et al., *Fast ion transport and high capacitance of polystyrene-based hierarchical porous carbon electrode material for supercapacitors.* Journal of Materials Chemistry, 2011. **21**(6): p. 1970-1976.
218. Zhi, J., et al., *Study on the relation between pore size and supercapacitance in mesoporous carbon electrodes with silica-supported carbon nanomembranes.* RSC Advances, 2014. **4**(76): p. 40296-40300.
219. Zhu, J., et al., *Fe-Catalyzed Synthesis of Porous Carbons Spheres with High Graphitization Degree for High-Performance Supercapacitors.* Journal of Electronic Materials, 2017. **46**(10): p. 5995-6000.
220. Chen, N., et al., *A high-performance asymmetric supercapacitor based on vanadyl phosphate/carbon nanocomposites and polypyrrole-derived carbon nanowires.* Nanoscale, 2018. **10**(8): p. 3709-3719.

Appendix A: Raman Spectra with curve fitting

(I) Activated carbon derived from Marabú

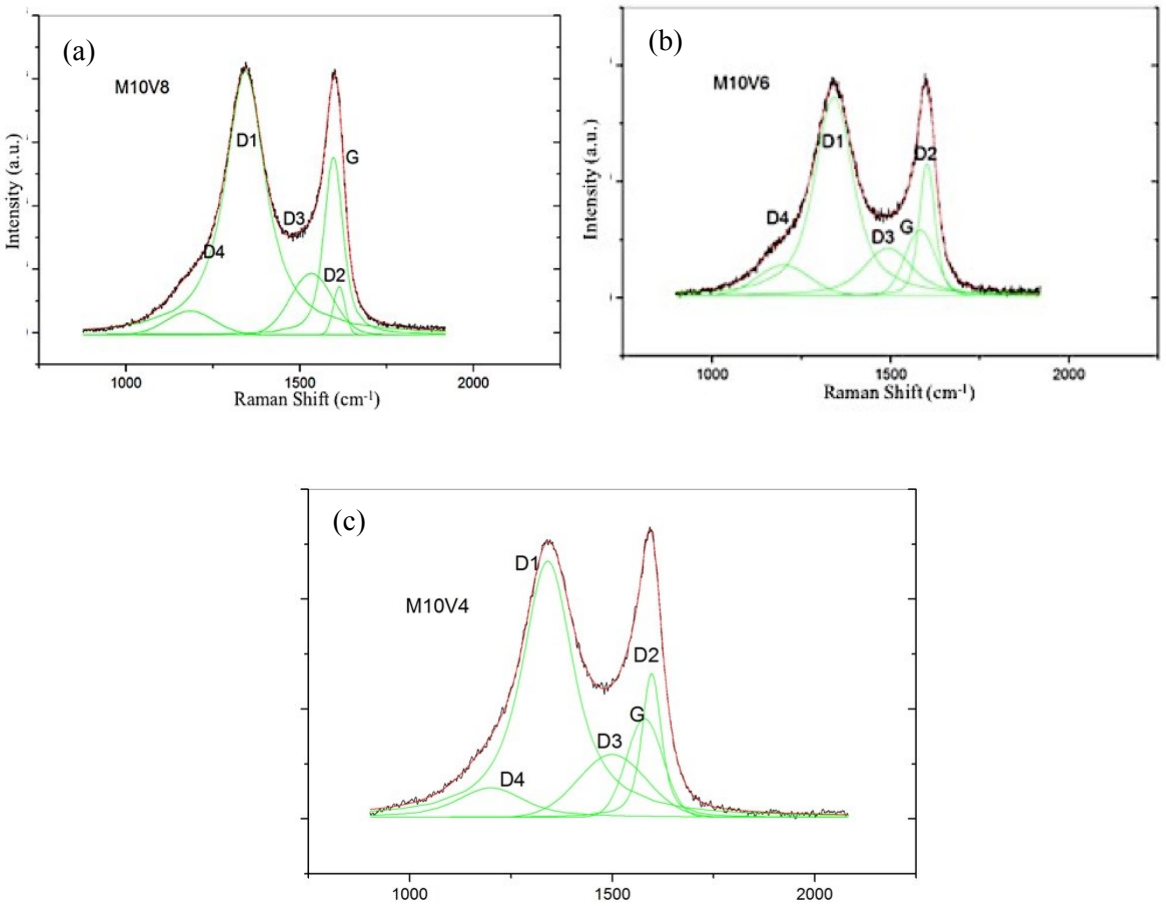

Figure A- 1: Raman spectra of (a) M10V8, (b) M10V6 and (c) M10V4 with 5 curve fitted peaks

(II) Activated carbon derived from Spent Coffee Ground (CG)

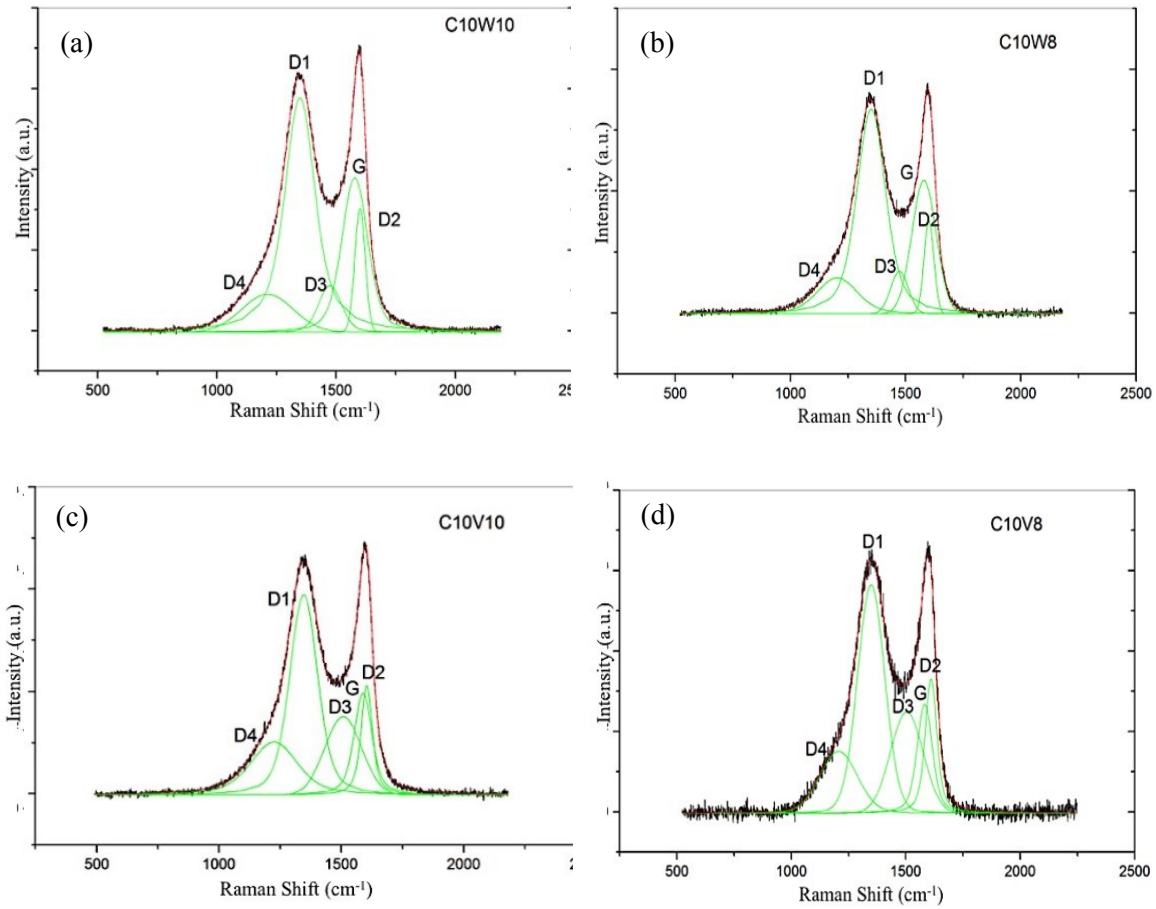

Figure A- 2: Raman spectra of (a) C10W10, (b) C10W8, (c) C10V10 (d) C10V8 with 5 curve fitted peaks.

(III) Activated carbon derived from Malaysian wastes biomass: AC derived from EFB pellets.

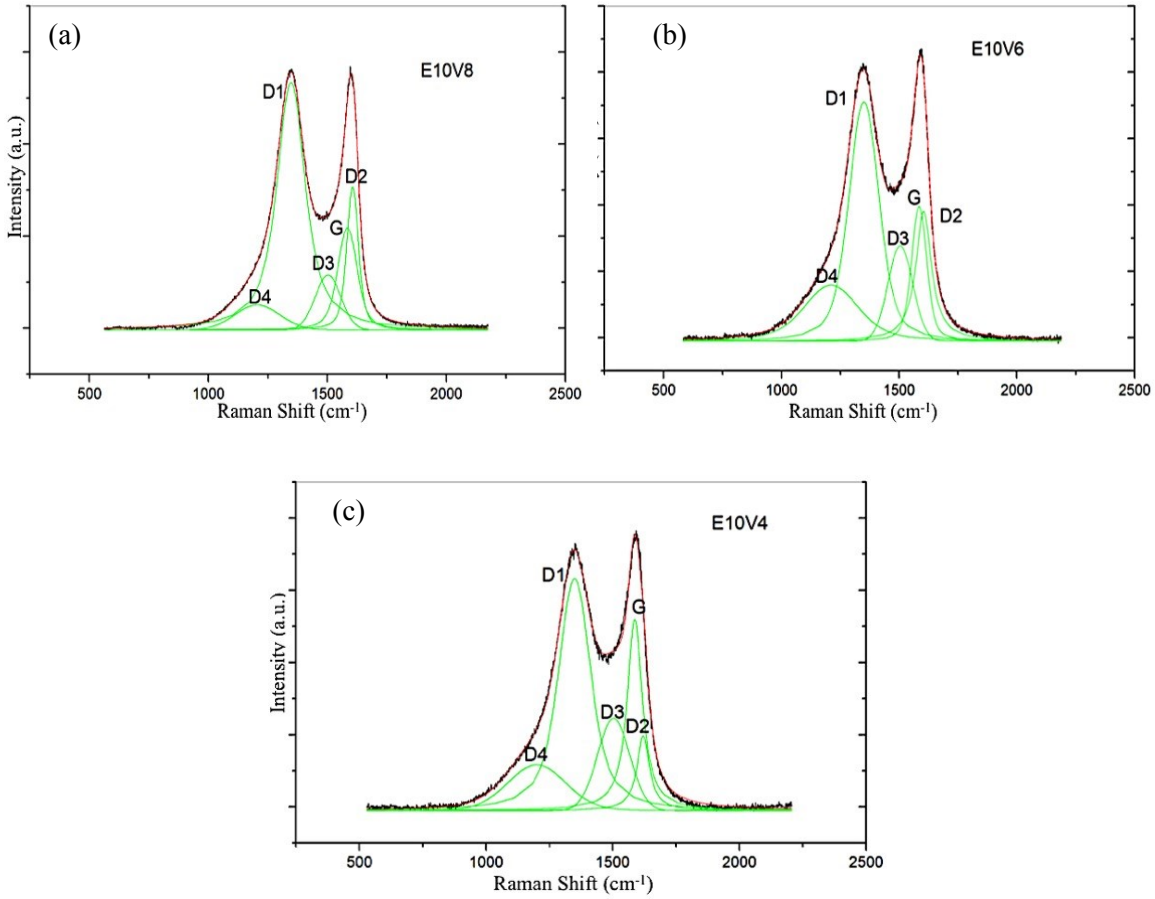

Figure A- 3: Raman spectra of (a) E10V8, (b) E10V6 and (c) E10V4 with 5 curve fitted peaks.

(IV) Activated carbon derived from Malaysian wastes biomass: AC derived from Malaysia wood pellets.

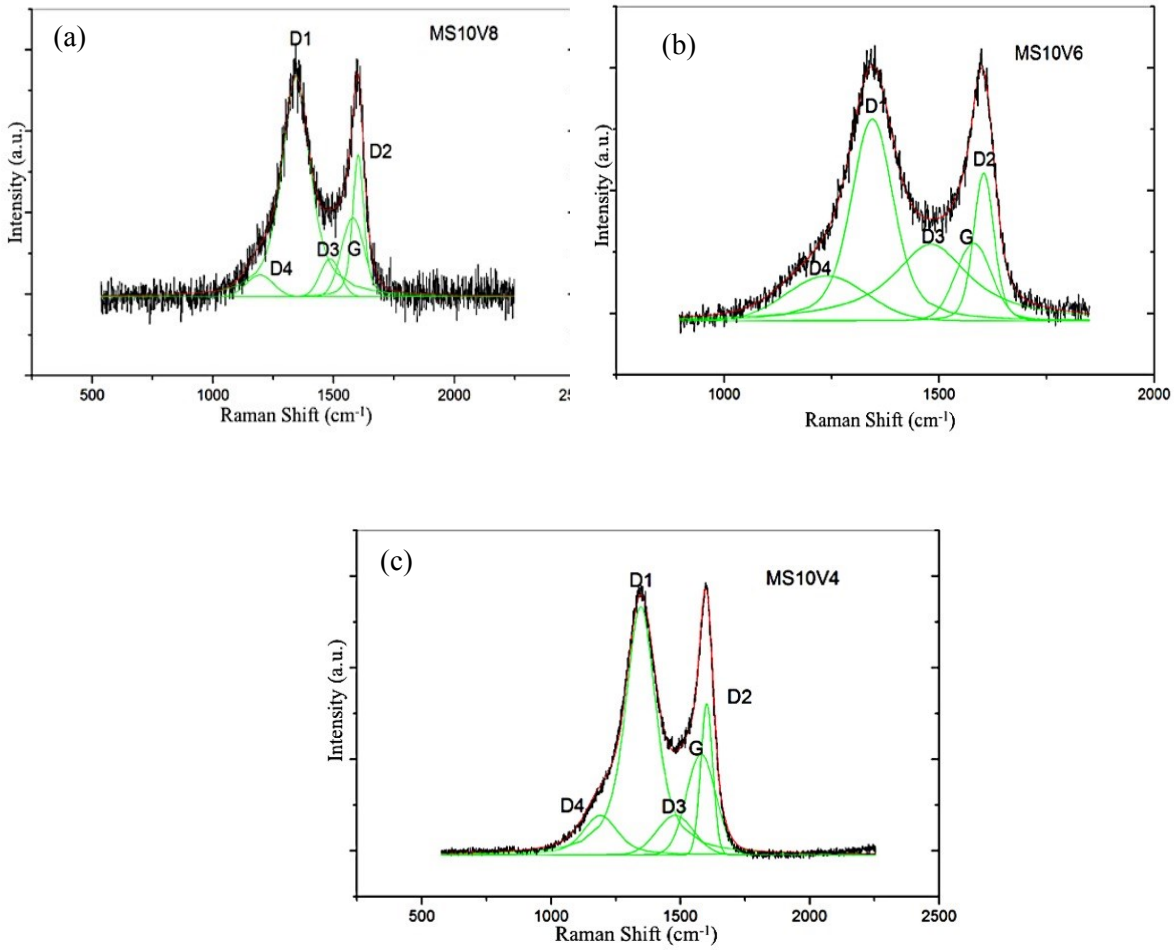

Figure A- 4: Raman spectra of (a) MS10V8, (b) MS10V6 and (c) MS10V4 with 5 curve fitted peaks.

Appendix B: EDX Analysis

Appendix B: EDX Analysis

(I) EDX analysis for R10V8

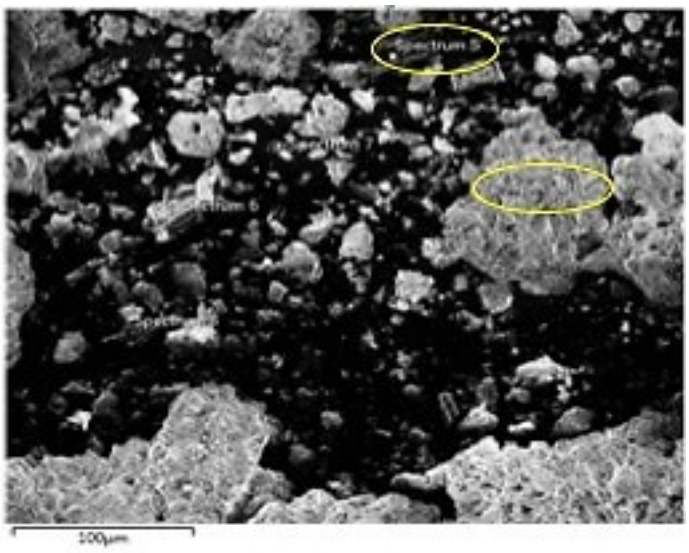

Figure B-1: EDX electron image for R10V8

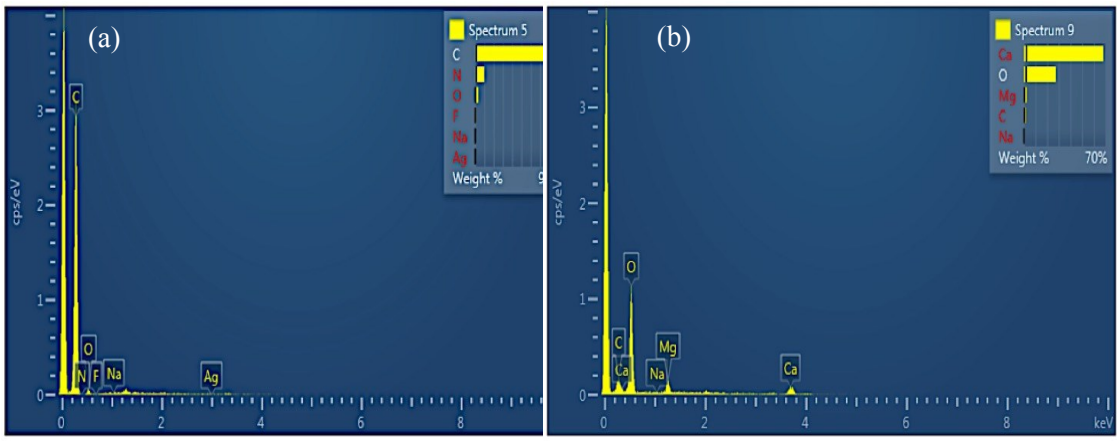

Figure B-2: Electron image (a) carbon (spectrum 5) (b) ash (spectrum 9) in the R10V8 from electron image.

(II) EDX analysis for E10V8

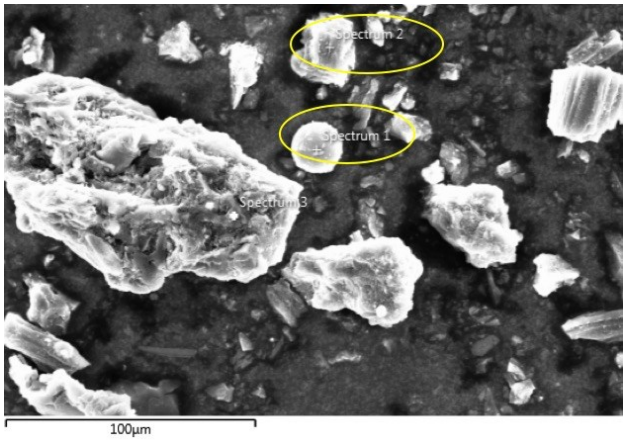

Figure B-3: (a) Electron image for E10V8

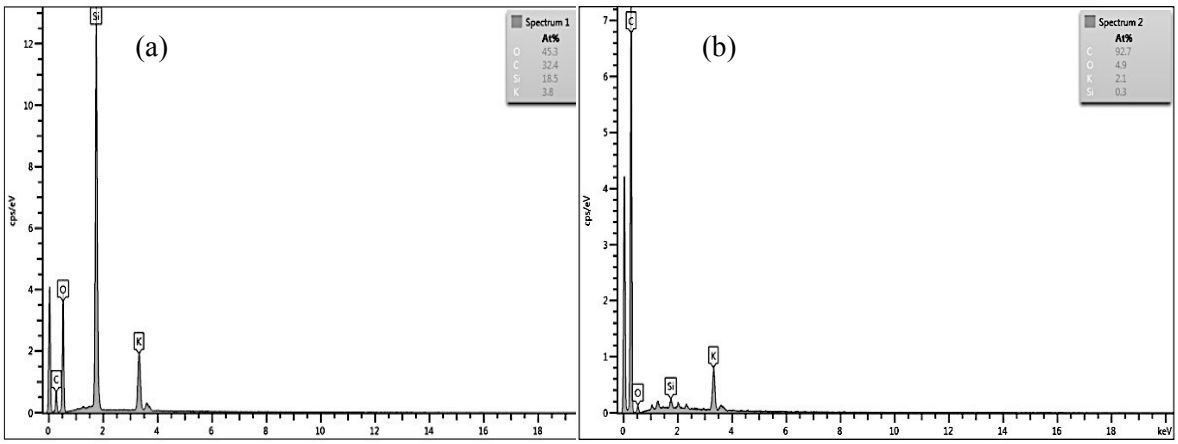

Figure B-4: Electron image (a) Spectrum 1 containing high in Si (b) Spectrum 2 containing high in carbon for E10V8